

Universiteit
Leiden
The Netherlands

Molecular electronics: controlled manipulation, noise and graphene architecture

Tewari, S.

Citation
Tewari, S. (2018, March 27). *Molecular electronics: controlled manipulation, noise and graphene architecture*. Casimir Research School, Delft. Retrieved from https://hdl.handle.net/1887/58611

Version:	Not Applicable (or Unknown)
License:	Licence agreement concerning inclusion of doctoral thesis in the Institutional Repository of the University of Leiden
Downloaded from:	https://hdl.handle.net/1887/58611

Note: To cite this publication please use the final published version (if applicable).

Cover Page



Universiteit Leiden



The following handle holds various files of this Leiden University dissertation:
http://hdl.handle.net/1887/58611

Author: Tewari, S.
Title: Molecular electronics: controlled manipulation, noise and graphene architecture
Issue Date: 2018-03-27

Molecular Electronics

Controlled manipulation, Noise and Graphene architecture

Molecular Electronics

Controlled manipulation, Noise and Graphene architecture

Proefschrift

ter verkrijging van
de graad van Doctor aan de Universiteit Leiden,
op gezag van Rector Magnificus prof. mr. C.J.J.M. Stolker
volgens besluit van het College voor Promoties
te verdedigen op dinsdag 27 maart 2018
klokke 15:00 uur

door

Sumit Tewari

geboren te Nainital, India
in 1985

Promotor:	Prof. dr. J.M. van Ruitenbeek	(Universiteit Leiden, The Netherlands)
Promotiecommissie:	Prof. dr. E.R. Eliel	(Universiteit Leiden, The Netherlands)
	Prof. dr. ir. T.H. Oosterkamp	(Universiteit Leiden, The Netherlands)
	Prof. dr. E. Scheer	(Universität Konstanz, Germany)
	Dr. M.P. Allan	(Universiteit Leiden, The Netherlands)
	Dr. M. Kumar	(École Normale Supérieure de Paris, France)

ISBN: 978-90-8593-336-6
Casimir PhD series, Delft-Leiden 2018-04



Universiteit Leiden







Cover photo (Front): Courtesy Matt Crux @PhoenixLove.net
Cover photo (Back) is prepared using our low temperature scanning tunneling microscope © Sumit Tewari
Cover design: Sumit Tewari
Copyright © 2018 Sumit Tewari

Contents

1 Introduction 1

1.1 The concept of the atom 2

1.2 From macro to nano 3

1.3 Molecular electronics 5

1.4 Experimental techniques 6

1.4.1 Mechanically controllable break junctions 6

1.4.2 Electromigration break junctions 8

1.4.3 Methods based on scanning probe microscopy 10

1.4.4 Data analysis and conductance histograms 11

1.5 The notorious lot 12

1.5.1 Benzenedithiol 13

1.5.2 Alkane dithiols 15

1.6 Shot noise 20

1.7 Two-level fluctuations 21

1.8 Organization of the thesis 22

I Part One: Atomic and Molecular Manipulation

2 Human-machine augmented system to control single atoms . . . 26

2.1 Introduction 28

2.2 Experimental setup 29

2.3 Real-time molecular dynamic simulation 30

2.3.1 Implementation 32

2.3.2 Speed-up techniques 34

2.4 Experimental measurements 36

2.4.1 Obtaining the positions of the background substrate atoms . . . 37

2.4.2 Point contact pushing 38

2.4.3 Lifting of gold atomic chain 40

2.4.4 Parity oscillations 42

2.4.5 Lifting of a gold atomic chain along a step edge 44

2.5 Discussion **45**
2.6 Conclusion and outlook **46**

3 Single molecule STM control: GPU implementation 48
3.1 Introduction **50**
3.2 Single-shot measurements - Overview **51**
3.3 Molecular dynamics **53**
3.3.1 Challenges in making real-time MD simulations 54
3.4 Molecular dynamics - GPU implementation **55**
3.4.1 Gold-gold forces 56
3.4.2 Forces on molecule atoms 59
3.5 Results and discussion **62**
3.6 Conclusion and outlook **66**

II Part Two: Shot Noise

4 Shot noise measurements in the MHz regime 68
4.1 Introduction **70**
4.2 Principles of the method **73**
4.3 Description of the instrument **75**
4.3.1 Mechanical design 75
4.3.2 Analog electronics 77
4.3.3 Digital electronics and data manipulation. 80
4.4 Testing, calibration, and accuracy **84**
4.5 Measurements on Au and Pt atomic contacts **85**
4.6 Conclusions **89**

5 Anomalous non-linear shot noise at high voltage bias 90
5.1 Introduction **92**
5.2 Measurement setup **93**
5.3 Shot-noise measurements **93**
5.4 Quantum interference model **96**
5.4.1 Extraction of the voltage and energy dependent transmission 101
5.4.2 Analysis of the experimental data 101
5.5 More general energy and voltage dependent transmission functions 103
5.6 Discussion **105**
5.7 Conclusion and outlook **106**

6 Two-level fluctuations in molecular junctions . . . 108

6.1 Introduction 110

6.2 Literature review 110

6.3 Experimental setup 114

6.4 Measurements on a D_2 molecule 114

6.4.1 Step down in junction conductance . . . 115

6.4.2 Inelastic electron noise spectroscopy (IENS) . . . 117

6.5 Inelastic tunneling versus two-level fluctuations? 118

6.5.1 Step-up in junction conductance close to 1 G_0 . . . 119

6.6 Conclusion 121

III Part Three: Graphene Architecture

7 Graphene based circuit . . . 124

7.1 Introduction 126

7.2 Graphene vs metallic electrodes 127

7.3 Electromigration, electroburning vs direct cutting methods 128

7.3.1 Estimation of nanogap size . . . 131

7.3.2 Direct cutting methods . . . 131

7.4 Our approach 132

7.4.1 Helium-ion milling . . . 132

7.4.2 Scanning probe microscopy based cutting . . . 135

7.5 Conclusion 140

Appendix A. Atomic manipulation . . . 143

A.1 Force derivation 143

A.2 Lifting of gold atomic chain 146

A.3 Point-contact push manipulation technique 147

Appendix B. Molecular manipulation . . . 149

B.1 GPU programming 149

B.1.1 Programming in the CUDA framework . . . 150

B.2 Intramolecular forces 154

B.3 Gold-molecule force calculations 155

B.3.1 Morse potential: Au-N bond . . . 155

B.3.2 Lennard-Jones (LJ) potential . . . 156

Appendix C. Shot noise . . . 159

C.1 Excess Noise derivation 159

C.2 Two channel fit 160

Appendix D. Robust procedure for creating and characterizing the atomic structure of scanning tunneling microscope tips 163

Appendix E. Inhomogeneous broadening of the conductance histograms for molecular junctions 169

Summary **173**

Samenvatting **177**

Acknowledgement **181**

Curriculum vitae **183**

Publications **185**

Index **187**

An expert is a person who has made all the mistakes that can be made in a very narrow field.
-Niels Bohr

1. Introduction

Greek and Indian philosophers were the first to give an atomic theory of matter. In their description, the atom, the smallest constituent of the matter was indestructible. However, we know now that the atoms are more than willing to share a part of them, i. e. electrons. In fact, by sharing these electrons, atoms form molecules, which consequently form the matter. Hence, by philosophying the atom as indestructible, the very existence of matter was dismissed. Furthermore, the flow of these electrons in matter is what gives current. It is fascinating to observe that it is now routinely possible to wire an organic molecule, an object as small as one nanometer, between two metallic leads and measure its electronic transport characteristics. In parallel, many theoretical tools have been developed and refined for describing such transport properties and for obtaining numerical predictions. The theoretically predicted trends nowadays reproduce the experimental findings quite well for series of molecules with a single well-defined control parameter, such as the length of the molecules. The quantitative agreement between theory and experiment usually is less convincing, however. Many reasons for quantitative discrepancies can be identified, from which one may decide that qualitative agreement is the best one may expect with present modeling tools. For further progress, benchmark systems are required that are sufficiently well-defined by experiment to allow a quantitative testing of the approximation schemes underlying the theoretical modeling.

1.1 The concept of the atom

Greek philosopher Leucippus (with his disciple Democritus) and Indian philosopher Kanada were the first to give an atomic theory of matter[1]. In their description, the atom, the smallest constituent of the matter was indestructible. It only became clear in early 20th century, by the work of Thomson[2], Lewis[3] and Langmuir[4] that atoms join together by sharing a part of them i. e. electrons, to form molecules.

Next, came the development of quantum mechanics, which changes the way we imagine the fundamental particles. A core concept of quantum mechanics is the wave nature of electrons postulated by Louise de Broglie[5] in 1929. Soon after, Schrödinger gave a differential wave equation, known as the Schrödinger equation to study quantum mechanical systems. This gave birth to the notion of the wavefunction. Consequently, this picture of a wavefunction had many implications. What followed were partially counterintuitive and exotic phenomena like quantum tunnelling, Heisenberg uncertainty principle, quantum superposition, quantum interference etc.

Researchers from IBM utilised the phenomenon of quantum tunnelling to image single atoms and molecule. They invented[6,7] in 1981; the machine called the scanning tunnelling microscope (STM), which makes use of the fact that the electron wave functions extend in space out of their parent atom in an exponentially decreasing fashion. After the advent of STM, it became possible to image conducting surfaces with atomic resolution. STM operates by bringing the apex of a fine metallic wire into tunnelling distance from a surface of interest. By providing feedback in the tunnel current and scanning the tip above the surface, one can make topographic maps of the surface with atomic resolution. STM has found its applications in many fields of science. Apart from studying surface topography, STM has been used for manipulating single atoms[8–10], for doing spectroscopy[11], for fabricating nano-structures with new tweaked electronic properties[12], for studying surface chemistry[13], for probing collective[14] and local[15] electronic behavior, and much more.

[1] R. A. Horne. In: *Ambix* 8 (1960), p. 98.
[2] Sir J. J. Thomson O.M. F.R.S. In: *The London, Edinburgh, and Dublin Philosophical Magazine and Journal of Science* 27 (1914), p. 757.
[3] Gilbert N. Lewis. In: *Journal of the American Chemical Society* 38 (1916), p. 762.
[4] Irving Langmuir. In: *Journal of the Franklin Institute* 187 (1919), p. 359.
[5] Louis De Broglie. PhD thesis. Migration-université en cours d'affectation, 1924.
[6] Gerd Binnig et al. In: *Phys. Rev. Lett.* 49 (1982), p. 57.
[7] Gerd Binnig and Heinrich Rohrer. In: *Rev. Mod. Phys.* 59 (1987), p. 615.
[8] Donald M. Eigler and Erhard K. Schweizer. In: *Nature* 344 (1990), p. 524.
[9] Joseph A. Stroscio and D. M. Eigler. In: *Science* 254 (1991), p. 1319.
[10] Saw Wai Hla. In: *Reports on Progress in Physics* 77 (2014), p. 056502.
[11] R. Wiesendanger. Scanning Probe Microscopy and Spectroscopy: Methods and Applications. Cambridge University Press, 1994.
[12] H. C. Manoharan et al. In: *Nature* 403 (2000), p. 512.
[13] Joost W. M. Frenken and Irene Groot. Vol. 114. Operando research in heterogeneous catalysis. Springer, 2017.
[14] Hanno H. Weitering et al. In: *Science* 285 (1999), p. 2107.
[15] S. H. Pan et al. In: *Nature* 403 (2000), p. 746.

1.2 From macro to nano

As the nanoscale dimensions became accessible, it became a hot topic to understand how electronic transport occurs in such nanoscale devices. Molecular electronics is an approach to study nano-electronics on the scale of single atoms and molecules. From Ohm's law, we know that conductance scales with the area of the macroscopic conductor: $G = \sigma \frac{A}{l}$, where A is area and l is the length of the macroscopic wire. Based on dimensions of the system, electronic transport can be divided into two regimes: diffusive and ballistic. When the size of the system is larger than the mean free path[1] of an electron, then the electron loses part of its momentum to other electrons and atoms in the lattice before crossing the system. Such transport is called diffusive transport. Maxwell gave an expression for conductance of a point contact in such diffusive regime[16] as $G = 2\sigma R$, where R is the radius of the cross-section of the contact.

On the contrary, when the size of the system shrinks below the mean free path of the electrons, then the electron crosses the system ballistically without losing its momentum. This regime is thus called the ballistic regime. Sharvin in 1965[17], showed that the conduction electrons passing through an orifice (in a ballistic manner) should change their velocity by an amount $\Delta v \approx eV/p_F$, where eV is the potential drop across the orifice, and p_F is the Fermi momentum. From this, the Sharvin conductance for the ballistic contact can be derived as:

$$G = \frac{2e^2}{h}\left(\frac{k_F R}{2}\right)^2 \tag{1.1}$$

Which is directly proportional to R^2 but it is independent of the length of the conductor. Here $k_F (= p_F/\hbar)$ is the Fermi wave-vector. The Heisenberg uncertainty principle for Fermi electrons in a narrow-contact, $2p_F R \geq \hbar$ gives a small correction (called Weyl correction)[18] to the Sharvin conductance:

$$G = \frac{2e^2}{h}\left(\frac{k_F R}{2}\right)^2 \left(1 - \frac{2}{k_F R} + ...\right) \tag{1.2}$$

This equation is now valid for a contact down to a few nanometers in diameter (in the form of wire, not orifice) and is often used to establish the relationship between the conductance and the radius of a contact.

When the size of the contact becomes so small that the wave-nature of an electron can no longer be ignored and the quantum mechanics has to come in, then the correct expression for the conductance is given by Landauer (for low-bias regime) as[2]:

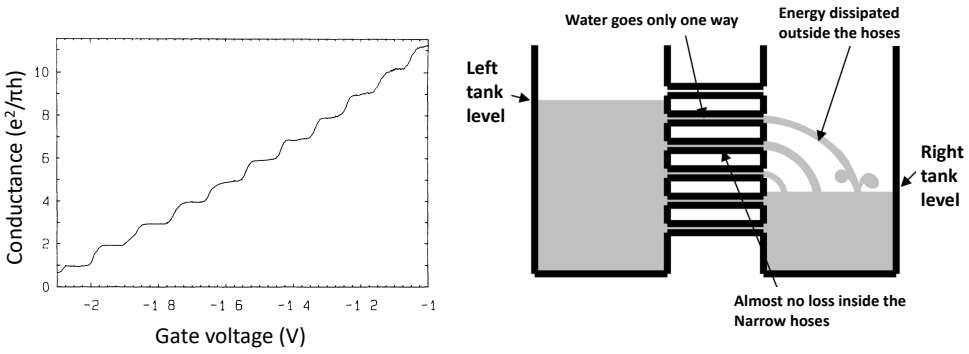
[1] Mean free path is the distance an electron can move in a medium without losing its momentum.

[2] The expression given here is for spin degenerate systems. For spin split systems, the expression becomes: $G = \frac{e^2}{h} \sum T_n$.

[16] Juan Carlos Cuevas and Elke Scheer. Molecular electronics : an introduction to theory and experiment. New Jersey [u.a.] : World Scientific, 2010.

[17] Yu V. Sharvin. In: *J. Exptl. Theoret. Phys. (U.S.S.R.)* 48 (1965), p. 655.

[18] Nicolás Agraït et al. In: *Physics Reports* 377 (2003), p. 81.



(a) (b)

Figure 1.1: (a) Conductance quantization measured in a 2DEG system by van Wees *et al*.[20](b) A pictorial explanation of conductance quantization from the book by Ouisse[21].

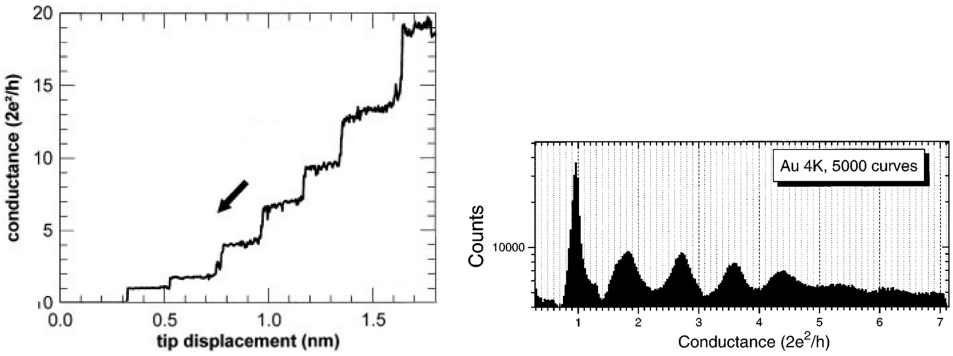
$$G = \frac{2e^2}{h} \sum_{n=1}^{N} T_n \tag{1.3}$$

Here, conductance is directly proportional to sum over transmission through different channels (given by index n). In a metallic conductor of cross-section area A, the total number of independent transmission channels N is given by A/λ_F^2, where λ_F is the Fermi wavelength[19]3. Such conductance quantisation was measured experimentally by van Wees *et al*.[20] in 1988 in a two-dimensional electron gas (2DEG) system. With the help of a gate electrode, the researchers were able to start from a completely pinched off regime and controllably open channels one after the other measuring step-wise increase in conductance as shown in Figure 1.1(a). Figure 1.1(b) shows a pictorial analogy of the conductance quantisation to a water tank experiment (taken from the book by Ouisse[21]). In the picture, the two parts of a water tank are separated by a series of water channels. The water level on left and right side depicts the Fermi level of electrons on the left and right leads connecting to the point contact. As the water level (Fermi level) rises on one side of the tank (leads), more and more water channels (electronic transport channel) are opened and thus increasing the total flow of water (total conductance) from left to right reservoirs.

Soon after, such conductance quantization was observed also in a three dimensional metallic point contacts by Krans *et al*.[22,23] in 1993. They measured it using

3 Fermi-wavelength in bulk gold is around 0.5 nm.

[19] C. W. J. Beenakker, Christian Schönenberger, et al. In: *Physics Today* 56 (2003), p. 37.
[20] B. J. van Wees et al. In: *Phys. Rev. Lett.* 60 (1988), p. 848.
[21] Thierry Ouisse. Electron transport in nanostructures and mesoscopic devices: an introduction. John Wiley & Sons, 2013.
[22] J. M. Krans et al. In: *Phys. Rev. B* 48 (1993), p. 14721.
[23] C. J. Muller et al. In: *Phys. Rev. B* 53 (1996), p. 1022.



(a) (b)

Figure 1.2: (a) Conductance steps associated quantization measured in a gold (Au) point contact (b) A typical conductance histogram of Au atomic point contacts. Above Figures are taken from Rubio *et al*.[24] and Costa-Krämer *et al*.[25]

a mechanically controlled break junction technique to controllably break and form single atom contacts. Due to complex dynamics of these metallic systems, a large conductance data-set is often recorded for different contact configurations and a conductance histogram is prepared. Figure 1.2 shows an example of such conductance quantization and histogram taken from Rubio *et al*.[24] and Costa-Krämer *et al*.[25]. The step-wise conductance in this case is a result of a combination of conductance quantization and discrete atomic configurations.

1.3 Molecular electronics

Molecular electronics is like a Utopian[4] dream for future electronic circuits where molecules will become the building blocks. Here, the electronic components based on silicon technology will be replaced by single molecules with similar and even more functionalities. Switches made from single molecules will give an exceptionally high switching rates and clock frequency, increasing the computational power of the current circuits by manifolds. These molecules will convert heat and light to electricity far more efficiently than current technology. Not to forget the small molecules will bring with them pleasant surprises using their quantum mechanical properties even at room temperature. In spite of all this and many more benefits, the power consumption of these circuits will be significantly smaller than current circuits due to less heat loss and efficient electron transfer.

This led researchers from different fields (experimental physics, theoretical physics, synthetic chemistry, biology and industries) to come together and work for the realization of such a dream. A lot has been done starting from connecting single molecules between metallic leads, studying their mechanical and electronic transport properties, their quantum mechanical behaviours and so on. Einstein said once, *"As our*

[4] Utopian in terms of idealistic but not impossible.

[24] G. Rubio et al. In: *Phys. Rev. Lett.* 76 (1996), p. 2302.
[25] J. L. Costa-Krämer et al. In: *Phys. Rev. B* 55 (1997), p. 12910.

circle of knowledge expands, so does the circumference of darkness surrounding it." that is, the more we will know the more of the unknown will be visible. In fact, this is also the current situation with molecular electronics, there are many things we have learned so far but many still to be understood and put under control from both fundamental and technological point of view.

Now that we understand and control the basic properties of molecular junctions the time is ripe to critically evaluate the question how well we understand electron transport in molecular junctions. Theory inevitably needs to take into account many details of the arrangements of the atoms and the molecule that make up the junction. Since self-assembly is an essential element in the formation of molecular junctions and imaging of the resulting structures has not been possible, experiment usually does not provide all the information needed for comparison with theory. The problem that we want to address arises largely because of a want for suitable benchmark systems that have been sufficiently characterized by experiment such that they may be used for a critical evaluation of the theories. The problem is the more important since interpretation of the experiments often heavily relies on a comparison with model calculations.

Despite many experimental hurdles the understanding of electron transport of single-molecule junctions has seen impressive progress in recent years[16]. It is fascinating to observe that it is now routinely possible to wire an organic molecule, an object as small as one nanometer, between two metallic leads and measure its electronic transport characteristics. Several approaches even allow bringing a third metal lead close enough to serve as a gate electrode, through which the conductance of the molecule can be adjusted electrostatically.

1.4 Experimental techniques

In this section we briefly present various techniques used for studying electronic transport through single molecules. For a more detailed presentation of single-molecule techniques and their integration into various advanced measurement schemes we refer to following reviews[18,26–28]. Since molecules have a typical size of 1 nm all existing top-down microfabrication techniques lack the required resolution for controlled wiring of molecules. Therefore, the methods employed rely on a combination of electromechanical fine tuning of the nanometer-size gap between the contact electrodes and self-assembly of the molecules inside this gap. The three most frequently employed techniques are the mechanically controlled break junction (MCBJ) technique, the electromigration break junction (EBJ) technique and methods using scanning tunneling microscopes (STM).

1.4.1 Mechanically controllable break junctions

The MCBJ technique was developed for the study of atomic and molecular junctions[29] based on an earlier method which aimed at studying vacuum tunneling between

[26] Dong Xiang et al. In: *Advanced Materials* 25 (2013), p. 4845.
[27] Dong Xiang et al. In: *Chemical Reviews* 116 (2016), p. 4318.
[28] Sriharsha V. Aradhya and Latha Venkataraman. In: *Nature Nanotechnology* 8 (2013), p. 399.
[29] C. J. Muller et al. In: *Physica C: Superconductivity* 191 (1992), p. 485.

superconductors.[30] We distinguish two fabrication methods: the notched-wire MCBJ, and the lithographically fabricated MCBJ. The first is the simplest and has the advantage that it can be easily adapted to nearly all metal electrodes. It is made starting from a macroscopic metal wire into which a weak spot is created by cutting a notch. The notched metal wire is placed on top of a flexible substrate (which is commonly stainless steel or phosphorous bronze) covered by an insulating sheet, usually Kapton. The wire is fixed by epoxy onto the substrate at either side and very close to the notch. This is then mounted in a three-point bending mechanism as shown in Figure 1.3(a), where the flexible substrate is held down at the two ends and pushed up in the middle. Bending the substrate increases the strain in the wire, which is concentrated at the weak spot created by the notch, until the wire breaks. The junction is first broken with a coarse mechanical drive, thus exposing two fresh electrode surfaces. By relaxing the bending and using fine control of the separation gap by means of a piezo-electric actuator atomic-size contacts can be reformed and broken many times.

The lithographically fabricated MCBJ[31] (shown in Figure 1.3(b)) shares the same principle as the notched-wire MCBJ except that the pre-notched metal wire is replaced by a freely-suspended bridge in a thin metal film produced by electron-beam lithography. This metal film is electrically isolated from the flexible substrate using a $3-5\ \mu$m polyimide layer. The unsupported section of the bridge is reduced by about two orders of magnitude compared to the notched-wire MCBJ to about $2\ \mu$m. This has the effect that the mechanical displacement ratio, i. e. the ratio between the change of the gap size and the actuator motion, is reduced to about 1×10^{-5}. The gain of the lithographic technique is that the junctions are very insensitive to external mechanical perturbations as a result of the small displacement ratio. The added complications of clean-room preparation are offset by the possibility of producing multiple MCBJ samples on a single wafer[32]. A drawback is the fact that by the very small displacement ratio the maximum extension of a typical piezo actuator produces less than 0.01 nm change in the distance between the electrodes. Therefore, the control of this distance is achieved by an electro motor driven gear. Since such electromechanical control is much slower than piezo-electrical control it is much more time consuming to obtain enough statistics for a large number of contact breaking events (see below).

For most types of metal electrodes one can only take full advantage of the MCBJ method by performing the first breaking at cryogenic temperatures or under ultra-high vacuum (UHV). Otherwise, the surfaces will be contaminated with oxides and adsorbents will cover the surface within a fraction of a second, so that the atomic-size contact characteristics of the pure metal are lost. The main exception is Au[33], for which even under ambient conditions most of the intrinsic quantum conductance properties survive as a result of the low reactivity of the Au surface[34].

For the same reason Au stands out as the preferred electrode material for all other single-molecule transport experiments. Specific binding to target molecules can be achieved by selecting suitable anchor groups for the molecules. Sulfur

[30] John Moreland et al. In: *Applied Physics Letters* 43 (1983), p. 387.
[31] J. M. van Ruitenbeek et al. In: *Review of Scientific Instruments* 67 (1996), p. 108.
[32] Christian A Martin et al. In: *New Journal of Physics* 10 (2008), p. 065008.
[33] B. Hammer and J. K. Norskov. In: *Nature* 376 (1995), p. 238.
[34] J. I. Pascual et al. In: *Phys. Rev. Lett.* 71 (1993), p. 1852.

groups are widely exploited for this purpose, but several other possibilities have been explored[35]. Typically, such molecules having suitable anchor groups are deposited onto the bridge of the MCBJ from solution, under ambient conditions. This has been first explored for lithographic MCBJ systems[36], and this continues to be the most commonly employed approach. A few groups[37–39] though also work with notched-wire MCBJ technique for connecting single molecules and have recently demonstrated sharp conductance histogram measurements over an oligo phenylene-ethynylene (OPE-3) molecule[39].

The intrinsic cleanliness of the broken metal surfaces can be fully exploited by working under UHV and/or under cryogenic conditions. The deposition of molecules in these experiments proceeds by deposition onto the broken junction from the gas phase, either using an external vapor source[40,41] or employing a local cell for sublimation[42,43]. By working under cryogenic or under UHV conditions it is possible to explore other metal electrodes and other forms of metal-molecule bonding. For example, hydrogen, H_2, binds to clean Pt electrodes without the need for anchoring groups[40], and this applies more widely also for many organic molecules such as benzene[41], oligoacenes[44] and pyrazene[42].

1.4.2 Electromigration break junctions

Electromigration in metals[45] results from an atom diffusion process driven by the 'electron wind' force[46] exerted by the conducting electrons on the atoms in the system, under large current bias. This effect can be used to create nanogaps in metallic leads[47,48], small enough for a single molecule to bridge. Such systems are prepared by first pre-patterning a narrow metal wire of about 100 nm in a thin metallic film on an insulating substrate (usually SiO_2 on a Si wafer) using electron lithography. Passing a large current through such narrow metallic leads gives rise to displacement of atoms, which is observed as an increasing resistance due to the gradual opening of a gap in the narrow wire. Initially the reliability of the method was compromised by the fact that the strong local Joule heating leads to the formation of metallic nanoparticles in almost 30% of the junctions[48,49], which give rise to characteristics resembling those of molecules. However, by using a feedback circuit the electromigration process can

[35] Chuancheng Jia and Xuefeng Guo. In: *Chem. Soc. Rev.* 42 (2013), p. 5642.
[36] J. Reichert et al. In: *Phys. Rev. Lett.* 88 (2002), p. 176804.
[37] M. Kiguchi et al. In: *Journal of Physics: Conference Series* 100 (2008), p. 052059.
[38] T. Yelin et al. In: *Nano letters* 13 (2013), p. 1956.
[39] Julian M. Bopp et al. In: *Low Temperature Physics* 43 (2017), p. 905.
[40] R. H. M. Smit et al. In: *Nature* 419 (2002), p. 906.
[41] M. Kiguchi et al. In: *Phys. Rev. Lett.* 101 (2008), p. 046801.
[42] Satoshi Kaneko et al. In: *Nanotechnology* 24 (2013), p. 315201.
[43] D. Rakhmilevitch et al. In: *Phys. Rev. Lett.* 113 (2014), p. 236603.
[44] T. Yelin et al. In: *Nature materials* 15 (2016), p. 444.
[45] P. S. Ho and T. Kwok. In: *Reports on Progress in Physics* 52 (1989), p. 301.
[46] H. B. Huntington and A. R. Grone. In: *Journal of Physics and Chemistry of Solids* 20 (1961), p. 76.
[47] Hongkun Park et al. In: *Applied Physics Letters* 75 (1999), p. 301.
[48] Herre S. J. van der Zant et al. In: *Faraday Discuss.* 131 (2006), p. 347.
[49] A. A. Houck et al. In: *Nano Letters* 5 (2005), p. 1685.

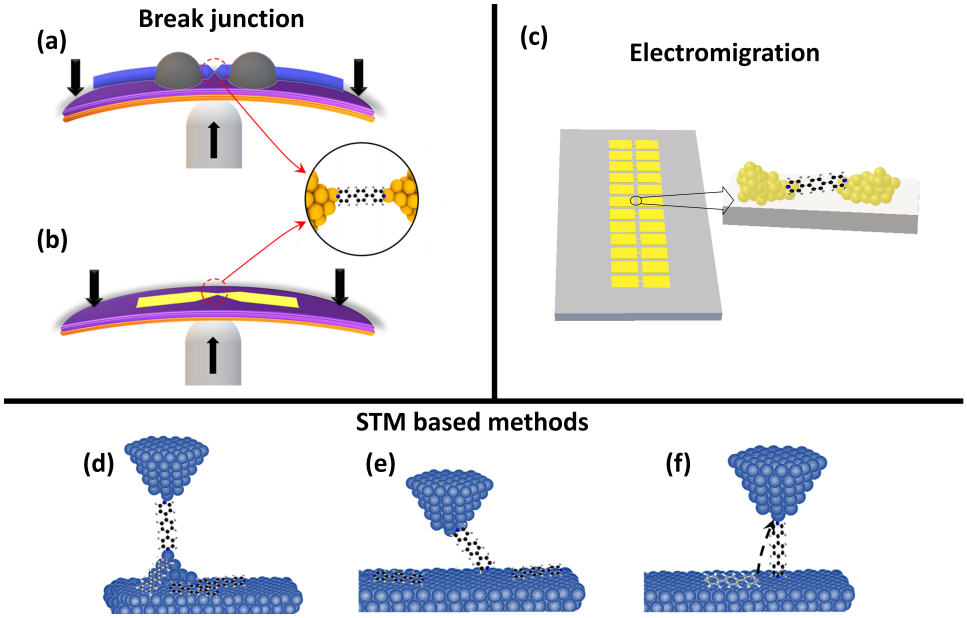


Figure 1.3: Overview of experimental techniques aimed at measuring single-molecule transport. (a) Notched-wire MCBJ mounted in a 3-point bending configuration and wire is anchored to the substrate with black stycast epoxy, (b) Lithographically prepared gold MCBJ mounted also in 3-point bending configuration, (c) Electromigration based junctions where the size of gap is not adjusted to the size of the molecule as shown in the blown up picture of the junction, (d) STM break junction setup, where after a few indentation cycles the atomic configuration of the electrode on the surface side becomes unknown, (e) I(t) and I(s) technique done at room temperature in STM where the tip is not indented on the surface and (f) Recent developments in controlled formation of single molecule junctions using low temperature UHV systems.

be more precisely controlled, and further improvements are obtained by relying on self-breaking in the last stages of gap formation[50]. A schematic is shown in Figure 1.3(c).

Molecules are deposited onto the nanowire before electromigration, and one relies on a molecule finding its way to the gap during the electromigration process. Alternatively, molecules can be allowed to self-assemble into the gap from solution after the electromigration process has been completed[51]. In contrast to the other break junction techniques, junctions formed by electromigration can only be broken once and cannot be reformed. The gap distance depends on the details of the feedback breaking process, but it cannot be targeted very precisely. One cannot obtain a very precise value for the size of the gap, but a fair estimate can be obtained from fitting the IV characteristics to the Simmons model[52,53]. For imaging techniques the gap

[50] K. O'Neill et al. In: *Applied Physics Letters* 90 (2007), p. 133109.
[51] Edgar A. Osorio et al. In: *Nano Letters* 7 (2007), p. 3336.
[52] John G. Simmons. In: *Journal of Applied Physics* 34 (1963), p. 1793.
[53] Ayelet Vilan. In: *The Journal of Physical Chemistry C* 111 (2007), p. 4431.

is better accessible than any of the other techniques discussed here. High-resolution transmission electron microscopy imaging using transparent SiN_x membranes was done for gold electromigration junctions[54,55] for stuying the breaking process and detecting the nanogap size. Due to the three dimensional shape of leads it is difficult to obtain precise values for the gap. The imaging resolution of transmission electron microscopy has not yet proven sufficient for detecting the position of an organic molecule.

The search for junctions bridged by a molecule is based on producing many (of order several hundred) electromigration break junctions on a wafer, breaking each of them separately, and scanning the resulting junctions for interesting IV characteristics at room temperature, that may point at the presence of a molecule in the bridge. Such junctions, which are a minority of order a few percent, are then further studied, usually by more elaborate techniques. Although the method intrinsically permits very limited statistics over molecular junction configurations, and every junction formed has its particular characteristics, the more elaborate experiments make very interesting case studies. Moreover, the rigid attachment of the electrodes to the substrate allows temperature and field cycling, it allows the fabrication of a metallic gate at close proximity to the junction[47,48], and it permits easy optical access for Raman scattering[56]. Such experiments provide evidence for the presence of the molecule in the junction by giving exquisitely detailed excitation spectra of vibrations in inelastic tunneling[51], in the simultaneously detected Raman spectrum[56,57], and of magnetic excitations in the differential conductance[58].

1.4.3 Methods based on scanning probe microscopy

The break junction methods described above do not permit imaging of the molecule in the junction. In contrast, scanning tunneling microscope (STM) or atomic force microscope allow imaging molecules on a surface before contacting them. This is possible only for very stable systems under UHV and at cryogenic temperatures[59,60]. By imaging and manipulating single molecules on an atomically flat and clean metal surface it is possible to verify that the STM tip interacts with a single target molecule and the shape of the bottom electrode contacting the molecule (the metal surface) is known. However, information on the shape of the tip cannot be easily obtained from experiments. Moreover, when approaching the tip for contacting the molecule and lifting it up from the surface the molecule and the metal atoms contacting it rearrange in ways that cannot be seen by the instrument. In Chapter 3, we will discuss further in more detail on such techniques. A schematic showing controlled manipulation is given in Figure 1.3(f).

While cryogenic UHV STM holds great promise, it is also a very demanding technique. A very powerful and versatile method for investigating the conductance of single molecules at room temperature and in solution was introduced by Xu *et*

[54] Douglas R. Strachan et al. In: *Phys. Rev. Lett.* 100 (2008), p. 056805.
[55] B. Gao et al. In: *Nanotechnology* 20 (2009), p. 415207.
[56] Daniel R. Ward et al. In: *Nano Letters* 8 (2008), p. 919.
[57] Madoka Iwane et al. In: *Sensors* 17 (2017), p. 1901.
[58] R. Gaudenzi et al. In: *The Journal of Chemical Physics* 146 (2017), p. 092330.
[59] R. Temirov et al. In: *Nanotechnology* 19 (2008), p. 065401.
[60] Torben Jasper-Tönnies et al. In: *Phys. Rev. Lett.* 119 (2017), p. 066801.

al.[61] (schematic shown in Figure 1.3(d)), which has inspired many other researchers. Ignoring the scanning capability of STM, the instrument is used for approaching the tip to the surface and repeatedly indenting the tip into the surface and retracting. This resembles closely the MCBJ type of experiments, with the added advantage that it permits simple adaptations for operating in a solution of the target molecules. The indentation of the (Au) tip into the (Au) metal surface to a depth corresponding to a conductance of 10–40 times the conductance quantum ($G_0 = 2e^2/h$) restructures the shape of the electrodes with every indentation. Upon retraction a neck is formed that thins down until it snaps. The resulting gap is then frequently bridged by a molecule equipped with suitable anchoring groups through a self-organization process, which is observed as a plateau in the conductance during retraction. These plateaus usually have a lot of structure and appear at different levels for each retraction event. Therefore, the indentation and retraction cycles are repeated many times and the resulting conductance traces are then combined in form of conductance histograms, as had been previously introduced for MCBJ experiments[22,40].

Using a conducting probe AFM one can simultaneously measure both the conductance and force between the tip and the molecule[28,61]. These room temperature experiments have the great advantage that they permit evaluating single-molecule junctions much faster than the other available techniques, and thereby allow exploring trends as a function of molecular composition.

1.4.4 Data analysis and conductance histograms

Most of the MCBJ and STM experiments have in common that, as a result of the self-organization process involved in the formation of the junction, very little is known about the atomic-scale shape and structure of the electrodes, about the configuration of the molecule in the junction, and about its bonds to the metal surfaces. The effect of these parameters on the conductance is observed as a variation, usually by about an order of magnitude or more, in the observed conductance between independent realizations of molecular junctions. The solution that is widely adopted is to repeatedly form and break many junctions, record the digitized conductance during the contact breaking process, and collect all data in a histogram. The underlying assumption is that sufficiently deep indentation restructures the metal leads and the molecule, and randomizes the path followed in configuration space during the contact breaking process. The peaks in the histogram can then be interpreted as representing the energetically favorable junction configurations, and these are the most relevant parameters used for comparison with model calculations. By combining the displacement length measured from the point of metal-metal contact breaking with the evolution of the conductance one can also build two-dimensional histograms[32], which are helpful for detecting multiple stable configurations and for obtaining a measure of the molecular bridge length.

In the breaking process the last-atom metal-to-metal contact is usually clearly visible as a plateau near 1 G_0, and this produces a sharp peak in the conductance histogram. Breaking of this last metal contact is followed by a jump out of contact[62] to a conductance that is one or two orders of magnitude lower. In many cases, after this jump the current exponentially decreases with increasing separation of the electrodes,

[61] Bingqian Xu and Nongjian J. Tao. In: *Science* 301 (2003), p. 1221.
[62] N. Agraït et al. In: *Phys. Rev. B* 47 (1993), p. 12345.

as expected for vacuum tunneling. Only for a fraction of the breaking events one or more plateaus appear signaling the bridging by a molecule. The large number of traces without a molecular signal results in a large background in the histograms. Initially, curves without a clear molecular signature were manually removed from the data set. This practice has some danger of introducing experimenter-bias in the data selection, and this practice has now been abandoned. The background problem can be reduced by the use of automated routines, for example routines that detect the last step in the conductance[63]. Other solutions proposed include the application of an AC modulation of the gap distance[64]. A widely adopted solution to the background problem uses histograms of the logarithm of conductance, rather than the linear conductance[65]. In this case the background tunneling contribution reduces to a nearly constant contribution and the relevant features related to the molecule will be more clearly visible in a data-set that now comprises all breaking traces.

The appearance of the shape of the histograms and the positions of the peaks for the same metal-molecule system do not reproduce perfectly between experimental groups, and even from one experimental run to the next. This implies that the underlying assumption that the repeated indentation effectively averages over all configurations is not fully justified. For example, one may anticipate that the results will be sensitive to parameters such as the voltage or current bias applied, and the depth of indentation. This has motivated Haiss *et al*. to avoid indenting the surface, in order to maintain a common surface and tip structure. They developed the so-called I(t) and I(s) techniques[66,67] shown in Figure 1.3(e). These techniques operate near room temperature and rely on bringing the STM tip close to the surface by the usual current feedback control. For low surface coverage molecules with suitable anchoring groups are expected to jump stochastically into and out of contact with the tip. The difference between I(s) and I(t) is that the tip is moved in and out of close distance to the surface repeatedly for the former, while in the latter case, the tip is held at a stable tunneling distance and the events are recorded as a function of time. The conductance values measured by I(t) or I(s) are found to be up to an order of magnitude smaller than the ones obtained from histograms produced by MCBJ or STM techniques.

1.5 The notorious lot

Apart from the interesting work that has been done so far in single-molecule transport measurements and the new important physics that has been probed in these systems, there is still a "notorious lot" which needs to be highlighted and not put under the carpet. Thiol (-SH) anchoring group and gold electrode make a congruous combination for doing single-molecule electronics. This combination has been used since researchers started to study self-assembled mono-layers of molecules. It is still heavily used for anchoring various single-molecules between gold electrodes. However, some simple key dithiol molecules that have been studied by many group

[63] Sung-Yeon Jang et al. In: *Nano Letters* 6 (2006), p. 2362.
[64] J. L. Xia et al. In: *Nano Letters* 8 (2008), p. 1960.
[65] M. Teresa González et al. In: *Nano Letters* 6 (2006), p. 2238.
[66] Wolfgang Haiss et al. In: *Journal of the American Chemical Society* 125 (2003), p. 15294.
[67] Wolfgang Haiss et al. In: *Phys. Chem. Chem. Phys.* 6 (2004), p. 4330.

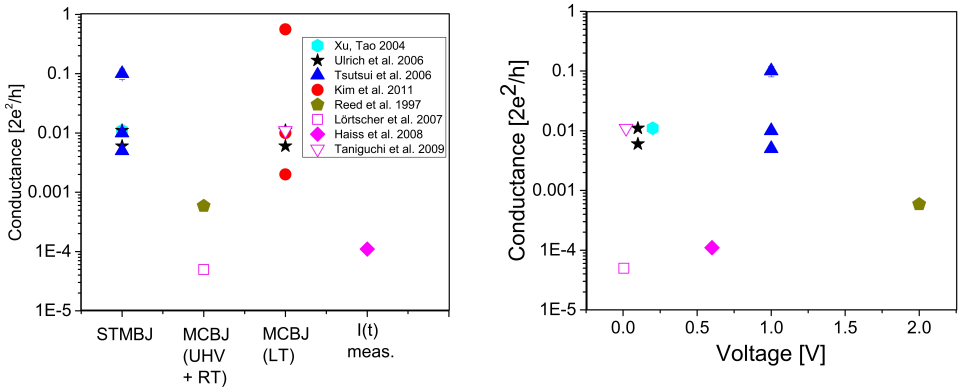
in early 21^{st} century, have shown a large spread (over few orders of magnitude) in their conductance values. This include the famous Benzenedithiol molecule and the family of Alkane dithiols. I will give a brief review of these two sets because they clearly illustrate the need for more advanced techniques, to which the rest of this thesis is devoted.

1.5.1 Benzenedithiol

The first electronic transport measurement over a single molecule dates back to 1997 by Reed *et al*.[68], where a benzene-1,4-dithiol molecule was measured between two gold electrodes. A benzene-1,4-dithiol molecule sandwiched between two gold leads forms 1,4 benzene-dithiolate (BDT) after the two hydrogen atoms are lost from the sulfurs. The benzene ring provides the π electrons for conduction, and the sulfur is supposed to bind in a covalent manner to the gold leads. The conductance measurement done over the molecule has shown a conductance gap of around 0.7 V which was attributed to a gap between the leads Fermi level and the lowest unoccupied molecular orbital (LUMO) of the molecule. At positive and negative bias the conductance is shown to rise in a step manner with the first plateau around 2 V having a value of 45 nS (or 5.8×10^{-5} G_0). This is considered as the characteristic conductance of the BDT molecule. Followed by this several theoretical models were proposed[69–72] to understand the above experimental result, but surprisingly the conductance calculated for BDT came out to be 2 to 3 orders of magnitude higher than what was measured. The experiment done by Reed *et al*.[68] was done in a break junction setup but not using the statistical method of making a histogram. Soon after, a higher conductance of BDT (around 0.011 G_0) was reported experimentally[73] and was also found matching with theoretical results published by[70] where the electrodes were treated using a jellium model. A series of experiments studying BDT[73–79] and other molecules followed thereafter, using a variety of different statistical techniques (STMBJ, MCBJ etc.) both at room temperature and low temperature. A collection of some of these experiments on BDT is shown in Figure 1.4(a) with the measured conductance plotted against different techniques. The first experiment made by[68] is also included there.

Figure 1.4 (b) also shows the voltage at which the data points shown in the figure are measured. What we see is that although in some works[68,76] it is shown that the differential conductance increases with applied bias in a step manner, the different measurements tabulated in the Figure 1.4(b) don't follow any specific trend with bias.

[68] M. A. Reed et al. In: *Science* 278 (1997), p. 252.
[69] Eldon G. Emberly and George Kirczenow. In: *Phys. Rev. B* 58 (1998), p. 10911.
[70] M. Di Ventra et al. In: *Phys. Rev. Lett.* 84 (2000), p. 979.
[71] K. Stokbro et al. In: *Computational Materials Science* 27 (2003), p. 151.
[72] A. M. Bratkovsky and P. E. Kornilovitch. In: *Phys. Rev. B* 67 (2003), p. 115307.
[73] Xiao et al. In: *Nano Letters* 4 (2004), p. 267.
[74] Jochen Ulrich et al. In: *The Journal of Physical Chemistry B* 110 (2006), p. 2462.
[75] Makusu Tsutsui et al. In: *Applied Physics Letters* 89 (2006), p. 163111.
[76] Emanuel Lörtscher et al. In: *Phys. Rev. Lett.* 98 (2007), p. 176807.
[77] Wolfgang Haiss et al. In: *Journal of Physics: Condensed Matter* 20 (2008), p. 374119.
[78] Masateru Taniguchi et al. In: *Nanotechnology* 20 (2009), p. 434008.
[79] Youngsang Kim et al. In: *Nano Letters* 11 (2011), p. 3734.



(a) (b)

Figure 1.4: (a) Spread of measured conductance values of BDT molecule with gold leads under different conditions (UHV, RT, LT) and different measurement techniques (STMBJ, MCBJ, I(t)). The different symbols signify different authors and the two unfilled symbols are the only ones measured at bias less than 50mV. (b) This graph shows the corresponding voltage bias at which the data points in (a) are measured.

The wide spread in the conductance of BDT was attributed to the different manner (orientation, contact site, nature of the bond etc.) the BDT could attach to the gold leads. The exact atomic structure of the gold electrode, the position of the Fermi level at the gold leads with respect to the HOMO and LUMO of the molecule, number and type of other molecules in the close vicinity (i.e., the environment of the molecule, presence of solvent molecules etc.) are also contributing to the spread. These uncertainties from the experiment side lead the theory to provide also a variety of different conductance (few mG_0 to 0.5 G_0[80]) values for BDT depending on the chosen position (orientation) of the molecule and the structure of the leads. Recent theoretical account of this is given elsewhere[81–84]. Also, a difference in the conductance gap is reported both among experiments[68,76] and among the theory[69,70].

Inelastic electron tunnelling spectroscopy (IETS)[5] measurements have also been reported[78,79] on the BDT molecule contacted between gold electrodes. Here the different vibration mode energies of the molecule have been shown to match with the theory presented in the individual article. The BDT junction over which these IETS measurements have been reported have conductance ranging from 0.002 to 0.5 G_0. Karimi *et al.*[85] have shown by doing shot-noise measurements, that electronic

[5] A discussion on it is given in Chapter 6

[80] Nikolai Sergueev et al. In: *Phys. Rev. B* 82 (2010), p. 073106.
[81] Mikkel Strange et al. In: *The Journal of Physical Chemistry Letters* 1 (2010), p. 1528.
[82] Renato Borges Pontes et al. In: *ACS Nano* 5 (2011), p. 795.
[83] William R. French et al. In: *The Journal of Physical Chemistry Letters* 4 (2013), p. 887.
[84] Amaury de Melo Souza et al. In: *Nanoscale* 6 (2014), p. 14495.
[85] M. A. Karimi et al. In: *Nano Letters* 16 (2016), p. 1803.

transport through BDT molecules takes place via a single channel over a wide range of conductance values (i. e. 0.01-0.24 G_0).

It has been reported recently[86] using transition voltage spectroscopy (TVS) that on stretching of the BDT molecule, the HOMO level which lies far below the Fermi level is pulled up towards it, giving rise to an increase in conductance due to resonance tunnelling. This increase can be up to few orders of magnitude. When the molecule is compressed (or titled) between the leads, there is again an increase in conductance due to increase in coupling of the π electrons in the benzene ring to the leads.

1.5.2 Alkane dithiols

Alkane dithiol (ADT) molecules coupled between two gold electrodes were the model system in the first decade of 21st century for single molecule electronics experiments. Before this period most of the electronic transport experiments in molecular electronics were mostly done on self assembled monolayers (SAM)[87] where 10s of molecules where contacted and measured. Cui *et al*.[88] were the first who have contacted and measured a single 1,8-octanedithiol (ADT8) molecule. They inserted a small concentration of ADT8 molecules in 1,8-octanethiol monolayer over a flat Au(111) surface. The octanethiol molecules acted as insulator and were used to separate single ADT8 molecules from one another. Now, on inserting this into a gold nano-particle solution, the dithiol molecules made a -SAu chemical bond with the nano-particles which were further probed using a conducting AFM tip. They reported conductance of around 1.43×10^{-5} G_0 at 0.1 V bias in Toulene solution environment. Later on the same group published data also for decanedithiol (ADT10) and dodecanedithiol (ADT12) and showed that the conductance of the ADT molecules decreases (with length of the molecule) exponentially with a decay constant β of 0.58 ± 0.06 per $-CH_2$ group. In 2003, Tao *et al*.[61,89] used an STM break junction method to probe hexanedithiol (ADT6), ADT8 and ADT10. They reported very different (almost one order of magnitude higher) conductance values than Cui *et al*.[88,90] at the same bias and a decay constant β of 1.04 ± 0.05 per $-CH_2$ group, which is similar to value a known for alkane thiols self-assembled mono-layers. Similar to Cui *et al*. , the measurements were also conducted in solution. The lower conductances measured in the previous work[88] was then speculated to be due to finite resistance between the AFM tip and the gold nano particle causing charging effects on the nanoparticle itself. Soon after in 2004 Haiss *et al*.[67] used the I(t) measurement technique to probe a similar set of molecules i.e., ADT6, ADT8 and nonanedithiol (ADT9). They found conductance values and a decay factor close to what was reported by Cui *et al*.[88,90]. After this, many groups measured different ADT molecules mainly using different versions of break junction techniques due to its simplicity, and also some I(t) and I(s) measurement.

A collection of the measured conductance values for different chain lengths of ADT molecules as obtained by single-molecule measurement techniques is collected in Figure 1.5. The conductance is placed on the y-axis in log scale, while x-axis is formed by the length of the ADT molecules in terms of the number of CH_2 groups

[86] Bruot Christopher et al. In: *Nature Nanotechnology* 7 (2011), p. 35.
[87] A. Salomon et al. In: *Advanced Materials* 15 (2003), p. 1881.
[88] X. D. Cui et al. In: *Science* 294 (2001), p. 571.
[89] Bingqian Xu et al. In: *Journal of the American Chemical Society* 125 (2003), p. 16164.
[90] X. D. Cui et al. In: *The Journal of Physical Chemistry B* 106 (2002), p. 8609.

in them. We see here orders of magnitude variation in conductance reported by different groups for each length of the molecule. Several groups have reported multiple conductance peaks, which are shown with different symbols in the Figure. We will discuss them in detail later. The two green ellipses define two regions of length of the molecules. For smaller length, the measured conductance is mostly constant, while for longer derivatives an exponential decay can be defined by fitting a straight line to the data. The slope of this fit, called the decay factor (or β) per CH_2, is measured by different groups. The inset of Figure 1.5 shows a histogram based on different β values recorded by different groups. A similar spread as shown in Figure 1.5 is also reported by Hihath *et al*.[91] while comparing the effects of different anchoring groups on the conductance values for alkane chains.

The orders of magnitude variations shown in the conductance measured for a simple family of alkane molecules questions our mastery of measuring and controlling electronic transport through single molecules. All the work done made us learn more about electronic transport through the molecule but also points towards our limited understanding of many aspects. We will go through a list of such aspects here.

The foremost one which is expected to be a major reason of variation in measured conductance is the lack of knowledge and control over the geometry of the contact between the molecule and the leads. It is seen from the limited number of configurations studied theoretically[111,112], that the conductance of the molecule can vary by more than an order of magnitude just based on the electrode configuration. In some later experiments it was also observed that there can be two[92–94,96,107] or even three[99,100,104] peaks in the histogram of conductance which are not integer multiples of the lowest conductance peak. Different characteristics conductance values observed in histograms for one molecule was attributed to the three possible combinations of binding sites for the sulphur(-S) atom on the gold leads. The -S atom can bind either to the hollow site between the gold atoms (which increases the conductance 'H') or on the top of the gold atom (which lowers conductance 'L'). Now three possible combinations are that (i) -S sits on an H-spot on both leads i.e., 'HH' or high conductance (HC) state, (ii) -S sits on both sides on an L-spot i.e., 'LL' or low conductance (LC) state and (iii) -S sits on one lead on an H spot and on the other lead on an L-spot i.e., 'LH' or 'HL' which is medium conductance (MC) state. These three conductance states were the most accepted explanation for the measured conductance peaks in the histogram. The probabilities (P) of these states occurring in the

[91] Joshua Hihath and Nongjian Tao. In: *Semiconductor Science and Technology* 29 (2014), p. 054007.
[111] K. H. Müller. In: *Phys. Rev. B* 73 (2006), p. 45403.
[112] John Tomfohr and Otto F. Sankey. In: *The Journal of Chemical Physics* 120 (2004), p. 1542.
[92] Jin He et al. In: *Faraday Discussion* 131 (2006), p. 145.
[93] Xiulan Li et al. In: *Journal of the American Chemical Society* 128 (2006), p. 2135.
[94] Fang Chen et al. In: *Journal of the American Chemical Society* 128 (2006), p. 15874.
[96] Emil Wierzbinski and Krzysztof Slowinski. In: *Langmuir* 22 (2006), p. 5205.
[107] Youngsang Kim et al. In: *Phys. Rev. Lett.* 106 (2011), p. 196804.
[99] Ayano Nishikawa et al. In: *Nanotechnology* 18 (2007), p. 424005.
[100] Chen Li et al. In: *Journal of the American Chemical Society* 130 (2008), p. 318.
[104] Wolfgang Haiss et al. In: *Phys. Chem. Chem. Phys.* 11 (2009), p. 10831.

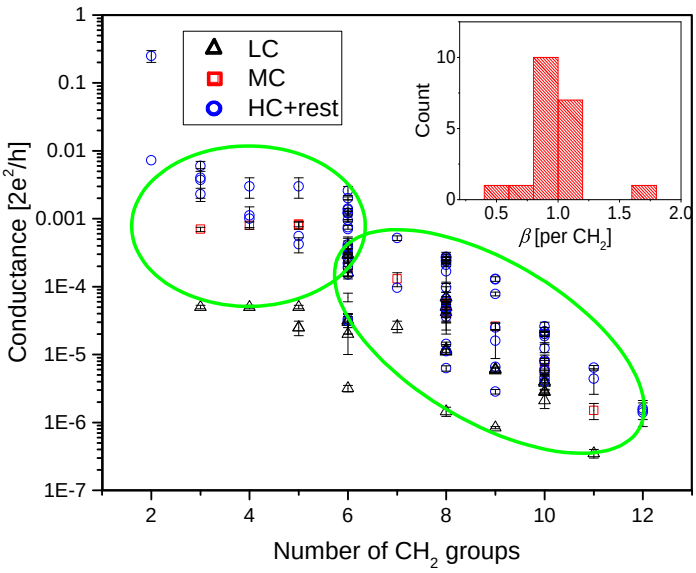


Figure 1.5: Spread of measured conductance values of ADT molecules vs their lengths in terms of number of $-CH_2$ groups in the backbone. The data is a collection of most of the published work[37,61,63–65,67,74,88,89,92–110] on ADT divided into four categories: low conductance (LC), medium conductance (MC), high conductance (HC) and 'rest' for the data not been classified by the respective authors in any of the three conductance states. Inset shows a histogram of reported[61,63,67,93–95,98,100,103–105,109,110] decay constants (β).

experiments were given as $P(LC) > P(MC) > P(HC)$, which was acceptable by the fact that the conductance of the molecule is measured while pulling the electrodes away from each other in break junction setup, which makes the -S atom sitting in the hollow site in both the gold electrodes under a tensile stress as least likely. It was also reported that other than these conductance states which depend only on the position of -S atom on Au electrodes, there could be more conductance states due to the conformation changes (trans or gauche)[99] of the molecule sitting in between the leads. Chen *et al*.[100] argued that many combinations of such contact geometries and conformations could coexist, which makes it difficult to even understand why in experiments one measures any peaks in the histogram. They explained on the basis of ab initio calculations, that the different junctions conformations are correlated and clustered together. This shows that one could expect peaks in the histogram but a single peak results from averaging over many junction configurations and does not point towards one favorable configuration. From the simulation Chen *et al*. also extract the information that the MC and HC configuration described above are due to all $trans$ conformers with atop-atop and bridge-bridge configuration respectively for S atom on Au leads. The LC configuration is supposedly originating form the

mixed *gauche* conformations which suggests that the LC series might not show pure exponential decay. This may explain why Haiss *et al*.[67] measured a smaller decay constant. Chen *et al*.[100] also provide an estimate that the combined effect of the uncertainty in contact geometry and conformation changes could give up to 2 orders of magnitude variation in conductance.

Irrespective of the large variation of the values of the measured conductance shown in Figure 1.5, it was reported repeatedly by many groups that there is an exponential decay of the conductance with length of the molecule. Although a varying set of decay constants have been reported as well, as shown in the inset of Figure 1.5, the exponential behavior suggests elastic tunneling or a superexchange process as the predominant electron transport mechanism for ADT molecules given by $G(N) = G(0)\exp(-\beta N)$. This length dependence appears to be followed for the larger length molecules ($N > 7$), as can be seen in Figure 1.5. The deviation from the exponential behavior for smaller length has been attributed to the fact that for smaller molecules the conductance could be more critically effected by the coupling of the chain through the sulphur groups[92].

It is experimentally also reported that the LC and HC conductance states for ADT8 are temperature independent between 269 to 315 K[93] and also from 4 to 40 K[108], while others show[113] for four different molecules from ADT family that the single molecule conductance are strongly dependent on temperature between 293 to 353 K. They attribute this to changes in the conformation of the molecule. The same group reports that this temperature dependence becomes suppressed as the molecules is squeezed or stretched not allowing the temperature induced conformation changes to take place[114].

Another question on the understanding of the formation of these molecular junctions is how does the molecule arrive between the electrodes? Huisman *et al*.[102] has provided an insight to this by pointing out the modified or enhanced plateau length of the Au-Au point contact plateau at 1 G_0 conductance. They have shown that in the presence of the molecules the 1 G_0 conductance plateau length is increased significantly, suggesting that the molecules already bridge the two electrodes before the first JOC is seen. With a simple spring model and taking the ratio of the length of the plateau with and without the molecules from the experiments they were able to show that the number of molecules that must be bridging the two electrodes were between 1 to 3. Dithiol molecules are in general also easy to polymerize due to oxidative disulfide formation and this could lead to contacting more than one molecule in series between the leads. Another aspect which is not known is the absence or presence of H atom in the sulphur gold bond i.e., -SAu (thiolate bond) or -SHAu (thiol bond). The occurrence of both the bonds is equally likely as both have similar binding energy, but it is known from theory that there can be around one order of magnitude variation in the conductance from one case to other[71], thiolate bond being more conducting. Most of the theory calculations done for dithiol molecules in order to compare with the experiments are done assuming thiolate bonds on both electrodes.

[108] Youngsang Kim et al. In: *ACS Nano* 5 (2011), p. 4104.
[113] Wolfgang Haiss et al. In: *Faraday Discuss.* 131 (2006), p. 253.
[114] Wolfgang Haiss et al. In: *Nature Materials* 6 (2006), p. 995.
[102] Everardus H. Huisman et al. In: *Nano Letters* 8 (2008), p. 3381.

The conductance histogram measured in the break junction experiments could also depend on the size of the Au-Au contact (junction conductance) formed upon indentation before separating the two electrodes and also on the speed of electrode separation. It has been reported that a maximum junction conductance of around 20 G_0 gives sharper peaks in the conductance[106]. Junction conductance from 0.2 G_0 (in tunneling) to 40 G_0 or higher have been reported. The need to make a sufficiently large junction was motivated by the idea of randomizing the tip structure and molecule coupling, giving more statistical parameter space to be explored. On the other hand the I(s) method proposed by Haiss *et al.* ,[67,104,114] and other non-contact experiments[95,100] have tried to minimize the variations coming from tip structure and avoid the strain due to jump out of contact on the breaking of gold atomic chain backbone. A systematic study of the effect of different indentation depth in break junction experiments to the non-contact case in I(s) type measurements in the single molecule conductance value and the FWHM of the histogram peak is missing from the literature. Another thing that is missing as mentioned earlier is the effect of different stretching rate or electrode speed on the conductance.

Some studies on the effect of the stretching rate on the length of the conductance plateaus have been done[97,115]. They have shown that for very slow (<4.4 nm/s) and very fast (>22 nm/s) stretching rate the stretching length remains independent of stretching rate but for the mid range the stretching length increases linearly with the logarithm of the stretching rate and this behavior is the same for molecular and metallic junctions. This further suggests that the final breakdown of the molecular junction might also be taking place at the Au-Au bond close to the metal molecule contact rather than at the Au-S bond. In fact, the stretching rate may also play a role on the measured conductance histogram of the molecule itself[65], as depending on the junction geometry and stretching rate it may be possible that the formation of Au-S chemical bond is getting effected[96] in the small millisecond time scale in which the measurement is performed and this could effect the conductance drastically.

Another interesting characteristics that has been seen in the single molecule conductance traces taken via break junction type techniques was a rise of conductance on stretching the molecule just before the breaking of the molecular junction. This type of increase contributes partly to the large spread in conductance histogram and so it is important to understand. Fujihira *et al.*[116] have pointed out that about 80% of the traces with molecules have this feature. One explanation to the increase was given in terms of transformation of the molecule conformation from $gauche$ to $trans$. A similar increase of conductance with stretching is also seen regularly in other molecules like benzenedithiol. Here the conductance increase is attributed to the shifting of HOMO related states close to the Fermi level during stretching[86] and the rise in conductance during stretching could even be up to one order of magnitude.

The effect of background in the statistical data is a problem in the analysis. When the measurements are done (specially break junction type), a large part of the traces have no signatures of the presence of a molecule, which gives after the Au contact

[106] C. A. Martin. PhD thesis. Kavli Institute of Nanoscience Delft, 2010.
[95] Slawomir Sek et al. In: *The Journal of Physical Chemistry B* 110 (2006), p. 19671.
[97] Huang et al. In: *Journal of the American Chemical Society* 129 (2007), p. 13225.
[115] Zhifeng Huang et al. In: *Nature Nanotechnology* 2 (2007), p. 698.
[116] Masamichi Fujihira et al. In: *Phys. Chem. Chem. Phys.* 8 (2006), p. 3876.

is broken a tunneling decay curve. The exact nature of the tunneling curve depends on the shape of the electrodes and the presence of local impurities (even the test molecules) on the two electrodes. These curves without molecules bridging the junction forms a large tunneling background in the histogram and could hide in it the useful features relevant to the molecules. In the previous section 1.4.4 on data analysis we have covered some common techniques to avoid such background effects. In an article by Rascon-Ramos *et al.*[110], the authors have shown that by adding an AC modulation to z motion of one of the electrode one could extract the mechanical properties of the contact and also get an idea of the most preferential binding site of S atom on Au leads. Such experiments help in reducing the unknowns and understanding to some extend the origin of the wide spread in the conductance histogram of molecules.

Using the examples of benzene dithiol and alkane dithiols, we discussed above the effects of different parameters on the measured conductance values and the limitations of the statistical measurement techniques. A better control of various input parameters can be achieved by moving towards single-shot measurements discussed in Part 1 of this thesis.

1.6 Shot noise

In addition to conductance, electronic transport through single molecules is also probed previously using shot-noise measurements. It is used mostly for determining the number of transmission channels involved in the electronic transport[85,117,118]. However, recently attempts have been made to use noise measurements also as a spectroscopic tool[119]. In this work, it is shown that there are signatures of electron-phonon interactions in usual noise spectra. Here, a gold metallic point contact is studied, and on exciting an electron-phonon vibration mode in gold (which is around 10-20mV), a linear kink in the noise spectra was recorded[120]. Figure 1.6 shows the result of such noise spectroscopy taken from the PhD Thesis of Manohar Kumar[119].

Shot noise occurs due to fluctuations in the number of electrons that are crossing a junction for an applied current or voltage bias. This fluctuation in electron number also exists for a macroscopic size contact. However, as the mean value of current can be very large, so these fluctuations are hardly visible. In nanocontacts, this fluctuation in the number of electrons passing through a cross-section gives a finite noise over the mean current. Moreover, in an independent electron system, the electron crossing time follows a statistical Poisson distribution. The noise generated by these fluctuations is called shot noise. An important difference between these fluctuations and thermal fluctuations is that the former will be present even at absolute zero temperature unlike the later. According to perturbation theory, the crossover from thermal noise (proportional to $k_B T$) to shot noise (proportional to eV) occurs at a voltage $eV = 2k_B T$. A correlation function P_{LR} for the fluctuations in current over the

[110] Habid Rascón-Ramos et al. In: *Nature Materials* 14 (2015), p. 517.
[117] D. Djukic and J. M. van Ruitenbeek. In: *Nano Letters* 6 (2006), p. 789.
[118] Regev Ben-Zvi et al. In: *ACS Nano* 7 (2013), p. 11147.
[119] Manohar Kumar. PhD thesis. Leiden Institute of Physics (LION), Leiden University, 2012.
[120] Manohar Kumar et al. In: *Phys. Rev. Lett.* 108 (2012), p. 146602.

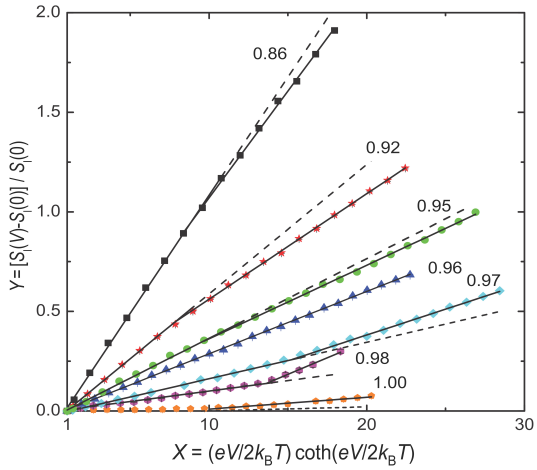


Figure 1.6: Kink in shot noise for a range of transmission values (from 0.86 to 1.00) of Au atomic chain: In this reduced axis plot the noise data below the vibron energy are described by a linear dependence (fitted with a solid line up to the kink, and extrapolated by a dashed line). Above the phonon energy, a new linear dependence is observed. Figure taken from the PhD Thesis of Manohar Kumar[119].

mean current (i. e. $\Delta\hat{I}_\alpha(t) = \hat{I}_\alpha(t) - \left\langle \hat{I}_\alpha \right\rangle$) in the left and the right leads can be written as –

$$P_{\mathrm{LR}}(t,t') = \frac{1}{2}\left\langle \Delta\hat{I}_{\mathrm{L}}(t)\Delta\hat{I}_{\mathrm{R}}(t') + \Delta\hat{I}_{\mathrm{R}}(t')\Delta\hat{I}_{\mathrm{L}}(t)\right\rangle \tag{1.4}$$

For stationary random fluctuations, i. e. for no time-dependent external fields, the noise power ($S_{LR}(\omega)$) associated with this correlation is directly given by its Fourier transform, which is also called Wiener-Khintchine theorem.

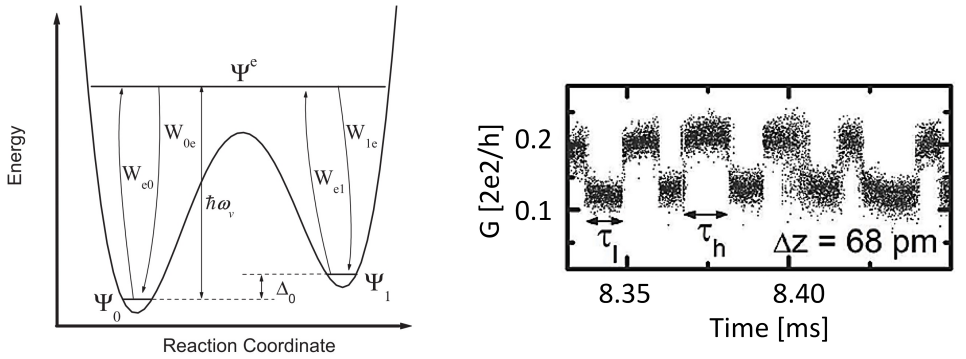
$$S_{\mathrm{LR}}(\omega) = \int_{-\infty}^{+\infty} \mathrm{d}\tau P_{\mathrm{LR}}(\tau = t - t')e^{-j\omega\tau} \tag{1.5}$$

In this thesis, we will use only the noise power or power spectral density ($S_{\mathrm{LR}}(\omega)$) and not the current correlation function ($P_{\mathrm{LR}}(t,t')$), as the former is the direct output from our FPGA based noise spectrum analyser as described in Chapter 4.

1.7 Two-level fluctuations

Two-level fluctuations are common in nanoscale junctions. They occur due to stochastic fluctuations of an atomic or molecular junction between two stable conductance states. These fluctuations are measured by bringing an STM tip above a molecule adsorbed on a surface[121] and also for molecular and atomic junctions formed using mechanically controlled break junction[122,123]. Figure 1.7(a) is a schematic depiction

[121] N. Néel et al. In: *Nano Letters* 11 (2011), p. 3593.
[122] Alexei Marchenkov et al. In: *Phys. Rev. Lett.* 98 (2007), p. 046802.
[123] W. H. A. Thijssen et al. In: *New Journal of Physics* 10 (2008), p. 033005.



(a) (b)

Figure 1.7: (a) An energy diagram of a two level system taken from Thijssen *et al.*[124]. It shows the reaction kinetics involved in transfer of energy from a molecular vibration to excitement to a different conductance state. (b) Conductance fluctuation measured over a C_{60} molecule[121] once an STM tip is brought towards it.

(taken from Thijssen *et al.*[124]) of such bistable conductance states separated by a small energy barrier. It has been shown[124] that these two-level fluctuations can also be induced by an electron-phonon interaction, which could provide sufficient energy to cross the barrier. This process takes place along a certain reaction coordinate. Persson and Ueba[125] have shown that similar inelastic interaction can be used to move molecules over a metallic surface using STM tip.

Figure 1.7(b) shows a conductance fluctuation example taken from Néel *et al.*[121], where a two-level fluctuation is seen over a C_{60} molecule once an STM tip is brought towards it. This is a typical example of a two-level fluctuation, where two different conductance states occur with different mean residence times for the high (τ_1) and low state (τ_2). The power spectral density for the noise generated by such two-level fluctuations is Lorentzian in shape and is given by –

$$S_{2L}(\omega) = 4\Delta R^2 \frac{{\tau_{\text{eff}}}^2}{\tau_1 + \tau_2} \frac{1}{1 + \omega^2 {\tau_{\text{eff}}}^2} \tag{1.6}$$

here, $\frac{1}{\tau_{\text{eff}}} = \frac{1}{\tau_1} + \frac{1}{\tau_2}$ and ΔR is difference in the resistance values of the two states.

1.8 Organization of the thesis

More than three decades have passed since the first single-molecule experiment was performed by Reed *et al.*[68]. The main techniques that are used to study single-molecule transport to date do not provide many crucial pieces of information about the system. Most important are the atomic structure of the contacting leads and the binding configuration of the molecule.

There are three main questions that this thesis is aiming to answer –

[124] W. H. A. Thijssen et al. In: *Phys. Rev. Lett.* 97 (2006), p. 226806.
[125] B. N. J. Persson and H. Ueba. In: *Surface Science* 502-503 (2002), p. 18.

The first question that this thesis is going to answer is how can we make the single-molecule transport measurements more controlled? What extra information can we obtain from these measurements to bridge the gap between experiments and theory? These questions will be the subject of Part 1 of the thesis. Here we prepare a benchmark single-molecule test setup for single-shot measurements.

The second question that we are aiming at is, can we do more with shot-noise measurement? Shot noise is the second cumulant of current while conductance is the first. Thus shot noise is more sensitive to electron-electron and electron-phonon interactions. In spite of that, most of the shot-noise measurements done on single-molecules and atomic junctions have aimed at low energy regime to mainly obtain the information about the number of channels involved in the transport. Recently, it has been shown that shot noise can also be used to probe inelastic electron-phonon interactions in Au metallic contacts. However, no measurements have been done on probing such interactions in single molecules. In Part 2 of the thesis, we will study shot noise at high bias probing single atomic point contacts in non-linear regime and single molecules.

Third and the last question that we also worked on is related to the use of graphene-based electrodes in molecular electronics. Graphene offers a unique platform to study single-molecules. The two-dimensional structure of this material offers the flexibility to image the contacts atomic structure and molecules binding configurations. To this end, we need to have atomic-scale control of the nanogaps formation in graphene. The commonly used electroburning technique does not provide such a control. Thus, in Part 3 of this thesis, we will explore other techniques to make controlled nanogaps in graphene.

I

Part One: Atomic and Molecular Manipulation

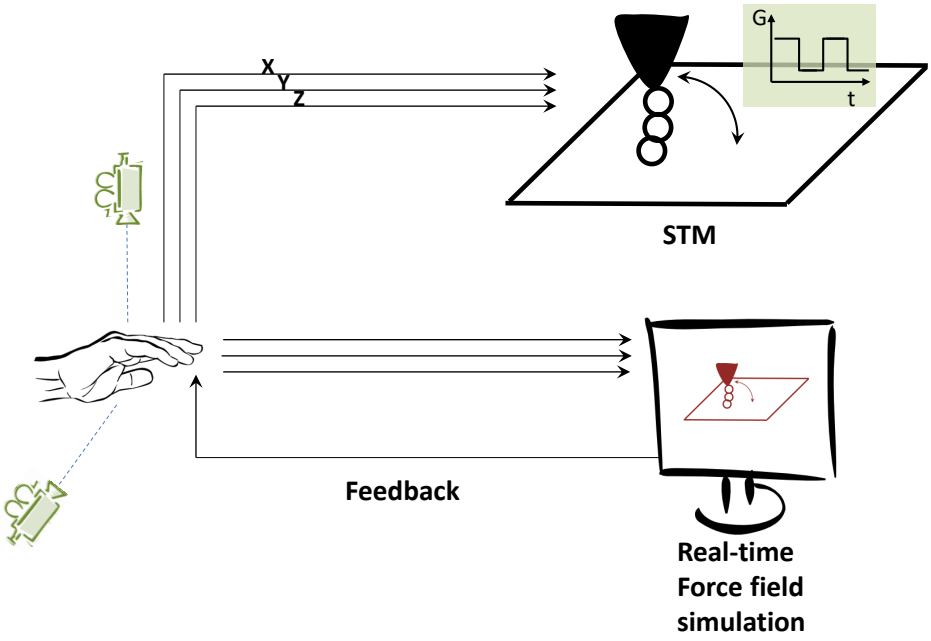
2 Human-machine augmented system to control single atoms 26

2.1 Introduction
2.2 Experimental setup
2.3 Real-time molecular dynamic simulation
2.4 Experimental measurements
2.5 Discussion
2.6 Conclusion and outlook

3 Single molecule STM control: GPU implementation 48

3.1 Introduction
3.2 Single-shot measurements - Overview
3.3 Molecular dynamics
3.4 Molecular dynamics - GPU implementation
3.5 Results and discussion
3.6 Conclusion and outlook

Graphical Summary



2. Human-machine augmented system to control single atoms

A new way to control individual molecules and mono-atomic chains is devised by preparing a human-machine augmented system in which the operator and machine are connected by a real-time simulation. Here a 3D motion control system is integrated with an ultra-high vacuum (UHV) low temperature scanning tunneling microscope (STM). Moreover we coupled a real-time molecular dynamics (MD) simulation to the STM which provides a continuous visual feedback to the operator during atomic manipulation. This allows the operator to become a part of the experiment and to make any adaptable tip trajectory which could be useful for atomic manipulation in 3 dimensions. The strength of this system is demonstrated by preparing and lifting a mono-atomic chain of gold atoms from the Au(111) surface in a well-controlled manner. We also show here a new geometric procedure to infer the ad-atom positions and therefore information about the substrate atoms which are not easily visible in clean metallic surfaces like gold. This method enables a new controlled atom manipulation technique which we will refer to as point contact pushing (PCP) technique. Finally we discuss the effect of unknown spring stiffness of STM tips in addition to the unknown atomic configuration of tip apex on the accuracy of atomic manipulations.

The work is done in collaboration with - Jacob Bakermans[1], Christian Wagner[2], Federica Galli[1] and Jan M. van Ruitenbeek[1]
[1]Huygens-Kamerlingh Onnes Laboratorium, Universiteit Leiden, The Netherlands.
[2]Peter Grünberg Institut (PGI-3) Jülich, Germany.

2.1 Introduction

Manipulating single atoms and molecules on metal surface using STM is not new. In early 1990s, while studying the adsorption of Xenon atoms[1] on a Pt surface using STM, researchers at IBM observed that the STM tip is not only imaging the surface but also occasionally dragging the adsorbed atoms on the surface. Consequently, they found out that by bringing the tip closer to the adsorbed atoms, the van-der Waals (vdW) force between the tip and the ad-atom becomes large enough to overcome the corrugation barrier of the surface making it easier to drag the atom[1–4]. Such manipulation of atoms or molecules along the surface is called lateral manipulation (LM), and is further classified[5–7] into three types: pulling, pushing and sliding. LM is performed while using the STM in a constant current mode with a tunnel gap. LM has also been demonstrated on a single Br atom at room temperature[8] over Cu(001) surface in UHV condition. Various complex 2D nano-structures[3,9–14] have been made by manipulating single atoms and molecules and it has also been demonstrated that these LM techniques can be performed in an automated way[14,15] to create a desired 2D lattice. An independent vertical manipulation (VM) technique has also been developed which could be used in making 3D nano-structures. These vertical manipulation techniques are known to rely either on a local field emission process[16] or on multiple excitation of the substrate ad-atom vibration mode due to inelastic electron tunneling[17]. These are not considered as accurate and reliable as LM in positioning the ad-atom[15].

STM opens up the possibility of this atomic scale control because of its capability to image single atoms and molecules when they are on the surface. However, during atomic and molecular manipulation operations it is not possible to image the underlying dynamics using STM because the very tip used for imaging is also used for manipulation. The system that we have developed addresses this problem. We have

[1] Xe makes a relatively weak bond with Platinum

[1] Donald M. Eigler and Erhard K. Schweizer. In: *Nature* 344 (1990), p. 524.
[2] Joseph A. Stroscio and D. M. Eigler. In: *Science* 254 (1991), p. 1319.
[3] P. Zeppenfeld et al. In: *Ultramicroscopy* 42 (1992), p. 128.
[4] D. M. Eigler. In: *Atomic and Nanometer-Scale Modification of Materials: Fundamentals and Applications*. Ed. by Phaedon Avouris. Dordrecht: Springer Netherlands, 1993, p. 1.
[5] L. Bartels et al. In: *Phys. Rev. Lett.* 79 (1997), p. 697.
[6] Saw-Wai Hla. In: *Journal of Vacuum Science & Technology B: Microelectronics and Nanometer Structures Processing, Measurement, and Phenomena* 23 (2005), p. 1351.
[7] Gerhard Meyer et al. In: *Single Molecules* 1 (2000), p. 79.
[8] T. W. Fishlock et al. In: *Nature* 404 (2000), p. 743.
[9] Michael F. Crommie et al. In: *Science* 262 (1993), p. 218.
[10] H. C. Manoharan et al. In: *Nature* 403 (2000), p. 512.
[11] Saw-Wai Hla et al. In: *Nano Letters* 4 (2004), p. 1997.
[12] N. Nilius et al. In: *Science* 297 (2002), p. 1853.
[13] Kenjiro K. Gomes et al. In: *Nature* 483 (2012), p. 306.
[14] Marlou Slot et al. In: *Nature* 13 (2017), p. 672.
[15] Robert J. Celotta et al. In: *Review of Scientific Instruments* 85 (2014), p. 121301.
[16] In-Whan Lyo and Phaedon Avouris. In: *Science* 253 (1991), p. 173.
[17] D. M. Eigler et al. In: *Nature* 352 (1991), p. 600.

added a 3D motion control system to our STM which helps in making any required tip trajectory and combined it with a molecular dynamics (MD) simulator which simulates in real-time the manipulation process going on in the STM. The operator now receives visual feedback from this 3D molecular dynamic simulation permitting better control of the manipulation process. This is especially important in the case of 3D manipulation of single molecules and atomic chains, as there are a no pre-defined trajectories[18,19] that one can set to do those manipulations. Therefore an adaptable trajectory is the only solution where the operator can continuously communicate with the experiment through the real-time MD simulation and define the trajectory at will. This human-machine augmented system thus provides a far better control on the manipulation process and can moreover be used for 3D manipulation. In this chapter first we will start with describing the experimental setup and sample preparation technique. Later in section 2.3 we will discuss the main outline and assumptions made in preparing the real-time MD simulation. After that we report on using this system for a new lateral manipulation methodology which we refer to as point contact pushing (PCP) technique, followed by a 3D trajectory which enabled us to lift in a controlled way a chain of gold atoms above the metal surface. These atomic chains are known to show parity oscillations in conductance[20] while going from even to odd number of atoms in the chain. We detect this phenomena while controllably lifting the chain of atoms and putting it back on the surface. At the end, we will also discuss an un-addressed issue of STM tip spring stiffness and its effect on sub-atomic precision in manipulation.

2.2 Experimental setup

The experimental setup used here is a home built cryogenic STM head[21] which is cooled by an Oxford Heliox UHV system custom built for Leiden[22] The system operates at 10^{-10} mbar pressure and most of these experiments were performed at 3 K temperature (the base temperature of 300 mK was not required). A home built 3D motion control system running under LabVIEW is used to control the STM tip during manipulation. Figure 2.1 shows the schematic diagram of the complete setup with 3D motion controller and the MD real time simulator. The 3D motion control system is a simple LED tracker made with two cameras tracking the x-y and y-z motion of the LED respectively. The LED is connected on top of the operator hand (with a glove in this case), so the trajectory is drawn by the operator hand and tracked by the two cameras. Then a LabVIEW program filters and converts these x,y,z signals with proper scaling factors before sending it out to the STM tip and the simulation. The scaling factor converts approximately 10 cm of hand movement to 2 Å displacement of the STM tip. The usual imaging in STM is done using a commercial RHK SPM100 ver.8E controller. A mono-crystalline gold sample, cut in the (111) surface direction, is prepared by repeated argon sputtering and annealing cycles to obtain an atomically flat Au(111) facet showing herringbone surface reconstruction. We further prepare

[18] Matthew F. B. Green et al. In: *Beilstein journal of nanotechnology* 5 (2014), p. 1926.
[19] Philipp Leinen et al. In: *Beilstein journal of nanotechnology* 6 (2015), p. 2148.
[20] R. H. M. Smit et al. In: *Phys. Rev. Lett.* 91 (2003), p. 076805.
[21] A. F. Otte. PhD thesis. Leiden Institute of Physics (LION), Leiden University, 2008.
[22] Simon J. Kelly. PhD thesis. Leiden Institute of Physics (LION), Leiden University, 2012.

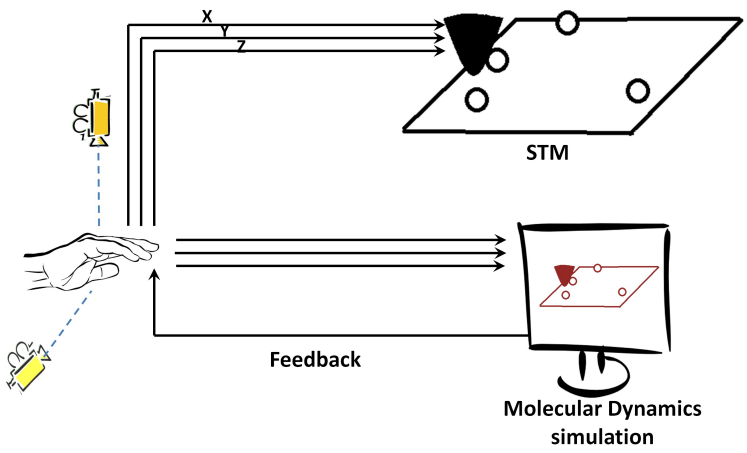


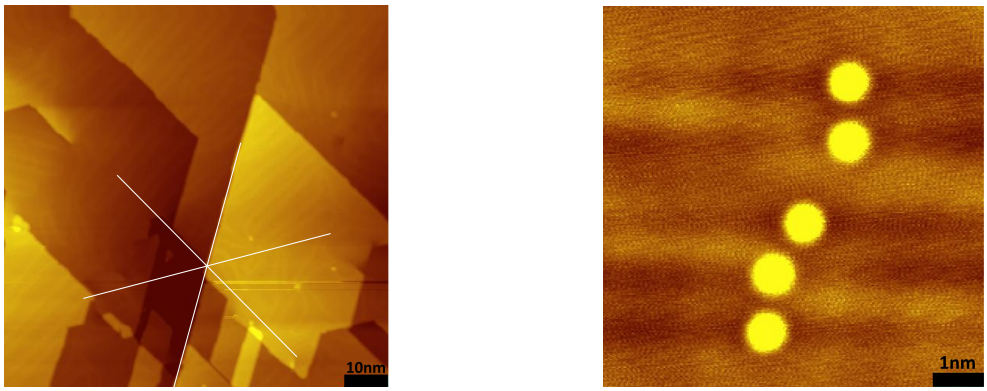
Figure 2.1: Schematic of the experimental setup. The components of the setup include a cryogenic UHV STM, a 3D motion controller and a MD simulator where the motion tracker controls both the STM and the MD simulation.

the surface at low temperature by creating a localized stress pattern[23–26] on the surface using gentle indentation of the STM tip at a spot on the surface remote from the area of investigation. This makes new crystalline (111) facets and provides straight step edges in the three crystallographic directions of Au(111) as shown in Figure 2.2(a). Additional gold atoms (ad-atoms) are deposited[27–29] on the Au(111) surface at the target sites of investigation (Figure 2.2(b)) by establishing point contact with the surface using STM tip at 100 mV bias.

2.3 Real-time molecular dynamic simulation

A conventional atomic manipulation operation using STM involves a pre-determined trajectory (controlled by the operator or by an automated procedure) of the STM tip. For example reducing the tip-sample distance and moving the tip in a desired direction assuming an isotropic nature of adsorption bonds[30] in metallic systems. In such a procedure the operator does not have any feedback while the manipulation is executed and so cannot influence the trajectory based on the complexity in the dynamics of the tip-adatom-surface system during the manipulation. In contrast, in our setup the operator receives a continuous visual feedback from real time MD simulation and can respond to different dynamics involved during the manipulation operation and

[23] D. J. Oliver et al. In: *Nanotechnology* 25 (2014), p. 025701.
[24] Francesca Moresco et al. In: *Phys. Rev. Lett.* 91 (2003), p. 036601.
[25] Francesca Moresco. In: *Physics reports* 399 (2004), p. 175.
[26] Francesca Moresco et al. In: *Applied Physics A* 80 (2005), p. 913.
[27] Saw Wai Hla. In: *Reports on Progress in Physics* 77 (2014), p. 056502.
[28] Jianshu Yang et al. In: *The European Physical Journal Applied Physics* 73 (2016), p. 10702.
[29] Sumit Tewari et al. In: *Beilstein Journal of Nanotechnology* 8 (2017), p. 2389.
[30] Phaedon Avouris. Vol. 239. Springer Science & Business Media, 2012.



(a) (b)

Figure 2.2: (a) Atomically flat Au(111) surface with herringbone reconstruction and straight step edges in crystallographic directions prepared by stress induced lattice deformations at low temperatures, (b) Gold ad-atoms deposited on a Au(111) surface from the STM tip. Images obtained at about 3 K after the temperature was stabilized within a few mK.

alter the trajectory at will. Figure 2.1 shows how the communication between the operator and STM is made using the MD simulator. The 3D motion control sensor gives the same x,y,z signals to both the STM and the simulator simultaneously and therefore the MD simulation is required to have a minimal time delay in its response for smooth real-time operation. We do a classical MD calculation here where we ignore the electronic effects[2](which in fact give rise to the inter-atomic forces) and take the forces as coming from parametrized equations which only depend on the inter-atomic distances. The simulation we discuss in this chapter is only made for metallic systems, so in this case all the atoms involved are Au atoms. The simulation including a molecular entity along with the metallic tip and sample will be discussed in the next chapter. Here a semi-empirical potential described by Tomanek et al.[31] and Cortes-Huerto et al.[32] is used to model the Au-Au interaction. This allows for fast computation and large number of atoms involved because of its simple analytical potential functions. The potential energy is taken to be given by

$$E = -\zeta \sum_{i}^{N} \sqrt{\sum_{j \neq i}^{N} e^{-2q(r_{ij}/r_0 - 1)}} + A \sum_{i}^{N} \sum_{j \neq i}^{N} e^{-p(r_{ij}/r_0 - 1)} \tag{2.1}$$

where r_{ij} is the distance between two atoms i and j, r_0 is the equilibrium distance, and ζ, q, A and p are parameters that can be determined by fitting bulk material properties

[2] A more accurate method would be obtained by using ab-initio calculations which takes into account of both the nuclear and electronic degrees of freedom. These ab-initio calculations are however computationally very expensive and thus are not suitable for our purpose

[31] D. Tománek et al. In: *Phys. Rev. B* 32 (1985), p. 5051.
[32] R. Cortes-Huerto et al. In: *Physical Review B* 88 (2013), p. 235438.

to experimental values. The energy of Equation 2.1 consists of an attractive term (i.e., the energy decreases when the distance between two atoms decreases; the first term of Equation 2.1) and a repulsive term (the energy increases when the distance between two atoms decreases; the second term of Equation 2.1)[31]. The increase in kinetic energy for the conduction electrons trapped within two approaching atoms gives rise to this repulsive term[33], while the attractive interaction originates from the band structure and is found by a second moment approximation to the tight binding Hamiltonian[31]. From this potential energy, forces can be calculated using

$$\vec{F} = -\vec{\nabla} E. \tag{2.2}$$

The force on an atom a is therefore given by (derivation of this is given in the Appendix A.1)

$$\begin{aligned}\vec{F}_a(\vec{r}_1, ..., \vec{r}_N) = &-\zeta \frac{q}{r_0} \sum_{i \neq a}^{N} \frac{e^{-2q(r_{ia}/r_0 - 1)}}{\sqrt{\sum_{j \neq i}^{N} e^{-2q(r_{ij}/r_0 - 1)}}} \frac{(\vec{r}_a - \vec{r}_i)}{r_{ia}} \\ &- \frac{\zeta (q/r_0)}{\sqrt{\sum_{j \neq a}^{N} e^{-2q(r_{aj}/r_0 - 1)}}} \sum_{j \neq a}^{N} e^{-2q(r_{aj}/r_0 - 1)} \frac{(\vec{r}_a - \vec{r}_j)}{r_{aj}} \\ &+ 2A \frac{p}{r_0} \sum_{j \neq a}^{N} e^{-p(r_{aj}/r_0 - 1)} \frac{(\vec{r}_a - \vec{r}_j)}{r_{aj}}\end{aligned} \tag{2.3}$$

2.3.1 Implementation

The molecular dynamics simulation is written in C++ to guarantee high computational performance. Figure 2.3 shows a schematic flowchart of the simulation execution. Since providing visual feedback is one of the main objectives of the simulation, a graphics library is necessary to show visual output on the screen. For performance reasons and the ease of implementation the *Simple and Fast Multimedia Library* (SFML) is used for this purpose. We choose an object-oriented approach to keep the code well structured. A separate class is used to keep track of the individual atoms; another one to calculate energy and forces, and to integrate the equations of motion; and a third separate class to visualize the atoms.

We differentiate between three types of gold atoms, corresponding to the role they play in the simulation. In Figure 2.4 a snapshot of the simulation shows the different atom types. First, there are *normal* gold atoms (drawn in blue), that only feel the forces of the other atoms through Equation 2.3. Then, there are *boundary* atoms (drawn with green and red). These are gold atoms that feel an additional force to confine their positions. A parabolic potential well for each boundary atom, centered at the place we want it to be, keeps the system fixed by fixing the boundaries. The potential wells mimic the presence of atoms beyond the boundaries. This approach allows dynamics even for the boundary atoms, making it possible to apply a thermostat and have realistic interaction with the other normal gold atoms. There are two types of such boundary atoms: tip boundary atoms and surface boundary

[33] Fabrizio Cleri and Vittorio Rosato. In: *Phys. Rev. B* 48 (1993), p. 22.

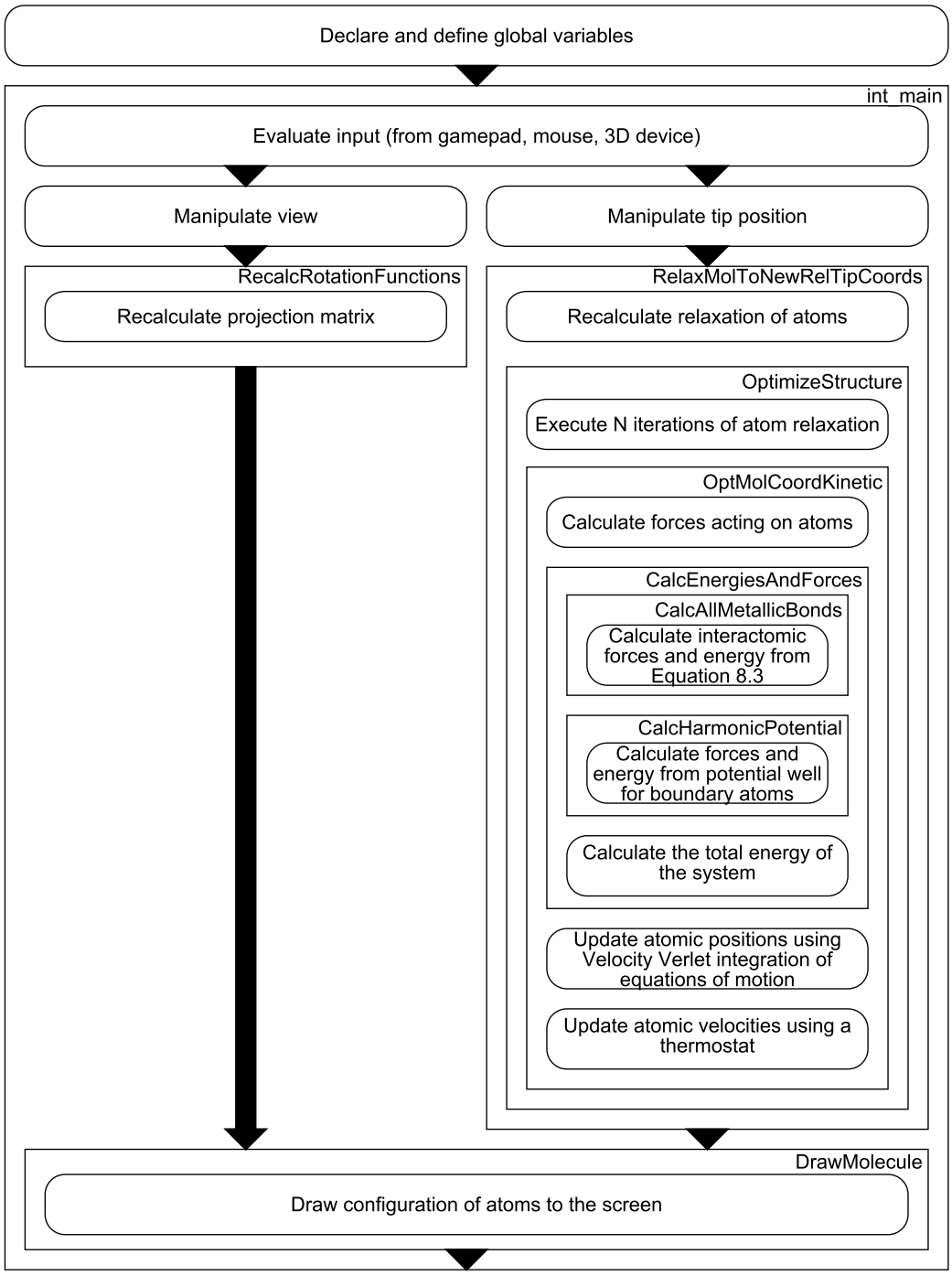


Figure 2.3: Schematic flowchart of simulation execution. Functions are represented by rectangular boxes with their name in the upper right corner. The actions they perform are shown in the boxes with round edges.

atoms. For surface boundary atoms, the position of the potential well stays the same throughout the simulation. For tip boundary atoms, the position of the potential well can be changed to simulate tip motion. As there is a huge discrepancy in time scales between experiment and simulation, a tip motion of some Å in several seconds in experiments happens within picoseconds in the simulation, yielding a much higher tip velocity and acceleration in the simulation. This large amount of kinetic energy pumped into the system has to be drained out using a suitable thermostat. A Berendsen thermostat[34] is implemented into the simulation, which provides a gradual temperature decay instead of sudden re-scaling. Here the instantaneous temperature changes proportional to the temperature difference with the reference temperature T_0 with an adjustable coupling to a heat bath.

$$\dot{T} = \tau_{\mathrm{B}}^{-1}(T_0 - T(t)) \tag{2.4}$$

where τ_B is the temperature relaxation time, related to the strength of the coupling. The velocities of all atoms are rescaled at every timestep (Δt) with the same factor

$$\lambda_{\mathrm{B}}(t) = \sqrt{1 + \frac{\Delta t}{\tau_{\mathrm{B}}}\left(\frac{T_0}{T(t)} - 1\right)} \tag{2.5}$$

A typical value for τ_B in condensed systems is of the order of 0.1 ps[35]. In our case only the boundary atoms are subject to temperature control by a thermostat. This way kinetic energy is transferred through the normal atoms to the boundary atoms, where temperature is controlled, as is also done by Henriksson *et al.*[36]. In order to prevent strongly disturbing the system a special procedure is used to displace the tip boundary atoms. By simply moving the potential wells, the tip boundary atoms would feel strong forces and acquire high velocities. As described above, this amount of kinetic energy would be problematic for the thermostat to dissipate. Instead, we change the position of the tip boundary atoms and their potential wells simultaneously by directly adding smooth displacements. This way, they will change position without additional velocity, and therefore they will not acquire a high temperature. The thermostat then only has to take care of the velocities induced by interactions with the normal atoms in the tip.

2.3.2 Speed-up techniques

Several optimizations and approximations are implemented to speed up the computation so that the simulation can run in real-time. First, we introduce a cut-off radius of 7 Å in the calculation of forces and energy between pairs of atoms. The exponential functions from Equation 2.1 are computationally heavy ; a cut-off radius reduces the number of exponential functions that are calculated. If r_{ij}, the distance between two evaluated atoms, is larger than the cut-off radius, this pair of atoms will not be taken into account in the energy and force calculations. Because of the exponential decay with distance in the potential, their contribution is very small. As described in the

[34] H. J. C. Berendsen et al. In: *The Journal of Chemical Physics* 81 (1984), p. 3684.
[35] Philippe H. Hünenberger. In: *Advanced computer simulation* (2005), p. 130.
[36] K. O. E. Henriksson et al. In: *Phys. Rev. B* 71 (2005), p. 014117.

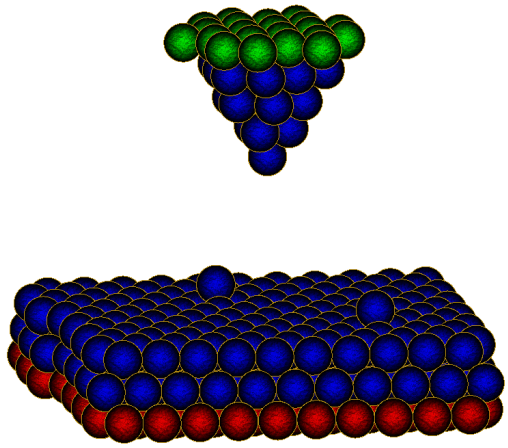


Figure 2.4: Snapshot of the Molecular Dynamics Simulation showing the different atom types. *Normal* gold atoms are drawn in blue, *tip boundary* atoms in green and *surface boundary* atoms in red.

book by Andrew Leach[37], just using a force cutoff would not give a decent speed-up as to use a force cutoff radius one has to compute first all the atomic radii (which involves evaluating a square root which is also computationally expensive) and then measure the forces only within the cutoff radius. In the system we study through molecular dynamics, most of the atoms don't change their nearest neighbours very often and so we introduce another cut-off radius, now for the calculation of the distances between atoms. The other possibility is to use a Verlet's nearest neighbour list, which also requires creation and update of at least two extra arrays (a nearest neighbour array and a pointer array).

Moreover, we do not need to know the distance between atoms that are far apart, since their contributions will not be taken into account because of the cut-off radius for forces and energy. Therefore we only update inter-atomic distances at every simulation step if the previous distance was smaller than a cut-off radius of 7 Å. The larger distances are updated less frequently: only once every 50 simulation steps. Secondly, we implement a lookup table to increase the calculation speed of the exponential functions that still need to be found. This means that the exponential function is evaluated for a long list of relevant inter-atomic distances at the initialization of the simulation. Every time it needs to be calculated during runtime, a linear interpolation of the pre-calculated values around the given distance is used instead of calculating the exponential itself. Looking up the value from the lookup table is faster than calculating it, resulting in better performance. We have compared this speed up in simulation due to the aforementioned approximations with a standard implementation of the MD simulations without any approximations. For this we performed a structural relaxation step in a system analogous to the one shown in Figure 2.4 and checked the difference in the final relaxed state total energy between our method and

[37] Andrew R. Leach. Molecular modelling: principles and applications, Pearson education, 2001.

a conventional approach. We found that the error in final total energy induced by the cut-off radii and lookup table is very small (approximately 10^{-4} percent), while the speed up of almost 10 fold in energy and force calculation is recorded by a standard profiling tool.

A supporting program has also been developed to setup a simulation stage based on the STM images taken during the experiment prior to the start of the main program. To prepare an exact stage as in the experiments, it requires not only the exact knowledge of the positions of ad-atoms on the surface but also the atomic configuration of the surface and the STM tip. Standard STM images of Au(111) surface can provide the information about the crystallographic directions from the Herringbone reconstructions[3] or atomically sharp step edges and the location of FCC or HCP packing. The atomic configuration of the metallic surfaces like Au(111) is not readily available in STM images (see Figure 2.2(b)) due to the delocalized nature of the valence electrons in metals[38]. It is possible to image the atomic configuration by functionalizing the STM tip by adsorbates (for example CO molecules)[39]. To keep the surface clean we did not introduce impurities in the system and we devised a simple geometric technique (explained in the next section) to get the information of the surface atoms positions without the need to resolve the individual surface atoms. The atomic shape of the tip is always an unknown quantity in STM. Although one could obtain partial information before the start of the experiment using field ion microscope (FIM), but after a few manipulations steps the tip shape would become unknown. We developed a localized tip shaping procedure published elsewhere[29] which helps in preparing a crystalline tip apex up to the second atomic layer from the apex atom. A brief description of this work is given in Appendix D.

2.4 Experimental measurements

In this section we will show how the above system with the real-time MD simulation works using some simple lateral manipulation test followed by an experiment where we lifted a chain of Au atoms out of the surface in a controlled manner forming a free standing atomic chain between the tip and the sample. Some challenges in creating such a free standing atomic chain using a controlled STM technique are addressed by Tartaglini *et al.*[40]. These atomic chains are ideal 1D systems and are known to be formed only in pure metals like Au, Pt and Ir metals. They derive their origin from relativistic effects[41][4] which cause a contraction of the s-shell and increases its occupation at the expense of the d-electrons. This leads to strengthening of the d-bond and thus a higher stability to form atomic chains. These chains have been studied experimentally using statistical methods like MCBJ[20,42] and STMBJ[43]

[3] Herringbone surface reconstructions have a 120 degree spatial symmetry and run perpendicular to the crystallographic directions

[4] For detail explanation, see reference Agraït *et al.*[41] and the references therein

[38] J. Wintterlin et al. In: *Phys. Rev. Lett.* 62 (1989), p. 59.
[39] N. J. Zheng and I. S. T. Tsong. In: *Phys. Rev. B* 41 (1990), p. 2671.
[40] E. Tartaglini et al. In: *Low Temperature Physics* 39 (2013), p. 189.
[41] Nicolás Agraït et al. In: *Physics Reports* 377 (2003), p. 81.
[42] A. I. Yanson et al. In: *Nature* 395 (1998), p. 783.
[43] Hideaki Ohnishi et al. In: *Nature* 395 (1998), p. 780.

where two macroscopic size electrodes are pulled apart until the last atom contact is formed and then on further pulling of the junction new atoms from the leads join thereby forming atomic chains. From an atomistic point of view, the reason why new atoms from the bulk (where they are having more than one bond with other atoms) are pulled out to form an atomic chain can be understood by the fact that in metals the bond strength increases as the coordination number is decreased. This causes a single linear bond to become comparable to three bonds (for gold) in the bulk. Since our MD simulation uses an embedded atom potential which measures pair interactions, the effect of coordination number is automatically accounted for within the approximate atomic interaction force.

Another interesting phenomenon from the electronic point of view that was also found experimentally[20] was that the conductance of these atomic chains oscillates as function of number of atoms in the chain and this effect is known as 'parity oscillations'. These oscillations were explained (Reference Agraït *et al*.[41] and Cuevas *et al*.[44] and the references therein) as an interference effect occurring due to back-scattering of electronic waves at the interface between the bulk and the atomic chain. This back-scattering makes this phenomena similar to the Fabry-Pérot interferometer in optics. This was demonstrated in experiments by making length histograms[20] of conductance and it was observed as oscillations in conductance. Therefore free standing atomic chains can be used to test our set up, and the formation of chains can be checked by the observation of parity oscillations.

2.4.1 Obtaining the positions of the background substrate atoms

At the start of the experiment we deposit single Au ad-atoms on the middle of the FCC sector of the herringbone reconstruction on a clean Au(111) surface with the STM tip as explained earlier (Section 2.2). Then a simulation has to be prepared with the ad-atoms lying on the exact same atomic configuration on the surface as in the experiment. To get the information about the background atoms (without functionalizing the tip), we use a geometry based technique. After our surface preparation we can get directly from the orientations of the straight step edges (Figure 2.2(a))[5] the angle of the three crystallographic directions (shown with white lines) in our STM images. Once the three crystallographic directions are established [6] the next step is to find out whether the ad-atom sits on the left (L) or right (R) of the triangular hollow site (shown in Figure 2.5(a)) .

This means that within a linear translation of the lattice, there is a 50% chance of being correct if we choose one of the two hollow sites (L or R). But in fact with the help of just two ad-atoms and a geometric argument we could tell with 100% certainty the position of both the ad-atoms and have a complete information about the background atoms. If we take any two ad-atoms placed near to each other in the experiment, they could be lying either on similar orientated hollow sites (LL or RR) or opposite oriented

[5] These steps appear after locally distorting the surface by tip indentation at a place remote from the measurement location

[6] The crystallographic directions of the surface locally can also be obtained using the angles of the Herringbone reconstruction in (111) surfaces provided that the location is far from any defect sites or corners of the Herringbone as these can change or alter the orientation locally.

[44] Juan Carlos Cuevas and Elke Scheer. Molecular electronics : an introduction to theory and experiment. New Jersey [u.a.] : World Scientific, 2010.

hollow sites (LR or RL). We overlay the measured STM image with the known lattice periodicity, as shown in Figure 2.5. If they are placed on the opposite oriented hollow sites (as shown in Figure 2.5(b)), then within the translational symmetry of the background lattice there is only one possible orientation: either we find that the top left atom sits in the L site and the lower right one in the R site, or the other way around. For example if we try to translate the background lattice scheme such that the bottom right ad-atom in Figure 2.5(b) shifts from the R hollow site (where it is lying) to a L hollow site as shown in Figure 2.5(a), then one can see that the top left ad-atom does not fit anymore in any hollow site. This shows that only the positioning of the ad-atoms shown in Figure 2.5(b) is correct. On the other hand if they are placed on similar hollow sites (LL or RR), then it is not possible to directly conclude their positions by doing the linear translation described above. The solution is to perform one atomic manipulation move of one of the two ad-atoms to bring them in the opposite oriented hollow sites.

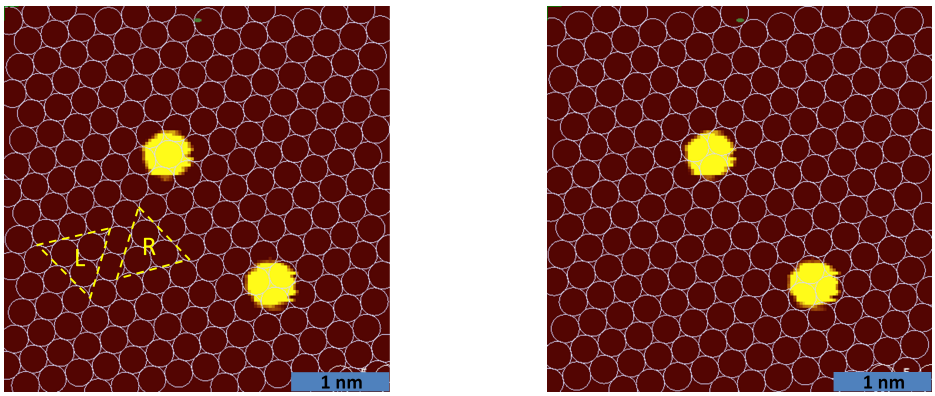
This elegant and accurate approach allows us to determine the background lattice without the need to work towards atomic resolution of the Au(111) surface each time. The method is not only limited to the Au(111) surface but a similar geometrical argument can be used on other surfaces as well, and it can be used to determine the binding sites of deposited molecules. An approach by tracking an ad-atom movement to get the information about the background lattice has been reported earlier by Böhringer *et al*.[45]. Currently available techniques for determining surface atomic configuration using STM are either based on functionalising the STM tip with another molecule (like CO) or by doing point contact scanning[46]. After having determined the structure of the background lattice and the position of the ad-atoms with respect to it, the next step is to construct a simulation stage which has the same structure as in the experiment.

2.4.2 Point contact pushing

We start now our experiment in the configuration shown in Figure 2.6(a) and the corresponding simulation picture in Figure 2.6(d). Usual lateral manipulation[5–7](LM) is done by keeping a tunnel gap between the tip and surface (or ad-atom) operating in a constant current mode with feedback loop switched on. Different settings of the tunnel resistance can lead to different modes of manipulation. For example for gold the numbers reported[28] are 150 kΩ for pulling, 330 kΩ for pushing and 500 kΩ for quasi (near) sliding. In our case, manipulation can be started in a new point contact pushing (PCP) mode with feedback loop switched off. The difference between our PCP mode and usual LM modes is that we do not move the tip in a straight path but we move from hollow site to hollow site by bringing the tip always in-line with the path to the next hollow site and then push the ad-atom. This is done so that the ad-atom position can be known and controlled at each step of the manipulation and avoids the complex jumps and movement of the ad-atom depending on the relative alignment of the underlying lattice and the manipulation direction[47].

In our manipulation method we first perform a tip height match between the simulation and the experiment by going above an ad-atom in point contact in the

[45] M. Böhringer et al. In: *Surface Science* 419 (1998), p. L95.
[46] Yong-hui Zhang et al. In: *Nano letters* 11 (2011), p. 3838.
[47] Saw-Wai Hla et al. In: *Phys. Rev. B* 67 (2003), p. 201402.



(a) (b)

Figure 2.5: Determination of substrate atoms configuration via geometric argumentation. The two panels show the STM images with the topography color scale tuned to reduce the apparent size of the two ad-atoms to match the superimposed background lattice pattern. The actual apparent size of Au ad-atoms on Au(111) is around 1 nm as shown in Figure 2.2(b). The right image with one atom on 'L' and the other on 'R' is showing the correct positioning of the ad-atoms with reference to background lattice.

experiment resulting in a jump to contact and a stable level at 1 G_0 conductance. This is different from some previous works which have shown that a jump to contact occurs only when approaching a bare metallic surface, while when approaching an ad-atom on the surface there is a smooth transition from tunnelling to contact[48,49]. This absence of a jump to contact has been attributed to an increased bond strength of the adsorbed atom on the surface because of the surface dipole creation due to the Smoluchowski effect. We have very rarely seen a smooth transition to contact and we attribute those rare events to either a blunt tip or to the presence of unwanted adsorbates which were present in the UHV chamber, most likely hydrogen. In fact we have observed this jump to contact when approaching a Au ad-atom from the top more than 80% of the times and we attribute it to the relaxation[50] of tip and surface atoms. At this point, after matching the contact position of the tip in both simulation and experiment we retract the STM out of contact and position the tip about 1 nm "behind" the ad-atom, at a height corresponding to 0.4 μA tunneling current at 100 mV bias (which is around 250 kΩ tunnel resistance and approximately 1.2 Å above the surface). Then the tip is moved towards the ad-atom in feedback-off condition keeping z constant. Similar to the jump to contact (JC) phenomenon that happens while approaching a surface or an ad-atom from the top, a JC also occurs while approaching the ad-atom laterally parallel to surface. Because the corrugation energy in metallic surfaces is usually 1/10 to 1/3 of the adsorption energy[2], this jump

[48] J. Kröger et al. In: *New Journal of Physics* 9 (2007), p. 153.
[49] L. Limot et al. In: *Phys. Rev. Lett.* 94 (2005), p. 126102.
[50] W. A. Hofer et al. In: *Phys. Rev. Lett.* 87 (2001), p. 236104.

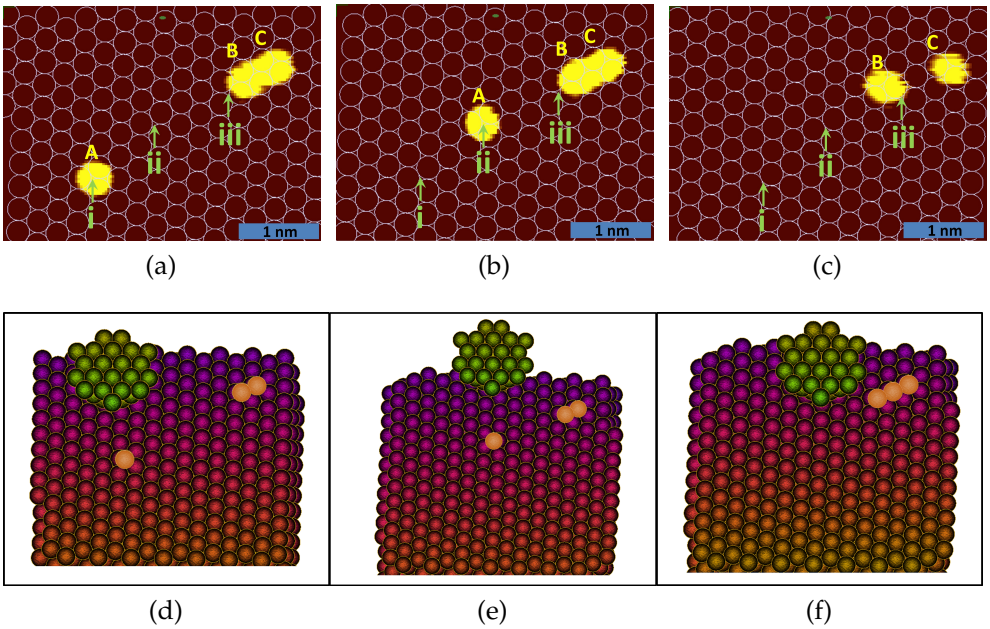


Figure 2.6: The top three panels show the STM images with the topography color scale tuned to show a smaller apparent size of the ad-atoms 'A', 'B' or 'C'. The scale bar in the bottom-right corner is 500 pm. The bottom three panels show the corresponding simulation setup. (a),(d) shows the initial positions of ad-atoms 'A', 'B' and 'C' with 'A' at position 'i'. (b),(e) shows the position of ad-atom 'A' after the first move and one can see that the ad-atom arrives at the exact same position 'ii' in both experiment and simulation. (c),(f) shows the STM image and simulation after the gold atomic chain has been lifted.

can even be larger in the lateral direction than while approaching from the top. We used this procedure to first move the ad-atom 'A' shown in Figure 2.6 from position 'i' to 'ii' and then a STM image (Figure 2.6(b)) is taken so that one can compare the position of the ad-atom with the simulation (Figure 2.6(e)). The motion control and visual feedback from the simulation are essential in this procedure, because we need to move the tip in a zig-zag fashion behind the atom in the line of the next hollow-to-hollow hop for each lattice step. The resulting positions in Figure 2.6(b) and (e) match very well.[7].

2.4.3 Lifting of gold atomic chain

In the second step, we start now from position 'ii' and move the ad-atom 'A' to position 'iii' and then continue with the operation of lifting-off the atomic chain followed by taking the STM image at the end(Figure 2.6(c)). Figure 2.7(a) shows the tip trajectory[8] for the second step and Figure 2.7(b) shows the corresponding conductance and Z

[7] The corresponding x, y, z and x, y, G curves for this operation are given in the Appendix A.2
[8] The corresponding x, y, G graph for this operation is given in the Appendix A.2

coordinate variation over the time. The points from 1-10 shown in the two graphs mark the same points in time. A schematic explaining the manipulation process is given in Figure 2.7(c). Starting points 1 to 4 show the start operation which includes the tip height matching and positioning the tip behind the ad-atom as explained in section 2.4.2. After this the tip is moved forward (keeping the Z constant) in feedback-off state towards the ad-atom. Next, a lateral jump to contact happens[9], which gives a sudden change in conductance to approximately 1 G_0, as can be seen from point 5 to 5′ in Figure 2.7(b).

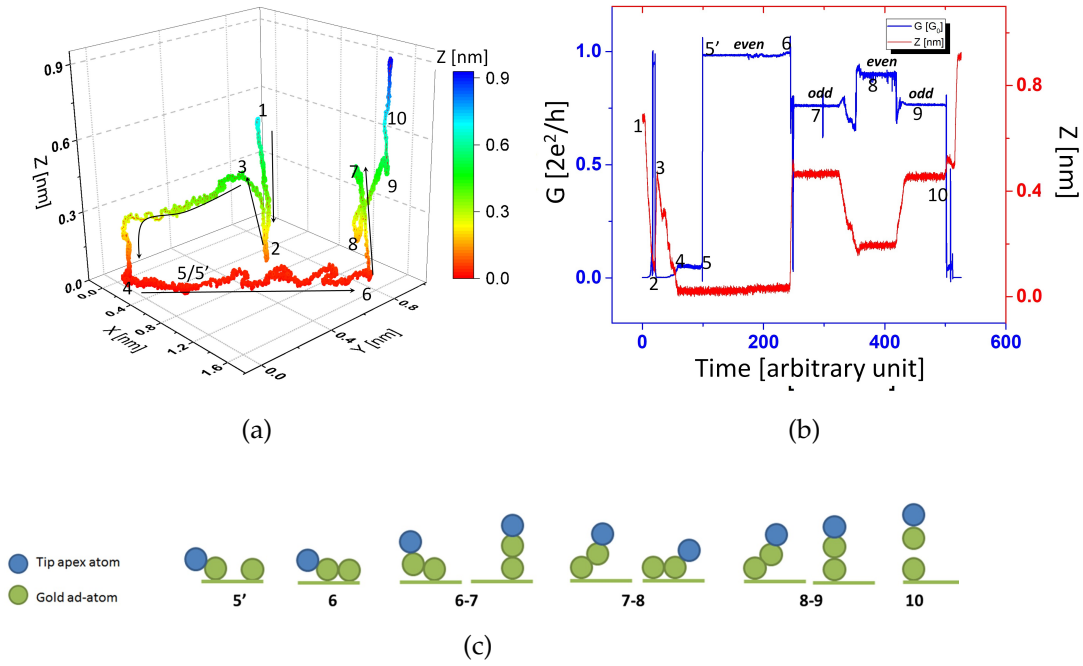
Next the ad-atom is moved towards the other pair of atoms 'B' and 'C' to position 'iii' going from one hollow site to the next hollow site (L to R or R to L) shown as the meandering part in Figure 2.7(a) from point 5′ to 6. Now after the ad-atom 'A' has reached position 'iii' the tip is controllably moved from point 6 to point 7 shown Figure 2.7(a) and (b). This places the ad-atom 'A' above ad-atom 'B' which together with the tip-apex atom[10] forms a three atom chain as shown in Figure 2.7(c). This causes a decrease in conductance which can be seen clearly in Figure 2.7(b). Note that the Z-position in Figure 2.7(b) shows at point 7 the 'Z' value of 0.45 nm, and adding to this 0.12 nm (which is the Z=0 point given by the tip height from surface during pushing) gives 0.57 nm, which is very close to twice the covalent diameter[11] of a single Au atom (i.e. 0.288 nm). After keeping the tip at this position for some time we bring the ad-atom 'A' back to the surface (point 8). The number of atoms in the chain changes back from three to two giving a step increase in conductance, shown in Figure 2.7(b). Note that this conductance value (point 8) is lower than the earlier value between points 5′ and 6. The difference results from the fact that between point 5′ to 6 the tip is not above the ad-atom 'A', but is actually on its back in a pushing mode. Thus the overlap of the wave functions on the atomic chain and those in the tip are enhanced at this position, giving rise to a higher transmission and conductance. Then we bring the ad-atom again 'A' above the ad-atom 'B' (making a three atom chain) and we see again a conductance drop to exact same value as earlier (point 9 in Figure 2.7(b)).

Eventually, when attempting to pull the tip further expecting the ad-atom 'C' to join-in the chain, the chain broke. The STM image taken at the end (Figure 2.6(c)) shows two ad-atoms left on the surface, supposedly 'B' and 'C'. The positions of 'B' and 'C' have changed but the exact sequence of steps that led to those movements cannot be determined because our simulation didn't follow the experiment after point 6. In the experiment, the ad-atom 'A' was moved above the ad-atom 'B', while in the simulation the trimer('A-B-C') was left on the surface once the tip was pulled up (Figure 2.6(f)). A possible reason why the simulation did not follow the experiment is that the atomic shape of the actual tip apex was possibly different from the crystalline one which we assumed in our simulation. This would lead to a different shape of the double potential well making the potential well for the tip used in the experiment deeper than the one on the surface side. Thus, breaking the ad-atom bond to the

[9] Note that a lateral jump to contact will also occur when ad-atom 'A' is brought closer to ad-atom 'B', but as 'B' and 'C' are very close the jump of 'B' towards 'A' should be very short range.

[10] We have developed a robust procedure to prepare STM tip apex structure using mechanical annealing procedure described in Appendix D. This helps us in confirming an atomically sharp tip structure up to the second atomic layer behind the tip-apex atom.

[11] https://www.webelements.com/gold/atom_sizes.html



(a) (b)

(c)

Figure 2.7: (a) Complete tip trajectory for the second step starting from position 'ii' in the lattice and (b) variation in conductance (blue) and Z coordinate (red) of the tip over the time of operation. The numbered points shown in the two graphs (a) and (b) correspond to the same points in time. (c) Schematic of the manipulation process explaining different points in the curves above.

surface becomes easier as compared to that in the simulation. Another explanation could be that our simulation does not take into account excitation of the substrate ad-atom vibration modes due to inelastic electron tunneling[17,51], which is expected to promote pick up of the ad-atoms from the surface. Finally, of course, the effective atom-atom interaction employed for the simulation is a crude approximation for the true interatomic potentials, and this approximation may break down for these extremely under-coordinated atoms.

2.4.4 Parity oscillations

The conductance of a macroscopic conductor decreases with increase in its length. However in small atomic scale devices due to the ballistic nature of electronic transport, the conductance should not change with the length of the device. However, chain length dependent oscillations in the conductance in mono-atomic chains have been reported by the name of parity oscillations or even-odd oscillations. Experimentally in gold atomic chains, such parity oscillations are demonstrated by making length histograms using a mechanically controlled break junction (MCBJ)

[51] Phaedon Avouris. In: *Accounts of chemical research* 28 (1995), p. 95.

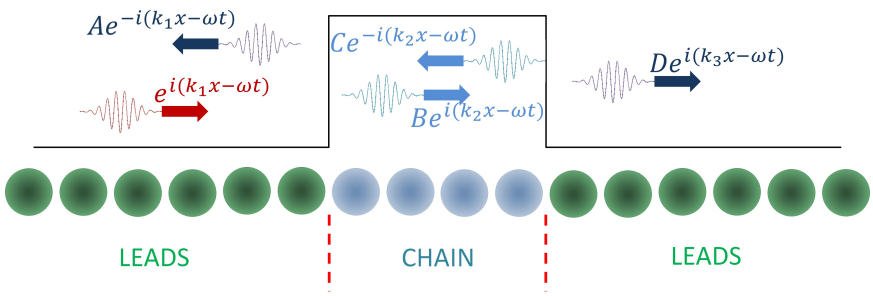
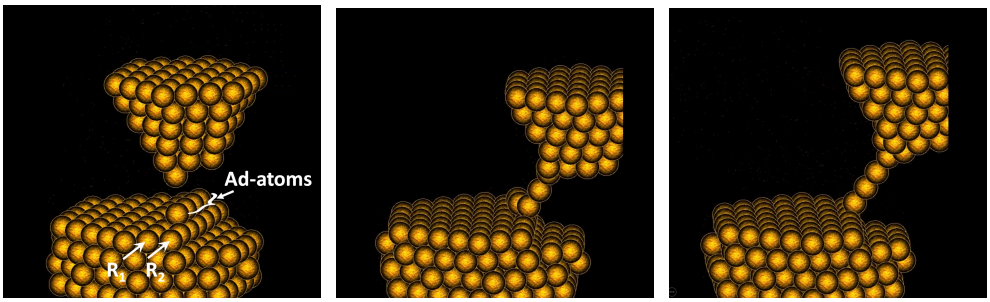


Figure 2.8: A one-dimensional model of electronic transport through a mono-atomic chain[53]. To differentiate between the atomic chain and the leads, a different wave-vector k_2 is allotted to the chain as compared to k_1 and k_3 for the leads. This difference in wave-vector can be manifested as a potential barrier and the electrons form standing waves inside the barrier. Depending on the length of the barrier one can have different interference patterns of these standing waves giving oscillations in the conductance. This is similar to a Fabry-Pérot interferometer. The different colours of atoms here do not imply different types of atoms but are used only to differentiate between the leads and the atomic-chain.

setup[20,52,53]. These oscillations can be explained using a simple one-dimensional (1D) chain model (description given in the Figure 2.8) and its existence has been confirmed also by various detailed theoretical calculations[20,54–58]. However, there is a disagreement about the phase of these oscillations among different models. The phase defines whether the conductance of the chain with an even number of atoms will be larger than that of the chain with an odd number of atoms, or the other way around. A phase change can arise with the type of monovalent atom forming the chain (alkali metals or noble metals)[58] but can also arise due to the geometrical shape of the electrodes[57] and the coupling between the electrode and the atomic chain[56].

The controlled experiment described in Figure 2.7 not only shows clearly these even-odd oscillations but also fixes their phase. We can determine here with certainty that the even number of atoms in the chain leads to a higher conductance. As compared to previous experimental results on gold atomic chains obtained using the MCBJ technique, we have well-defined electrode shapes. One of the electrodes is an atomically flat Au(111) FCC facet and the other electrode is an atomically sharp tip apex prepared using the mechanical annealing technique[29].

[52] R. H. M. Smit et al. In: *Nature* 419 (2002), p. 906.
[53] R. H. M. Smit. PhD thesis. Leiden Institute of Physics (LION), Leiden University, 2003.
[54] N. D. Lang. In: *Phys. Rev. Lett.* 79 (1997), p. 1357.
[55] Mads Brandbyge et al. In: *Phys. Rev. B* 60 (1999), p. 17064.
[56] Rafael Gutierrez et al. In: *Acta Physica Polonica. Series B* 32 (2001), p. 443.
[57] P. Havu et al. In: *Phys. Rev. B* 66 (2002), p. 075401.
[58] Y. J. Lee et al. In: *Phys. Rev. B* 69 (2004), p. 125409.



(a) (b) (c)

Figure 2.9: (a)-(c) The sequence of the lifting a gold atomic chain at a step edge. The row of atoms forming the last row of a step edge is labeled as 'R_2' and the row behind it is labeled as 'R_1'. Four ad-atoms are placed at the step edge, which are lifted off the surface by the tip, forming suspended chain.

2.4.5 Lifting of a gold atomic chain along a step edge

As the discrepancy between the experiment and the simulation due to lack of knowledge of atomic configuration of the tip cannot be easily overcome, the following question rises: Is there a possible configuration of tip-ad-atom-surface system or a possible trajectory of the STM tip where even with the tightly packed crystalline tip assumed in the simulation, one could lift a chain of atoms? With the help of the MD simulations we found that if the chain of atoms can be prepared along the step edge in a crystalline direction, then even with the crystalline tip and a suitable tip trajectory this chain could be lifted off the surface, as shown in Figure 2.9 (a)-(c). This result may seem counter-intuitive as it is known that the step-edges are more reactive (that is the reason why adsorbate molecules are pinned to them) because of the under-coordinated row of atoms on the step edge. Figure 2.9 (a) shows a row of four ad-atoms lying parallel to the step edge. The last row R_2 below the 4 ad-atoms has no atoms on its right, which means that they are less co-ordinated and thus make a stronger bond to the 4 ad-atoms. However, the procedure to lift the chain of four atoms off the surface is not to go vertically up trying to break three bonds at the same time but rather first pull the ad-atom to the right, in the direction of the lower plateau (as shown in Figure 2.9(b)). Next, once the bonds with the row R_1 are broken then on going vertical the ad-atom can be pulled out. On applying a similar procedure for detaching the next atoms in the chain a free standing atomic chain between the tip and surface can be obtained (Figure 2.9(c)) even with for the limitations imposed by the simulation.

We set out to prepare such an atomic chain on a step edge in the experiments, but this turned out not entirely trivial. The major hurdles for doing so are: First, as the Herringbone reconstruction on Au(111) is known to end perpendicular to the crystalline step edges, the chain has to be prepared along the width of the FCC region rather than along its length as before. Secondly, as explained above, a lateral jump to contact will occur while bringing the second ad-atom to the step edge and this will lead to dimer creation mostly in the crystallographic direction of the incoming ad-atom, which will be most likely different from the crystallographic direction of

step edge. A possible way around could be to make something similar to what was prepared by Nazin et al.[59] on the NiAl(110) surface i.e., a "metallic chain - molecule - metallic chain" system. Bringing a molecule on the step edge first and then attaching Au atoms on its end to form a chain is a possible way to avoid this lateral jump to contact.

2.5 Discussion

In the previous section we showed that we were able to controllably form a free standing atomic chain, put it back down on the surface and lift it up again. Furthermore we have observed clear parity oscillations as a signature of the atomic chain formation. In this paragraph we will address the effect of the shape of the tip in these experiments. Any modification of the tip apex atom position with respect to the bulk of the tip during manipulation should influence the accuracy and the outcome of the manipulation. In spite of this, formation of complex 2D structures[3,9–15] are reported in the past with lateral manipulation technique with precise positioning. However, the accuracy and error in this positioning step are generally not reported. It is possible that recursive methods were used as reported by some groups[14,15], where multiple iterations were done to finally converge to a pre-determined position.

Another important item that will play a role in lateral manipulation (other than tip apex atomic structure) is the assumption of isotropic spring stiffness of the tip. To study the effect of the spring stiffness on manipulation, one can project it (as shown in Figure 2.10) along the crystallographic directions of the surface (three in case of Au(111) surface). In case of a real tip structure it is possible that the three projections (κ_1, κ_2 and κ_3) of the stiffness along the three crystallographic directions of the surface (1, 2 and 3) are not the same. This implies that the lateral deflection of the tip apex atom (δ_1, δ_2 and δ_3) during lateral manipulation along different crystalline orientations will be different.

Important to note here is that for harder materials like Tungsten (W) which is used as a tip material in many atomic manipulation experiments, the three tip stiffness constants(κ_i's) may be very large and so even though the deflections (δ_i's) are possibly different, they will be very small to detect. Even for softer materials (like Au or Au covered PtIr tips), due to the quadratic nature of the spring energy ($\frac{1}{2}\kappa_i\delta_i^2$) the spring will deflect only at the start and for longer manipulation distance it will remain almost constant. Therefore, the relative error in the positioning of an ad-atom over the surface (defined as expected position minus the measured position divided by the expected position) can be large for small movements while will become smaller for larger distance. We have investigated the role of this anisotropic spring stiffness. In order to do this we needed to avoid the lateral jump to contact behavior mentioned earlier. For this purpose our 3D motion control system is once more convenient: this time instead of approaching the ad-atom from the side on the surface where we detect the lateral jump to contact, we devised a new routine where we approach the ad-atom from the top, and establish a point contact. Subsequently, we make a quarter circular motion (while keeping in contact with the ad-atom) and thus the tip comes into the pushing position as before without having any lateral jump to contact. A figure to explain this pictorially is given in the Appendix A.3. After this preparation

[59] G. V. Nazin et al. In: *Science* 302 (2003), p. 77.

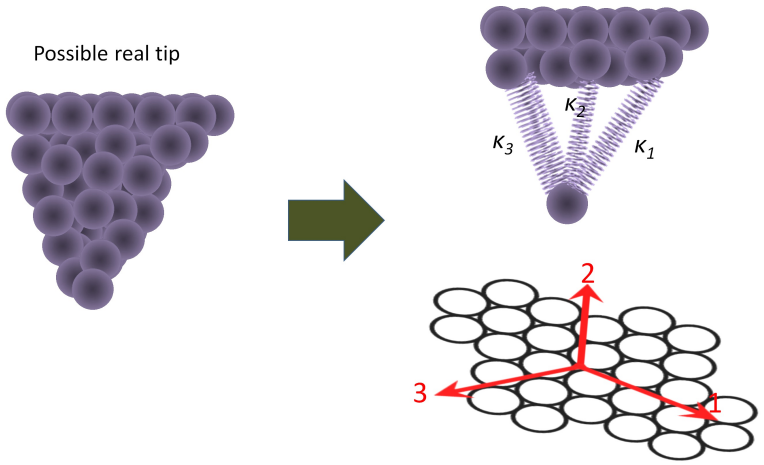


Figure 2.10: A spring stiffness model, showing how an anisotropic tip could have an anisotropic spring stiffness.

procedure we studied experimentally (using randomly formed tip structures) only the single hollow site push occurrences because, as explained before, the major part of the error should happen at the start of the manipulation only. We observed almost 50 % zero error motion. We compared this with single-site displacements made with the molecular dynamics simulation after preparing randomly formed tip structures (produced by a mechanical annealing procedure in the simulation) and found a similar behavior in terms of accuracy. This suggests that the anisotropic lateral spring stiffness[12] of the tip other than the atomic configuration of the tip apex is also an important unknown ingredient which could influence the precision of an atomic manipulation operation.

2.6 Conclusion and outlook

To summarize, we have modified our low temperature ultra-high vacuum STM with the integration of a 3D motion control system and a real-time molecular dynamic simulation. This human-machine augmented system where the operator can become part of the experiment and make adaptable STM tip trajectories based on the visual feedback from simulation, provides a better control for (3D) atomic manipulation. This method should become particularly useful for molecular manipulation. We prepared our surface using local strain induced technique where fresh step edges along crystallographic directions can be formed at cryogenic temperatures. We then showed how a simple geometric technique based on placing two ad-atoms can give information about the atomic configuration of the metallic substrate. We used this as the input to setup the same environment in the coupled real-time simulation and demonstrated the controlled lift-off of single atomic chain. For this purpose, we

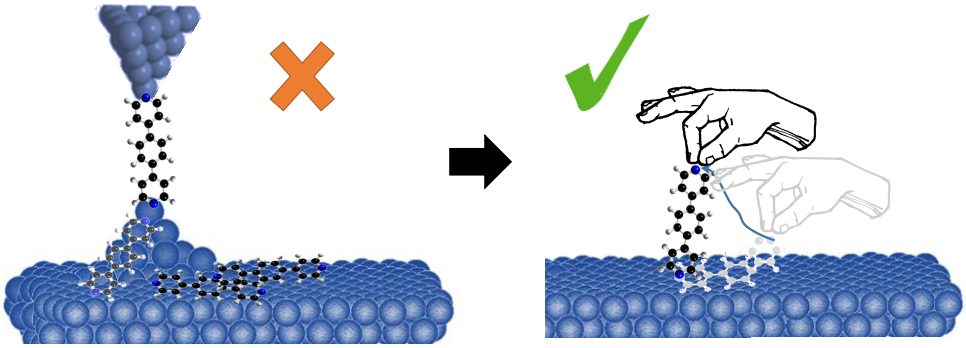
[12] In fact the vertical spring stiffness also plays a role. Specially in case of jump to contact phenomena, different vertical spring stiffness should give different conductance values at which the jump occurs.

developed a new point contact pushing technique which can directly be followed by the manipulation into the third dimension at the end. By putting this atomic-chain back and forth into and out of the surface we studied the parity oscillation behavior in conductance which occurs due to interference of electronic waves in different length of the chain. Finally, we also discussed how the spring stiffness of the tip can influence the accuracy of atomic manipulation operations, which is extremely important in complex 3D manipulation of single molecules and atomic chains. The next step will be to modify the real-time simulation to include molecules in the system (see Chapter 3). Experiments on other surfaces like Au(211) can be tried which is not effected by surface reconstructions and still has (111) facets and clean long step edges. For a better comparison with theory and a possible direct feedback loop from the experimental conductance values, a real time conductance estimation based on the atomistic positions given by the MD simulations could be useful. Tight binding models have been known[60] to give a relatively fast (as compared to DFT and other computationally expensive methods) estimation for the conductance values numerically. At the moment we have not added any such electronic transport model in our system but it can be a possible upgrade which should help in further guiding the experiments[61][13].

[13] With the rapid developments in the field of deep learning algorithms[61], an interesting possibility would be to "train" such an algorithm by using many simultaneous force and conductance calculations for varying tip shapes, so that it can find out the exact atomic tip structure used in experiments by studying and recognizing features in conductance traces.

[60] T. N. Todorov and A. P. Sutton. In: *Phys. Rev. B* 54 (1996), R14234.
[61] Jürgen Schmidhuber. In: *Neural networks* 61 (2015), p. 85.

Graphical Summary



3. Single molecule STM control: GPU implementation

Molecular electronics saw its birth with an idea to build electronic circuitry with single molecules as individual components. Even though commercial applications are still modest, it has served an important part in the study of fundamental physics at the scale of single atoms and molecules. It is now a routine procedure in many research groups around the world to connect a single molecule between two metallic leads. What is unknown is the nature of this coupling between the molecule and the leads. We have shown in previous chapter our new setup based on a scanning tunnelling microscope, that can be used to controllably manipulate single molecules and atomic chains. In this chapter, we will present the extension of our molecular dynamic simulator attached to this system for the manipulation of single molecules in real-time using a graphics programming unit (GPU). This will not only aid in controlled lift-off of single molecules, but will also provide details about changes in the molecular conformations during the manipulation. This information could serve as an important input for theoretical models and for bridging the gap between the theory and experiments.

The work is done in collaboration with - Dyon van Vreumingen[1,2], Fons Verbeek[2] and Jan M. van Ruitenbeek[1]
[1]Huygens-Kamerlingh Onnes Laboratorium, Universiteit Leiden, The Netherlands.
[2]Leiden Insitute of Advanced Computer Science, Universiteit Leiden, The Netherlands.

3.1 Introduction

Researchers are trying to study different electronic and molecular properties of single molecules. Small molecules due to confinement of electrons exhibit large energy level spacing and can thus show quantum dot characteristics even at room temperature. Single molecules can show conformational variations[1] which could be used to make a switch, as these different conformations can vary significantly in their conductance. Quantum interference[2,3], thermo-electricity[4,5] and molecular spintronics[6,7] are some of the many exotic phenomena that one can study in single molecules. There are many things we have learned so far but many are still to be understood and put under control from both fundamental and technological point of view. One of these things is the coupling between the molecules and the leads at the atomic scale. In particular, the atomic scale structure of the contacts and the details of the binding of the molecule to these leads have to be known. These details include knowledge of the binding sites, nature of the bond, the conformational state of the molecule, the bond angles etc. These are important parameters to know because our understanding of electronic transport through single molecules depend on the output of various computational models like density functional theory (DFT), non-equilibrium Greens function (NEGF) theory etc., which requires these parameters as inputs. Lack of such information can cause a mismatch between the theory and experiments which affects our understanding of electron transport through single molecules.

Furthermore, one can ask, is it possible to set some benchmark experiments which could help in testing different computational models and also enhance our understanding of electron transport through single molecules? Most commonly used single-molecule measurement techniques include - various break junction techniques (notched-wire[8–10], lithographic[11–13], scanning tunneling microscope[14] based) and electromigration made junctions (metallic[15,16] and graphene based[17,18]). However, these techniques can not give complete information about the coupling between the molecule and the leads. The break-junction techniques are mostly statistical

[1] James K. Gimzewski and Christian Joachim. In: *Science* 283 (1999), p. 1683.
[2] Constant M Guedon et al. In: *Nature nanotechnology* 7 (2012), p. 305.
[3] Stefan Ballmann et al. In: *Phys. Rev. Lett.* 109 (2012), p. 056801.
[4] Pramod Reddy et al. In: *Science* 315 (2007), p. 1568.
[5] Sriharsha V. Aradhya and Latha Venkataraman. In: *Nature Nanotechnology* 8 (2013), p. 399.
[6] Lapo Bogani and Wolfgang Wernsdorfer. In: *Nature materials* 7 (2008), p. 179.
[7] Enrique Burzurí and Herre S. J. van der Zant. In: *Molecular Magnets: Physics and Applications*. Berlin, Heidelberg: Springer Berlin Heidelberg, 2014, p. 297.
[8] T. Yelin et al. In: *Nano letters* 13 (2013), p. 1956.
[9] M. Kiguchi et al. In: *Phys. Rev. Lett.* 101 (2008), p. 046801.
[10] Julian M. Bopp et al. In: *Low Temperature Physics* 43 (2017), p. 905.
[11] C. Kergueris et al. In: *Phys. Rev. B* 59 (1999), p. 12505.
[12] J. Reichert et al. In: *Phys. Rev. Lett.* 88 (2002), p. 176804.
[13] Christian A Martin et al. In: *New Journal of Physics* 10 (2008), p. 065008.
[14] Bingqian Xu and Nongjian J. Tao. In: *Science* 301 (2003), p. 1221.
[15] Hongkun Park et al. In: *Applied Physics Letters* 75 (1999), p. 301.
[16] Herre S. J. van der Zant et al. In: *Faraday Discuss.* 131 (2006), p. 347.
[17] Amelia Barreiro et al. In: *Nano Letters* 12 (2012), p. 6096.
[18] C. S. Lau et al. In: *Phys. Chem. Chem. Phys.* 16 (2014), p. 20398.

techniques and deal with averaging over many molecule-electrodes configurations during trace-retrace cycles where the two electrodes are brought into large metallic contact and subsequently broken.

3.2 Single-shot measurements - Overview

Scanning tunnelling microscope (STM) owing to its nano-scale imaging possibilities has also been used to probe single molecules for single-shot measurement. If a molecule is attached between a tip and a surface of an STM then the atomic configuration of one electrode (the surface) is precisely known. Note that this is not a case when STM is used in break junction mode.

First such controlled single molecule measurement where the STM surface atomic structure was intact was reported in 1995 by Joachim et al.[19] where they connected a single C_{60} molecule between the STM tip and an atomically flat Au(110) surface at 300 K under ultra-high vacuum (UHV) conditions. Later, single planar molecules connected between STM tip and sample while keeping the atomic structure of surface intact were studied using I(t) and I(s) measurements reported by Haiss et al.[20,21] in ambient conditions. However, these measurements are statistical as the STM tip is brought close to the flat metallic surface (with a low coverage of molecules) and current jumps are detected as molecules spontaneously make and break contact between the tip and the surface. Next, they also studied variation in conductance of the molecule with tilt angle dependence and temperature dependence[21]. The first controlled peel off of a single planar molecule was performed by Temirov et al.[22] in 2008, where they showed successful removal of a PTCDA (Perylenetetracarboxylic dianhydride) molecule from a Ag(111) surface using a W-tip. Even though PTCDA has an axially rigid structure, variations in the behavior of the conductance traces were observed while peeling off the molecule. These variations could be attributed to different conformational changes that the molecule undergoes during the peel off or the changes in the binding sites of the molecule to the electrodes.

Recently, a simple conductance measurement for a free-standing tripod molecule showed an order of magnitude variation[23] between Au(111) surface and Au STM tip depending on the different bond formation configurations between the tip and the molecule. This work again points towards the need to have a well-defined contact geometry of a metal-molecule-metal junction. Using a simple vertical tip retraction of the STM tip a controlled peeling off of a 20 nm long polymer[24,25] and a graphene nanoribbon[26] was demonstrated. Such a polymer was later also produced bridging between two parts of a metallic substrate going over a few insulating NaCl

[19] Christian Joachim et al. In: *Phys. Rev. Lett.* 74 (1995), p. 2102.
[20] Wolfgang Haiss et al. In: *Phys. Chem. Chem. Phys.* 6 (2004), p. 4330.
[21] Wolfgang Haiss et al. In: *Nature Materials* 6 (2006), p. 995.
[22] R. Temirov et al. In: *Nanotechnology* 19 (2008), p. 065401.
[23] Torben Jasper-Tönnies et al. In: *Phys. Rev. Lett.* 119 (2017), p. 066801.
[24] Leif Lafferentz et al. In: *Science* 323 (2009), p. 1193.
[25] Gaël Reecht et al. In: *The journal of physical chemistry letters* 6 (2015), p. 2987.
[26] Matthias Koch et al. In: *Nature nanotechnology* 7 (2012), p. 713.

layers[27]. In another approach, two C_{60} anchoring groups[28] connected to single molecules were used to do controllable single molecule measurements using STM at ambient conditions. Recently, a highly conducting molecular chain made of repeated donor and acceptor units[29] was pulled off from the surface using the STM tip. Furthermore, using a *q-plus* sensor in a combined AFM/STM setup Fournier et. al[30] provided additional mechanical information which could help further in knowing the tip-molecule-sample configuration and it can also provide the individual binding energies of different molecule-metal bonds. These q-plus sensors provide simultaneously both conductance and force information but one has to be careful that even though these sensors are very stiff and operate at low oscillation amplitudes, these amplitudes are still finite (around 0.2 Å) and would require sufficiently strong bond between the tip and the molecule for a stable junction. These measurement techniques using scanning probe microscope (SPM) are the state of the art techniques that can be used to make a free-standing molecule between the SPM tip and sample. However, as during manipulation operation, the STM cannot image, it is "blind", the above experiments provide no information about the conformations of the molecule between the tip and the surface.

We suggest here a way for providing an "eye" to the STM during the manipulation process. Although this cannot replace experimental observations it can serve as a tool for guiding the experiments. For this, we developed a system (Chapter 2) where we attach a real-time molecular dynamics simulation to a low-temperature UHV STM. This simulation first takes the STM image as input to create a 3D simulation stage similar to the experiment. The same x,y,z signals are sent to both the STM and the simulation. The simulation computes in real-time the dynamics of each atom in the system and provides a visual feedback to the operator who can then choose an adaptable trajectory while monitoring its effect in real-time on a computer screen. We also attached for the ease of making adaptable 3D trajectories a home-built 3D motion control sensor similar to Green et al.[31]. The real-time simulation employed for the experiments described in the previous chapter was applied for only metallic systems with gold STM tip, Au(111) metallic surface, and with gold ad-atoms. Using this a controlled creation and peel off of a chain of gold ad-atoms over atomically flat Au(111) surface was demonstrated (Chapter 2).

In this chapter, we will describe an extension of this real-time molecular dynamics simulation to include organic molecules. As a result of the higher frequencies for vibrations on the molecule we need to reduce the time step in the calculations, which slows them down considerably. In order to amend this problem we prepared the simulation on a graphics processing unit (GPU) using nVidia CUDA architecture. GPU implementation of molecular dynamics has been demonstrated earlier. However, real-time simulations to control molecular manipulation using STM have not yet been demonstrated. In the following section, we will start by discussing some basics of molecular dynamics (MD) and GPU programming and mention the previous implementations of MD using GPU programming. Next, we will discuss

[27] Christian Bombis et al. In: *Angewandte Chemie International Edition* 48 (2009), p. 9966.
[28] Edmund Leary et al. In: *Nano letters* 11 (2011), p. 2236.
[29] Christophe Nacci et al. In: *Nature communications* 6 (2015).
[30] N. Fournier et al. In: *Phys. Rev. B* 84 (2011), p. 035435.
[31] Matthew F. B. Green et al. In: *Beilstein journal of nanotechnology* 5 (2014), p. 1926.

the challenges involved in making this simulation real-time and then present the solutions we provided explaining the assumptions and improvements we made.

3.3 Molecular dynamics

Molecular dynamics (MD) simulations have been used widely to understand bulk mechanical properties of materials arising from collective atomic behaviour. The MD simulation presented here is intended to study and aid single molecule manipulation experiments done using scanning probe microscopes. Our system thus consists of metal atoms which form the tip and the sample used in the experiment, and other atoms (H, C, N etc.) which constitute the molecule. The molecule that we studied to test our simulation is 1,4-bis(4-pyridyl)benzene shown in Figure 3.1. The gold-gold interaction is modelled as before (Chapter 2) using a semi-empirical potential. The atoms making up the molecule are joined together by covalent bonds for the chosen molecule and are thus modelled as spring-mass systems using harmonic potentials. Other than pair forces, molecule's atoms will also feel angular forces due to equilibrium bond angles between two covalent bonds formed between 3 atoms and torsional forces due to equilibrium dihedral angles between a group of 4 atoms. All these bond pair forces, angular forces and torsional forces are computed to obtain the details of the molecular conformations. Lastly, the interaction between the the atoms on the molecule and the gold atoms in the substrate and tip are modelled depending on the type of molecule atom. Atoms like N and S are known to form a stronger bond than H and C with gold and are thus called anchoring bonds. These anchoring bonds are modelled here using a Morse potential, while other gold-molecule bonds were modelled using the standard Lennard-Jones potential. A description about this is given in the AppendixB.3.

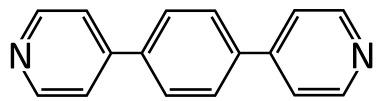


Figure 3.1: 1,4-bis(4-pyridyl)benzene implemented in the simulation.

For the simulation to run in synchronisation with the STM manipulation experiment, a 3D motion control system is linked to both the experiments and the simulation using a home-built Labview program. Using this the operator sends x,y,z signals to the actual STM-tip in the experiment and also to the top layer of the STM tip in the simulation. As the operator uses the simulation output as the feedback to decide on the tip trajectory the simulation should run in real-time. Important to note is that the force calculations mentioned above have to be repeated for each atom. At each moment in time, these forces are all treated as functions of the inter-atomic positions of each atom. Thus for a given position of all atoms, these calculations are all mutually independent and can be performed simultaneously, making the calculation suitable for parallel processing. We will discuss in the coming subsection the challenges in making a real-time simulation, and then we will discuss our implementation using GPU programming which can do parallel processing of a large part of the computation.

3.3.1 Challenges in making real-time MD simulations

There is always a finite number of atoms (N) simulated in molecular dynamics (MD) calculations and the computation time of a classical MD simulation scales as N^2; this means that a need to crank-up the simulation speed is always there as you can then simulate more atoms at a time. The timescales involved with inter-molecular motions are on the order of femtoseconds[32]. This is why speeding up the simulation to calculate inter-molecular motions and vibrations in their native time-scales is not possible with the current computing power. This implies that a real-time MD simulation should not be confused with native time-scale (NTS) computations. However, real-time molecular dynamics can be performed on any system in the quasi-static regime. The quasi-static regime is where the relaxation time[1] in the simulation (which will depend on the computation speed of our system) is smaller than the pump and probe period.

The real-time simulation which we are targeting is an extension of a simulation we prepared earlier for an all-metallic system (Chapter 2). There the simulation consisted of only Au atoms (which forms the tip, substrate and ad-atoms on the substrate) while now we want to introduce an organic molecule. Same as before, the simulation should have the possibility of interactive steering of the STM tip with a 3D motion control sensor (Chapter 2) and have a running graphics output displaying the current state of the simulation in 3D for better control. The substrate size has to be also increased in case we want to include more than one single molecule in the system; this means the speed of the simulation has to be cranked up further to include more substrate atoms. The primary challenge that we face is due to the very small mass of the atoms constituting the molecules (like H, C, N etc.) in comparison to the mass of the Au atoms which form the tip and the substrate. From Newton's first law it can be seen that a smaller mass will lead to much higher acceleration under the same force and thus it is required to use much smaller time-step in the simulation. The larger time-step applicable for the gold-gold system will not work here as it will lead to stretching of bonds between smaller atomic masses and thus can lead to spurious decomposition of the molecule in the simulation. Using a smaller time-scale optimized for the smaller mass should ideally work for all the masses. However, it will lead to two problems in our situation. Firstly, this time-scale has to be larger than the one associated time-scale of the external impulse used to steer the STM tip. Otherwise, the Au atoms in the tip being heavier will not follow the external steering input coming from the 3D motion control system. Secondly, if we make the external steering too slow, then the simulation will not work on the time-scale of real STM manipulation experiment.

GPU programming will help in cranking up the speed but will not be enough to achieve real-time implementation when using the smallest single time-step. We have solved this time-step problem using a multiple time-step technique similar to what was proposed by Tuckerman et al.[33] in 1991. A discussion about it will follow

[1] time it takes for the atoms in the system to relax to the equilibrium position within certain accuracy

[32] Andrew R. Leach. Molecular modelling: principles and applications, Pearson education, 2001.

[33] Mark E. Tuckerman et al. In: *The Journal of Chemical Physics* 94 (1991), p. 1465.

below.

For readers not familiar with GPU programming, a small introduction is given in the Appendix B.1, and for details we refer the CUDA programming guide by Cook[34].

3.4 Molecular dynamics - GPU implementation

As was explained earlier in the molecular dynamics (MD) section, the bulk of the execution time in MD simulations is consumed by routines calculating the interatomic forces, which do not in any way depend on one another. After all, these forces are derived from potentials that are functions only of atom positions. And so, such mutually independent calculations can easily be formulated in a parallel computing format. In fact, there are even dedicated special purpose parallel computing systems built for molecular dynamics simulations called MDGRAPE made by RIKEN research institute in Japan. This machine is used to study protein folding predictions[35]. The latest MDGRAPE-3 is a supercomputer with 947 TFLOPS (terra FLOPS) level of floating point performance. Other than this specialised hardware, many GPU based implementations[36–38] of molecular dynamics have also been demonstrated.

GPU (Graphics processing unit) was originally designed to do specific tasks of graphics processing, but soon it became obvious that making these GPUs do a more versatile job and handle different types of functions would enhance their potential. It was this observation that led to the introduction of general purpose computing on GPU (GPGPU) programming which found its applications in seismic, weather and medical research, in neural networking and atomic simulations. An important advantage of GPGPU is that it allows data or information transfer in both directions, from CPU to GPU and GPU to CPU.

There are two most widely known programming frameworks for GPGPU: Compute unified device architecture (CUDA), which was developed by nVidia, and the Open compute language (OpenCL) API, maintained by the Khronos group[2]. OpenCL is open-source and is supported in more applications than CUDA, and most notably it is aimed at cross-platform development (extending to digital signal processors, field-programmable gate arrays (FPGAs) and others). On the other hand, CUDA is a proprietary framework created by nVidia, and so CUDA generates better performance results in nVidia GPUs. Another point of consideration is that OpenCL is much more verbose and has a steeper learning curve[39] than CUDA. As the GPU card we use is an nVidia GeForce GTX 960 (details are given in Table 3.1) hence we decided to use CUDA as our GPGPU programming framework.

The benefit of implementing a molecular dynamics simulation on a graphics card lies in the high degree of parallelism that can be achieved when many independent

[2] https://www.khronos.org/opencl/

[34] Shane Cook. Newnes, 2012.
[35] Yutaka Kuroda et al. In: *Scientific reports* 6 (2016), p. 19479.
[36] Jacobus Antoon Van Meel et al. In: *Molecular Simulation* 34 (2008), p. 259.
[37] Joshua A. Anderson et al. In: *Journal of Computational Physics* 227 (2008), p. 5342.
[38] Xiao Zhang et al. In: *Proceedings of the International Conference on Parallel and Distributed Processing Techniques and Applications (PDPTA)*. 2013, p. 524.
[39] Maria Malik et al. In: *Concurrency and computation: practice and experience* 24 (2012), p. 179.

Table 3.1: Device structure related properties

CUDA Device Name	GeForce GTX 960
Compute Capability	5.2
Floating-point performance	2.413 TFLOPS
GPC count	2
SMM per GPC	4
Cores per SMM	128
Threads per SMM	2048
Max # of *threads* per *block*	1024
Max *block* Size	1024 x 1024 x 64
Max Grid Size	2147483647 x 65535 x 65535
Warp Size	32 *threads*
Max # active *warps* per SMM	64 *warps*

tasks are executed simultaneously. But not every component is suitable for running on a GPU: while the graphics chip may contain much more processing cores than the CPU, they run at a lower clock speed and lack an interface for correspondence with any other devices. So, we carefully selected the parts that are most suitable for being computed in GPU and those are: force calculations, velocity Verlet integration and the thermostat. The elements then remaining on the CPU include handling the data from the input apparatus and moving any recorded force values to a small LabView graphing program for real-time plotting (if needed). At the moment plotting and controlling the visualisation of the atoms on the screen is done on an integrated graphics chip in the CPU using a graphics library[3] which has been implemented in terms of a CPU-callable method. Figure 3.2 shows a flowchart that includes all core tasks performed by the program. The parts implemented inside GPU are shown within the green box. The time runs along the vertical axis and the execution of the processes is in the order from top to bottom. We will now go through the details of the kernel implementations which distribute the tasks among different thread blocks.

3.4.1 Gold-gold forces

The algorithm that we use for calculating the interaction forces between the gold atoms in the substrate and the tip is based on the cell list method[40]. This approach differs from other methods such as the neighbour list method[41] where each atom is assigned its unique index. In the cell list method, each atom is placed in one of many cells that together make up the whole structure. In our implementation, the dimensions of these cells are set to be equal to a cut-off radius. This cut-off radius is normally defined to speed up an MD simulation[32], where the forces acting on an atom are only computed from atoms lying within this cut-off radius, assuming the inter-atomic interactions are negligible beyond this cut-off radius. In this way, we

[3] https://www.sfml-dev.org/

[40] Zhenhua Yao et al. In: *Computer physics communications* 161 (2004), p. 27.

[41] Ariel A. Chialvo and Pablo G. Debenedetti. In: *Computer physics communications* 60 (1990), p. 215.



Figure 3.2: Flowchart showing the execution scheme of the program. Time runs in the vertical direction, thus subroutines placed next to eachother run in parallel. Parts of the chart contained in dashed boxes run as many times as stated to the right of said box.

can guarantee that all neighbouring atoms that are located within the cut-off radius of atom i, must lie in one of the cells directly neighbouring the cell that atom i was placed in, see Figure 3.3. This method has several significant advantages: Firstly, it imposes a data structure on the atom objects according to their position, something which is not directly achievable with a simple atom list. Secondly, since we know that all atoms interacting with atom i must be in one of the neighbouring cells (due to the cut-off radius), only a few instead of all distances between atoms now have to be calculated. Thus the number of pair distances to be computed in each run becomes independent of the size of the system and therefore it reduces the complexity of the algorithm from O(N^2) to O(N). For the ease of implementation, we choose a two-dimensional grid structure for these cells. Here, in the third dimension (z-direction) all cells stretch from negative infinity to positive infinity.

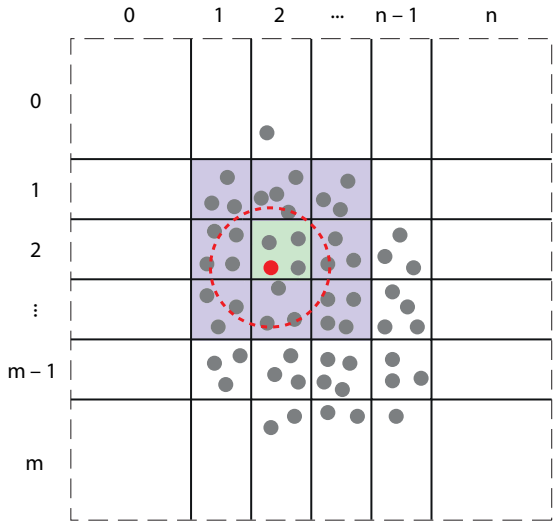


Figure 3.3: Gold substrate divided into cells. For the atom coloured in red, the cut-off radius is indicated as a red, dashed circle, while its own cell is depicted in green and its neighbouring cells are coloured in blue. Atoms whose positions are outside the cut-off sphere of the indicated atom are not taken into account in calculating the total force on the said atom. Note that the outermost cells have no boundary; this measure was taken to fit all of the 3D space—an atom may end up anywhere, after all—into a finite number of cells.

Now from the GPU memory model side, each atom cell is assigned to one thread block where computation of gold-gold forces on each atom is assigned to one thread inside the thread block. The threads in the thread block are arranged in a one-dimensional order with an individual index (say $(\tau_1, 0, 0)$) for each thread. A cell count list is also prepared to keep track of the number of atoms in a cell. This helps the kernel to command each thread to loop over (a *for-loop*) all the neighbouring atoms and calculate the forces within the cut-off radius. These forces are summed

and integrated over a time-step Δt [4]. As the kernel can only assign a task to the threads in the group of 32 given by the *warp-size*, so the number of atoms in a cell shown in Figure 3.3 has to be a multiple of 32. However, due to the constraint imposed by the size of the shared memory used for each cell, which must be satisfied for the simulation to work properly, the number of atoms that can fit in a cell is 32. Thus any atom exceeding this limit is not taken into account in the force calculation. Because of this, the substrate may consist of only a few layers, depending on the cut-off radius[5].

Important to note is that threads in each thread-block can only access information between each other using the shared memory and not among other thread blocks (or other cells in our case). Thus, it makes sense to have the threads in each block first load all of these positions (of atoms in a cell and its neighbour cells) into shared memory, before checking whether the distances fall within the cut-off radius and eventually calculating the forces. Note that this would not have worked out without the cell structure since the atom positions of the whole substrate would require such a large chunk of shared memory which would severely limit the number of blocks that could run on the GPU at the same time. Thus the cell structure offers a nice way to make use of thread blocks and, more importantly, shared block memory. It goes without saying that all the functions accounting for this data structure management can run for all atoms in parallel, which ensures that the caused overhead stays small relative to the total force computation time. It turned out that refreshing the cell index and cell count lists only once every 20 iterations had barely any effect on the accuracy of the simulation; thus, we chose not to call this routine every iteration.

3.4.2 Forces on molecule atoms

The gold-molecule forces on molecule atoms and the intramolecular forces within the molecule are essential as they are responsible for manipulation of the molecule over and out of the surface. As mentioned earlier due to the small masses of the atoms constituting the molecule the equations of motion calculations cannot be done with the same time-step as for the gold atoms, and thus we need to choose another time-step for the molecule. But this will give an inconsistency in the interface at the junction between gold and molecule. To solve this issue, we use a method similar to what was proposed by Tuckerman et al[33]. They have shown that for a system with heavy and light particles which requires different time steps, one can keep the background of heavy particles fixed to their positions while light particles forces and positions are being computed using the smaller time steps. The larger particles are then computed and updated only in the larger time steps. They further show that for systems with a large number of heavy particles and a small number of light particles the above multi time-step technique can also provide a huge speed-up in the computation.

Following this idea, we decided to compute the gold-molecule forces and the intramolecular forces with a smaller time step (δt). Moreover, for every number α ($\propto \Delta t/\delta t$) iterations of small time steps computed, one iteration of gold-gold

[4] Notice that if the number of gold atoms is less, then to increase the occupancy of threads we could use a higher dimensional thread block with indices (τ_1, τ_2, τ_3) and thus also avoiding the *for-loop*. However this is not essential at this stage as we have a sufficiently large number of gold atoms to be computed.

[5] For a larger substrate or for a molecule a 3D cell structure can be used.

interactions updating the positions of gold atoms is done using a larger time-step (Δt) as described in the previous section. Now to compute these gold-molecule forces and also intramolecular forces two-dimensional thread blocks are employed. This is useful for increasing the thread occupancy of the GPU as the number of molecule atoms are not many. To avoid data race conditions[6] while computing and summing the net force on each atom in a parallel manner, the so-called *parallel reduction method*[42] is used. The memory allocations for gold-molecule forces and intramolecular forces are done differently from each other in their respective kernels as is discussed below.

Gold-molecule forces

It is important to understand the computational difficulties that arise at the gold-molecule interface. As explained in Figure 3.2, we run gold-gold computations in parallel to the computations for the molecule. For an efficient division of tasks among the two parallel computations, we use the scheme described in Figure 3.4. Here in the top figure, a spring-mass system is shown with an external force input (blue arrow), a heavy mass (M) and a small mass (m). In a conventional force-field simulation, a small time-step can be employed and by solving the equations of motion a new equilibrium position of the system can be computed. To have a real-time response, we use a larger time-step for M and a smaller time-step for m iterating many times over the small time-step during one large time-step. We divide the system into two parts as shown in Figure 3.4: sub-system-(I) with the heavy mass M connected to a wall (via a spring) which is pulled with an external force input and the other sub-system-(II) with the small mass m connected to a fixed boundary and also to the same mass M which is now freely floating. In our molecule-metal atom system, this is similar to dividing the system into only the gold-atoms sub-system and an extended molecule sub-system (i. e. system with the molecule including the interface gold atoms). An interface gold atom (let's say the tip apex atom which is in contact with the molecule), is affected both by the external input to the tip and the molecule relaxation. In the sub-system-(I), the mass M will move in each large time step with the external input without opposing force on it. The second sub-system-(II) executes a fixed number of iterations in the time one iteration of the sub-system-(I) is performed. At the end of one of such k-iterations cycle (shown in Figure 3.2) the results for the position for the common mass M in the two sub-systems are added. Then the system waits for the next external force input and starts with the whole cycle again.

For its implementation in the GPU, we introduce here another cell index which makes it easy to differentiate between molecule and gold atoms in the same cell. Then similar to the gold-gold interaction case, for any molecule atom, the gold atoms which are close enough are identified for the force computation by looking at the neighbouring cell indices. Then a two-dimensional thread block is launched with size $32 \times 27 \times 1$. The 32 columns in it correspond to the 32 atoms per cell, while each column is assigned 27 threads which are taken because it is the largest multiple of

[6] Data races are a common problem in parallel programming, and happen when two threads try to change some value in the same memory address: both read and change the value at the same time, which causes the returned value of the fastest thread to be overwritten by the other thread, thus giving the wrong result.

[42] Mark Harris. In: *Nvidia developer technology* (2008).

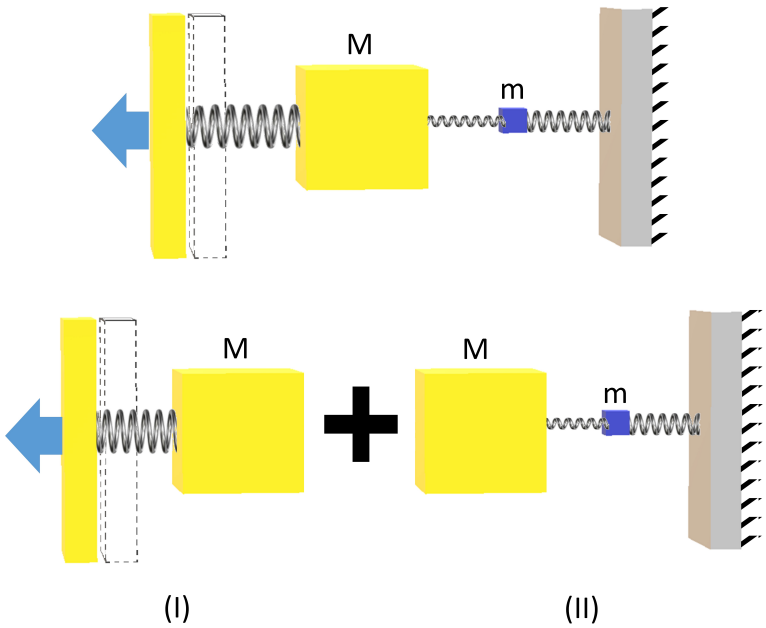


Figure 3.4: The schematic shows a simple spring-mass system with two masses M and m used to demonstrate the division of task in our parallel computation scheme. The heavy mass M is connected to a wall which is free to move with external input, while the small mass m is connected to a fixed wall. The system is divided into two sub-systems: (I) a sub-system with only heavy mass (M) and the external input, this is similar to an all-gold system described in Chapter 2 and (II) a subsystem with the small mass (m) connected also to the heavy mass M, similar to an extended molecule system with the interface gold atoms.

9 (the number of cells that need to be considered for each atom) smaller than 32. Thus, bringing the number of threads per block as close as possible to the limit of the nVidia Maxwell architecture, which is $1024 = 32 \times 32$. So, in comparison to gold-gold interaction case where we had one thread per atom in the cell, now we have 27 threads per atom in the cell. These 27 threads help in computing the forces from the neighbouring gold atoms in parallel. Depending on the chosen cutoff radius, it might be the case that the number of neighbouring gold atoms is more than 27 and thus each of these 27 threads might also have to run a small *for-loop* over a few neighbouring atoms indices.

Intramolecular forces

The intramolecular force calculations involve only forces between the molecule atoms and all the external forces from surrounding gold atoms calculated above will be added later. Since we have only molecule atoms connected to each other by covalent bonds, we can have a more simplified cell structure. Here, all molecule atoms have up to three references to three neighbouring molecule atoms. The intramolecular forces consist of bond forces, angular forces and torsional forces. For a molecule, with

maximum n bonds per atom[7] the maximum number of bond forces calculations n_b per atom is n. Next, the maximum number of angular forces calculations n_a per atom is $\frac{3}{2}n(n-1)$ and the maximum number of torsional forces calculations n_t per atom is $2n(n-1)^2$. A derivation of these maximum limits is given in the Appendix B.2. Similar to gold-molecule forces to implement these force calculations using a GPU we utilise a two-dimensional thread block with each column in this case describing the different intramolecular forces on each molecule atom. The maximum number of force calculations that can be done simultaneously for each atom is decided by the number of threads per column which similar to before cannot be larger than 32 per thread block.

For a maximum number of bonds per atom $n = 4$, the molecule can be non-planar (example: tetrahedral geometry). Although, for this, the maximum number of bond pairs calculations ($n_b = 4$) and the maximum number of angular force calculations ($n_a = 18$) are well within the 32 number limit, but, the maximum number of torsional force calculations ($n_t = 72$) are much larger than 32. This could still be computed by using three thread-blocks and/or pre-calculating the groups for a specific molecule. However, for this first implementation we will limit ourselves to molecules with $n = 3$ i. e. planar molecules. By this restriction we have for each atom the maximum number of bond pairs calculations ($n_b = 3$) and the maximum number of angular force calculations ($n_a = 9$) and the maximum number of torsional force calculations ($n_t = 24$). Hence, one thread-block is still not large enough and we use two thread blocks, one for calculating bond pairs and angular forces per atom and the other for doing torsional force calculations for each atom.

All these intramolecular forces and forces due to gold atoms on each molecule atom are added and then integrated with the smaller time-step δt. For simplicity, a thermostat consisting of a constant friction factor is incorporated in the simulation to dissipate the excess energy pumped into the system from the hand controlled tip movement. Depending on the choice of the substrate material and the molecule one may have to test suitable thermostats.

3.5 Results and discussion

This GPU implementation allowed us to extend our previous all-metallic real-time simulation by including an organic molecule. In this implementation, all the intramolecular forces, i.e. bond forces, angular forces and torsional forces are computed. Along with this, the force that the metal atoms within a pre-defined cut-off radius (in STM tip and substrate) apply on each molecule atom are also computed. All these force calculations, allow us to keep track of the conformation changes that accompany a molecular manipulation operation. To test the performance of this GPU implementation, we successively increased the size of the substrate on which the simulation is performed and we compare in Figure 3.5 the total time that is required to execute one hundred iterations on both CPU and GPU. We can immediately see a striking difference in performance between the two: where the execution time of the CPU implementation quadratically increases and quickly reaches to the order of seconds, the GPU computation increases linearly and stays under 100 milliseconds even at a much higher number of gold atoms. Note that the linear dependence of

[7] Here, single, double or triple covalent bonds are all counted as one bond.

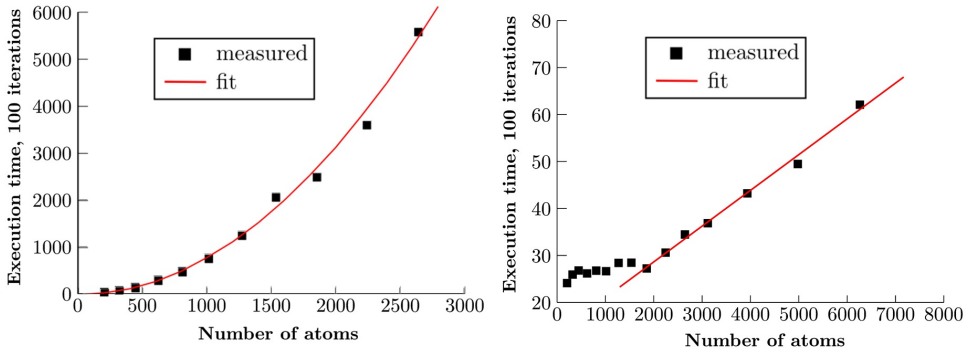


Figure 3.5: Total execution time, in milliseconds, for 100 iterations of atom relaxation with only gold interaction and motion enabled. The left graph shows the performance of the old CPU simulation, while the calculation speed of our GPU simulation is displayed in the right graph. In addition to the notable difference between the two implementations, we see that the time it takes the GPU to execute 100 iterations is nearly constant for a small number (less than 2000) atoms, while a linear relation is observed in the cases with a higher number of atoms.

the execution time on the number of atoms, which is inherent to the use of a cell list data structure, only appears to hold from about 2000 atoms. A possible explanation for this is that the GPU is not yet filled before the end of an iteration, and could take on more threads. In other words, for smaller numbers of atoms, the latency caused during synchronization with the CPU is limiting the execution time. The system we study here contains only gold interaction and we consequently increase the size of the gold substrate during the performance test. As the number of atoms in the molecule cannot be increased in the current GPU implementation due to the limit of 32 atoms per cell imposed by the warp size, in order to test the performance of our system we increase only the number of gold atoms.

A similar performance analysis as before, while including also the molecule in the system, by increasing subsequently the substrate size is given in Figure 3.6. The GPU implementation of the simulation including the molecule takes longer than the one for only the metallic substrate and reaches quickly one hundred milliseconds per 100 iterations for a small substrate size, but the simulations still runs smoothly in real-time. A possible reason for the stagnation of the performance (as compared to the pure gold system) is that the GPU memory is getting filled up causing the rest of the operations to be stalled[43]. Another source of delay, revealed by a profiling tool that is part of the CUDA development kit, is the kernel launching overhead. Since the threads operate on little data and thus finish their job quickly, this overhead becomes relatively large and can even dominate the execution scheme in terms of latency.

Figure 3.7 shows snap-shots of the real-time simulation output demonstrating a sequence of images showing dragging and lifting of a single molecule by the tip over a Au(111) substrate. Here, the positions of the gold atoms in contact with the molecule are calculated taking into account both the external input and the relaxation of the

[43] Johnathan Alsop et al. In: *Performance Analysis of Systems and Software (ISPASS), 2016 IEEE International Symposium on*. IEEE. 2016, p. 172.

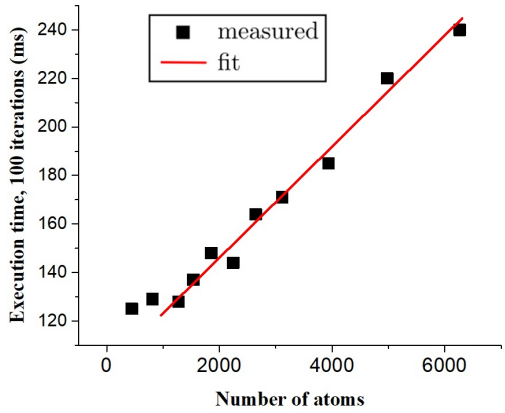


Figure 3.6: Total execution time, in milliseconds, for 100 iterations of atom relaxation including both gold and molecule computations. A linear relation between the substrate size and the execution time is observed. Again for smaller number of substrate atoms, the execution time is nearly constant pointing towards not complete utilization of all GPU threads.

molecule. The interaction between the substrate gold atoms is calculated using an embedded atom-potential described in chapter 2, while the tip gold atoms are treated using a harmonic potential[8]. The lifting of a molecule in experiments is helped by the higher reactivity of the tip apex atoms (as a consequence of the lower coordination number) as compared to the substrate gold atoms. However, as the Morse potential, used here for simulating the Au-N bond, is a pair potential so we need to separately enhance the reactivity of the tip as compared to the substrate gold atoms. To this effect, we manually defined a different affinity for the N atom in the molecule towards the tip gold atoms and the surface gold atoms. The manipulations that are shown in Figure 3.7 are performed with a real-time user-input and thus demonstrate a successful implementation of the real-time molecular dynamic simulation using the GPU programming.

Although the implementation is successful, the actual physical parameters used in the simulation need to be adjusted based on the experimental inputs. One such input comes by comparing the structure of a molecule when adsorbed on a metallic substrate[44] between the experiment and the simulation. Note that the molecule shown in the simulation is lying flat on the gold surface. In reality, each atom of the molecule (N, C, H) makes a different bond (with different bond strength and bond length) with the substrate gold atoms. This means different parameters (in the Lennard Jones potential) for different substrate-molecule atom combination has to be used and these values should be tested against the experiment. For simplicity, we have used the same parameters for all the substrate-molecule atom combinations as described in Appendix B.3.2, which gives a flat molecule structure over the metallic

[8] The parameters used in the simulation are given in Table B.1.

[44] A. Kraft et al. In: *Phys. Rev. B* 74 (2006), p. 041402.

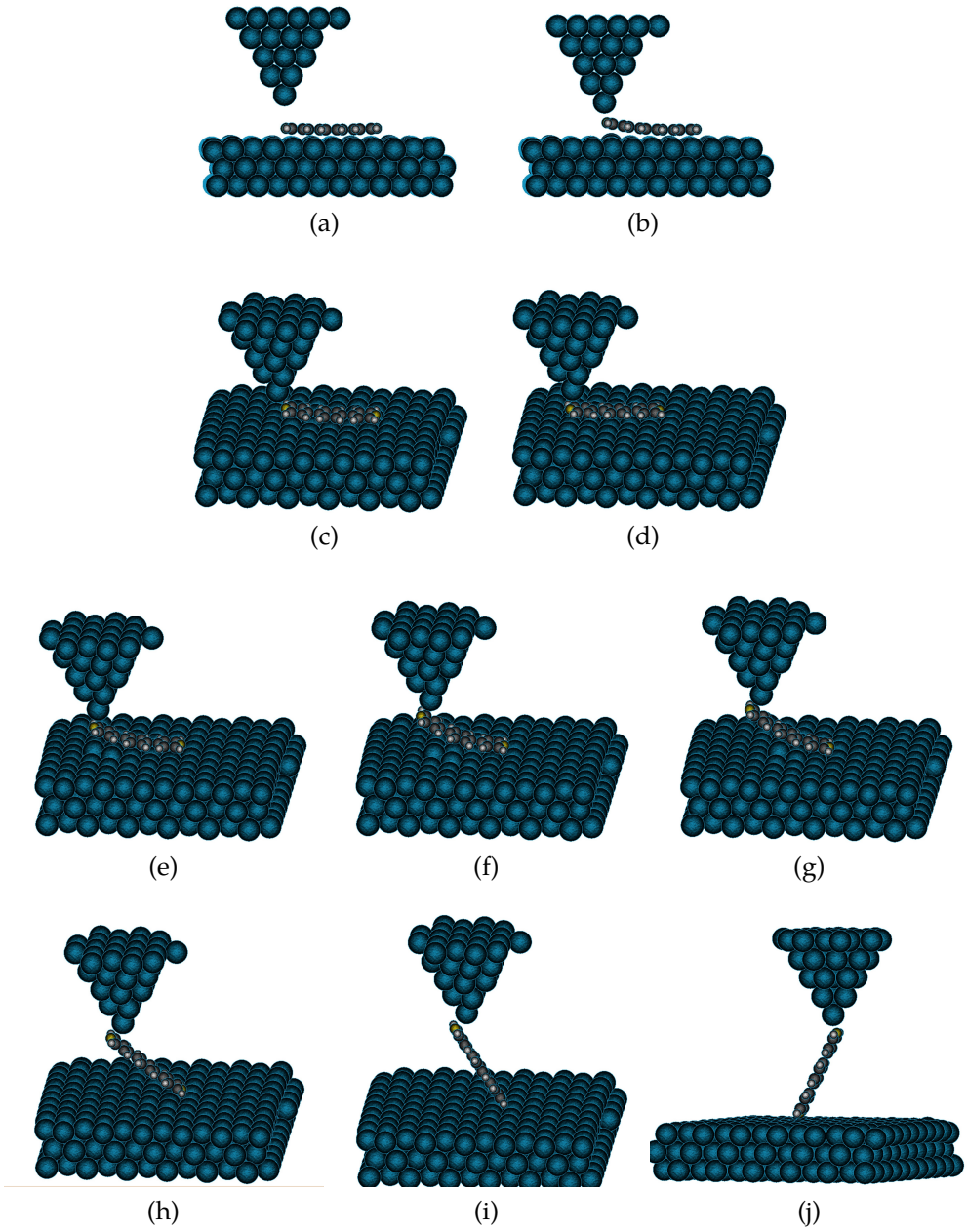


Figure 3.7: Snap shots for different manipulation operations performed using our GPU implementation of the real-time MD simulation. (a) The metallic tip is brought close to the N atom in the 1,4-bis(4-pyridyl)benzene molecule followed by a bond formation at (b). (c),(d) The molecule is dragged over the Au(111) surface using the Au tip. After this sequence (e)-(j) shows a lifting operation of the molecule from the metallic substrate.

substrate.

3.6 Conclusion and outlook

We developed a continuous steering real-time molecular dynamic simulation which can provide real-time feedback while doing a controlled molecular manipulation using low-temperature SPM. We prepared this simulation in a general purpose GPU programming language using CUDA architecture, which allows us to compute different parts of the simulation in parallel. Most importantly the multiple time-step problems arising from a large difference in mass of metallic atoms and their molecular counterparts is solved by a judicious distribution of computations between different thread-blocks and thus running many molecule iterations in parallel to a single iteration of the metallic system. All the intramolecular interactions and the metal-molecule interactions were computed while maintaining the real-time performance of the system. This program allows one to track the changes in the molecule conformations and rotations during molecular manipulation.

A system combining a low-temperature STM, a 3D motion control system and a real-time molecular dynamic simulation is useful for realizing a benchmark testing machine for single molecule electronic transport. From here different conductance values recorded during the experiment can be attributed to particular metal-molecule-metal configurations suggested by the MD simulation. These configurations can then be used as input for more detailed electronic transport calculations (DFT, NEGF etc.) and the values of conductance thus predicted by the theory can be compared hand in hand with the experimental data. As an outlook, the simulation can be further upgraded to include 3D molecules and not only planar. This upgrade will require rewriting the shared memory allocation differently, as more atoms data has to be shared among all the thread blocks.

II

Part Two: Shot Noise

4 Shot noise measurements in the MHz regime 68

4.1 Introduction
4.2 Principles of the method
4.3 Description of the instrument
4.4 Testing, calibration, and accuracy
4.5 Measurements on Au and Pt atomic contacts
4.6 Conclusions

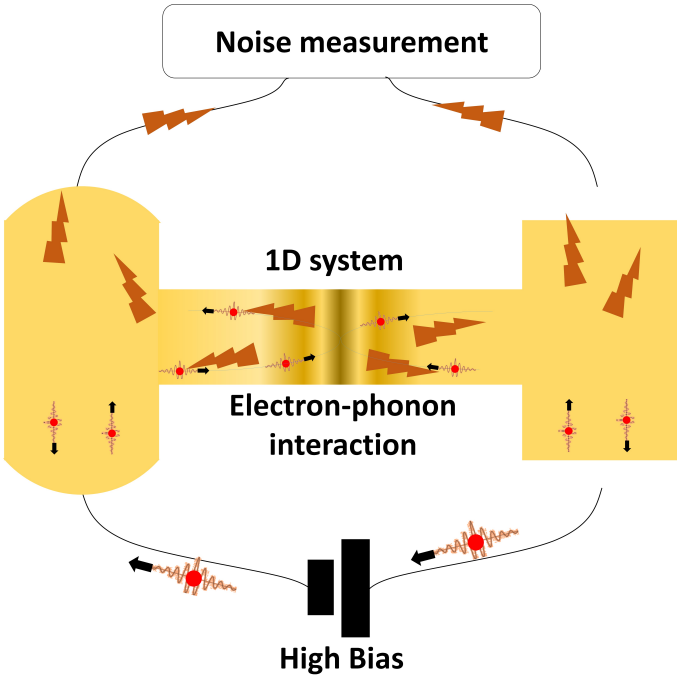
5 Anomalous non-linear shot noise at high voltage bias 90

5.1 Introduction
5.2 Measurement setup
5.3 Shot-noise measurements
5.4 Quantum interference model
5.5 More general energy and voltage dependent transmission functions
5.6 Discussion
5.7 Conclusion and outlook

6 Two-level fluctuations in molecular junctions 108

6.1 Introduction
6.2 Literature review
6.3 Experimental setup
6.4 Measurements on a D_2 molecule
6.5 Inelastic tunneling versus two-level fluctuations?
6.6 Conclusion

Graphical Summary



4. Shot noise measurements in the MHz regime

Shot-noise measurements on atomic and molecular junctions provide rich information about the quantum transport properties of the junctions and on the inelastic scattering events taking place in the process. Dissipation at the nanoscale, a problem of central interest in nano-electronics, can be studied in its most explicit and simplified form. Here, we describe a measurement technique that permits extending previous noise measurements to a much higher frequency range, and to much higher bias voltage range, while maintaining a high accuracy in noise and conductance. We also demonstrate the advantages of having access to the spectral information for diagnostics.

The work is done in collaboration with - Carlos Sabater[1], Manohar Kumar[1], Stefan Stahl[2], Bert Crama[1] and Jan M. van Ruitenbeek[1]
[1]Huygens-Kamerlingh Onnes Laboratorium, Universiteit Leiden, The Netherlands.
[2]Stahl Electronics, Hauptstrasse 15, 67582 Mettenhein, Germany.

4.1 Introduction

Atomic-size contacts and single-molecule junctions have proven to be wonderful platforms for exploring the properties of electron transport in the quantum conductance regime.[1,2] The structure of quantized conductance channels and their connection to atomic and molecular orbitals has been elucidated[3–7]. For such investigations mere measurement of the conductance of the junction provides insufficient information on the composition of the junction. Indeed, in the coherent quantum limit the conductance is given by Landauer's expression as $G = G_0 \sum T_n$, where $G_0 = 2e^2/h$ is the conductance quantum, and the sum runs over the transmission probabilities T_n of each of the participating conductance channels. This sum hides all the details of how many channels are involved and what is the relative weight of each of these.

Several techniques have been developed over the years that give access to more detailed knowledge. The most powerful of these methods exploits multiple Andreev reflection, using superconducting metal leads.[3,4] The combination of the quantum structure of the atomic-size junction with the energy gap structure of the superconducting leads gives rise to strongly non-linear current-voltage (IV) curves with rich finestructure, from which in many cases the full set of transmission probabilities $\{T_n\}$ can be extracted. This set $\{T_n\}$ is often referred to as the mesoscopic PIN code of the junction, since knowledge of this code is sufficient to predict quantitatively all other electronic properties of the junction.[8,9]

Shot noise has become an equally important tool in analyzing the quantum conductance structure of atomic-size junctions. The information that it provides is more restricted compared to the use of superconducting subgap structure, but it has the advantage that it is more widely applicable, since many junctions of interest cannot easily be formed by the use of superconducting leads. Moreover, the requirement of cooling to well below the superconducting critical temperature does not apply, by which the method again gains wider applicability.

The study of shot noise in atomic-size junctions has gained further interest by the observation of signals due to inelastic scattering of the electrons.[10,11] Atomic and molecular junctions offer a unique opportunity for observing inelastic contributions to noise in detail, and the effect opens new avenues for investigating atomic and molecular junctions.[12–14]

[1] Nicolás Agraït et al. In: *Physics Reports* 377 (2003), p. 81.
[2] Juan Carlos Cuevas and Elke Scheer. Molecular electronics : an introduction to theory and experiment. New Jersey [u.a.] : World Scientific, 2010.
[3] E. Scheer et al. In: *Phys. Rev. Lett.* 78 (1997), p. 3535.
[4] E. Scheer et al. In: *Nature* 394 (1998), p. 154.
[5] R. H. M. Smit et al. In: *Nature* 419 (2002), p. 906.
[6] M. Kiguchi et al. In: *Phys. Rev. Lett.* 101 (2008), p. 046801.
[7] Richard Berndt et al. In: *Physical Chemistry Chemical Physics* 12 (2010), p. 1022.
[8] R. Cron et al. In: *Phys. Rev. Lett.* 86 (2001), p. 4104.
[9] A. Levy Yeyati et al. In: *Phys. Rev. Lett.* 87 (2001), p. 046802.
[10] Manohar Kumar et al. In: *Phys. Rev. Lett.* 108 (2012), p. 146602.
[11] Ruoyu Chen et al. In: *Scientific reports* 4 (2014), p. 4221.
[12] R. Avriller and A. Levy Yeyati. In: *Phys. Rev. B* 80 (2009), p. 041309.
[13] Federica Haupt et al. In: *Phys. Rev. Lett.* 103 (2009), p. 136601.
[14] T. L. Schmidt and A. Komnik. In: *Phys. Rev. B* 80 (2009), p. 041307.

Shot noise results from the discrete character of the charge of electrons. For a tunnel junction the transmission of electrons is a stochastic process described by a Poissonian distribution, giving rise to a current noise power spectral density $S_I = 2eI$, where e is the electron charge and I is the mean current[15]. A quantum conductance channel with perfect transmission has zero shot noise because the electron wavefunction is completely delocalized between left and right contacts, so that the current loses its particle-like discreteness. A general expression for noise at finite temperature and voltage, and for an arbitrary set $\{T_n\}$ has been obtained by Lesovik and others[16–18], and can be represented as,[10]

$$Y(V,T) = [X(V,T) - 1]\,F \tag{4.1}$$

Here, $Y(V,T) = (S(V,T) - S(0,T))/S(0,T)$ is the reduced noise power.[1] It measures the noise above the zero-voltage thermal noise, and scaled to the thermal noise. The control parameter $X(V,T)$ is given by $X(V,T) = x\coth x$, where x is the ratio of the voltage and temperature in the experiment $x = eV/2k_BT$. The noise spectrum is white up to very high frequencies ω for which $\hbar\omega$ becomes comparable to eV or k_BT. The so-called Fano factor F gives the slope of the reduced noise power as a function of X, and this is the quantity containing the relevant information, which we will be interested in measuring. In the absence of inelastic scattering F depends only on the transmission probabilities $\{T_n\}$, as

$$F = \frac{\sum T_n(1-T_n)}{\sum T_n}. \tag{4.2}$$

The central problem of concern in noise measurements is the impedance of the device under test, in this case the junction resistance R_s. The scale is set by the quantum of resistance $R_q = 1/G_0$, which is about 12.9 kΩ. When the junction contains many channels with high transmission probabilities the information obtained from the Fano factor F in combination with the conductance G is very limited, because there are too many unknown parameters. For this reason we will be mostly interested in the range of resistances $R_s \gtrsim 1$ kΩ. On the other hand, when the junction resistance R_s becomes very high this fact alone implies that all conductance channels have a small transmission probabilitity. From the expression (4.2) we conclude that the Fano factor approaches 1 in this limit, and it will be difficult to draw strong conclusions from small deviations from unity. In practice this limits the range of interest to $1\text{ kΩ} \lesssim R_s \lesssim 100\text{ kΩ}$, and $R_s \simeq 10$ kΩ being of particular interest.

Since shot noise is white up to very high frequencies we may choose to measure it in any convenient frequency window. However, practical limitations are set from two sides. At the low side of the spectrum ubiquitous 1/f-noise dominates the measured

[1] We discuss voltage noise rather than current noise, because this is the parameter we directly measure. The conversion is straightforward, obtained through the resistance R_s of the junction as $S_V = S_I R_s^2$. When the resistance is voltage dependent the comparison with theory may require more careful consideration, but this is outside the scope of this paper.

[15] W. Schottky. In: *Annalen der Physik* 362 (1918), p. 541.
[16] G. B. Lesovik. In: *JETP Lett.* 49 (1989), p. 592.
[17] M. Büttiker. In: *Phys. Rev. Lett.* 65 (1990), p. 2901.
[18] Ya. M. Blanter and M. Büttiker. In: *Physics Reports* 336 (2000), p. 1.

noise. This 1/f-noise is attributed to two-level fluctuations of various origin,[19] and is present in the amplifiers as well as in the sample itself. The latter source of noise is particularly troubling since it is resistance noise, for which the voltage noise power increases with the applied voltage bias over the junction as V^2. Since shot noise is linear in V, for high bias 1/f noise is likely to dominate. Since 1/f-noise decays roughly as ω^{-1} we will want to measure the noise spectrum at high frequencies.

The high end of the spectrum is limited by the bandwidth of the measurement, which is set by the RC time of the combination of the junction resistance R_s together with the capacitance of the cables and the amplifier input. With a typical cable capacitance of 100 pF/m, two cables connected, and $R_s = 10$ kΩ the bandwidth is limited by a corner frequency of $f_c = 1/2\pi RC \simeq 80$ kHz. For metal atomic junctions at moderate voltage bias this leaves a window of about two decades between 1 and 100 kHz for measurement.[20]

Let us now define the goals of the present experimental setup: (1) we want to increase the voltage bias range in order to explore inelastic effects at higher bias, which will dramatically increase the amplitude of 1/f-noise and push the lower limit of the useful spectral range to higher frequencies. This is further exacerbated by moving from metallic atomic junctions to organic molecular junctions, which display a higher tendency of developing two-level fluctuations. In order to compensate for the loss in spectral range we want to push the upper limit of the spectrum to higher frequencies. (2) Noise measurements at low frequencies are slow. The measurement time is set by the intrinsic stochastic character and the associated requirement of long averaging times needed for determining accurate noise power levels. We will be interested in high accuracy and speed, such that we can detect small inelastic corrections and that we can follow these quasi-continuously as a function of control parameters such as bias voltage or mechanical stretching of the junction. The recording time for each data acquisition scales inversely with the lowest frequency of the spectral window. By shifting the lower limit of the frequency window from 1 kHz to 100 kHz the speed of measurement is increased hundred fold, provided the speed of data manipulation can be adjusted to the high data acquisition rates.

Other factors of concern are the noise introduced by the electronics of the amplifier chain, and pick up of spurious signals. Spurious signals are easily identified when the Fourier spectrum over a wide range is available for inspection, which is why we have decided to focus on broad band spectrum-based noise measurements. Amplifier noise may limit the accuracy, which is why we have decided to adopt the method introduced by Glattli and coworkers,[21] based on measuring the noise signal twice, through two parallel and independent chains of amplifiers with high input impedance. The noise signal is then obtained from calculating the cross spectrum of the two signals, from which the uncorrelated noise of the two amplifiers is strongly suppressed after averaging. In order to widen the bandwidth the first-stage amplifiers are mounted in the cryogenic environment at close proximity to the break junction device. This allows us to push the upper limit of the usable frequency spectral range up by nearly two orders of magnitude, from 100 kHz used previously[8,20,22] to 6 MHz,

[19] Sh Kogan. Cambridge University Press, 2008.

[20] H. E. van den Brom and J. M. van Ruitenbeek. In: *Phys. Rev. Lett.* 82 (1999), p. 1526.

[21] A. Kumar et al. In: *Phys. Rev. Lett.* 76 (1996), p. 2778.

[22] Ran Vardimon et al. In: *Phys. Rev. B* 88 (2013), p. 161404.

similar to the approach used by DiCarlo *et al*.[23] and by Jullien[24] for measuring the cross correlation of two separate sample signals.

Several alternative strategies have been explored by other groups, depending on the problem to be addressed. Thibault *et al*.[25] demonstrated noise measurements over a very wide frequency range, even into the GHz range. The fact that they could tune the resistance of their sample to match the 50 Ω impedance of the cables and amplifier input explains why this was possible in their experiments. In general, the applicability of the technique is subject to limitations set by the actual resistance of the sample under test. Yet, even for high sample resistances it has been demonstrated that noise can be effectively measured in the GHz regime.[26–28] Although there are advantages of noise detection in the GHz regime, the main disadvantage is that the Fourier spectrum is not readily available for diagnostics and detection of spurious signals. In these experiments only the integrated noise is detected by a power detector.

Having decided that we want to employ high-input impedance amplifiers, as a consequence the bandwidth is limited to a few MHz, resulting from the sample resistance in the range of the quantum resistance and a few pF of input capacitance that cannot be avoided. Two further strategies have been demonstrated for pushing the bandwidth still higher. Birk *et al*. employed active feedback of the measured AC signal, back to the input amplifier stage, in order to compensate for the input capacitance.[29] This allows increasing the bandwidth by two to three orders of magnitude. Although this will be a very attractive option when we want to explore higher junction resistances, at this point it is not needed. It would add amplifier noise and would not be compatible with the configuration of two parallel sets of amplifiers. A second strategy, which was also implemented by DiCarlo and coworkers[23] and by Jullien[24] is to add an inductor in parallel to the capacitance in order to convert it from a low-pass filter into a band pass filter centered at higher frequencies ($\omega_0 = 1/\sqrt{LC}$). Although this reduces the bandwidth (i. e. $\omega_0{}^2$RC) to only about 100 kHz, this is still a very interesting option for further raising the measurement frequencies.

4.2 Principles of the method

Atomic-size contacts and molecular junctions are formed by mechanical adjustment of the gap between two metal electrodes using the mechanically controllable break junction (MCBJ) technique.[30,31] This allows forming fresh metal electrodes by breaking of a weak spot produced in a wire or microfabricated bridge. The mechanical adjustment is controlled by a combination of a mechanical screw translation stage and a piezo electric element for fine adjustments. The junction can be broken at liquid-

[23] L. DiCarlo et al. In: *Review of scientific instruments* 77 (2006), p. 073906.
[24] Thibaut Jullien. PhD thesis. Université Paris Sud-Paris XI, 2014.
[25] K. Thibault et al. In: *Noise and Fluctuations (ICNF), 2015 International Conference on*. 2015, p. 1.
[26] M. Reznikov et al. In: *Phys. Rev. Lett.* 75 (1995), p. 3340.
[27] P. J. Wheeler et al. In: *Nano Letters* 10 (2010), p. 1287.
[28] F. D. Parmentier et al. In: *Rev. Sci. Instrum.* 82 (2011), p. 013904.
[29] H. Birk et al. In: *Rev. Sci. Instrum.* 67 (1996), p. 2977.
[30] C. J. Muller et al. In: *Phys. Rev. Lett.* 69 (1992), p. 140.
[31] J. M. van Ruitenbeek et al. In: *Review of Scientific Instruments* 67 (1996), p. 108.

He temperatures under vacuum, so that contamination can be avoided for extended periods of time. Molecules can be introduced to the junction, either through a capillary connected to a room-temperature vapor source, or by deposition from solution prior to cool-down. A discussion of the benefits of this method has been presented elsewhere,[1] and details of its present implementation adjusted for high-frequency noise measurements will be given below.

Low temperatures are required for suppressing atom mobility, for spectral resolution of vibration modes of the junction in differential conductance measurements, and for reducing 1/f-noise and thermal noise of the junction. Since variation of temperature is usually not required, a practical choice is given by the temperature of a liquid He bath at ambient pressure, about 4.2 K. This temperature is low enough such as to make the sample thermal noise comparable to instrumental noise sources. The mechanical construction of the vacuum can takes the form of a dip-stick that can be lowered directly into a liquid-He storage vessel, which permits fast cycling between experiments.

Wide-band noise measurements on the junctions are permitted by mounting two parallel low-noise cryogenic amplifiers at close proximity to the junction, by which cable capacitance is limited. These first-stage amplifiers have a high input impedance, and a 75 Ω output. The junction is biased from a voltage source through a series resistor, and the conductance of the junction is measured by means of an audio-frequency lock-in technique. Decoupling of the cable capacitances of the biasing and the voltage sensing line is accomplished by inserting a second series resistor near the junction in the cold. The frequency window chosen for the noise analysis is 1 to 6 MHz. While the transfer characteristics of the electronic circuit in this window is already decaying as a result of the unavoidable input capacitance, the transfer characteristics can be accurately taken into account and the signal-to-noise permits measuring Fano factors with an accuracy better than 1%.

The higher spectral frequency range permits shorter acquisition times, and for the data analysis to be able to keep up with acquisition the Fourier transforms, computation of cross spectra, and averaging are handled by a Field Programmable Gate Array (FPGA) unit. All other processing is done under LabView control on a standard desktop computer. Table I summarizes the properties of the system, and a detailed description of each of the components follows below.

TABLE I. Parameters characterizing the instrument.

Spectral acquisition speed*	12 s^{-1}
Noise spectral frequency range	0.1 – 10 MHz
Sample conductance range	0.1 – 10 G_0
Bias voltage range	at least ± 100 mV
Accuracy of conductance measurement	< 1%
Accuracy of Fano factor	< 0.01
Temperature	4.4 ± 0.2 K

* For a standard number of 10,000 times averaging.

4.3 Description of the instrument

4.3.1 Mechanical design

The dipstick has been designed to fit directly into a He transport vessel, which sets its dimensions as 50 mm in diameter and 1.5 m long. At the top of the tube a connector head is mounted, shown with some of the covers removed in Fig. 4.1a. It has ports for electrical connections, vacuum pumps and pressure gauges, a connection to a capillary for injection of molecular vapor, and a rotary feed-through in the top lid for mechanical adjustment of the junction. The central tube contains ducts for wiring, for the gas dosing capillary, and an axis for mechanical control. The dipstick unit accommodates the first-stage noise amplifiers at close proximity of the break junction. The working temperature of the amplifiers affects gain and noise performances so that it is of importance to take care of proper thermalization of the amplifiers and of all the wires going to and out from the cryogenic amplifiers. The thermalization is provided by a copper block (Fig. 4.1b) that connects the main tube to the sample space, houses the amplifiers (Fig. 4.1c), and is in direct contact with the helium bath. Copper wool is added between the gold plated base of the low temperature amplifiers and the copper bock for better thermalization. The capillary tube for admitting gasses is isolated from the Cu block using a Teflon ring and has an extension at the cryo end with a gas dozer nozzle facing the sample.

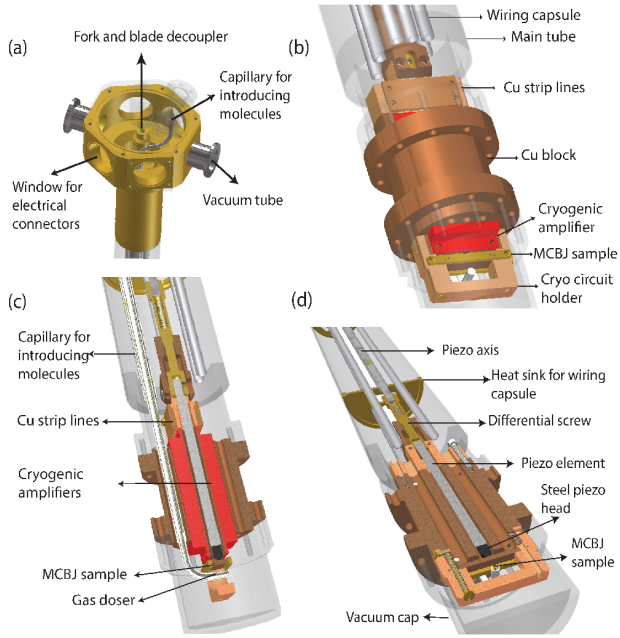


Figure 4.1: Layout of the dipstick (pitures taken from Manohar Kumar's thesis). (a) Top flange with connector head. (b) Cu block serving for thermalization of the cryo-electronics. (c) Cross section of the lower part of the insert showing the position of the amplifiers (shown schematically in red) inside the Cu block . (d) Cross section of the lower part of the insert showing the position of the piezo element and the mounting of the sample.

The wires running down the central tube are held by capsules, which are formed by semi-cylindrical tubes (a tube cut in half along its length). All the wires coming from the head at room temperature are Manganin (Cu(86%) Mn(12%) Ni(2%)) wires, which provide a good compromise between a high electrical conductance and a low thermal conductance. The wires are glued onto the inside of the semi-cylindrical tubes by GE varnish. These half-cylindrical tubes are inserted by sliding from the top into the fine hollow tubes, which in turn are fixed to the main tube of the dipstick using silver welding for good thermal and mechanical anchoring. This arrangement has the advantage that it helps anchoring the wires thermally and mechanically to the inner wall of the rod efficiently, while the wires can be easily removed from the wiring capsule for maintenance and modifications. At the bottom end all wires are soldered onto electrically isolated Cu strips on the cold finger extending from the Cu block, where they are cooled efficiently by the liquid He bath.

A mounting stage for the sample is fixed to the bottom of the copper block. The sample has the form of a bendable substrate of about 3 by 20 mm carrying the notched sample wire. The side carrying the notched sample wire faces down and is held against two fixed supports at either end. The top of the piezo element pushes in the middle against the back of the substrate, from above, for control of the bending. The sample space is enclosed by a brass cap that is mounted onto the lower end of the copper block by ten 3 mm bolts, and sealed with a thin indium ring. The sample space is in contact with the main volume of the central rod through openings in the copper block, permitting efficient vacuum pumping. During the measurements the actual pressure in the sample space is further improved by cryo-pumping of the walls of the container. A container with active coal is mounted in the cryo cap for enhanced cryogenic pumping. Changing samples just requires opening the cap, so that only the input side of the low temperature amplifiers and the sample are exposed. All the rest of the wiring is fixed within the copper block. By placing the copper block directly in contact with the He bath an efficient thermalization of the sample and the amplifiers is achieved, giving a cooling time of about 2hrs to the base temperature of 4.2K. We paid special attention to attaining good mechanical stability, since future measurement runs stretching over several hours of measurement time on a single contact setting are anticipated. Instabilities in the atomic contacts can be grouped into two classes, those inherent to the properties of the sample, i. e. due to the microscopic structure and atomic arrangement very close to the atomic contact, and the other due to external electro-mechanical disturbances to the atomic contact. Instabilities inherent to the sample can often be improved by annealing the sample in the cryogenic vacuum at high currents. External mechanical instabilities can result from electrical noise in the piezo voltage, or vibrations coupling mechanically or acoustically into the setup. The piezo wires are held apart from the sensitive measurement wires by mounting them in separate wire tubes. For mechanical stabilization the screw drive axis can be decoupled from the lower parts using a fork blade configuration, which is positioned at the top of the insert. Further reduction of mechanical and acoustic disturbance is achieved in the usual way by placing the experiment inside an acoustically shielded Faraday cage suspended on pneumatic vibration dampers. Further details about the mechanical design of the dipstick are given in Manohar Kumar's thesis[32].

[32] Manohar Kumar. PhD thesis. Leiden Institute of Physics (LION), Leiden University, 2012.

4.3.2 Analog electronics

Low-frequency components

Figure 4.2 shows the lay out of the electronic circuit. A central star grounding scheme for all signal circuits was used with the star point at the cryo head, in order to avoid ground loops. Apart from the two parallel noise signal amplifiers the atomic-size junction is connected through a single line that provides the voltage bias and permits measurement of the conductance of the junction. Each additional line connected to the sample adds capacitance and reduces the bandwidth. Therefore, the number of lines was limited to just one, and a resistor R_1 near the sample serves to decouple the capacitance of the wire from the sample noise signal. The choice of this resistor $R_1 = 10\ \mathrm{k}\Omega$[2] is a compromise between optimal decoupling, for which the resistance should be as high as possible, the desired accuracy in the conductance measurement, and Joule heating in the resistor at high bias. An inductor has been considered as an alternative, but inductors have the disadvantages that magnetic cores cause non-linearities at high dc bias currents, and unfilled coils require too much space. Since the frequency response and the thermal noise associated with R_1 are known they can be included in the signal analysis described below.

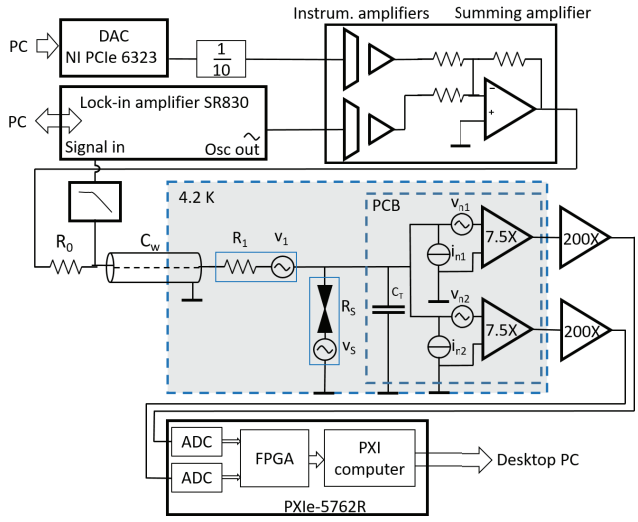


Figure 4.2: Schematic of the circuit used for measurements of conductance and noise on break junction samples (indicated by the two touching black triangles). The components enclosed in the shaded block are at liquid-helium temperatures. The noise sources of the sample, the resistor R_1 and the current noise and voltage noise sources at the inputs of the amplifiers have been given explicit symbols.

The differential conductance as a function of applied dc bias is measured employing a two-probe ac technique by applying a small-amplitude modulation voltage on the bias line, corresponding to values of a few $\mathrm{mV_{rms}}$ across the sample, at a frequency of 677 Hz. The modulation is supplied by the internal oscillator of a SR830

[2] The exact resistance value at low temperature is measured first by shorting the sample. This is then taken into account for H_1 transfer function calculation which is used in equation 4.4.

lock-in amplifier, and the resulting voltage at the top of the insert is measured by the same instrument. We found that connecting the input of the lock-in introduces high-amplitude disturbance over the full range of our noise spectra, but this can be fully suppressed by means of a low-pass filter, for which we employ a T-filter configuration having 1 MΩ at the signal side, 100pF to ground, followed by 10 kΩ towards the input of the lock-in. The resistance of the junction is calculated back from the voltage division over the biasing resistor R_0 (100 kΩ) and the sample resistance in series with the resistor R_1 (10 kΩ), taking phase shifts and signal reduction due to known (stray) capacitances into account. There is some loss in accuracy compared to a scheme with a separate voltage sensing line at the sample, behind R_1. However, additional lines introduce additional capacitance which deteriorate the bandwidth. We have also tested a low-temperature buffer amplifier for dc or audio-frequency voltage sensing, but we were not satisfied with the accuracy and reproducibility after cycling the amplifiers to room temperature. We further tested a miniature relay near the junction, but found that the switching caused unwanted junction breaks, both, as result of mechanical vibrations as well as electrical spikes. The solution given here is simple and sufficiently accurate for our purposes. The overall accuracy of the ac conductance measurement was tested against fixed calibration resistors, giving reproducibility better than 1%.

The dc bias voltage is supplied directly from a National Instruments data acquisition card (PCI DAQ-NI 6221). The DAQ card offers a digital-to-analog convertor with 16 bit digital accuracy, and is controled from the desktop computer through a dedicated Labview routine. We were initially suspecting that taking the bias voltage directly from the DAQ would introduce spurious signals in the spectra, but we found that the spectrum remains clean. However, in order to break ground loops we have introduced instrumentation amplifiers in the bias line, and the adder that combines the ac and dc bias signals is powered from a battery pack.

The combination of wires running down the insert bridging the temperature gradient between room temperature and liquid-He temperatures gives rise to a thermal voltage of 0.56 mV. In our circuit nearly 90% of this dc thermovoltage drops over R_0, so that the influence on the dc bias of the sample is very small. By improving the wiring symmetry the thermovoltage can be further reduced, but in our case we take this small offset into account in the numerical analysis of the data.

The fine tuning of the contact size at the atomic scale is controlled by a piezo element, as shown in Fig. 4.1d. The potential on the piezo element is controlled using a digital-to-analog channel on the same DAQ card, through a Physik Instrumente E-665 high-voltage amplifier.

The temperature of the junction is measured by a standard ruthenium oxide resistance thermometer in a four-probe low-frequency ac resistance bridge[3]. The resistance thermometer is glued to the brass break junction support at the point where the sample substrate is clamped. It is mostly used to verify deviations from the standard operation temperature of 4.2K, and this point has been accurately determined by placing the thermometer in contact with the liquid helium.

[3] It is disconnected during noise measurement.

High-frequency low-noise amplifiers

The cryogenic amplifiers (Fig. 4.3) are designed in close collaboration with Stahl Electronics. The design constraints for the amplifiers are given by the desired input current and voltage noise levels, by requirements for effective thermalization of all active and passive elements on the printed circuit board, and by size limitations. The design of the cryogenic amplifiers was insipred by the low noise amplifiers described by A. T.-J. Lee.[33] The amplifiers have two stages, the first of which is a dual-channel low noise cryogenic amplifier with operational frequency window of 160 kHz to 50 MHz. The output of this stage, with an impedance of 75 Ω is coupled to the input of the second-stage low noise amplifiers at room temperature, with operational frequency window of 400 Hz to 140 MHz, for which we have selected the NF SA-230F5. The advantage of this separation is the reduced heat load on He bath and the smaller size of the cryogenic amplifier. For the cryogenic stage we have used high electron mobility field-effect transistors (HEMT-FETs, ATF34143). The heat load on the He bath is limited to 12 mW. The cryogenic amplifiers as well as the room-temperature amplifiers are powered from battery packs.

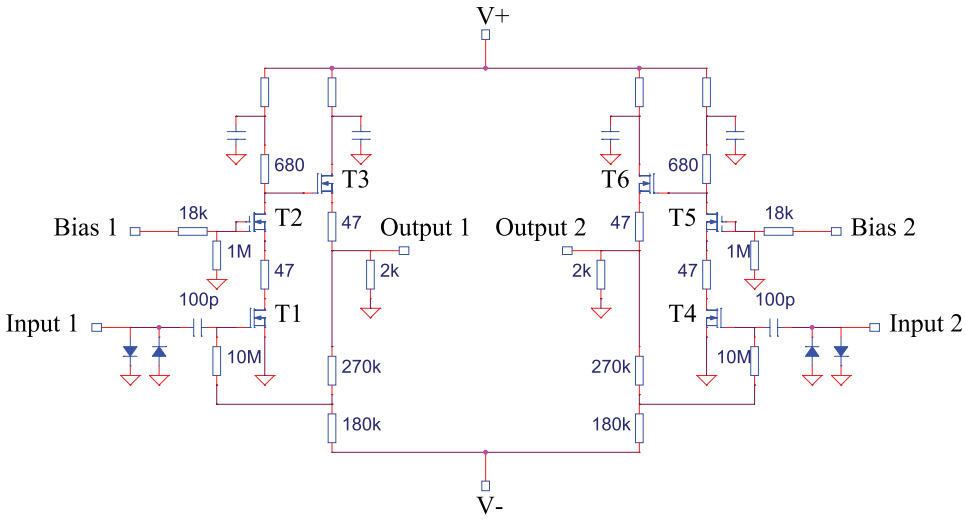


Figure 4.3: Schematic of the cryogenic low-noise amplifier stage. This design gives a broadband frequency response in the low-MHz regime. Both channels are mounted on the same printed circuit board. The amplifier settings can be tuned by the source follower biasing for both channels simultaneously, and through the cascode biasing for each channel independently.

The cryogenic amplifiers are based on cascode biasing to the source follower. The cascode stage eliminates the Miller effect, which is the drain to gate capacitive feedback. The Miller effect also decreases the stability of the circuit at higher frequencies, where effective feedback is positive due to the large phase shift (> 180°) between the input and the feedback signal. This feedback limits the upper cutoff frequency in the source follower circuit. The source follower is a high input impedance amplifier and

[33] Adrian T. Lee. In: *Review of Scientific Instruments* 60 (1989), p. 3315.

the output impedance of this stage matches the cable impedance hence improves the high-frequency performance.

The input capacitance of the two amplifiers combined, including the that due to the short cables of about 1 cm, amounts to a total of $C_T = 14.3$ pF. Assuming the impedance $|Z_{in}|$ of the circuit at the input, which we take to include the stray capacitance C_T, is much smaller than the amplifier input resistance, the effective noise due to the amplifiers detected in channel 1 is given by (see Fig. 4.2)

$$V_{n,1}^2 = v_{n,1}^2 + i_{n,1}^2|Z_{in}|^2 + i_{n,2}^2|Z_{in}|^2 + c_n^2 V_{n,2}^2. \tag{4.3}$$

Here $v_{n,i}$ and $i_{n,i}$ are the voltage and current noise, respectively, at the input of the amplifier number i, while the c_n is a factor describing the cross talk. The voltage noise of the first-stage amplifiers is 0.48 nV/$\sqrt{\text{Hz}}$. The current noise of 60 fA/$\sqrt{\text{Hz}}$ would normally dominate over the voltage noise for resistor values in the range of the resistance quantum. However, the current noise is suppressed by the instrumental bandwidth $|Z_{in}(\omega)|^2$ along with the sample noise signal, which does not apply for the voltage noise. The voltage noise of the two amplifiers, on the other hand, can be nearly fully suppressed by the cross spectrum technique, because they are uncorrelated. Both channels for the cryogenic amplifier are on same board, which gives rise to a small cross talk c_n of about 1% of the full signal at each stage. Although this limits the effectiveness of the cross spectrum and could be further improved by mounting the two channels on separate boards, in practice this is not a limiting factor.

The gain for each of the cryogenic amplifiers of 7.5× is high enough to make the input noise of 0.25 nV/$\sqrt{\text{Hz}}$ of the room temperature amplifier stages negligible. The gain of the cryogenic amplifiers is adjustable through the supply settings and the gain of two channels can be made to match to within less than 1dB. The room-temperature amplifiers have a gain of 200 and are mounted directly at the brass head on the top of the dipstick. The output lines are coupled to the input of the PXI data acquisition system through 50 Ω coaxial cables.

4.3.3 Digital electronics and data manipulation.

We have adopted a National Instruments data acquisition unit for the digitization of the signals. It comprises the NI 5762(-01) with two simultaneously sampled 16-bit analog-to-digital convertor (ADC) channels at 2 V range, 250 MS/s and 100 MHz bandwidth. The synchronization of the sampling by the two channels is critical for obtaining an undistorted cross spectrum. The channels are ac coupled and equipped with a 100 MHz elliptic filter. It has a low −110dBFS channel-to-channel crosstalk. The ADC adds noise of about 10 nV/$\sqrt{\text{Hz}}$ referred to the input of the ADC channels which is negligible in view of the amplification level before the ADC.

The data handling speed is accelerated by using a NI FlexRIO FPGA module (NI PXI-e-7966R). Due to the 32-bit PXI express bus with direct memory access capability data communication from the FPGA to the host computer and to the FPGA from the host computer within the PXI backplane can be done above 100MB/s and 50MB/s, respectively. The combination of the PXI express bus and FPGA allows the implementation of a real time cross spectrum analyzer. The FPGA is programmed for handling the consecutive blocks of 2048 digitized data points from both channels, for applying a Hann windowing function, performing fast Fourier transform (FFT) of both channels individually, computing the complex cross spectrum, vector averaging

by an adjustable number of up to 10^6 spectra, and computing the power spectrum of the result. The FFT processing time for blocks of 2048 data points is 4μs, implying that the computation time is less than the data acquisition time, making the latter the limiting factor in the speed of measurement. The final averaged power spectrum is transferred to a desktop PC for further processing and storage.

The measurements are controlled from a dedicated user-built Labview routine running on a desktop computer. A typical measurement procedure proceeds along the following steps. The routine automatically controls the breaking of an atomic junction through control of the piezo voltage, and searches for a target conductance value. Having arrived at a desired junction setting the bending force on the sample substrate is held stationary. The program then switches to taking a differential conductance spectrum by sweeping the bias voltage between user-defined limits, typically from −80 mV to +80 mV. After the dc bias has been returned to zero, a first noise spectrum is recorded, which is the thermal noise signal $S_\mathrm{m}(0)$, against which the noise at finite bias is compared. Next, shot-noise spectra $S_\mathrm{m}(V)$ are recorded at user-defined steps of typically 0.5 mV, up to a user-defined maximum, typically 80 mV. This series of spectra can be recorded in about 14 seconds. In order to test for changes in the atomic contact configuration during the measurements a differential conductance spectrum is taken again for the same junction setting. All raw data are stored for later inspection, but the analysis is done in real time by a parallelly operating routine. Figure 4.4 shows an example of a set of raw data. The small peak at 9 MHz is due to a signal picked up from the piezo-voltage source, but it does not affect our results, see below.

For the analysis of the Fano factor we would like to make use of relation (4.1), which has the advantage that it is linearly dependent on the quantity $X(V,T)$ and deviations from a linear dependence can be easily detected. However, this is only strictly valid on the condition that the measured zero-bias noise is purely the thermal noise of the junction under test. We have identified at least two additional external noise sources that need to be taken into account: the thermal noise of resistor R_1 in the bias line (see Fig. 4.2), and the current noise i_n injected by the input of the amplifiers into the junction circuit. When $S(V)$ describes the true noise power spectral density due to the junction, the measured noise power can be written as,

$$S_\mathrm{m} = |\beta(\omega)|^2 \left[S(V)|H_1(\omega)|^2 + \tilde{S}_\mathrm{x}(T,\omega) \right]. \tag{4.4}$$

The intrinsic and extrinsic noise sources can be added independently because they are uncorrelated. Here, $H_1(\omega)$ is the transfer function of the noise signal due to the junction, as seen at the input of the amplifiers. It is described in terms of the capacitors and resistors in the input circuit, including the junction resistance R_s and input capacitance C_T: $H_1 = Z/(R_\mathrm{s}+Z)$. Here, Z is the impedance of the input capacitance, $1/j\omega C_\mathrm{T}$ in parallel with $R_1 + Z_\mathrm{ext}$, where Z_ext represents the impedance of the circuit beyond resistor R_1. In (4.4) the term $\tilde{S}_\mathrm{x}(T,\omega)$ represents all noise sources other than that due to the atomic junction, and the frequency dependence of the transfer function is incorporated in its definition. Finally $\beta(\omega)$ is the transfer function of the amplifier chain, including the amplification factor.

By subtracting the zero-bias noise from the shot noise measured at finite bias, $S_\mathrm{m}(V) - S_\mathrm{m}(0)$, the external noise sources can be eliminated. From this difference we obtain the true excess noise $S(V) - S(0)$ by first dividing out the amplification characteristics $|\beta(\omega)|^2$ obtained from a calibration step described below, and dividing

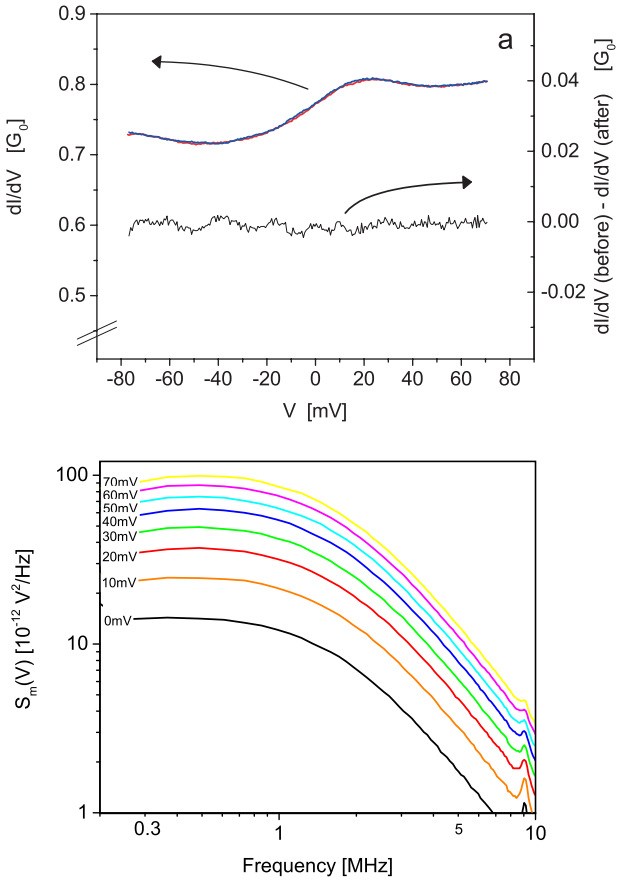


Figure 4.4: Example of raw measurement data for a Au atomic contact at 4.2 K. (a) Differential conductance characterizing the junction configuration before (red) and after (blue) recording the sequence of noise spectra. In this case the red and blue curves nearly coincide, and the difference between the curves is displayed by the black curve (right axis). The zero-bias conductance is $G(0) = 0.772\,G_0$. (b) Noise spectra for the same junction setting at various levels of applied dc bias voltage.

out the transfer function $|H_1(\omega)|^2$ that we obtain from the known components of the input circuit. We verify that the resulting excess noise spectra given by

$$S_\mathrm{e} = \frac{S_\mathrm{m}(V) - S_\mathrm{m}(0)}{|\beta(\omega)H_1(\omega)|^2} \tag{4.5}$$

are white (i.e. frequency independent) in an appropriate frequency window, see Fig. 4.5a. Linear fits to the spectra in Fig. 4.5a measure the slope and the mean noise power amplitude. A more detailed step by step derivation of equation 4.5 is given in the Appendix C.1.

The resulting mean excess noise is expected to be equal to the function $Y(V,T)$, Eq. (4.1), multiplied with the nominal thermal noise of the junction $4k_\mathrm{B}TR_\mathrm{s}$, for

the measured value of the junction resistance R_s. Thus, we proceed to plot the excess noise (4.5) against $4k_BTR_s(X(V,T)-1)$. In this product form for X the sample temperature is nearly perfectly eliminated from the analysis, since the coth function rapidly saturates at 1, and the term -1 is small compared to X. An example of the resulting plot is shown in Fig. 4.5b, from which the Fano factor F is determined as the slope of a linear fit to the data points. At the end of the noise measurement and analysis for a given junction setting the program searches for a new junction in the desired conductance range and restarts the sequence.

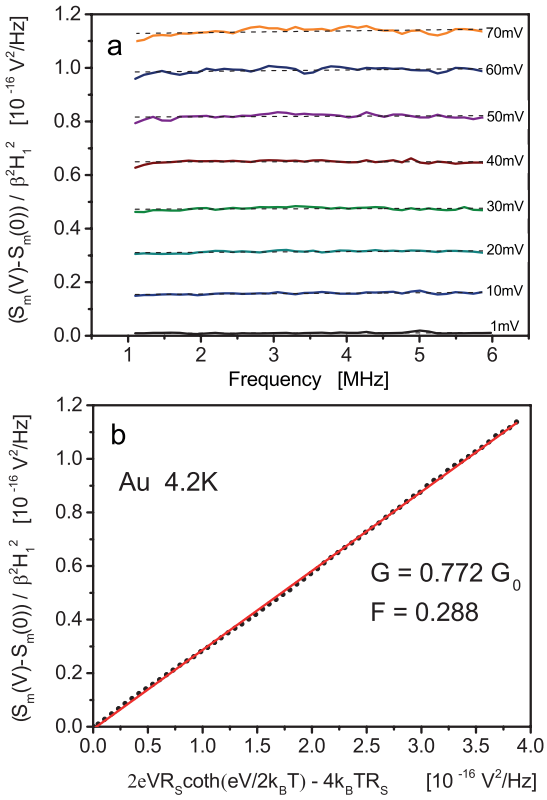


Figure 4.5: Determination of the Fano factor from shot noise measured on a Au atomic contact at 4.2 K. (a) The excess noise $S(V)-S(0)$ obtained from the measured data in Fig. 4.4, corrected for amplifier and transfer characteristics, shown for selected bias voltages as a function of frequency. The mean value for each curve is obtained from linear fits (shown with black dash lines), and the resulting values are plotted in panel (b) as a function of the scaled bias voltage $4k_BTR_s(X(V,T)-1)$, which can also be written as $2eVR_s\coth(eV/2k_BT)-4k_BTR_s$. Since the hyperbolic cotangent very quickly saturates at 1 the latter expression shows that the scale is nearly proportional to the applied bias voltage V, which in this case runs up to about 70 mV. The term $4k_BTR_s$ is only $0.038\cdot10^{-16}\,\mathrm{V}^2/\mathrm{Hz}$. From the slope of this reduced axis plot we obtain a Fano factor of $F=0.288\pm0.004$.

4.4 Testing, calibration, and accuracy

The gain β of the amplifiers and the input capacitance C_T are characterized by injecting a known white noise signal from an Agilent 33500B waveform generator through the bias line for infinite sample resistance (broken junction). The amplitude of the noise signal needs to be selected carefully. The peak events in the noise need to stay below the saturation level of 2 V of the second-stage amplifiers. With a combined amplification of the two stages of 1500× the peak voltage at the input must remain below 0.67 mV, which corresponds to approximately 0.2 mV_{rms}. Given the effective bandwidth of 1 MHz of the circuit this translates into a noise level of 100 $nV/\sqrt{Hz}$. At the lower end the calibration signal is limited by the requirement that it needs to be much higher than the other noise sources in the circuit, such as the thermal noise of 1.5 $nV/\sqrt{Hz}$ of resistor R_1. We use a signal level of 5 mV_{pp} terminated by 50 Ω at the bias line input, behind resistor R_0. We verified that the gain β obtained from this procedure is independent of the input amplitude to within 1%, over a range of a factor of 2 around this value. For larger and smaller amplitudes we find deviations, as expected.

The measured calibration noise power spectrum is closely reproduced by the circuit model parameters, with β and C_T as adjustable parameters. In good approximation the noise power shows a single corner frequency determined by the resistor R_1 and the input capacitance C_T. Since the amplification shows a small drift the calibration is done at the start and at the end of a measurement series, and occasionally also at intervals during a series.

The junction is expected to be at the bath temperature of 4.2K. However, due to heating of the amplifiers and the direct connection of short wires between the junction and the amplifiers a slight increase in sample temperature cannot be excluded. By fitting the measured noise $S_m(V,T)$ as a function of bias at low bias we obtain a measure of the true junction temperature as 4.4 ± 0.2K.

Let us now consider the factors that influence the accuracy of the Fano factor. By the signal analysis procedure outlined in the previous section we eliminate the influence of many possible sources of inaccuracy: the uncertainty in amplifier current noise and voltage noise, cross talk of the amplifiers, uncertainty in the resistance R_1 and its noise temperature, and uncertainties in the junction temperature. We found that grounding of all electronics needs careful attention. Subtle ground loops are detected as a spurious rounding of the Fano plot at low applied bias, as a result of small ac induced currents at nominally zero bias. Many tests on Au atomic junctions confirm that we have effectively eliminated this problem, as illustrated in Fig. 4.5b. The main uncertainty in the Fano factor derives from spontaneous (or current-induced) changes in the sample resistance during the noise measurements. This problem is addressed by comparing the differential conductance measured at the start and at the end of the cycle. We typically impose a limit of 5% in difference between the two and discard all data with a larger change in conductance. The final accuracy in F is limited by the calibration of the amplification β (about 1%) and by random statistics in the noise signal due to the finite averaging time, limiting the absolute accuracy to about 0.01.

We can introduce a standard deviation as a measure of the statistical accuracy of our noise measurement.ă The statistical uncertainty in the noise spectra can be reduced either by measuring for a wider bandwidth or averaging longer. Due to the

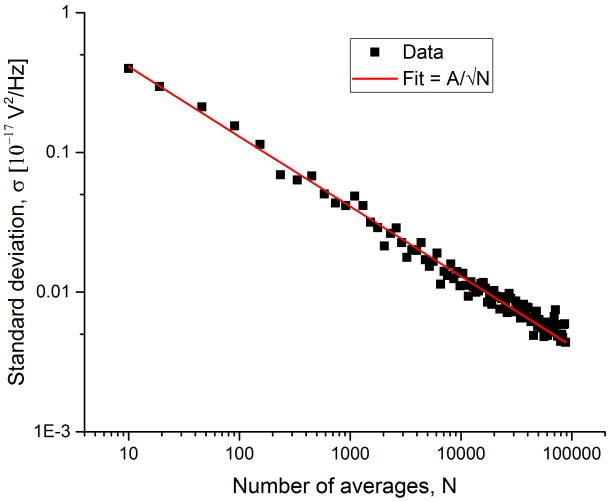


Figure 4.6: Plot of standard deviation of the measured noise over a fixed 10 kΩ resistor as a function of the number of noise spectra included in the averaging, N. A straight line fit (in red) shows a $1/\sqrt{N}$ relation pointing towards purely statistical character of noise, similar to what was shown by Di Carlo *et al*.[23].

fast acquisition provided by our FPGA system we can average 10000 spectra in about 85ms, which provides high accuracy. A plot of the standard deviation vs the number of spectra averaged is given in Figure 4.6, which is also a measure of the stability of the measurement.

The role of Joule heating in the sample and in the resistor R_1 was tested by placing a 10 kΩ resistor in the place of the sample and measuring the noise as a function of bias, as for atomic junctions. Since resistors have no shot noise any increase in noise detected can be attributed to Joule heating of the two resistors. It was necessary to increase the bias over the mock sample resistor up to 1 V in order to detect appreciable increase in noise. The noise increases approximately proportional to the square of the applied bias, as expected for Joule heating. This additional thermal noise remains well below 10^{-3} of the shot-noise signals measured here, even up to 1 V in bias.

4.5 Measurements on Au and Pt atomic contacts

The performance of the system was tested on the known noise properties of Au and Pt atomic contacts.[20,22] For many different junction settings noise spectra were recorded in a window from 122 kHz to 10 MHz, and for voltage bias values between 0 and 80 mV. An example of such series of spectra is given in Fig. 4.4(b) above, and the data was analyzed in terms of the excess noise and Fano factors as outlined above. The Fano factors obtained for the low-bias regime for over 200 Au and Pt atomic contacts are plotted against the conductance of the junctions in Fig. 4.7.

The solid black curve shows the absolute minimum for Fano factors for spin-

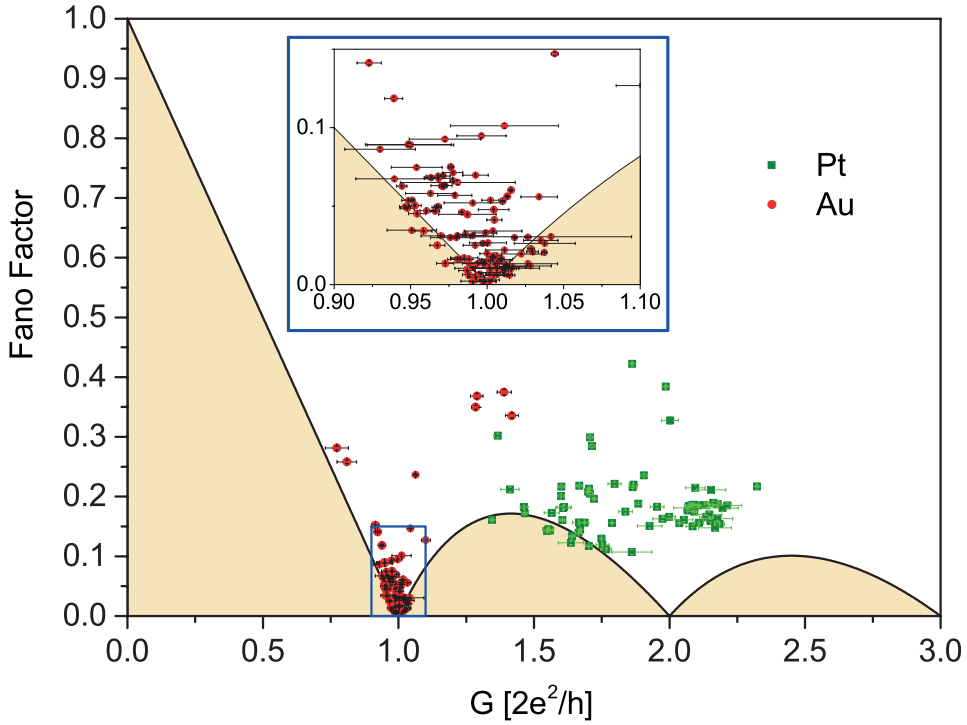


Figure 4.7: Fano factor plot for noise measurements on over 200 atomic configurations for Au and Pt. The Fano factors for all atomic contacts are above the theoretical limit of minimum Fano factor for a spin-degenerate Landauer conductor (full curve), within the accuracy of the measurements. The data cluster close to the boundary, indicating that a single partially transmitting channel frequently forms for such atomic contacts.

degenerate conductance channels. The curve forms the boundary for the shaded region below, that is inaccessible for non-magnetic junctions. For conductances at or below 1 G_0 the data for Au cluster close to the black curve, which is the expected dependence for a single conductance channel. Also, we observe a strong clustering of data near the sharp minimum in the Fano factor for conductance near 1 G_0. This is in agreement with the known properties for Au atomic junctions, which have a high probability to show a conductance near 1 G_0, and have a single conductance channel.[1,4,20]. The set of experimental data for Au form the most direct test of the experimental technique, and demonstrates the accuracy in G and F.

For comparison we also show data recorded for Pt atomic contacts. The data are much more scattered and are found at higher conductance, typically around 1.5 G_0, and higher Fano factors. Through participation of the d-orbitals Pt atomic contacts have access to five conductance channels, which may even have some spin splitting.[34] In agreement with previous measurements in the frequency window below 100 kHz[35] we find that all the data fall outside the region that is inaccessible

[34] Florian Strigl et al. In: *Nature communications* 6 (2015).

[35] Manohar Kumar et al. In: *Phys. Rev. B* 88 (2013), p. 245431.

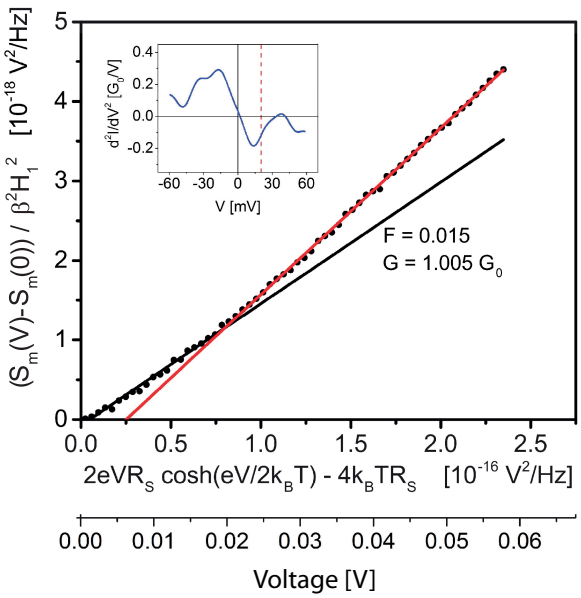


Figure 4.8: Excess noise as a function of the scaled bias voltage for a Au atomic chain, showing a characteristic kink attributed to inelastic scattering. The position of the kink lies close to the position of the vibration mode energy seen in the second derivative spectrum for the current, shown by the red broken line in the inset. The bottom scale in the main figure gives an approximate scale for the corresponding bias voltage.

for spin-degenerate systems, and there is some clustering at the boundary.

Figure 4.5 illustrates the fact that the present technique permits accurate measurements of shot noise to very high bias values. For the example given in the figure the inelastic scattering is weak (as also evidenced by the differential conductance spectrum in Fig. 4.4a) and we find that the excess noise is linear with the scaled bias parameter up to more than 70 mV. Interesting deviations from this purely ballistic electron transport are found for junctions with a stronger electron-vibron scattering amplitude. An example for Au atomic chains is given in Fig. 4.8, which shows a clear kink in the noise plot near the point where the peak in $\mathrm{d}^2I/\mathrm{d}V^2$ indicates the presence of a vibron excitation. Such inelastic scattering effects have been investigated in the low-bias regime for Au atomic chains in previous work,[10] which can now be extended by the present technique to molecular junctions with higher vibron mode energies.

The benefits of having access to the spectral information is further illustrated by the example for a Pt junction in Fig. 4.9. For bias voltage settings up to about 10 mV the noise remains white and the excess noise rises linearly with the scaled bias parameter, as expected. For higher bias the junction develops anomalous behavior, with giant deviations from the linear excess noise dependence. At the same time the appearance of the noise spectrum changes from the usual white spectrum into a spectrum with a pronounced rise towards lower frequencies. This spectral information assists in analyzing the source of this noise, which obviously is not just shot noise. Such

spectral shapes require processes with time scales that are long compared to typical atomic or electronic processes. We attribute the noise to two-level fluctuations, and in Chapter 6 we will show that by annealing the Pt-notched wire before breaking, we avoid this two-level fluctuation in the clean Pt junctions.

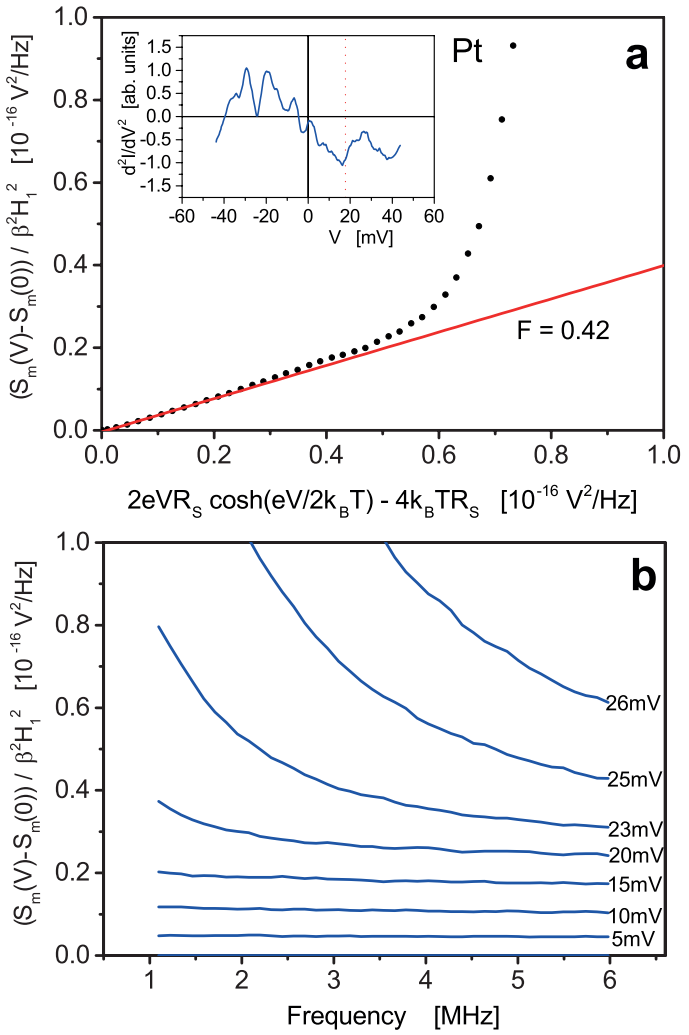


Figure 4.9: Example of a junction showing anomalous noise. (a) At low bias, up to about 7 mV, the excess noise is perfectly linear giving a Fano factor $F = 0.42$. At about 20 mV ($0.6 \cdot 10^{-16}$ in the reduced units) a very strong deviation develops. The differential conductance spectrum in the inset is suggestive of a vibron mode at this energy. (b) However, the freqency spectrum clearly shows that the noise is not white, and a very pronounced frequency dependence develops at higher bias.

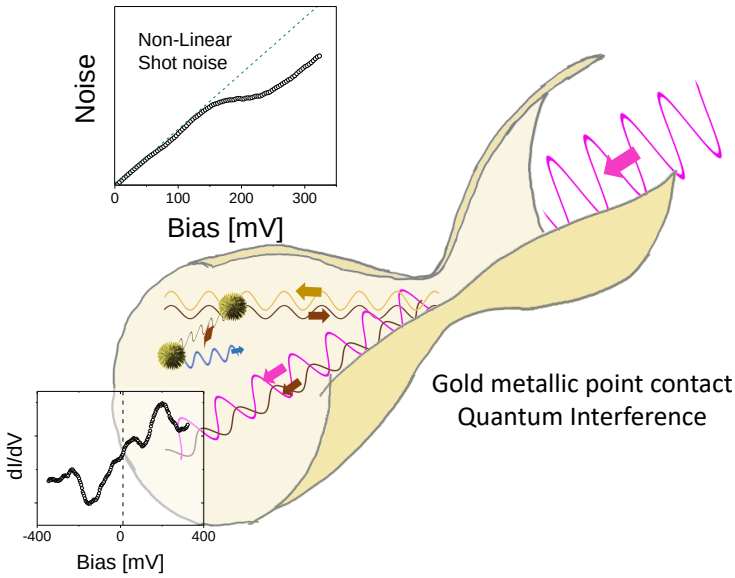
4.6 Conclusions

The benchmark method for shot-noise measurements on atomic contacts employs the cross spectrum of the signal from two sets of amplifiers in a frequency window up to 100 kHz. By introducing cryogenic amplifiers close to the atomic junction the input capacitance was reduced by nearly two orders of magnitude. The resulting wider frequency band allows us to measure spectra up to 10 MHz, which is necessary when $1/f$ noise is likely to interfere with the shot-noise signal, as expected to occur for molecular junctions and at higher voltage bias. Working at higher frequencies has the additional advantage that data acquisition and averaging of the spectra can be much faster. In order to profit from this advantage, the Fourier transform and other spectral manipulation is programmed on an FPGA module, such that the speed of measurement is only limited by data acquisition. The acquisition time scales with the inverse of the lowest frequency in the spectral window, and by shifting the spectral window for Fourier transform from 250 Hz–100 kHz to a window of 122 kHz–100 MHz the measurement time is reduced by a factor 500. The standard technique requires nearly a minute of signal averaging for each measurement of noise spectrum for a given junction and a given bias voltage. Since the Fano factor is obtained from the plot of noise for many bias setting, the measurement of the Fano factor for a junction takes many minutes. Detecting subtle deviations in the linear dependence of noise with bias[10] requires many bias points, and the total measurement time per junction setting may be as long as 30 minutes. The wide band technique introduced here reduces this measurement time to 3 – 4 seconds. This method may also find application in scanning tunneling microscopy experiments.[36]

Further improvements are possible. By redesign of the amplifier circuit board a further reduction of the input capacitance by a factor of three should be possible. However, a more significant increase in frequency can be obtained by adding an inductor in parallel to the junction.[23] For example, the present low-pass characteristics with a corner frequency of 1.5 MHz can be converted into a band-pass characteristics with a center frequency of 40 MHz for an inductor of 1 μH. This will be attractive when $1/f$ noise is still detectable near 1 MHz, and it will also permit further increasing the speed of measurement. We are preparing currently also a next version of this system for molecules with very high resistance (of the order of 100MΩ and higher). This system will also utilize a notched-wire break-junction for studying single-molecules due to its higher operation speed. We have demonstrated recently[37] that using a notched-wire break-junction can give exceptionally sharp conductance histogram peaks for an OPE3 molecule, which we attribute to precisely recurring molecular configurations. A summary of these results is given in the Appendix E.

[36] Andreas Burtzlaff et al. In: *Phys. Rev. Lett.* 114 (2015), p. 016602.
[37] Julian M. Bopp et al. In: *Low Temperature Physics* 43 (2017), p. 905.

Graphical Summary



5. Anomalous non-linear shot noise at high voltage bias

Since the work of Walter Schottky, it is known that the shot-noise power for a completely uncorrelated set of electrons increases linearly with the time averaged current. At zero temperature and in the absence of inelastic scattering the linearity relation between noise power and average current still holds even for correlated electrons. Through high-bias shot-noise measurements on single Au atom point contacts, we find that the noise power in the high-bias regime shows highly non-linear behavior even leading to a decrease in shot noise with voltage. We explain this non-linearity using a model based on quantum interference of electron waves with varying path difference due to scattering from randomly distributed defect sites in the leads, which makes the transmission probability for these electrons both energy and voltage dependent.

5.1 Introduction

It is known from the time Walter Schottky in 1918[1], that the noise power increases linearly with time averaged current $S_{\text{Poisson}} = 2e\langle I\rangle$. In mesoscopic devices, where the Pauli's exclusion principle introduces correlations among the electrons, the shot noise drops below this S_{Poisson} value[2]. This reduction has been measured experimentally both in 2DEG based point contacts[3,4] and metallic point contacts[5]. Even here, at zero temperature and in the absence of inelastic scattering, shot noise is known to increase linearly with average current (or applied bias), as given by the expression[6–8]

$$S_{\text{I}} = 2\frac{e^2}{h}\left\{4k_B\theta\sum_{n=1}^{N}T_n(E_{\text{F}})^2 + 2eV\coth(\frac{eV}{2k_{\text{B}}\theta})\sum_{n=1}^{N}T_n(E_{\text{F}})(1-T_n(E_{\text{F}}))\right\} \tag{5.1}$$

where θ is the temperature of the point contact and $T_n(E_{\text{F}})$ is the transmission probability of the n^{th} channel involved in the transport, measured at the Fermi energy E_{F} of the leads. Any deviation from this linearity relation has been attributed to interactions with other degrees of freedom, such as inelastic electron-phonon interaction[9], flicker noise, two level fluctuations[10], heating or non-equilibrium occupation of phonons[11]. The conductance of these point contacts is given by the celebrated Landauer's conductance formula[12], which describes conductance as directly proportional to the sum of the transmission probabilities of the channels involved ($G = 2e^2/h\sum T_n(E_{\text{F}})$). This sets an upper limit for the maximum conductance for a single channel taking part in transport, equal to the quantum of conductance ($G_0 = 2e^2/h$).

These properties for noise and differential conductance hold under quasi equilibrium or in the linear regime, where the transmission probability (T) of a channel is taken as constant, equal to its value at the Fermi energy (E_{F}). In general, the transmission probability of a channel can have both energy and voltage dependence $T(E,V)$. This could bring new pleasant surprises and could also upset current views based on the linear regime. Thanks to a newly developed setup[13] we are able to measure noise continuously as a function of bias, up to very high bias, where the T cannot be taken as constant and the energy and voltage dependence of T gives rise to highly non-linear behavior in shot noise. The non-linearity of shot noise with applied bias can be so strong that it can even lead to negative differential shot noise (NDSN). To understand these non-linearities we use a model based on quantum interference of

[1] W. Schottky. In: *Annalen der Physik* 362 (1918), p. 541.
[2] G. B. Lesovik. In: *JETP Lett.* 49 (1989), p. 592.
[3] M. Reznikov et al. In: *Phys. Rev. Lett.* 75 (1995), p. 3340.
[4] A. Kumar et al. In: *Phys. Rev. Lett.* 76 (1996), p. 2778.
[5] H. E. van den Brom and J. M. van Ruitenbeek. In: *Phys. Rev. Lett.* 82 (1999), p. 1526.
[6] C. W. J. Beenakker and H. van Houten. In: *Phys. Rev. B* 43 (1991), p. 12066.
[7] Th. Martin and R. Landauer. In: *Phys. Rev. B* 45 (1992), p. 1742.
[8] M. Büttiker. In: *Phys. Rev. B* 46 (1992), p. 12485.
[9] Manohar Kumar et al. In: *Phys. Rev. Lett.* 108 (2012), p. 146602.
[10] Ruoyu Chen et al. In: *Phys. Rev. B* 85 (2012), p. 235455.
[11] D. F. Urban et al. In: *Phys. Rev. B* 82 (2010), p. 121414.
[12] R. Landauer. In: *IBM Journal of Research and Development* 32 (1988), p. 306.
[13] Sumit Tewari et al. In: *Review of Scientific Instruments* 88 (2017), p. 093903.

electron waves which take varying paths while being scattered from randomly distributed defect sites in the leads in combination with the usual scattering at the point contact. This quantum interference model leads to energy and voltage dependence of T and explains various types of experimental noise measurements recorded at high bias.

5.2 Measurement setup

High-bias shot-noise measurements are challenging as 1/f noise or flicker noise increases with the square of the applied bias and so at high bias one is likely to be confronted with a large 1/f noise background over the desired shot noise. This forces us to perform measurements at high frequencies where the 1/f noise decreases. We have developed a new high-frequency shot-noise measurement setup described in chapter 4, which can measure noise in the MHz frequency range and can record the spectral information. This spectral information can be recorded with high speed up to 12 spectra/s. This system is connected to a mechanically controlled break junction setup to study shot noise in metallic point contacts and single-molecule junctions with a high mechanical stability. A schematic of the setup is shown in Figure 5.1.

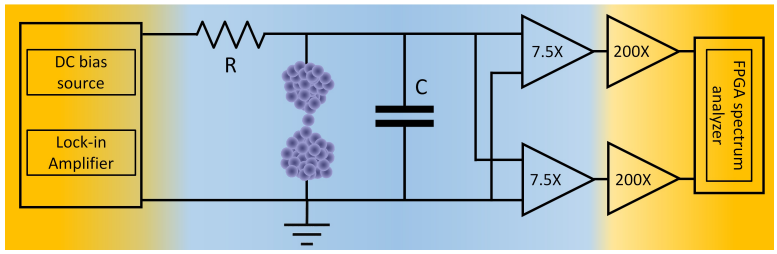
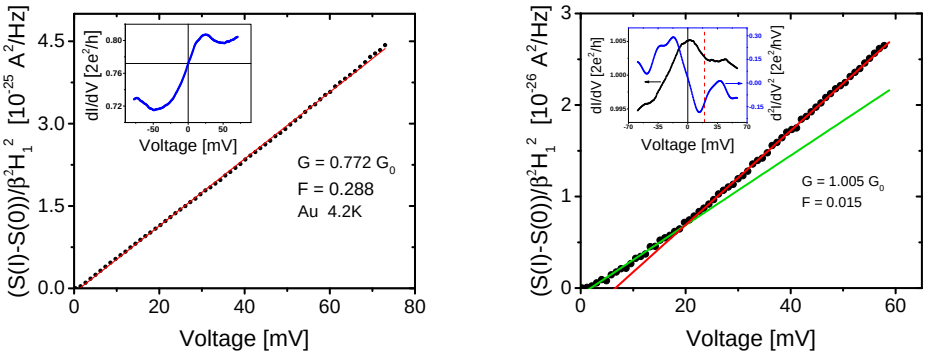


Figure 5.1: Schematic of the experimental setup. The color gradient shows qualitatively the operating temperature from 300 K (orange) to 4.2 K (blue). The setup consists of a cryogenic (7.5X) and room temperature amplifier (200X) together giving 1500 times amplification. The decoupling resistor R is 10 kΩ and the total stray input capacitance at the cryogenic amplifier is around 14 pF.

5.3 Shot-noise measurements

Ballistic single atom point contacts formed between metallic leads have been an important playground to study electronic transport in nano-structures. Both conductance and shot-noise measurements of these contacts have led researchers to understand interesting atomic-scale physics. We start by showing the low-bias shot-noise data, where the usual linear-regime behavior is expected. Figure 5.2(a) shows the linearly increasing shot-noise power as we ramp the voltage bias over a metallic point contact. Depending on the strength of the electron-vibron coupling, the electrons could also pass through the contact by inelastically exciting a vibration mode of atoms forming the junction. This opens an additional inelastic channel for the electron transport over the existing elastic channel. This is known to give a kink in the linearly increasing shot-noise power, as shown for a short chain of Au atoms in Figure 5.2 (b) and is also described in previous work by Kumar et al[9].



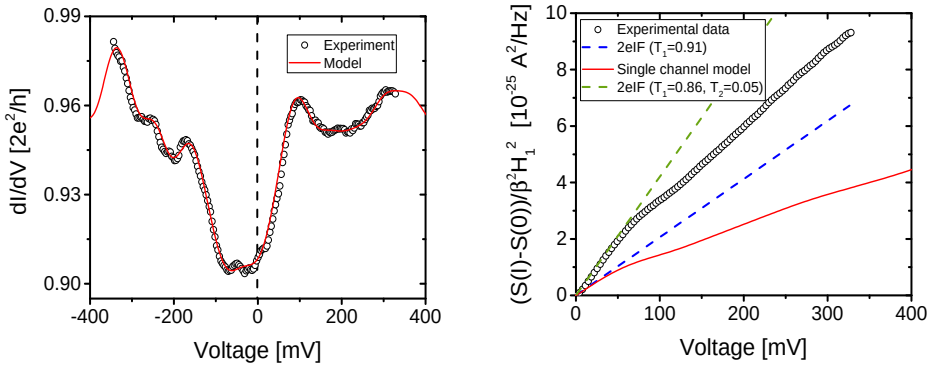
(a) (b)

Figure 5.2: (a) Linearly increasing shot noise with the applied bias over the Au point contact with inset showing the corresponding differential conductance of the contact, (b) Kink in shot noise due to electron phonon interaction close to the vibration mode in Au atomic chain at around 20 meV as seen in the $\mathrm{d}^2I/\mathrm{d}V^2$ shown in the inset

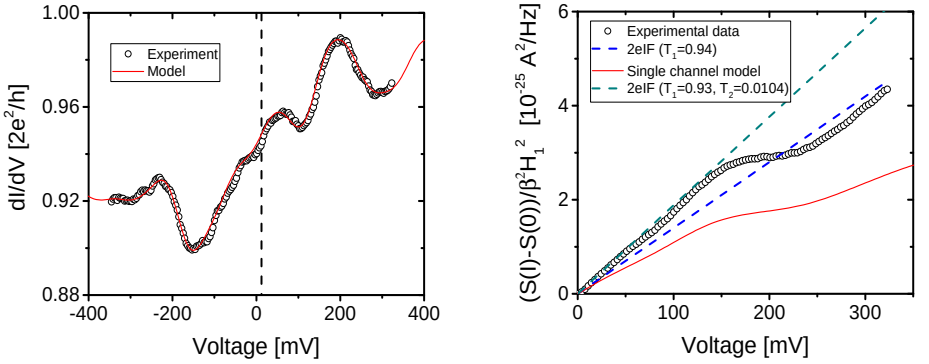
The results shown in Figure 5.2 is what we expect for the linear regime where the transmission is almost constant. But when we go to higher bias and the transmission is close to 1, the shot noise measured over single Au atom point contact shows highly non-linear behavior. A collection of three different examples which we will examine here is shown in Figure 5.3. These point contacts are formed using mechanically controlled break junctions. Differential conductance measurements are performed before and after the noise measurements to verify the stability of the contact. Figure 5.3 shows differential conductance (left) and excess shot noise (S(I)-S(0)) measured (right) for the three cases.

Selected examples shown in Figure 5.3 have differential conductance spectra that are quite different from each other. In example 1 the differential conductance is fairly symmetric and the measured noise (shown with circular points in the right panel of Ex 1) increases linearly at low bias and then it has a kink around 60 mV followed by a further increase up to 325 mV. This kink can not be due to electron-phonon interaction because the Debey energy for Au is around 20 mV. In example 2, the differential conductance is almost anti-symmetric about zero bias and the noise shown in column (b) of Ex 2 shows a different type of non-linearity. Here the noise has a staircase like structure, where the noise stagnates at the middle and rises again. Example 3 has a very strong asymmetry in the differential conductance of the contact accompanied by even stronger non-linearity in the shot noise, showing even a negative differential shot noise i.e., a decrease of shot noise with bias. Here the noise is measured up to 800 mV which is much higher than any previous shot-noise measurement done[14,15] over metallic point contacts. At these high-bias levels one would expect the noise measurement to become affected by 1/f noise and two-

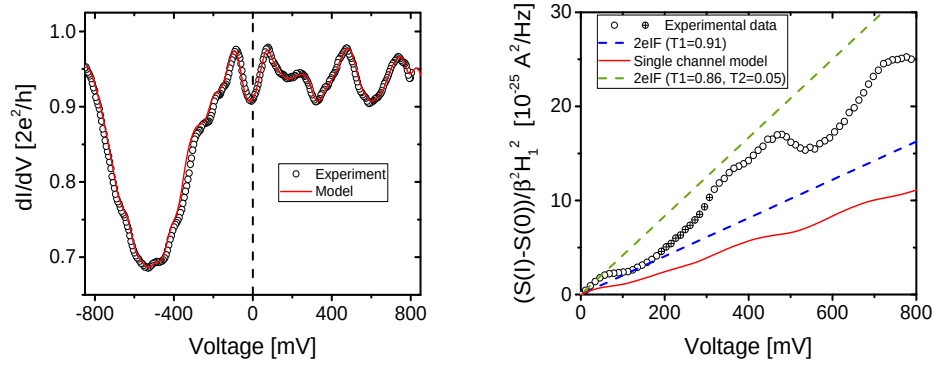
[14] Ruoyu Chen et al. In: *Scientific reports* 4 (2014), p. 4221.
[15] Ruoyu Chen and D. Natelson. In: *Nanotechnology* 27 (2016), p. 245201.



(a) Example 1: Differential conductance (left) with excess shot noise (right).



(b) Example 2: Differential conductance (left) with excess shot noise (right).



(c) Example 3: Differential conductance (left) with excess shot noise (right).

Figure 5.3: Non-linear shot-noise data: We show here three example (a),(b) and (c) of high-bias shot-noise data. The left graph in each panel shows the differential conductance of the three contacts measured and the right graph shows the corresponding shot-noise data. The experimental data is shown with black circles while the modeled $\mathrm{d}I/\mathrm{d}V$ or noise is shown by red solid curves. The points for which the noise spectra show non-white character are shown with filled circles.

level fluctuations (TLF). Thanks to our FPGA based spectrum analyzer for the noise, we can clarify this and identify any non-white occurrences (where we maintain a threshold of more than 5% deviation from the mean) in our data. This helps us in ensuring that these other noise sources are not the cause of the non-linearity in shot noise measured at high bias. Important to point out is that previous high-bias shot-noise measurements do not provide access to a spectrum to confirm the white noise character. In the noise plot of Figure 5.3 (c), there were some points with a small non-white contribution to the spectra at intermediate bias, for which the white noise part is extracted and the points are shown by filled circles in the plot. The occurrence of non-white character is attributed to two level fluctuations as explained elsewhere[13]. In the next part we will discuss the interpretation we propose for the non-linear noise based on quantum interference of electronic waves. A discussion on other possible sources of non-linearity and stability of atomic junctions at such high bias is given at the end of this chapter.

5.4 Quantum interference model

A symmetric differential conductance for positive and negative bias, could be expected for a simple point contact studied extensively in quantum transport measurements. However, experiments show that such point contacts can have very commonly a non-symmetric differential conductance. This asymmetry can be attributed to voltage dependence of transmission as will be explained below based on the Landauer formalism. Quantum interference (QI) of electronic waves due to scattering from defect sites (close to the point contact) can make the transmission voltage dependent. It is known[16–18] that such QI in the leads causes strong oscillations in the differential conductance and when the point contact transmission is near unity these oscillations become strongly suppressed. A schematic explaining this QI due to defect scattering is shown in Figure 5.4 (a). In the schematic the point contact is shown as a slit in a screen separating the two conductors left and right. Incoming electronic plane waves are shown as blue color wave-fronts. The defects are placed only on the right side of the point contact (or slit) for simplicity. The schematic shows that the electronic waves travel an additional path length on reflecting from the defect as compared to the directly transmitted wave. This creates a phase difference and the two parts of the electronic wave interfere with each other, forming constructive or destructive contributions to the current signal, depending on the position of the defects and energy of incoming beam. Compared to the analysis by[16,17] our approach differs in two important aspects: (1) We are not interested in ensemble averages but in the effects of individual defects. (2) We will be interested in the large voltage bias regime, beyond lowest-order corrections to the conductance and noise.

The first case that is considered is of a single defect at the right side of the contact where the electrons arrive after being accelerated at the contact, and add the other case later. Scattering on this defect leads to an interference term in the transmission probability. For an electron that starts from the negative-bias side with initial energy

[16] B. Ludoph et al. In: *Phys. Rev. Lett.* 82 (1999), p. 1530.
[17] B. Ludoph and J M van Ruitenbeek. In: *Physical Review B* 61 (2000), p. 2273.
[18] C. Untiedt et al. In: *Phys. Rev. B* 62 (2000), p. 9962.

E the transmission takes the form,

$$T(E,V) = T_0 + a\sin\left(2k(E,V)L + \phi\right), \tag{5.2}$$

where T_0 is the transmission that is mainly determined by the properties of the atomic contact itself, here taken to be energy and voltage independent. The amplitude a depends on the distance of the defect and the scattering probability. This amplitude decreases with the distance L between the defect and the contact as L^{-4}, as result of the solid angle under which the defect is seen from the contact and, after scattering on the return path, the solid angle under which the contact is seen from the defect position. Along its path the scattering partial wave accumulates a phase $2k(E,V)L$ with respect to the partial wave that is directly transmitted, plus a constant phase ϕ is added[18], which depends on the details of the scattering process. This makes the total transmission both energy and voltage dependent $T(E,V)$.

The wavenumber $k(E,V)$ depends on the total energy (E) of the incoming electron and the voltage drop (V) experienced at the point contact. Due to the acceleration of the electron at the contact site the wave-number of electrons after the contact will be,

$$k(E,V) = \frac{\sqrt{2m(E+eV/2)}}{\hbar} \tag{5.3}$$

So, for multiple defects the transmission takes the form:

$$T(E,V) = T_0 + \sum_{p=0}^{N_d} a_p \sin\left(2L_p \frac{\sqrt{2m(E+eV/2)}}{\hbar} + \phi_p\right) = T(E+eV/2) = T(\zeta) \tag{5.4}$$

where N_d is the number of defect sites. As the energy (E) and applied bias (V) enter in the above transmission picture only in the combination $E+eV/2$, we can write the total transmission as a function of a single variable: $\zeta = E + eV/2$. The above total transmission is written for a single channel; for multiple channels one has to use a second index n with transmission of n^{th} channel as $T_n(\zeta)$. As the transmission enters as $T(1-T)$, this energy and voltage dependent transmission could cause strong non-linearities in the shot noise. Before going ahead we discuss the assumptions made in the model. (1) We will assume for simplicity that only a single channel is taking part in transport. (2) We assume zero temperature, which helps us in getting rid of the Fermi functions from the integrals shown in the later part. This is a reasonable assumption as the experiments shown here are done at liquid helium temperatures, and we work in the regime $eV \gg k_B T$. (3) We assume that all the voltage drops over the point contact and not over the defects. (4) We leave out any intrinsic energy dependence of the transmission for the metallic point contacts[19]. (5) We take the waves to be reflected only once from the defect sites. More than one reflection will reduce the amplitude of the wave significantly. (6) We assume the transmission is entirely described by elastic processes. Inelastic scattering on vibration modes of the contact are briefly discussed below.

Under these assumptions the total transmission of the system can be taken as given in equation 5.4 due to QI of electronic waves. Because this transmission is both

[19] Mads Brandbyge et al. In: *Phys. Rev. B* 60 (1999), p. 17064.

energy and voltage dependent, we have to use the generalized non-linear Landauer's expression for time averaged current $\langle I \rangle (V)$ and noise $S_I(V)$ for spin degenerate systems[6–8,20,21].

$$\langle I \rangle (V) = 2\frac{e}{h} \sum_{n=1}^{N} \int_{-\infty}^{+\infty} \mathrm{d}E\, T_n(E,V)[f_L - f_R] \tag{5.5}$$

$$\begin{aligned} S_I = 4\frac{e^2}{h} \sum_{n=1}^{N} \int_{-\infty}^{+\infty} \mathrm{d}E \{ & T_n(E,V)[f_L(1-f_L) + f_R(1-f_R)] \\ & + T_n(E,V)(1-T_n(E,V))[f_L - f_R]^2 \} \end{aligned} \tag{5.6}$$

As we make the assumption that the approximation of zero temperature the Fermi functions f_L and f_R can be taken as Heaviside functions. On using the Leibniz integration rule one can write an expression for the differential conductance G_{diff} or $\frac{\mathrm{d}\langle I \rangle}{\mathrm{d}V}$[22,23] starting from equation 5.5,

$$\frac{\mathrm{d}\langle I \rangle}{\mathrm{d}V} = 2\frac{e}{h} \sum_{n=1}^{N} \left\{ \frac{e}{2} T_n(E_F + \frac{eV}{2}, V) + \frac{e}{2} T_n(E_F - \frac{eV}{2}, V) + \int_{E_F - \frac{eV}{2}}^{E_F + \frac{eV}{2}} \frac{\partial T_n(E,V)}{\partial V} \mathrm{d}E \right\} \tag{5.7}$$

which for a single channel becomes:

$$= 2\frac{e^2}{h} \left\{ \frac{T_H + T_L}{2} + \frac{1}{e} \int_{E_F - \frac{eV}{2}}^{E_F + \frac{eV}{2}} \frac{\partial T}{\partial V} \mathrm{d}E \right\} \tag{5.8}$$

where, $T_H = T(E_F + \frac{eV}{2}, V) = T(E_F + eV)$ and $T_L = T(E_F - \frac{eV}{2}, V) = T(E_F)$. The meaning of T_H and T_L is explained in the Figure 5.4 (b). Here a simple model curve $T(\zeta)$ for a single channel taking only one sine term in equation 5.4 is plotted against energy ζ. As a bias voltage is applied, an energy window of width eV centered at $E_F + eV/2$ is opened. T_H and T_L are the values of the transmission at the 'High' and 'Low' side of the window as shown in the Figure 5.4(b). If there is no voltage dependence of the transmission (i.e., $\frac{\partial T}{\partial V} = 0$), then only the width of the energy window changes but the center will stay at $\zeta - E_F = 0$ and the total conductance will be an arithmetic mean of the T_H and T_L. Moreover, for the case of only energy dependence, one needs to know the $T(E)$ over a window of size eV from $E_F - eV/2$ to $E_F + eV/2$. On the contrary, for the case of both energy and voltage dependence, transmission has to be known over a window of width 2 eV from $\zeta = -eV$ to $\zeta = +eV$ to know the complete differential conductance and shot noise from negative to positive bias. Further, it is important to note that if the transmission is constant or only energy dependent, then from equation 5.7, the $\mathrm{d}I/\mathrm{d}V$ will be symmetric

[20] Nicolás Agraït et al. In: *Physics Reports* 377 (2003), p. 81.
[21] Juan Carlos Cuevas and Elke Scheer. Molecular electronics : an introduction to theory and experiment. New Jersey [u.a.] : World Scientific, 2010.
[22] Eleuterio Castao and George Kirczenow. In: *Phys. Rev. B* 41 (1990), p. 3874.
[23] Gaibo Zhang et al. In: *Journal of Physical Chemistry C* 119 (2015), p. 6254.

for the positive and negative bias. Any asymmetry in $\mathrm{d}I/\mathrm{d}V$ is arising from the voltage dependence of the transmission. The asymmetry in $\mathrm{d}I/\mathrm{d}V$ is also attributed to asymmetric potential drop between the left and right reservoir[24], which could be due to potential drop over defects which are randomly placed.

Because the last term in the expression for the differential conductance given in equation 5.8 is an integration over only energy (E), we can write $\frac{\partial T}{\partial V}\mathrm{d}E = \frac{\mathrm{d}T}{\mathrm{d}\zeta}\frac{\partial \zeta}{\partial V}\mathrm{d}\zeta = \frac{1}{2}e\mathrm{d}T(\zeta)$.

$$\Rightarrow \int_{E_\mathrm{F}-\frac{eV}{2}}^{E_\mathrm{F}+\frac{eV}{2}} \frac{\partial T}{\partial V}\mathrm{d}E = \frac{1}{2}e\int_{E_\mathrm{F}}^{E_\mathrm{F}+eV}\mathrm{d}T(\zeta) = \frac{1}{2}e(T_\mathrm{H}-T_\mathrm{L}) \tag{5.9}$$

From equation 5.8 the differential conductance can be written as:

$$\Rightarrow \frac{\mathrm{d}\langle I\rangle}{\mathrm{d}V} = 2\frac{e^2}{h}\left\{\frac{T_\mathrm{H}+T_\mathrm{L}}{2}+\frac{T_\mathrm{H}-T_\mathrm{L}}{2}\right\} = 2\frac{e^2}{h}T_\mathrm{H} \tag{5.10}$$

If we include scattering over defects present both before (left) and after (right) the point contact, the expression for differential conductance over all defects will be:

$$\begin{aligned}\frac{\mathrm{d}\langle I\rangle}{\mathrm{d}V} = \frac{2e^2}{h}\Bigg[T_0 &+ \sum_{p=0}^{N_r} a_p \sin\left(2L_p\frac{\sqrt{2m(E_\mathrm{F}+eV)}}{\hbar}+\phi_p\right)\\ &+ \sum_{q=0}^{N_l} a_q \sin\left(2L_q\frac{\sqrt{2m(E_\mathrm{F}-eV)}}{\hbar}+\phi_q\right)\Bigg]\end{aligned} \tag{5.11}$$

Where N_l and N_r are the numbers of defects on the left and right of the point contact, respectively. As long as $eV \ll E_\mathrm{F}$ the sine terms in the summation for the left and right defects have the same dependence on V, so a defect sitting on the left will give the same frequency dependence (within a constant phase factor) as a defect at the same radial distance on the right. In our model we will use the expression with defects sitting only on one side of the point contact. As we are interested in studying non-linear shot noise, we want to also derive an expression for differential shot noise $\frac{\mathrm{d}S_\mathrm{I}}{\mathrm{d}V}$. We define a function $Z(E,V) = T(E,V)(1-T(E,V))$ and making again the zero temperature and single channel assumption, we rewrite equation 5.6 as :

$$S_\mathrm{I} = 4\frac{e^2}{h}\int_{E_\mathrm{F}-\frac{eV}{2}}^{E_\mathrm{F}+\frac{eV}{2}}\mathrm{d}E\,\{T(E,V)(1-T(E,V))\} = 4\frac{e^2}{h}\int_{E_\mathrm{F}-\frac{eV}{2}}^{E_\mathrm{F}+\frac{eV}{2}} Z(E,V)\mathrm{d}E \tag{5.12}$$

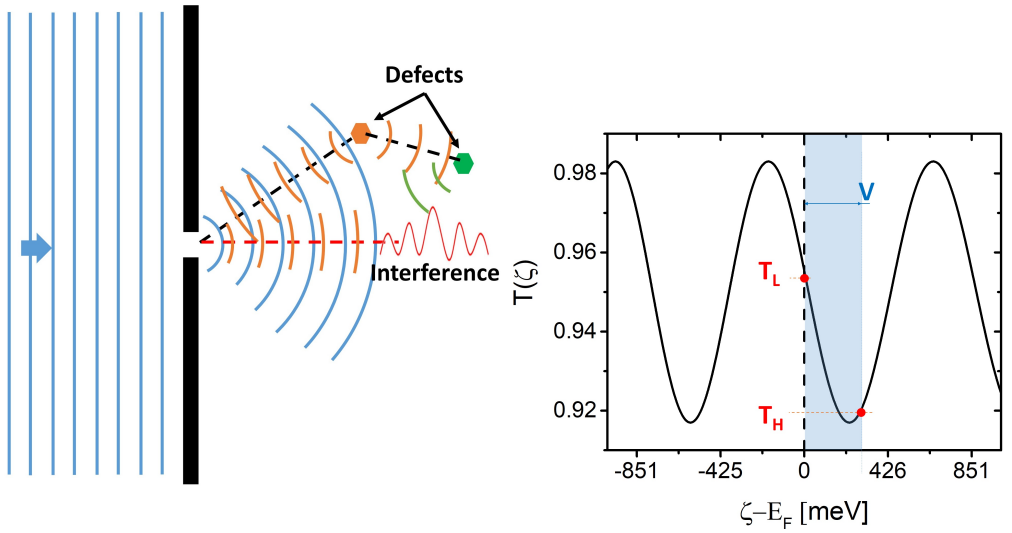
This expression for noise has the same form as the equation 5.5 for current. Without the need for repeating the exercise we did above for differential conductance we can immediately write the differential shot noise as:

$$\frac{\mathrm{d}S_\mathrm{I}}{\mathrm{d}V} = 4\frac{e^3}{h}Z_\mathrm{H} = 4\frac{e^3}{h}T_\mathrm{H}(1-T_\mathrm{H}) \tag{5.13}$$

[24] A. García-Martín et al. In: *Phys. Rev. B* 62 (2000), p. 11139.

It is important to note the difference between the above expressions for conductance and noise with those for the low-bias linear regime, where we assume constant transmission. In the linear regime, the differential conductance is given by the Landauer formula i. e. $G(E_F) = 2\frac{e^2}{h}T(E_F)$ and shot noise is given by $S_I = 2eIF = 2eVG(E_F)F$ with the Fano factor $F = 1 - T(E_F)$. This gives the noise for the linear regime constant transmission case as $S_I = 4\frac{e^3}{h}VT(E_F)(1 - T(E_F))$, which, of course, gives a linear increase in noise with bias, with complete suppression of noise at transmission close to $T(E_F) = 0$ and 1. In the quantum interference picture for the non-linear regime, the differential conductance (equation 5.10) has close similarity with the linear regime formula, with the difference that now the transmission should be evaluated at the high-bias end of the energy window. The expression for shot noise is however quite different. Equation 5.13 shows the expression for $\frac{dS_I}{dV}$ and not S_I. So, here as the transmission will go to 1, the noise is not going to be zero, but rather the slope of the noise will be zero and we will see a plateau appearing in the noise curve.

We would like to stress that the subtle similarities with the linear regime expressions for noise and differential conductance are only valid in the special case of single-channel quantum interference. To be more precise, they are valid in the case where the non-linear transmission is of the form $T(E, V) = T(E + eV/2)$. In a later section 5.5, we analyze a transmission of more general form $T(\alpha E + \gamma eV)$ and we have studied mathematically its effects on shot noise and differential conductance.

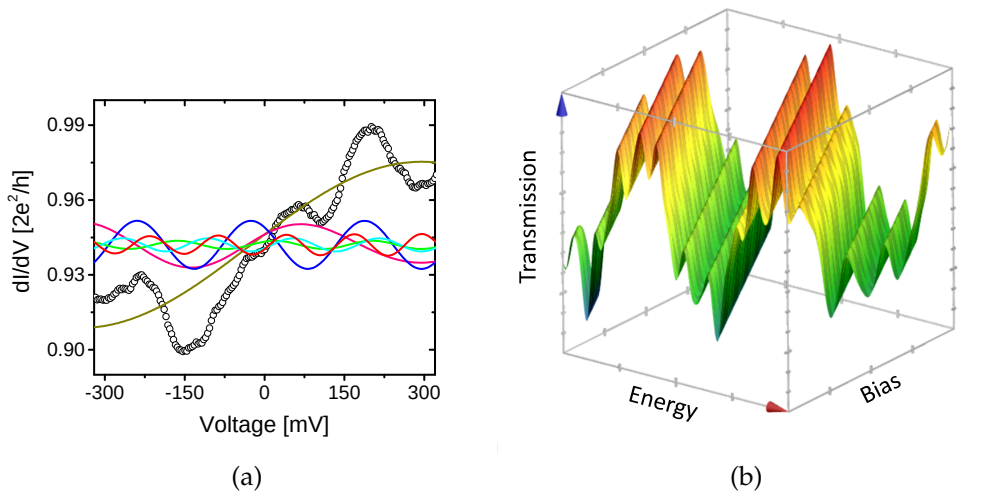


(a) (b)

Figure 5.4: (a) Model based on quantum interference of electronic waves due to scattering from defects in the leads. The point contact is represented as a single slit with defects only shown on the right side. Multiple reflections as shown for the green defect are not taken into account (b) Example of a model transmission for a single defect shown to explain the meaning of T_H and T_L.

5.4.1 Extraction of the voltage and energy dependent transmission

For the single channel quantum interference model, we can calculate back the transmission function given in equation 5.4. For comparing with the experimental differential conductance data we need to include more than just a single sine term in the sum in equation 5.4. For obtaining the unknown variables (a_p, L_p, ϕ_p) from experimental data we extract the different Fourier components constituting the measured differential conductance, an example is shown in Figure 5.5 (a). Next, by using one sine term at a time in T(E,V) (equation 5.4) we calculate the differential conductance from the model and match it with one of the Fourier components of the measured data. From this match we obtain the values of a_p, L_p and ϕ_p. The more Fourier components we use the more sine terms in the sum in the expression for T(E,V) we could compute. Once we have obtained the set of a_p, L_p and ϕ_p values we combine the sine terms from which we can calculate the complete T(E,V) surface shown in Figure 5.5 (b).



(a) (b)

Figure 5.5: (a) First 6 harmonics of the differential conductance associated to nearest six defects. (b) Complete T(E,V) surface extracted from the experimental data within the single channel quantum interference picture.

The complete function T(E,V) permits calculating also other properties, and specifically the shot noise for the same contact. However, by virtue of the analysis given above we can follow a simpler procedure.

5.4.2 Analysis of the experimental data

We start by taking a single-channel linear-regime assumption and show the noise ($S_I = 2eI(1-T)$) with the blue dashed lines for all the three examples in Figure 5.3, where we have obtained the transmission from the measured differential conductance ($T = G[G_0]$) at zero bias for the three data sets. From here we see that the experimental data suggest the presence of a second channel whose transmission at zero bias can be extracted by fitting the measured noise data with a straight line at low bias (see

Appendix C.2). This is shown by the green dashed lines in Figure 5.3 for the three examples and the extracted zero-bias transmission for the second channel (T_2) is also mentioned. Although, we know from this that the three examples we study here are not correctly described by just a single channel, we will first try to use our simple single channel model to understand the measured non-linearity in the shot noise.

Using equation 5.10, we can write $T_{\mathrm{H}} = \frac{h}{2e^2}\mathrm{d}I/\mathrm{d}V = G[G_0]$. This, $G[G_0]$ is the differential conductance in units of $G_0 = 2\frac{e^2}{h}$ and we measure this in experiments. From here we can rewrite equation 5.13 for the differential shot noise as:

$$\frac{\mathrm{d}S_{\mathrm{I}}}{\mathrm{d}V} = 4\frac{e^3}{h}G(1-G) \tag{5.14}$$

Next, we input the experimentally measured conductance values in equation 5.14 and integrate it over the whole bias range. The modeled noise thus obtained is shown with solid red curves in Figure 5.3 in the three examples. In all three examples, the noise reproduces qualitatively the non-linearities in the experimental data. This is a surprisingly good match considering the assumptions made in the model.

In example 1 and 2, the model explains the kink and the step structure arising in the noise as an intrinsic property of the contact depending on the position of the defect sites. In example 3 also the modeled noise explains the occurrence of rather complicated non-linearity in the measured shot noise, although the decrease of shot noise with voltage bias observed in the experiments cannot be reproduced. This can also be seen from the expression of $\mathrm{d}S_{\mathrm{I}}/\mathrm{d}V$ shown in equation 5.13, which shows that the $\mathrm{d}S_{\mathrm{I}}/\mathrm{d}V$ can never be negative for the current choice of T(E,V). Important to note is that our model is purely elastic, there are no inelastic effects included and no free parameters used for tweaking the shape of the modeled noise. We are showing here that pure elastic scattering can give large non-linearities in shot noise and we can measure these precisely in our experiments.

The quantitative mismatch and fact that our model does not follow the strong non-linearities such as the negative differential shot noise observed in the experiments could be attributed to two main reasons. (1) The inelastic effects: these are not included in our simple model, but they must be playing a role at such high bias. We know for contacts with conductance close to 1 G_0, the conductance decreases due to inelastic backscattering of electrons. Such effects are not included in the model. (2) The intrinsic energy dependence of the transmission of the point contact itself is ignored (T_0 is taken to be constant in equation 5.4). In reality T_0 can be dependent on both energy and voltage as can be seen in the article by Brandbyge *et al*.[19]. (3) As the transmission enters in the form $T(1-T)$ in the shot noise, which makes the noise for a channel with T close to 1 very small and even a small contribution from a second channel with transmission close to zero could become comparable, which is not included in our model. Simply adding a constant second channel will add to the noise but will also smooth out the non-linearities in our model (see Appendix C.2). Ideally, we need to include the second channel effect in the quantum interference model, but this goes at the expense of adding many free parameters.

For a complete match one has to find the complete expression for $T(E,V)$ including the inelastic effects, which is not trivial to extract from just shot noise and differential conductance data and further analysis awaits input from theory.

5.5 More general energy and voltage dependent transmission functions

As a formal exercise we discuss a more generalized expression for $T(E,V)$ where we take $T(E,V) = T(\alpha E + \gamma eV) = T(E + \beta eV)$ as opposed to $T(E + eV/2)$ coming from the QI picture. We show here that , despite the fact that the transmission is bounded in the range [0,1] and is a smooth function, it can lead to situations where the shot noise decrease with bias and differential conductance for a single channel becomes larger than 1 or smaller than 0. Note that at this point we do not attempt to associate the values for β with specific physical processes (other than for $\beta = \pm\frac{1}{2}$). Negative differential conductance has been long known, for example in two-dimensional electron gas (2DEG)[25], which results from QI, same as for the differential conductance of our atomic contacts. However, conductance of a single channel larger that 1 (super-Landauer single channel, SLSC) has not been known nor has a decrease of shot noise with bias or negative differential shot noise (NDSN) in ballistic point contacts as shown in Fig 5.3 (c).

Again we start by writing the function T(E,V) in terms of a single variable $\zeta = E + \beta eV$. Next, $\frac{\partial T}{\partial V}$ can be written as :

$$\frac{\partial T}{\partial V} = \frac{\partial T}{\partial \zeta}\frac{\partial \zeta}{\partial V} = \beta e \frac{\partial T}{\partial \zeta} \tag{5.15}$$

From here we can write an expression for the differential conductance,

$$\frac{\mathrm{d}\langle I\rangle}{\mathrm{d}V} = \frac{2e^2}{h}\left\{\tfrac{1}{2}(T_\mathrm{H} + T_\mathrm{L}) + \beta(T_\mathrm{H} - T_\mathrm{L})\right\} = \frac{e^2}{h}\left[(2\beta+1)T_\mathrm{H} - (2\beta-1)T_\mathrm{L}\right] \tag{5.16}$$

Moreover, from equation 5.12 we know that the time averaged current $\langle I\rangle(V)$ and $S_\mathrm{I}(V)$ share the same functional form, so without redoing the above calculation, we can write the form for differential shot noise $\mathrm{d}S_\mathrm{I}/\mathrm{d}V$ as:

$$\frac{\mathrm{d}S_\mathrm{I}}{\mathrm{d}V} = \frac{2e^3}{h}\left[(2\beta+1)Z_\mathrm{H} - (2\beta-1)Z_\mathrm{L}\right] \tag{5.17}$$

where, $Z_\mathrm{H} = T_\mathrm{H}(1 - T_\mathrm{H})$ and $Z_\mathrm{L} = T_\mathrm{L}(1 - T_\mathrm{L})$.

The main properties of the above equations are summarized in Figure 5.6 (a). When $T_\mathrm{H} < \frac{2\beta-1}{2\beta+1}T_\mathrm{L}$ then the single transmission channel shows negative differential conductance (NDC). This condition is shown as the blue triangular region on the left. When $(2\beta+1)T_\mathrm{H} - (2\beta-1)T_\mathrm{L} > 2$ the single transmission channel will have conductance larger than 1 G_0. This upsets the existing notion (correct in the linear regime) that a single channel can have at maximum one quantum of conductance. In the non-linear regime for transmission of the form $T(E + \beta eV)$ discussed here, equation 5.16 shows that the maximum conductance for the single channel can be as large as 1.5 G_0. We call this state super Landauer single channel (SLSC) and it is shown in Figure 5.6 (a) as the blue shaded triangular region on the right. From the relation of differential shot noise (equation 5.17) one can see that for $(2\beta+1)Z_\mathrm{H} < (2\beta-1)Z_\mathrm{L}$ the shot noise will decrease with increase in bias and we enter a regime called negative differential shot noise (NDSN). This is shown as the red shaded region

[25] R. J. Brown et al. In: *Journal of Physics: Condensed Matter* 1 (1989), p. 6285.

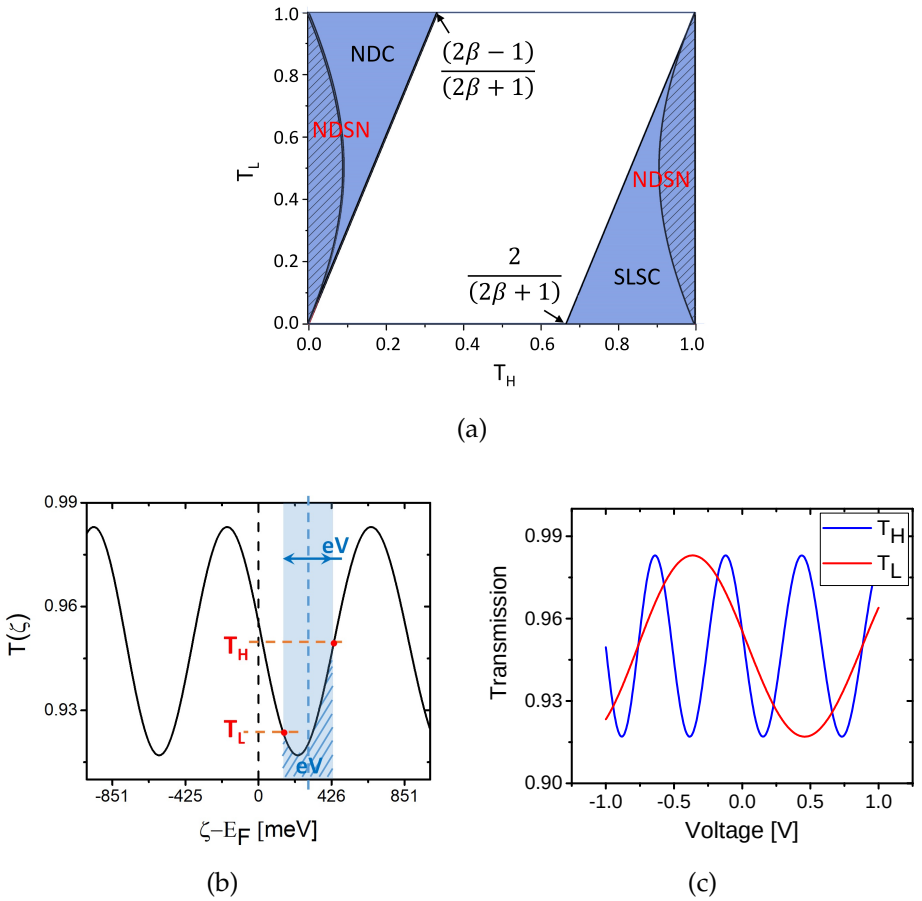
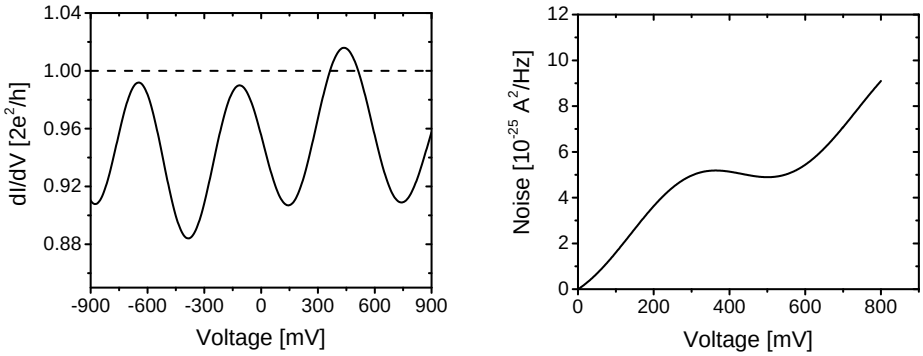


Figure 5.6: (a) Model based on a more general energy and voltage dependent transmission functions given by $T(E+\beta eV)$. The blue triangular region on the left is where the differential conductance is negative (NDC), while the similar blue region on the right shows the super Landauer single channel (SLSC) region where the differential conductance for a single channel exceeds 1 G_0. The shaded red regions on the left and right are where the differential shot noise is negative (NDSN). (b) Example of a model transmission for $\beta = 1$ shown to explain the meaning of T_H and T_L. (c) The T_H and T_L profiles extracted from the above transmission.

on the left and right. From the figure we also see that NDSN occurs when either NDC or SLSC is present but the presence of NDC and SLSC does not always means that we will have NDSE. To illustrate further, we present here an example with the single channel transmission at $\beta = 1$ shown in the Figure 5.6 (b). The differential conductance calculated from this is shown in Figure 5.7 (a) where we see that the dI/dV crosses 1 G_0 at around 450 mV. Figure 5.7(b) shows the corresponding noise where we see that the noise stagnates and starts to decrease around the same bias when the differential conductance is larger than 1 G_0.

Here we see that the transmission T(E,V) could take forms which are mathemat-



(a) (b)

Figure 5.7: (a) Differential conductance calculated for the transmission shown in Figure 5.6 with conductance crossing 1 G_0 (SLSC). (b) The noise calculated for the same model shows NDSN behavior in the regime for which the dI/dV is larger than 1 G_0.

ically allowed and lead to exotic states like NDC, NDSN and SLSC. We are aware that we are not providing a physical basis for values of β other than $\beta = \pm 1/2$ which is associated with the quantum interference of electronic waves discussed in this chapter. The question whether other values of β are possible is a part of a broader question which possible functions $T(E, V)$ are allowed.

5.6 Discussion

In the previous section we have offered an interpretation for the non-linear dependence of shot noise on the applied bias. We have seen that, qualitatively, the effects are related to those in the differential conductance, and these are likely due to quantum interference as a result of electrons scattering from defects near the contact. For a quantitative explanation more elaborate models are required, and the observed negative differential noise is particularly exotic. High-bias shot-noise measurements have been reported earlier for Au atomic contacts up to 300 mV in room temperature[14] and 250 mV at low temperatures[15]. These measurements were performed using a high bandwidth radio-frequency (rf) technique, where only the integrated noise is detected by a power detector. The reported non-linearity in shot noise was shown only as a rise in noise power. In case of the room temperature measurements[14] the non-linear increase in shot noise was attributed to either electron-phonon interaction or local heating of the electronic fluid which crosses the ballistic junction. At low temperature[15] the non-linear rise is explained using the linear regime Landuaer formalism relations, which in general should not be applicable at high bias as explained earlier. Also an occurrence of decrease in shot noise with bias has been reported[26] on a n-GaAs MESFET system where due to correlated resonant tunneling (which

[26] S. S. Safonov et al. In: *Phys. Rev. Lett.* 91 (2003), p. 136801.

involves two interacting resonant states) first an enhancement in the shot noise over the Poisson value ($2eI$) occurs and then a decrease in shot noise with bias. Other possible explanations proposed for non-linearity in shot noise[27] are bias-dependent channel mixing and nonequilibrium phonon back-action. A non-equilibrium phonon distribution[11] could develop but as a result of the strong coupling to the phonon bath in the Au leads, the non-equilibrium is expected to remain small. Such effects are more important in systems where the vibrons of the system are weakly coupled to the phonon bath of the leads. On the theory side, Lesovik and Loosen[28] have shown that the excess noise ($S(I) - S(0)$) could even become negative for a sharp peak in transmission, close to zero bias, whose width is much smaller than k_BT. This is a very rarely occurring possibility and has not been found yet in the experiments.

Stability and heating of atomic point contacts at such high bias can also be a concern and has been studied earlier as well[29], where it was reported that Au atomic contacts could even sustain up to 2 V and more than 150 μA current. Using a semi-classical approach[20,30,31] , it has been shown that in the ballistic regime, where the size of the contact is much smaller than the mean free path, the heat carried by electrons under an applied bias is dissipated far away in the banks via scattering with phonons. As a result, even at such high bias, the effect of heating on noise and G_{diff} can be ignored, as the electronic temperature in the vicinity of ballistic point contact does not rise much. We measured the global heating effect in our samples by replacing the Au point contact with a standard film resistor of 13 kΩ (close to 1 G_0) and recording the noise. From the noise measurement we conclude that the rise in effective temperature for up to 1 V bias over the 13 kΩ resistor, is around 0.075 K which is equivalent to 0.23 nV/$\sqrt{\text{Hz}}$ in thermal noise.

5.7 Conclusion and outlook

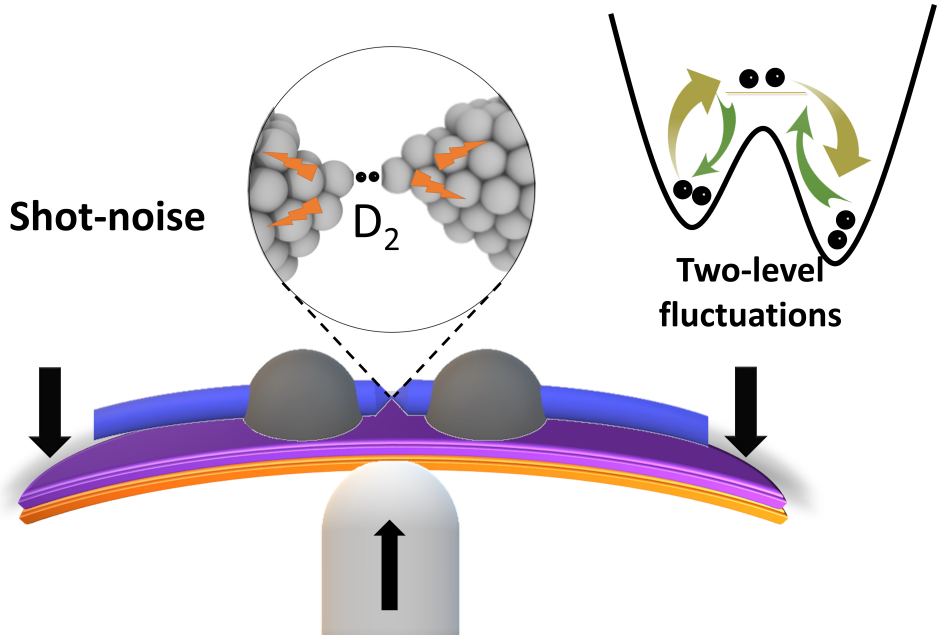
In conclusion, we have performed shot-noise measurements over Au single atom point contacts in the non-linear regime, even up to 800 mV bias as shown in the 3$^{\text{rd}}$ example in Figure 5.3. These shot noise data show highly non-linear behavior with applied bias, which has no specific trend and which is different for every different contact. We have shown that these non-linearities arise due to quantum interference of electronic waves which take multiple paths due to elastic scattering on the defects present in the leads close to the point contact. This makes the transmission probability of the contact energy and voltage dependent, which means usual assumptions based on the linear regime breakdown. We can qualitatively explain the main features in the measured non-linearity but there could also be other energy and voltage dependent effects present, due to the intrinsic transmission of the point contact itself, the effect of other channels and the voltage drop over the defect sites. Any inelastic effects, including non-equilibrium phonon back action and back-scattering of electrons which could lower the junction conductance is also not included in the model. We have

[27] Loah A. Stevens et al. In: *Journal of Physics: Condensed Matter* 28 (2016), p. 495303.
[28] Gordey B. Lesovik and Roland Loosen. In: *Zeitschrift für Physik B Condensed Matter* 91 (1993), p. 531.
[29] S. K. Nielsen et al. In: *Phys. Rev. Lett.* 89 (2002), p. 066804.
[30] Yu V. Sharvin. In: *J. Exptl. Theoret. Phys. (U.S.S.R.)* 48 (1965), p. 655.
[31] A. G. M. Jansen et al. In: *Journal of Physics C: Solid State Physics* 13 (1980), p. 6073.

presented experimental data where the non-linearity is such that the shot noise even decreases with increase in bias (NDSN). We argue that this is not permitted within the standard description of elastic scattering, but we have discussed mathematically a possibility that certain forms of T(E,V) could even lead to more exotic states like NDC and SLSC. The results presented in this chapter suggest that if the position of defects in the vicinity of the point contact can be controlled, then by exploiting the quantum interference of electronic waves, one could design the transmission at will and achieve desired properties in conductance and noise. In a metallic point contact it is not easy to control the position of defects, but in a pre-designed molecular system and mesoscopic systems like 2DEG[32] this may be feasible.

[32] M. A. Topinka et al. In: *Science* 289 (2000), p. 2323.

Graphical Summary



6. Two-level fluctuations in molecular junctions

Conductance measurements in single-molecule junctions (SMJs) are on many occasions accompanied by inelastic spectroscopy and shot-noise measurements in order to obtain information about different vibration modes (or vibrons) and channels involved in the transport respectively. We have extended the single-molecule shot-noise measurements, which were previously performed at low bias, to high bias and we have studied the effects of these vibrons on shot noise for a Deuterium (D_2) molecule between Pt leads. We report here three important findings from these measurements. First, we find in our noise measurements that at the vibron energies of the molecule, a two-level fluctuation (TLF) is excited in the junction. Second, we show that in the presence of this TLF, a form of enhanced noise spectroscopy can be performed to detect inelastic electron-vibron interactions, by studying the third derivative of the noise ($\mathrm{d}^3 S_I/\mathrm{d}V^3$). This is possible because TLFs are insensitive to elastic scattering of electrons from defects, which nevertheless leave their signature in the usual inelastic electron tunnelling spectroscopy (IETS) measurements. Third, we also report here the detection of a step-up in conductance for the Pt-D_2-Pt junction due to inelastic interactions. As the zero-bias conductance of these contacts lies close to 1 G_0, so the occurrence of step-up in conductance goes against the usual electron back-scattering picture. However, this can be explained as a consequence of the coupling of d-orbital of Pt contacts with the usual s-orbital taking part in transport.

The work is done in collaboration with - Carlos Sabater and Jan M. van Ruitenbeek
Huygens-Kamerlingh Onnes Laboratorium, Universiteit Leiden, The Netherlands.

6.1 Introduction

Single molecule conductance measurements are possible now from nearly three decades. Soon after the first single molecule experiment[1], researchers started to explore the other degrees of freedom, for example, the effect of molecular vibrations[2,3] on electronic transport and shot-noise measurements[4]. The study of molecular vibrations using charge transport measurements helped to further strengthen the claim of contacting single molecules and the study of low-bias shot noise provides information about the number of channels involved in the charge transport. The vibration measurements are also compared frequently with other single molecule vibration measurement techniques like surface enhanced Raman or infra-red spectroscopy. Important to note is that in all these measurements of the vibrations of a single molecule the molecule remains connected to metallic leads, the coupling to which influences the vibration frequency and the nature of the modes. In this chapter, we will refer to a vibration mode of the molecule as a vibron and the vibrations in the bulk metallic lead as phonons.

The vibration measurements done by studying charge transport through a single molecule depend strongly on the electron-vibron (e-vib) coupling strength. For stronger coupling between electrons and vibrons, the electrons could have large transit times on the molecule and this could even polarize the molecule. This is seen as polaron formation and the transport in this regime is incoherent hopping transport[5]. In the other limit, for weak electron-vibron coupling the traversal time for an electron to cross the molecule is much smaller than the oscillation period of with the vibron modes of the molecule. Conversely, this electron-vibron coupling strength determines how quick the excited vibrons in the molecule pass their energy back to the electrons and consequently to the metallic bath, where the electrons loose their energy. On applying a bias $V \geq \hbar\omega/e$ across the molecule, the electrons crossing the molecule loose part of their energy to emit/excite a vibron of the molecule. This is visible in the differential conductance as a small step-change, at least for simple coherent off-resonant transmission and for weak electron-vibron coupling.

6.2 Literature review

The first measurements aimed at studying such electron-vibron interaction on single molecules[2] were done for electrons crossing a single acetylene (C_2H_2) molecule absorbed on a Cu(100) surface. A step-up or increase in conductance at a voltage equal to $\hbar\omega/e$ (the energy of a vibron associated with the molecule) was recorded. This measurement was done in tunneling mode (with transmission, $T << 1$) using a scanning tunneling microscope (STM) and the increase in conductance at energy $\hbar\omega$ was attributed to the opening of a second inelastic channel. In another measurement done

[1] M. A. Reed et al. In: *Science* 278 (1997), p. 252.
[2] B. C. Stipe et al. In: *Science* 280 (1998), p. 1732.
[3] Nicolás Agraït et al. In: *Phys. Rev. Lett.* 88 (2002), p. 216803.
[4] D. Djukic and J. M. van Ruitenbeek. In: *Nano Letters* 6 (2006), p. 789.
[5] Juan Carlos Cuevas and Elke Scheer. Molecular electronics : an introduction to theory and experiment. New Jersey [u.a.] : World Scientific, 2010.

on single H_2 molecule attached between two Pt leads[6,7], a step-down or decrease in the molecular conductance was recorded. This measurement was done in point contact mode with transmission (T) close to unity. A similar decrease in conductance is also recorded in mono-atomic chains made of gold atoms[3,8], where the transport is again ballistic. For these contacts with high transmission ($T \approx 1$), backscattering of electrons due to unavailability of empty states in the forward direction is considered to be a reason for the decrease in conductance.

To study the crossover between the two transport regimes, from the low transmission ($T << 1$) where the conductance shows a step-up to the high transmission regime ($T \approx 1$) where the conductance shows a step-down, a single vibron model in the weak electron-vibron coupling regime[5] is developed. Using this single-vibron model it can be shown that other than the elastic and inelastic (due to vibron emission or absorption) contribution, there also exists a contribution due to interference between direct elastic transport and a two-step process involving virtual emission and absorption of a vibron. It is called an 'elastic correction' as the energy is conserved here and depending on whether this interference is constructive or destructive the forward or the back scattering probability is enhanced, thus giving a positive or a negative contribution to the conductance respectively. The model further suggests that for symmetric contacts, that have the same scattering rates to the left (Γ_L) and right electrodes (Γ_R), the sign of the inelastic signals lies exactly at transmission $T = 1/2$[9]. Important to point out is that the assumption of same scattering rates to the two electrodes is not always true, for example in the tunneling case, the scattering rates on two sides are very different and so this cross-over point depends in reality on the asymmetry of the contact[10] defined as $\alpha = \Gamma_R/\Gamma_L$.

This crossover between the step-up and step-down regime has been also observed in experiments[11,12]. Contrary to the above, Kristensen *et al*.[13] have shown through first-principles calculations that the transverse vibration mode of a H_2 molecule in a Pt-H_2-Pt junction can also cause a step-up in conductance even when a single channel is involved in the transport and the transmission is close to 1. The reason behind the increase in conductance was investigated by a scattering theory calculation showing that due to transverse vibration of the molecule, d-orbitals of the Pt-leads start to couple with the s-orbital, and thus also begins to take part in transport. The authors have not observed such an increase in case of a Au-H_2-Au system, where no such d-orbital is present in the leads. Figure 6.1 taken from Kristensen *et al*.[13] shows such a step-up in conductance. This is a surprising result as from the single channel single vibron-mode model explained above, one expects the step-up in conductance to occur only at transmission much smaller than unity. And also in experiments done for Pt-H_2-Pt or Pt-D_2-Pt systems such increase in conductance has not been reported[4,6,7]. However, these steps are very small, around 1% of the conductance

[6] R. H. M. Smit et al. In: *Nature* 419 (2002), p. 906.
[7] D. Djukic et al. In: *Phys. Rev. B* 71 (2005), p. 161402.
[8] Nicolás Agraït et al. In: *Chemical physics* 281 (2002), p. 231.
[9] Magnus Paulsson et al. In: *Phys. Rev. B* 72 (2005), p. 201101.
[10] Magnus Paulsson et al. In: *Phys. Rev. Lett.* 100 (2008), p. 226604.
[11] O. Tal et al. In: *Phys. Rev. Lett.* 100 (2008), p. 196804.
[12] W. H. A. Thijssen et al. In: *New Journal of Physics* 10 (2008), p. 033005.
[13] I. S. Kristensen et al. In: *Phys. Rev. B* 79 (2009), p. 235411.

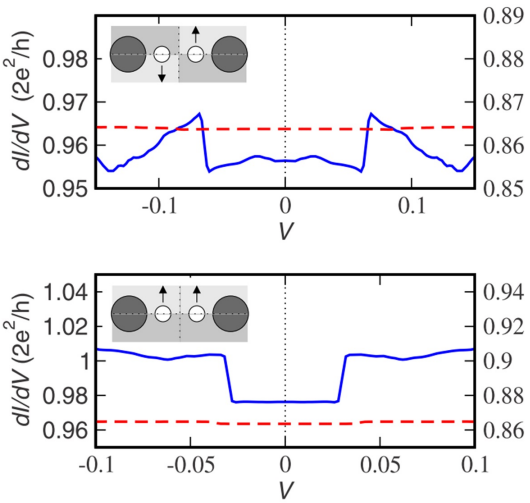


Figure 6.1: First-principles calculations from Kristensen *et al*.[13] showing differential conductance of the Pt-H_2-Pt (solid blue line) and Au-H_2-Au (dashed red line) junctions when scattering on a single transverse vibrational mode. The top figure shows a hindered rotations mode and the bottom figure shows a transverse center of mass mode.

values, and could be very difficult to detect, especially when we have oscillations in the conductance due to elastic scattering through defects[14–16].

Another interesting excitations that lies at energies close to vibrational energies of a molecule is the excitation of two-level fluctuations in the molecule. Thijssen *et al*.[17] have discussed in an experimental study, the effect of such two-level fluctuations on molecular conductance. They have reported measurement on different molecules (including also H_2 and D_2 molecules) and shown that in many occasions sharp spikes in the differential conductance are seen at energies close to a vibrational mode of the molecule. They explain these using a vibrationally induced two-level system which they call 'VITLS', where excitation of a vibron could change the molecular conformation between the leads which could change consequently the conductance and thus will be observed as a spike. Figure 6.2 shows one of their results. They have further shown that the strength of the observed spike in conductance for Pt-D_2-Pt system depends also on the stretching of the junction and could be suppressed completely once full stretched with the maximum in amplitude occurring somewhere at an intermediate stretch. They have also reported for the Pt-D_2-Pt system that the two-level fluctuation is excited only at energies close to the transverse mode of vibration. Similar peaks in the $\mathrm{d}I/\mathrm{d}V$ signals in Au-H_2-Au junctions, have also been observed by other[18] groups. Such two-level fluctuations are also reported in an STM

[14] B. Ludoph et al. In: *Phys. Rev. Lett.* 82 (1999), p. 1530.
[15] B. Ludoph and J M van Ruitenbeek. In: *Physical Review B* 61 (2000), p. 2273.
[16] C. Untiedt et al. In: *Phys. Rev. B* 62 (2000), p. 9962.
[17] W. H. A. Thijssen et al. In: *Phys. Rev. Lett.* 97 (2006), p. 226806.
[18] Manabu Kiguchi et al. In: *Phys. Rev. B* 81 (2010), p. 045420.

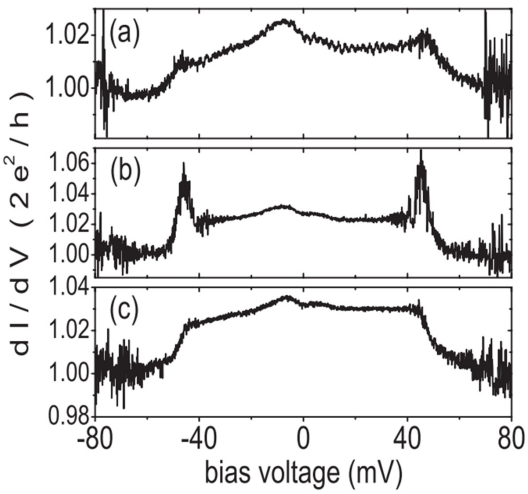


Figure 6.2: Differential conductance spectra for a Pt-D_2-Pt junction taken from Thijssen *et al*.[17]. (a-c) are spectra taken at different stretched states of the molecule. Vibration induced spikes are visible clearly at the shoulder positions.

configuration[19] for H_2 molecules over a Cu(111) surface.

In this chapter, we report a study performed on the Pt-D_2-Pt system to further explore the vibrational effects described above. We have done high-bias shot-noise measurements along with the usual differential conductance at energies where a vibron in D_2 molecule between Pt leads is excited. Previously, shot noise measurements were only performed at low bias values[4,20] to obtain information about the number of channels involved in the transport (at zero bias). We show here that, be it rarely, but we were able to detect in our measurements a step-up in conductance at energies close to the transverse vibrational mode for Pt-D_2-Pt junctions with conductance close to 1 G_0, as predicted by Kristensen *et al*.[13]. Most of the other conductance measurements show the usual step-down feature in conductance and almost all of our conductance measurements are smooth and do not have spikes-like features which were earlier attributed to two-level fluctuations[17]. Having said this, using our shot-noise measurement we have also detected the emergence of non-white noise spectra close to the energies corresponding to the vibration energy of the molecule. This is also the case with junctions which have shown a clean usual step-down or decrease in conductance at the vibrational energies. This challenges our understanding, both in qualitative and quantitative terms, of these IETS or PCS differential conductance signals and suggests that a model coupling vibration excitations and TLF could be more generally applicable in molecular junctions.

[19] J. A. Gupta et al. In: *Phys. Rev. B* 71 (2005), p. 115416.
[20] Regev Ben-Zvi et al. In: *ACS Nano* 7 (2013), p. 11147.

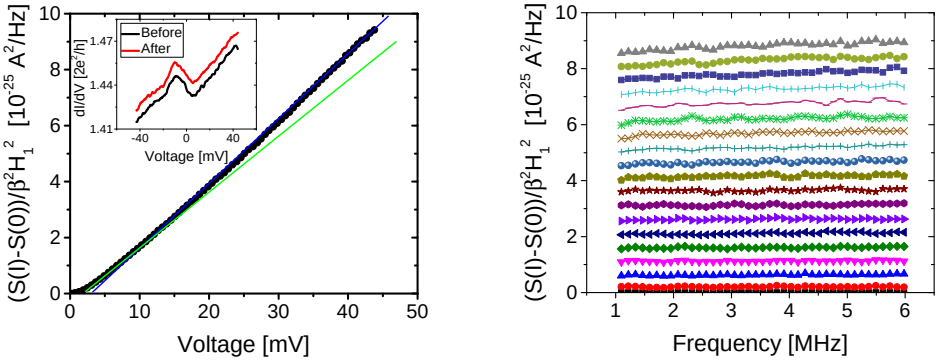
6.3 Experimental setup

To study shot noise at energies where the vibration modes of the single molecules are present, one has to fight with the notorious 1/f noise which scales with the square of the applied bias voltage. We have developed recently[21] a new high-bias shot-noise measurement setup which works in MHz regime and can be useful in studying such molecular systems. We have also demonstrated earlier using this setup shot-noise measurements up to 800 mV on a single Au-atomic point contact (see chapter 5) and have shown how at such high bias, the elastic and inelastic part of the transport, due to energy and voltage dependence of transmission can give highly non-linear shot noise. A schematic of the setup is shown in Figure 5.1 in the previous chapter. The setup is mounted on a cryogenic dipstick to do measurements at liquid He temperature. The gas molecules are deposited using a capillary tubing which goes all the way from a gas reservoir on the top to a break-junction sample mounted at the bottom. Noise measurements are done using a cross-correlation technique for which we have connected two cryogenic amplifiers in parallel at a short distance (approximately 1 cm) from the sample followed by two parallel room temperature amplifiers. For fast measurements of the noise, while still recording all the spectra at each applied bias voltage, we have incorporated a field programmable gate array (FPGA) in the spectrum analyzer. Conductance measurements are done by means of a lock-in amplifier using an input AC modulation signal of few mV amplitude over the sample and 677 Hz frequency. The details of the system and its benefits are discussed in chapter 4[21].

6.4 Measurements on a D_2 molecule

Single molecule measurements in general (not specific to D_2 molecule) are more likely to become affected by two-level fluctuations (TLF) than purely metallic atomic contacts. Such TLF are attributed to the switching between two (or more) conformational states with similar energy separated by a small barrier[17]. These TLF can also occur in metallic point contacts and atomic chains. There they can be attributed to changes in position of a defect in the leads, close to the point contact. Harder materials like Pt are more subjected to such TLF as compared to Au[21]. Here, we have taken special care to avoid such TLF in the Pt leads by pre-annealing the break-junction notched wire in a separate UHV setup (10^{-9} mbar) for 3-4 hours at 300°C. After this, we mounted carefully the sample back in the dipstick for pumping and cool down. Such a pre-annealing step is essential as we don't want the noise coming from TLF of the leads to affect our molecule noise measurement. For clean deposition of the molecules, the capillary was baked before cool down at high vacuum (10^{-6} mbar) and several flushing cycles with clean D_2 gas were done prior to breaking the Pt wire. For clean operation, the Pt wire is broken only when the system is cold and the sample is at cryogenic vacuum. Next, conductance and noise measurements of clean Pt were performed to check the cleanliness of the contact and also to train[22] the junction prior to molecule deposition. Figure 6.3 shows white noise spectra recorded (after the pre-annealing step) on a clean Pt atomic contact up to 4.9 μA current. This experiment shows the benefit of measuring shot noise at the MHz frequency range,

[21] Sumit Tewari et al. In: *Review of Scientific Instruments* 88 (2017), p. 093903.
[22] C. Sabater et al. In: *Phys. Rev. Lett.* 108 (2012), p. 205502.



(a) (b)

Figure 6.3: (a) shot-noise measurements on a clean Pt atomic contact up to 44 mV bias which for the zero bias conductance of the contact is equivalent to 4.9 μA current. The inset shows the differential conductance of the contact taken before (black) and after (red) the shot-noise measurements. Two linear fits (blue and green) to the shot noise data intercepts at the phonon frequency of the Pt junction which is around 10 mV. (b) White noise spectra recorded by our FPGA based spectrum analyser demonstrating the absence of 1/f noise and two-level fluctuations.

as we don't have any detectable 1/f noise signal in our measurements. The spectra also confirm that there are no two-level fluctuations initiated in the clean Pt junctions. The procedure that we follow in our measurement is to perform differential conductance measurements of the junction two times: before and after the shot-noise measurement series. This helps in confirming the stability of the junction during the noise measurements. A kink or a linear deviation in the shot-noise data can be seen in Figure 6.3 (a) which corresponds to the phonon frequency of the Pt junction which is around 10 mV. The rounding at the low bias ($\leq$ 2 mV) is due to submerging of the shot noise in the thermal noise background at the measurement temperature of 5 K.

6.4.1 Step down in junction conductance

While depositing the molecules, Pt contact forming and rupture traces are continuously monitored. It is known from previous conductance measurements for this system that a D_2 molecule attached between Pt leads gives rise to a last conductance plateaus at 1 G_0. So, once we started seeing such 1 G_0 plateaus appearing, we stop the deposition. Once the D_2 molecule is stable between the Pt leads, point contact spectroscopy or dI/dV measurements of such a junction are known to show a step-down or decrease of conductance due to inelastic interaction with the vibron of the molecule. This we also found in our experiments (see Figure 6.4 (a) and (c)) in agreement with the literature[4,6,7].

Next, we perform high-bias shot noise measurements on this junction. In Figure 6.4(b) we show the corresponding shot-noise measurement results. Initially, at low bias the shot noise shows a linear increase (shown with black solid symbols) and then approximately at the point where a vibrational mode is excited giving a step-

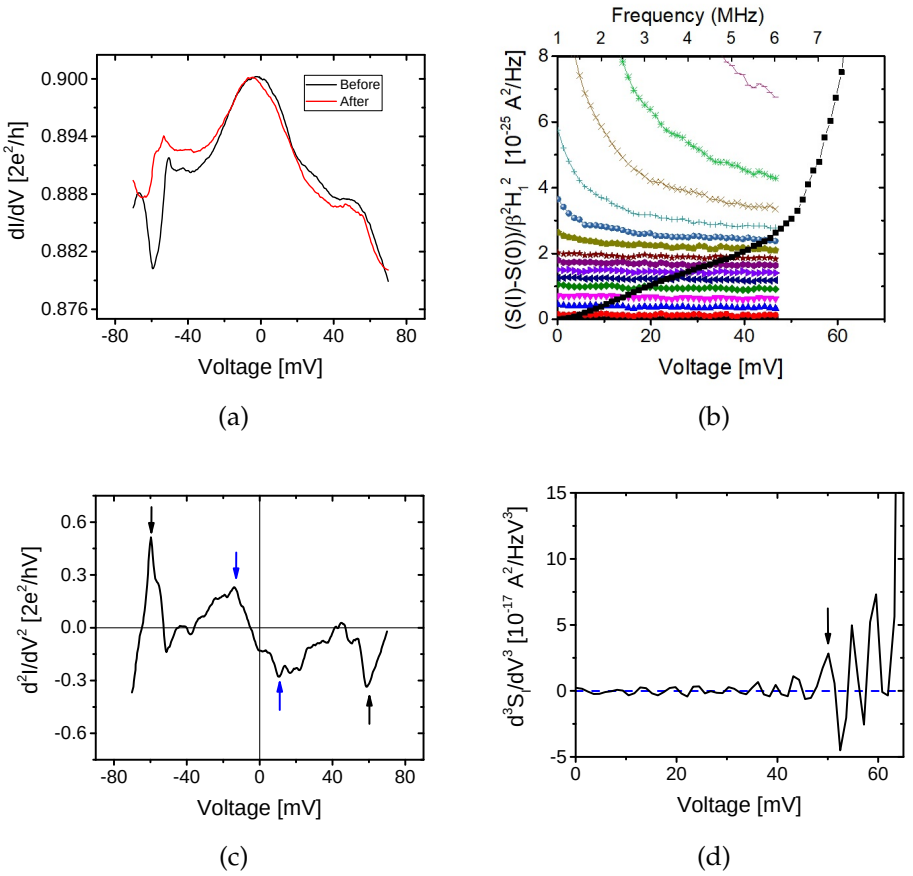


Figure 6.4: (a) A step-down in conductance for a Pt-D_2-Pt junction taken before (black) and after (red) the noise measurement. The left shoulder of the dI/dV spectrum shows a signature of two-level fluctuation similar to Thijssen *et al.*[17]. (b) High-bias shot-noise measurements (black) taken up to 60 mV bias (i. e. 4.2 μA for G(0V)=0.9 G_0). The noise spectra (in color and axis along the top) are shown from 1 to 6 MHz frequency. (c) Usual IETS spectrum of the junction showing the vibrational modes of the molecule (black arrows) and of the Pt leads (blue arrows). (d) The IENS-3 spectrum showing positions of inelastic interactions giving rise to two-level fluctuations in the molecule. The first peak marked with a black arrow, points towards a vibrational mode excitation of the molecule, while the other peaks correspond to inelastic interactions due to more complex atomic-scale dynamics occurring as the applied bias is increased further.

down in the conductance, we see a non-linear increase in the noise. We repeated this measurement for different stretching states of the molecular junction, which changes the vibrational energy[4], and we found that the locations where the shot-noise starts to deviate from linearity also changes accordingly. As we record the

spectral information of the noise, we see in Figure 6.4 (b) that the place where the noise starts to show a non-linear deviation, the spectra (taken between 1 to 6 MHz frequency) are no longer white. The detection of these non-white spectra suggests that two-level fluctuations are excited by the vibrons[1]. In the absence of such spectral information, one would be tempted to attribute this non-linear increase in shot noise to a non-equilibrium increase in population[23–26] of the vibrons due to their larger relaxation time. As mentioned in the last chapter elastic scattering through defects could also add to the non-linearities in the shot noise. But as our conductance values are not very close to 1 G_0, we expect to have very small of such contribution.

6.4.2 Inelastic electron noise spectroscopy (IENS)

The two-level fluctuations (TLF) mentioned above can, in fact, be used constructively. As described earlier, TLF are due to jumps of the system between two resistive configurations separated by an energy barrier. An inelastic interaction between an electron and a vibron can shift the molecule from one resistive configuration to other. TLF will not occur due to elastic interactions as there is no energy transfer. The sensitivity of two-level fluctuations to inelastic interactions and not to the elastic scattering of electron waves makes their detection via noise into a new tool for spectroscopy. Use of shot noise as a tool for spectroscopy has been shown previously as well with the name of inelastic electron noise spectroscopy (IENS)[24]. By studying inelastic interactions in Au atomic point contacts, deviations from the linear $2eIF$ relation for shot noise has been demonstrated. As the deviations were also linear, a plot of $\mathrm{d}^2S_\mathrm{I}/\mathrm{d}V^2$ as a function of bias forms an IENS spectrum and shows peaks at the positions of the kinks in noise. IENS is similar to inelastic electron tunnelling spectroscopy (IETS), where inelastic effects will be visible as peaks in $\mathrm{d}^2S_\mathrm{I}/\mathrm{d}V^2$ spectra or IETS spectra. The IETS and IENS spectra are directly affected also by the elastic interactions as a result of quantum interference. On the contrary, two-level fluctuations (TLF) increase as the square of the input current or applied bias, similar to 1/f noise. Thus, the $\mathrm{d}^3S_\mathrm{I}/\mathrm{d}V^3$ of the measured noise (S_I) should show peaks corresponding to the TLF excited by inelastic interactions. We call this inelastic electron noise spectroscopy-3 (IENS-3). IENS-3 holds a unique benefit over IENS and IETS because of the insensitivity of TLF to elastic scattering, this new mode of noise spectroscopy can give distinctly clear peaks due to inelastic interactions leading to TLF. To make the third-order derivative of the noise data, we used a commercial OriginPro software which does the 3^{rd} order derivative using a numerical differentiation technique starting from the raw noise data. It is important to take care of the boundaries while doing higher order numerical derivatives. A third-order derivative computed at a voltage bias value relies on the noise values on the two

[1] It is also possible that there are multiple two-level fluctuations excited by the vibrons giving a 1/f noise spectra, but this we cannot confirm with our setup as we cannot measure the full spectra up to the DC level.

[23] Loah A. Stevens et al. In: *Journal of Physics: Condensed Matter* 28 (2016), p. 495303.
[24] Manohar Kumar. PhD thesis. Leiden Institute of Physics (LION), Leiden University, 2012.
[25] Tomá Novotný et al. In: *Phys. Rev. B* 84 (2011), p. 113107.
[26] D. F. Urban et al. In: *Phys. Rev. B* 82 (2010), p. 121414.

adjacent voltage data points on either side.[2] In all the $\mathrm{d}^3 S_\mathrm{I}/\mathrm{d}V^3$ spectra presented in this chapter, the derivatives are shown up to a voltage bias where we have more than two data points after it.

Figure 6.5 shows a first example of the benefit of IENS-3 over IETS. Here one can see that the peaks in the IETS spectrum (Figure 6.5 (b)) due to inelastic scattering (in this example at +50 mV) are of similar amplitude as other structure that could be coming from elastic quantum interference effects. On the contrary, in the IENS-3 spectrum, the first peak (marked with an arrow) corresponds to the excitation of a TLF due to inelastic effects. This peak marks clearly the position of the vibration mode energy of the molecule and the spectrum is not affected by the background conductance fluctuations. As we keep increasing further the applied voltage bias, more complex atomic-scale dynamics can lead to other peaks and structures in the IENS-3 spectrum.

Some more examples for comparison between IETS and IENS-3 structures are shown in the Figure 6.5, 6.6 and 6.7. Here again one can see that IENS-3 shows clear peaks marking the position of inelastic interactions which could excite TLF. Important to note is that IENS will detect only those inelastic interactions which lead to two-level fluctuations. This probably explains why in the first example shown in Figure 6.7, the IETS spectrum shows the position of the vibration mode of the Pt metallic leads at a low bias of around 10 mV, while there is no signature in the corresponding IENS-3 spectrum shown in Figure 6.7 (d).

6.5 Inelastic tunneling versus two-level fluctuations?

Interesting to note is that all the examples shown in this chapter have no signature of two-level fluctuations in the $\mathrm{d}I/\mathrm{d}V$ measurements. The two-level fluctuations mentioned above can easily be on the time scale of tens of microseconds or smaller making them inaccessible in our AC conductance measurement, performed with a modulation frequency of 667 Hz and a bandwidth of 1 Hz, or less. Depending on the duty cycle[3] of these fluctuations, the measured conductance could be anywhere between the two conductance states. Thus when a two-level fluctuation (TLF) is excited, one would see a step (increase or decrease) in the differential conductance[4] which is different in its physical interpretation from the step due to usual inelastic back-scattering process. Moreover, changes in conductance due to TLF, also occurring at the vibrational energy of the molecule, will then be added to the usual step increase or decrease in conductance you expect from the inelastic effects.

Consequently, this questions the way we study the inelastic scattering in single molecules as these TLF are not included in the theory used for interpreting measured differential conductance for inelastic effects.

---

[2] $f'''(x_i) = \frac{f(x_{i+2}) - 2f(x_{i+1}) + 2f(x_{i-1}) - f(x_{i-2})}{2h^3}$
Here, $h = \Delta x$ = step-size.

[3] Duty-cycle defines the percentage of time the contact stays in high or low conductance states

[4] There will be a peak (or a dip) followed by a step in the differential conductance due to the excitation of the two-level fluctuations.

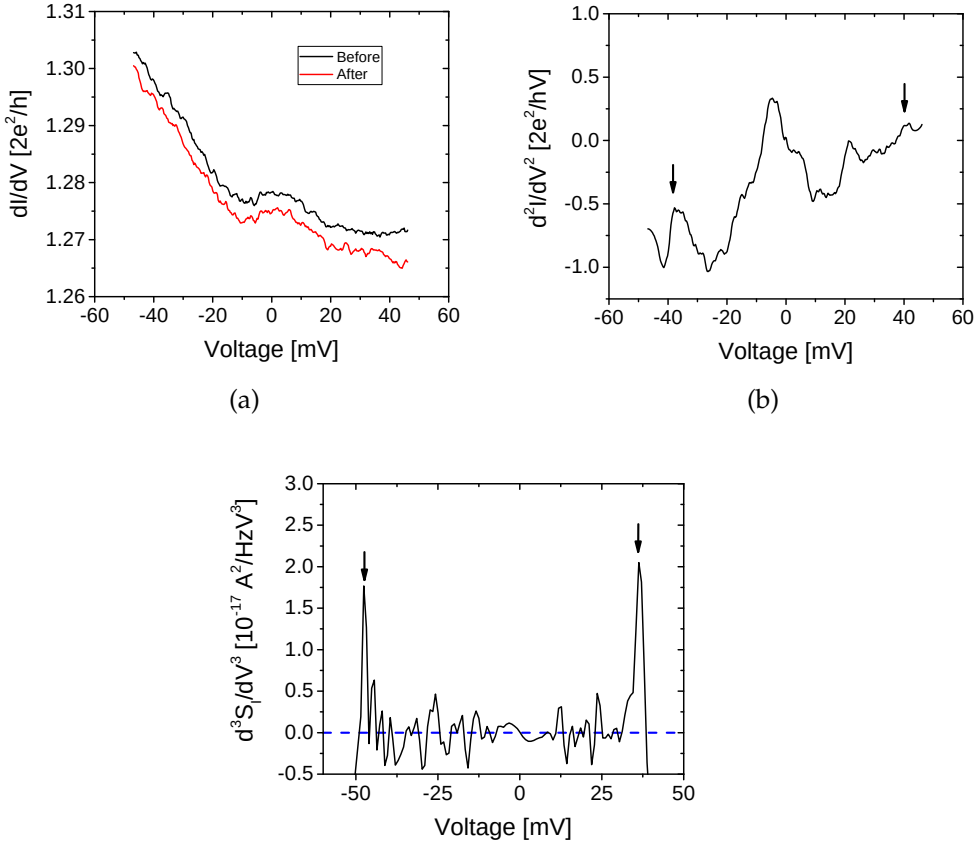


Figure 6.5: (a) Differential conductance for a Pt-D_2-Pt junction taken before (black) and after (red) the noise measurement. (b) Usual IETS spectrum of the junction showing the vibrational modes of the molecule (black arrows) with other equally large peaks possibly due to quantum interference of electron waves. (d) The IENS-3 spectrum showing enhanced peaks corresponding to the positions of the inelastic interactions giving rise to two-level fluctuations in the molecule. The first peak marked with a black arrow points towards a vibrational mode excitation of the molecule. Here the noise measurement is done both for positive and negative voltage bias.

6.5.1 Step-up in junction conductance close to 1 G_0

We report here the possible detection of a step-up or increase in conductance of a Pt-D_2-Pt junction. This has been predicted by Kristensen *et al.*[13] who suggested it as an outcome of coupling of the d-orbital with the usual s-orbital of Pt leads during a transverse hindered rotation mode of vibration. It goes against the conventional norm where contacts with conductance close to 1 G_0 should always have a step-down in conductance (as shown in Figure 6.4) due to back-scattering of electrons. Figure

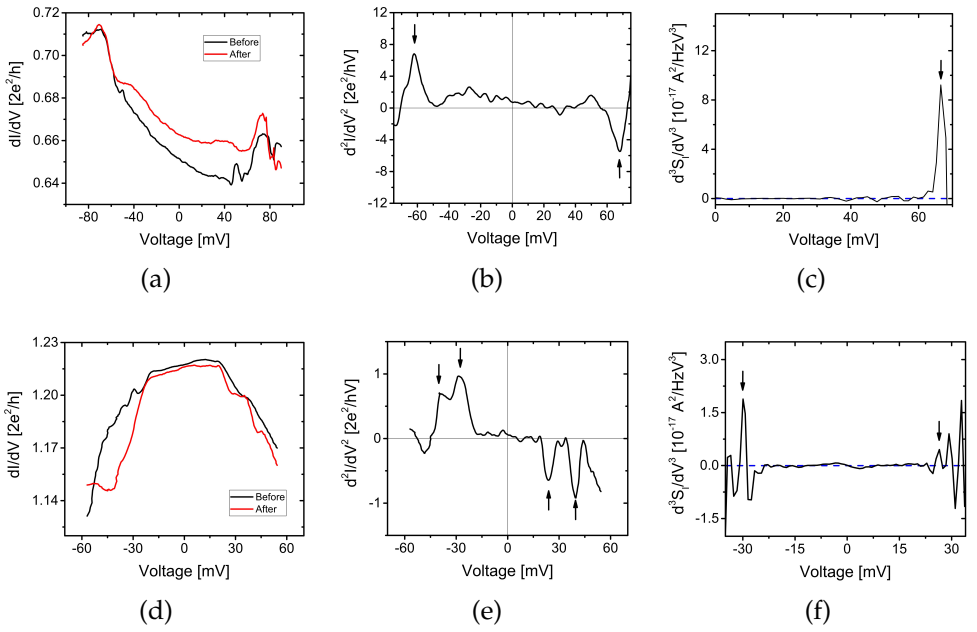


Figure 6.6: Junction 1: (a) Differential conductance for a Pt-D_2-Pt junction taken before (black) and after (red) the noise measurement. (b) Usual IETS spectrum of the junction showing the vibrational modes of the molecule (black arrows). (c) The IENS-3 spectrum showing an enhanced peak corresponding to the position of a vibrational mode of the molecule. Increasing the bias further, marks positions of other inelastic interactions (not shown here) corresponding to more complex atomic-scale dynamics. Here the noise measurement is performed for only positive bias. Junction 2: d) Differential conductance showing a step-down taken before (black) and after (red) the noise measurement. (e) Usual IETS spectrum of the junction showing the vibrational modes of the junction (black arrows). (f) The IENS-3 spectrum showing enhanced peaks corresponding to the positions of inelastic interactions. The first peak marked with a black arrow corresponds to the excitation of a vibrational mode of the molecule. Here the noise measurement is performed for negative to positive bias.

6.7 (a) shows an example of step-up in conductance for a Pt-D_2-Pt junction. In fact, it is similar to Figure 6.7, where now the conductance has been flipped upside down. Again it can be seen that the IETS spectrum in Figure 6.7 (b) shows two peaks with the lowest likely due to a Pt-Pt vibration mode and the higher associated with a Pt-D_2-Pt vibration mode.

Elastic scattering of electronic waves through defects could also cause features that resembles like a step-up in conductance. This possibility cannot be dismissed just by looking at the $\mathrm{d}I/\mathrm{d}V$ an IETS spectra. However, as for these contacts, the zero-bias conductance is sufficiently far from 1 G_0, so the elastic scattering of electronic waves (discussed in chapter 5) will cause a negligible effect on the linear shot-noise spectra. Thus, the IENS-3 peaks (shown in Figure 6.7 (c)) will pinpoint the inelastic

interactions with certainty. The first peak (marked with the black arrow) although small, should correspond to the excitation of a vibron in the molecule which triggers a TLF. This suggests that the step-up in conductance shown in Figure 6.7 (a) is occurring at a vibration energy of the D_2 molecule between the Pt leads and thus is less likely to be an outcome of a background conductance oscillations caused by elastic scattering.

The example shown in Figure 6.7 (d-f) does not fit in either step-up or step-down picture. We see here that the differential conductance first rises to a particular value and then decreases. This, however, holds similarity to the hindered rotation mode studied using first-principles calculations by Kristensen *et al*.[13] and shown in the top graph in Figure 6.1. The IETS spectrum of this differential conductance, showing step-up followed by the decrease in conductance, will have a peak followed immediately by a dip. A peak in the IETS spectrum usually points towards a step-up in the conductance, while a dip towards a step-down. The IETS spectra for our data (shown in Figure 6.7 (e)) also shows such a dip around 45 mV. Similar to the previous example we calculated the IENS-3 spectrum shown in Figure 6.7 (f). This shows a TLF excitation and so a vibration mode presence already around 30 mV bias. Important to note here is that in the IENS-3 spectra one cannot differentiate between step-up and down in conductance as the TLF triggered by a vibration excitation will always increase the noise. But we do see that the first vibration mode excited in the molecule leaves an IENS-3 peak pointing towards a triggered TLF around 30 mV, which is far from the dip seen in the IETS spectrum. In fact, around 30 mV there is a small peak in the IETS, which might be due to the first step-up in conductance, which is rounded by a conductance oscillations background.

In comparison to what was studied by Kristensen *et al*. , the energy of vibration is different in both the examples shown in Figure 6.7. Possible reasons for it could be different stretched state[4] of the molecule and/or different binding configurations to the leads. We encountered such step-up rarely as compared to the usual step-down behaviour show in the Figure 6.4. This observation does not resolve the discrepancy between theory and experiment, but it shows that the sign observed in the calculations is not fully excluded by the experiment.

6.6 Conclusion

In this chapter, we report using our newly built high-frequency setup[21], high-bias shot-noise measurements to study inelastic electron-vibron interaction for the Pt-D_2-Pt system. A pre-annealed Pt metallic contact is used to avoid unwanted two-level fluctuations in the leads. After that, doing high-bias shot-noise measurements on the Pt-D_2-Pt system, we show that at the energies where a vibrational mode or vibron of the molecule exists the noise changes character. It develops frequency dependence characteristic of TLF. Further, we propose that an enhanced noise spectroscopy can be done using these TLF, by studying the third derivative of the noise signal ($\mathrm{d}^3 S_I/\mathrm{d}V^3$). We call this inelastic electron noise spectroscopy-3 (IENS-3). We have shown using several examples how IENS-3 spectrum can possibly detect inelastic scattering processes more precisely than usual IETS spectrum. Moreover, there is no signature of these two-level fluctuations (TLF) in the $\mathrm{d}I/\mathrm{d}V$ measurements. Depending on the duty cycle of the TLF, a step-up or down (after a peak or dip) in the measured conductance can occur at the vibrational energies of the molecule. This change in conductance adds to the usual inelastic back-scattering signal of electrons. Hence, it

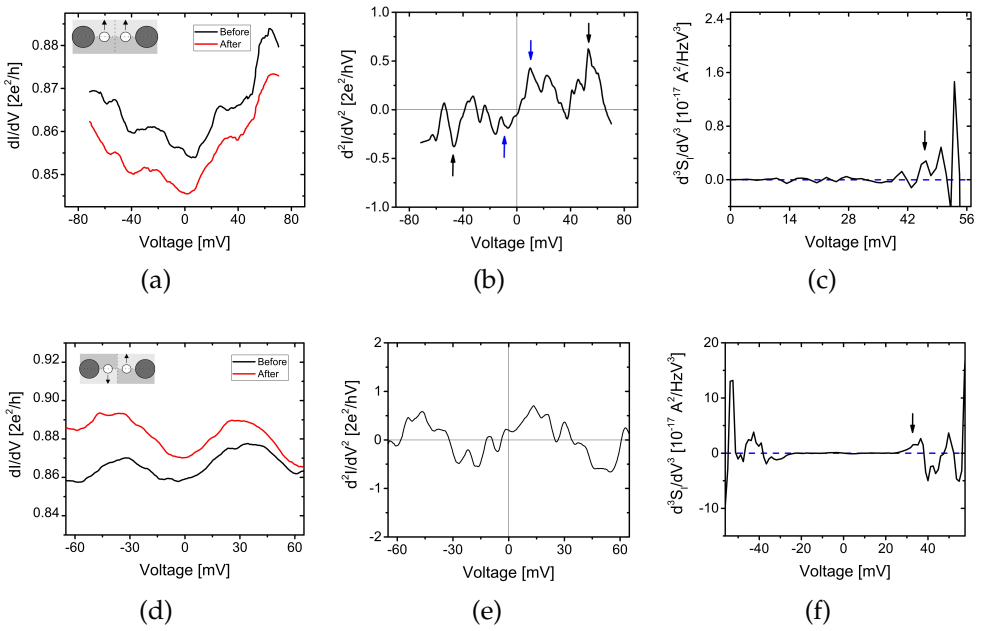


Figure 6.7: Junction 1: (a) Differential conductance for a Pt-D_2-Pt junction showing a step-up or increase in conductance. (b) IETS spectrum of the junction showing multiple peaks, including the vibrational modes of the molecule (black arrows) and that of the leads (blue arrows). (c) The IENS-3 spectrum showing enhanced peaks corresponding to the positions of inelastic interactions (black arrow). Here the noise measurement is performed for only positive bias. Junction 2: d) Differential conductance showing a step-up taken before (black) and after (red) the noise measurement. This is similar to hindered rotation mode shown in Figure6.1. (e) Usual IETS spectrum of the junction showing weak detection of the vibrational modes of the junction (black arrows). (f) The IENS-3 spectrum showing enhanced peak corresponding to the positions of inelastic interactions (black arrow). Here the noise measurement is performed for negative to positive bias.

questions our usual interpretation of the differential conductance measurements in the context of electron-vibron interaction in single-molecule junctions.

In addition, we report detection of a step-up or increase in differential conductance in a few of our Pt-D_2-Pt junctions. This increase is in contrast to the conventional picture where a junction with conduction close to 1 G_0 shows a step-down or decrease in conductance due to back-scattering of electrons. This increase has been attributed to the coupling of the d-orbital of Pt junction to its usual s-orbital[13], under a transverse rotational mode of vibration.

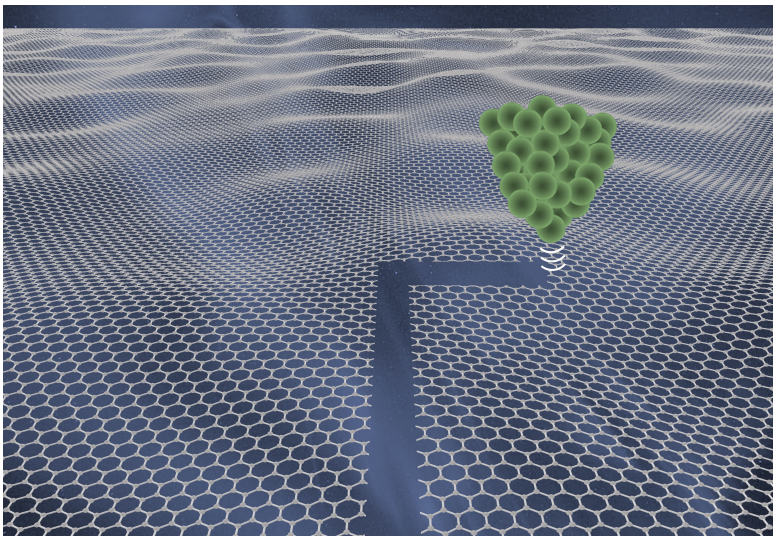
III

Part Three: Graphene Architecture

7 Graphene based circuit 124

7.1 Introduction
7.2 Graphene vs metallic electrodes
7.3 Electromigration, electroburning vs direct cutting methods
7.4 Our approach
7.5 Conclusion

Graphical Summary



7. Graphene based circuit

Use of graphene as an electrode for molecular electronics has several benefits. Foremost is the stability of the graphene lattice at room temperature which could help in making stable room temperature devices. Second thanks to its two-dimensional structure, it provides the possibility to modify and image its atomic structure. The electroburning technique used widely to make graphene nanogaps does not provide the control needed for proper characterization of the gap and its scalability to multiple electrode circuits. First, in this chapter an overview of previous work on graphene based electrodes, their achievements and limitations is presented. Followed by this a discussion of our results on exploring more direct cutting methods for making graphene nanogaps is presented. Specially, the STM tip based cutting which can provide controlled cuts up to 1.6 nm gap size.

The work is done in collaboration with - Kim Akius[1], Gaurav Nanda[2] and Jan M. van Ruitenbeek[1]
[1]Huygens-Kamerlingh Onnes Laboratorium, Universiteit Leiden, The Netherlands.
[2]Kavli Nanolab, TU Delft, The Netherlands.

7.1 Introduction

Silicon technology has a monopoly in electronics industry from the time the transistor was invented. The main reason behind it is the continuous development of lithographic techniques using excimer lasers like krypton fluoride (248 nm), then argon fluoride or deep ultra-violet (193 nm) and now extreme ultra-violet or EUV (13.5 nm). This allowed the silicon industry to reduce the size of the transistor from 800 nm in 1990 to 10 nm in 2016[1]. When the size of the transistors became smaller than 50 nm, problems started to appear. The leakage current between the source and drain terminals of the transistors even in an OFF state became comparable to the ON state current which has been reduced due to the small size of the gate electrode and thus small area of the inversion layer which is responsible for charge transport in the ON state. A workaround to this problem was brought by the use of finFET technology which increased the inversion layer area and thus increased the ON state current further. Another big issue at the moment is due to the large density of these transistors in a chip[2], because of which a large amount of heat is generated which ought to be removed. Silicon industry is continuously coming up with better architectures of transistors so that they can reduce their size further and could thus keep the Moore's law going. Recently, in June 2017 Intel showcased a 5 nm size transistor using their latest transistor architecture called GAAFET (gate all around FET). They claim that they can reach with the same architecture down to 3 nm.

The obvious question one can ask is how much smaller these transistors can be made under silicon technology and what will be next? We don't know the answer to this yet but possible paths could be: just 3D stacking of many logic dies, use of other III-V materials, carbon (graphene and nanotubes) and or use of individual molecules as electronic components. Regarding lithography techniques, the latest EUV lithography can lead the path forward. Electron beam lithography (EBL), has a higher resolution but is not favoured so far for large throughput work, due to its much larger writing times. Recent developments in EBL like using multi-column and multiple beam solutions[3] has reduced the EBL writing time and could thus also form a possible choice in lithography.

One may raise the question whether there is even a benefit of going further smaller in size using silicon. The next dimension scale that is waiting is the fundamental dimension limit formed by the basic constituents of matter like single molecules and single atoms. Study of organic molecules as electronic components has been an extensive field of research in itself since nearly 45 years, under the name of molecular electronics. A decade or two ago when silicon electronics was still operating in the size range of 100's of nanometers, molecular electronics showed a possibility of large benefits in dimension scaling on using single molecules. But today when silicon technology is standing already at the doorstep with transistors in the size scale of 5-10 nm, what does molecular electronics have to offer?

Molecules do have enough to offer! Molecular electronics is not only about scaling but also about functionalities. A silicon-based transistor however small it becomes is just a classical switch and an amplifier. Since the time of its invention what it does is controlling the current flowing between a source and a drain terminal by modifying

[1] These dimensions quoted are typically the channel length in the transistor.

[2] For example-there are around 3.3 billion transistors in each Apple A10 chip of 125 mm^2 area.

[3] This comes with the name of electron-beam direct-write (EbDW) technologies.

the voltage applied to the gate terminal. Single-molecule devices, on the other hand, can make use of the quantum mechanical properties[4] of individual electrons and provide various functionalities like quantum interference, spin selection or filtering, Coulomb blockade, electron-phonon interaction, thermoelectricity and much more. Desai *et al*.[1] have recently demonstrated a MoS_2 transistor with 1 nm gate length using a single-walled carbon nanotube as a gate electrode. Another new method picking up the reputation for making controlled nanoscale patterns other than usual lithographic techniques is directed self-assembly (DSA) of block copolymers[2]. Self-assembly of molecular circuits has been studied extensively, but these self-assembled structures are randomly distributed over large length scales. Using DSA, it has been shown that the growth of these self-assemblies can be controlled to make desired nanoscale patterns at much faster rate.

On the other hand it has to be noted that most of the molecular electronics research is done on platforms which are not scalable. By scalable I mean that in most of the measurement setups (like mechanically controlled break junction and STM break junctions) we can study single-molecules, but it is not possible to extend this to a multi-molecular circuit. Electro-migration based junctions are mostly fabricated with many junctions on the same chip, but due to the statistical nature of electro-migration, the location and width of these junction gaps are not very controlled, scaling of these to a multi-molecular circuit or even to multi-terminal devices is very challenging. Electro-migration junctions can be fabricated in thin metallic strips (mostly gold) and two-dimensional conducting materials like graphene[5].

We have used graphene as our material for making electrodes keeping in mind both controlled measurements for single molecules and possible scalability of the system. For these goals, we have decided to study other approaches to make nanogaps for connecting single molecules. In the coming sections, we will first discuss the choice of system and the approach we took and then we will present our findings.

7.2 Graphene vs metallic electrodes

There are certain advantages and disadvantages of both graphene and metallic electrodes. Metallic electrodes like gold electrodes have been used extensively for studying single molecules electronic transport due to their chemical inertness to impurities. Gold binds very strongly to sulphur and nitrogen atoms which makes thiols (-SH) and amines (-NH) popular as anchoring groups for attaching molecules chemically between two Au leads. In contrast, using graphene as electrodes for molecular electronics is rather new[3] and freshly exposed graphene edges during nanogap formation are very reactive and thus are prone to accumulate dirt on the edges. The

[4] Even in silicon-based devices the bulk band structure is defined by quantum mechanics and at small length scales quantum tunneling of electrons starts to cause increase in leakage current.

[5] In graphene, it is technically electroburning not electromigration

[1] Sujay B. Desai et al. In: *Science* 354 (2016), p. 99.
[2] Jeong Gon Son et al. In: *Advanced Materials* 25 (2013), p. 4723.
[3] Ferry Prins et al. In: *Nano Letters* 11 (2011), p. 4607.

anchoring groups, in this case, are mostly π-conjugated systems[3,4], fullerene[5] and amine groups[6,7][6]. Graphene electrodes are more stable in comparison to metallic electrodes, even at room temperature due to the reduced mobility of carbon atoms connected with sp^2 carbon bonds. The downside of graphene is that the mobility of electrons in graphene decreases dramatically with increasing concentration of defects[8,9]. Another benefit of metal electrodes is that the metallic bonds allow for repeated fusion and breaking of atomic-size contacts, in STM or MCBJ type of instruments.

Graphene-based single-molecule devices are predicted to have good thermoelectric properties[10]. Recent experiments[11] have shown that by careful tuning of molecular resonances large thermoelectric power factors can be achieved in such systems. Physisorbed molecular wires on graphene electrodes are predicted[12] to have a universal behaviour regarding the position of transmission resonances. This means that for various binding locations of the molecule with respect to the electrodes, the positions of transmission resonances with respect to Fermi energy remain intact, which is not expected for 3D metallic electrodes.

Out of all the properties of graphene, the one that I find most interesting comes directly from the fact that it is a 2D crystal, that means each atom of it is available to image and modify. In an ideal case, one can attach a molecule between graphene electrodes and image it, get all the information about the binding configuration and conformational state of the molecule with respect to the 2D electrodes. One can on-purpose make defects in the crystal at predefined positions to modify the charge transport by scattering of electrons through those defects (See Chapter 5). Another benefit of 2D electrodes is that one could use the STM tip to gate the molecule very locally and it would also be possible to probe it using light. A 2D structure will also reduce the screening of the gate potential in comparison to the metallic electrodes, and produce negligible image charge effects.

7.3 Electromigration, electroburning vs direct cutting methods

Making nanogaps using electro-migration in metallic electrodes is not new and has been demonstrated as a useful technique to study single molecules[13–16]. Graphene

[6] It is reported that these amine groups form covalent amide bonds with graphene, which are strong enough to withstand many chemical treatments.

[4] Jan A. Mol et al. In: *Nanoscale* 7 (2015), p. 13181.
[5] Konrad Ullmann et al. In: *Nano Letters* 15 (2015), p. 3512.
[6] Yang Cao et al. In: *Angewandte Chemie* 124 (2012), p. 12394.
[7] Yang Cao et al. In: *Angewandte Chemie International Edition* 52 (2013), p. 3906.
[8] Jeong-Yuan Hwang et al. In: *Nanotechnology* 21 (2010), p. 465705.
[9] Florian Banhart et al. In: *ACS Nano* 5 (2011), p. 26.
[10] Hatef Sadeghi et al. In: *Beilstein journal of nanotechnology* 6 (2015), p. 1413.
[11] Pascal Gehring et al. In: *Nano Letters* 17 (2017), p. 7055.
[12] V. M. García-Suárez et al. In: *Phys. Rev. B* 87 (2013), p. 235425.
[13] Hongkun Park et al. In: *Applied Physics Letters* 75 (1999), p. 301.
[14] Herre S. J. van der Zant et al. In: *Faraday Discuss.* 131 (2006), p. 347.
[15] Edgar A. Osorio et al. In: *Nano Letters* 7 (2007), p. 3336.
[16] Maria Rudneva et al. In: *Microscopy and Microanalysis* 19 (2013), p. 43.

electrodes on the other hand are mostly prepared using electroburning[3–5,11,17–28] techniques. Here, first a pre-patterned nano-ribbon or notch is made in the graphene using electron-beam lithography followed by oxygen plasma etching. The typical width of such a constriction is from 100 to 200 nm. For further narrowing down the notch, an electroburning process is used for which the presence of an oxygen environment is essential. In this process, at high current, a temperature activated reaction is started with the oxygen molecules striking the graphene lattice. This reaction removes the carbon atoms from the graphene lattice by oxidation. Due to highest current density the narrowest part of the junction gets heated most and burn. To add further control on the nanogap formation, a feedback loop is implemented. Here, first, the applied voltage across the pre-patterned junction is slowly increased (at a typical rate of 0.75 V/s to 1 V/s) with the feedback set to the measured current. Then as a drop in current is recorded, the voltage is ramped back to zero (at a typical rate from 0.225 mV/μs to 0.1 V/μs). This procedure is repeated until a tunnelling junction is formed, which is found mostly as having a resistance larger than 500 MΩ[7].

Just before the final breakdown to tunnelling, a sudden rise or peak in current in roughly 50 % of the junctions is reported. This mysterious peak was explained later[23] as a consequence of quantum interference with a crossover from multiple path connectivities of carbon atoms to single path connectivity. This is contradicted by another group[21,26] which claim to have not seen this peak in conductance and that there is a large chance of making uncontrollable gaps when the electro-burning is done in air. The same group[21,26] further claims to have achieved better control and large yield of nanogap formation while working in high-vacuum (10^{-7} mbar). They explain it as a sublimation process rather than an oxidation process as was the case in electroburning. Furthermore, the reason behind better control in high-vacuum is given based on the exothermic nature of the electroburning technique. Ullmann *et al*.[5] have performed also a similar high vacuum test (see their supplementary information) and reported no breakdown of the junction, rather emission of white light visible to the naked eye followed by a complete collapse of the structure. It is possible that the different substrates used in these experiments explains some of the differences in results.

Irrespective of the method used for making these graphene junctions, a large yield of formation (> 90 %) is claimed[3,21]. Important to note is that this yield does not

[7] IV measurements on single carbon atom chain[29] shows non-linear behaviour, but to a rough estimate for 150 mV it carries a current of 1 nA giving it a resistance of around 150 $M\Omega$.

[17] Enrique Burzur et al. In: *Graphene* 1 (2012), p. 26.
[18] Amelia Barreiro et al. In: *Nano Letters* 12 (2012), p. 6096.
[19] J. O. Island et al. In: *Journal of Physics: Condensed Matter* 26 (2014), p. 474205.
[20] C. S. Lau et al. In: *Phys. Chem. Chem. Phys.* 16 (2014), p. 20398.
[21] Cornelia Nef et al. In: *Nanoscale* 6 (2014), p. 7249.
[22] Pawe Puczkarski et al. In: *Applied Physics Letters* 107 (2015), p. 133105.
[23] Hatef Sadeghi et al. In: *Proceedings of the National Academy of Sciences* 112 (2015), p. 2658.
[24] Pascal Gehring et al. In: *Nano Letters* 16 (2016), p. 4210.
[25] Chit Siong Lau et al. In: *Nano Letters* 16 (2016), p. 170.
[26] Maria El Abbassi et al. In: *Nanoscale* (2017), pp. -.
[27] Laszlo Posa et al. In: *Nano Letters* 0 (2017), null.
[28] Syed Ghazi Sarwat et al. In: *Nano Letters* 17 (2017), p. 3688.

mean that this high percentage of junctions are usable. Gehring *et al*.[11] reports that only 16 % showed successful signatures of molecule deposition, which also include multi-molecule junctions. The success rate is reduced by the numbers of junctions that break but have a larger gap between graphene electrodes, multiple molecules binding or small weakly connected ($T < 0.5$) charging islands[3,20] left between the electrodes after electroburning. These islands can already give Coulomb blockade and Kondo signatures without any molecule deposition. Formation of similar islands is also seen in metallic junctions formed by electromigration in almost 30 % cases[14,30] and also in freestanding graphene[31]. A clear mechanism for the formation of these islands is not understood yet. It is believed that the formation of graphene quantum dots is due to electron-hole puddling or charge localisation, which could lead to the formation of these carbon islands as a leftover of electro-burning. In metallic junctions, this quantum dot formation was later avoided by using a self-breaking technique[32], where once a few conductance quanta were achieved by the usual electromigration technique, the contact is left to break by room-temperature thermal diffusion by putting the bias to zero. The quantum dot formation in graphene is not resolved yet.

This is a reason why many groups prefer using multi-layer graphene and graphene grown on SiC[5] because on doing this the formation of charge puddling is less. Burzuri *et al*.[17] have shown by measuring success statistics that the electroburning procedure is more controlled in this multi-layer graphene as compared to single layer graphene. As a draw-back, in case of multilayer graphene, the layers on the bottom (close to the substrate) are burned later than the ones on top, and thus the minimum gap width is near the substrate, which makes it difficult to image them using SPM.

The only other method used for making graphene electrodes for molecular electronics applications is dash-line lithography (DLL) technique developed by Cao *et al*.[6,7,33]. In the DLL technique sub 5 nm nanogaps are made in single-layer graphene on SiO_2 substrate using a combination of e-beam lithography and oxygen plasma etching. They first covered the graphene with PMMA, a window in the PMMA is opened using e-beam, and then by utilizing the gradual etching and undercutting of PMMA when exposed to oxygen plasma they were able to make graphene point contacts with sub 5 nm gaps. Conventional O_2 plasma etching (which is also normally used for pre-patterning the constriction in graphene for electroburning) produces a large number of defects on the edges and leads to coverage of the edges by carboxylic acid end-groups. Huang *et al*.[34] discusses a neutral beam method for making ultra low edge-defect graphene nanoribbons. In the neutral beam etching technique, the charged ions were neutralised, and the UV photons are reflected back by use of graphite based grids.

Thiele *et al*.[35] have used helium ion milling to make nanogaps of around 3 nm in graphene nanotubes where the gap size was estimated by studying the secondary electrons intensity profile. They demonstrated suspension of a 3.9 nm long OPE

[30] A. A. Houck et al. In: *Nano Letters* 5 (2005), p. 1685.
[31] J. Moser and A. Bachtold. In: *Applied Physics Letters* 95 (2009), p. 173506.
[32] K. O'Neill et al. In: *Applied Physics Letters* 90 (2007), p. 133109.
[33] Huimin Wen et al. In: *Science Advances* 2 (2016).
[34] Chi-Hsien Huang et al. In: *Carbon* 61 (2013), p. 229.
[35] Cornelius Thiele et al. In: *Applied Physics Letters* 104 (2014), p. 103102.

molecule in this gap using phenanthrene anchor groups. Other methods to do nanopatterning on graphene over SiO_2 includes selective carbothermal etching[36].

7.3.1 Estimation of nanogap size

The characterization of the width of the nanogap formed by electromigration or electroburning is difficult using direct measurement methods (like SEM/TEM/STM/AFM) and is commonly estimated by fitting the IV characteristics (or resistance) using the Simmons model[37,38]. Simmons' model can be used to calculate the current once a few free parameters are fixed: the gap width, the barrier height[3], cross-section area of the junction and the asymmetry in the bias voltage response . Nef *et al*.[21] point out that the Simmons model fitting should be valid for smaller bias only where the tunnel barrier can still be approximated by trapezoidal barriers. At higher bias, the trapezoidal tunnel barriers changed to a triangular shape and the effective gap size reduces. The voltage at which transition from trapezoidal to triangular shape tunnel barriers occurs can be estimated from a Fowler-Nordheim plot, i.e. plotting $\ln(1/V^2)$ vs $1/V$. However, the cross-section area of the junction is difficult to estimate, as there is no reason to assume the cut made by electroburning to form two parallel edges on the electrodes. Thus this value has to be adjusted by hand. Approximate values for the barrier height reported by different groups are around 0.24-0.5 eV which is much smaller than the work-function of graphite (around 5 eV). Moreover, in a recent article Posa *et al*.[27] have suggested that the substrate SiO_x may also take part in the tunnelling process which would lead to a broad range of possible values for the barrier height.

7.3.2 Direct cutting methods

Other than the above techniques there are many direct cutting methods which have been used for making structures in graphene and have not yet been explored from a molecular electronics perspective for making graphene-based electrodes. By direct cutting methods, we mean methods are not based on the selection of the desired gap distance from many attempts but rather can be used to make controlled and desired patterns in graphene. These include, focussed He ion beam[35,39–42], focused Ga ion beam[43], catalytic reaction based chiseling[44], and scanning probe microscopy tip induced cutting[45], which includes AFM[46] and STM[47,48]. Some studies on

[36] Péter Nemes-Incze et al. In: *Nano Research* 3 (2010), p. 110.
[37] John G. Simmons. In: *Journal of Applied Physics* 34 (1963), p. 1793.
[38] Ayelet Vilan. In: *The Journal of Physical Chemistry C* 111 (2007), p. 4431.
[39] Braulio S. Archanjo et al. In: *Applied Physics Letters* 104 (2014), p. 193114.
[40] Ahmad N. Abbas et al. In: *ACS Nano* 8 (2014), p. 1538.
[41] D. C. Bell et al. In: *Nanotechnology* 20 (2009), p. 455301.
[42] Nima Kalhor et al. In: *Microelectronic Engineering* 114 (2014), p. 70.
[43] Hu Li et al. In: *Scientific reports* 6 (2016), p. 19719.
[44] Wei Li Wang et al. In: *Nano Letters* 14 (2014), p. 450.
[45] Pasqualantonio Pingue. In: *Tip-Based Nanofabrication*. Springer, 2011, p. 357.
[46] Péter Nemes-Incze et al. In: *Scientific Reports* 7 (2017).
[47] Levente Tapaszto et al. In: *Nature Nanotechnology* 3 (2008).
[48] Gabor Zsolt Magda et al. In: *Nature* 514 (2014).

free-standing graphene using high-resolution TEM have also been performed[49,50] showing cutting (via a TEM sculpting process) and imaging of nanometer size gaps. The focused ion beam and electron beam etching techniques have not been tested very well for the amount of damage to the graphene lattice they do near the cut edge. The only images of the cuts are from secondary electrons and do not have the high resolution needed to address that.

7.4 Our approach

We decided to explore a few of the direct cutting methods, to study their potential for making graphene-based electrodes. The techniques that we choose for our study are the helium ion milling technique and cutting by scanning probe microscope tip. The benefit of direct cutting methods is that one can have well-defined gaps between the two electrodes which makes it possible to characterize them with STM at the atomic scale and the possibility to scale up to a circuit with many molecular units.

7.4.1 Helium-ion milling

The He ion milling (HIM) technique was claimed to give more narrow cuts and lower damage than e-beam techniques due to a smaller de-Broglie wavelength of helium ions[51,52] as compared to electrons. However, the amount of damage that occurs in the graphene lattice close to areas etched by HIM has not been shown at the atomic scale. We are targeting these HIM cuts for separating electrodes and hanging molecules between them, so the characterisation of the structure of graphene close to the edges is important. For this study, we choose graphene on boron nitride (BN) as our sample. The choice of BN as the substrate has three benefits. Firstly, as BN has a crystalline structure (compared to commonly used amorphous SiO_x) with lattice constant similar to that of graphene, the substrate corrugation is small which will make finding and imaging small cuts made by HIM easier. Secondly, BN is known to reduce charge puddling which increases the overall electron mobility of electrons. Thirdly, as BN forms a flat substrate for graphene with better lattice match, one can reduce the multiple scattering of secondary electrons, which is expected to reduce the damage near the etched area.

The graphene-BN sample was prepared in TU Delft with a multi-step wet transfer technique described by Dean *et al*.[53]. In this method, first the BN is exfoliated on a SiO_2 substrate while the graphene is exfoliated on a polymer stack consisting of PMMA and a water soluble layer. In the next step, the SiO_2 substrate is detached by floating the stack with graphene over a deionized water bath. After this the PMMA[8] with the monolayer graphene is clamped using a glass slide on a micro-manipulator. Then with the use of a modified optical microscope setup and an x,y,z micrometer

[8] The thickness of the PMMA is tuned to have a sufficient optical contrast for detection of the mono-layer graphene.

[49] Ye Lu et al. In: *Nano Letters* 11 (2011), p. 5184.
[50] Felix Bärrnert et al. In: *ACS Nano* 6 (2012), p. 10327.
[51] John Notte et al. In: *AIP Conference Proceedings* 931 (2007), p. 489.
[52] Max C. Lemme et al. In: *ACS Nano* 3 (2009), p. 2674.
[53] Cory R. Dean et al. In: *Nature nanotechnology* 5 (2010), p. 722.

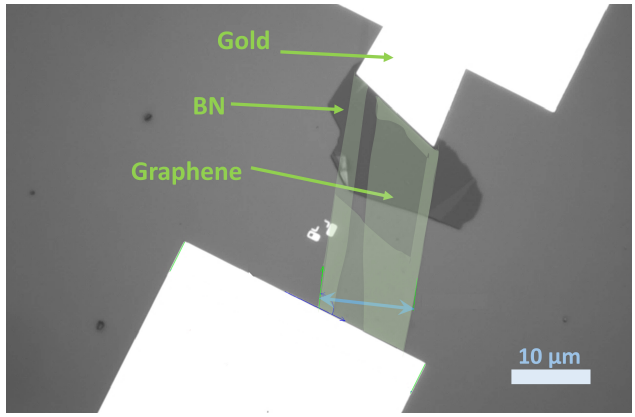


Figure 7.1: Graphene-BN sample prepared at TU Delft using the method described by Dean *et al*.[53].

stage, one can align the monolayer graphene over the multi-layer BN flake. Then by stamping graphene over BN and later dissolving the PMMA using acetone, one can transfer the graphene over the BN. An optical image of the sample is shown in Figure 7.1. Then Helium ion milling is used to make cuts in this graphene-BN sample using different ion doses (from 1×10^{16} to 8×10^{16} ions/cm^2).

The next task is to approach the STM tip on this small sample for imaging. Just to remind, the sample is prepared by exfoliation and so the size of such samples are of the order of a few tens of microns. Two methods were followed from here: first, an ambient JPK STM[9] was modified by use of an optical microscope to guide the STM tip to the small graphene flake. Second, for our UHV STM due to size constraint, it is not possible to mount an optical camera with sufficient resolution, which could guide the tip to the graphene flake. So, a capacitive sensing technique was implemented here. This is described in detail in the master thesis of Kim Akius[54]. A brief account is first given of the capacitive technique and then we will look into the helium ion beam induced cuts.

Capacitive scanning technique

The idea is to use the capacitance of the tip-sample system to navigate to the graphene flake, while avoiding the risk of crashing the tip on the non-conducting SiO_2 surface surrounding the graphene sample. The capacitance has an approximate $1/z$ dependence on distance between tip and sample which makes it more suitable for approach from large distance than the exponentially decaying tunneling current. Another fact that we use here is that the gradient of the measured capacitance signal with distance dC/dz is directly proportional to the gradient of the electric field dE/dz. By putting an equal and opposite bias voltage on the sample (i. e. graphene and gold pads) and the back gate (i. e. the highly doped Si substrate), one can enhance the electric field gradient (and thus the gradient of the capacitively measured signal) at the edges of

[9] https://www.jpk.com/

[54] Kim Akius, Master thesis, Leiden Institute of Physics (LION), Leiden University. 2015.

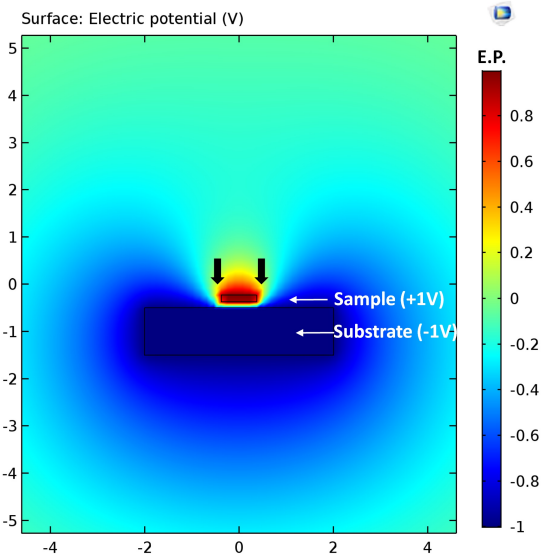
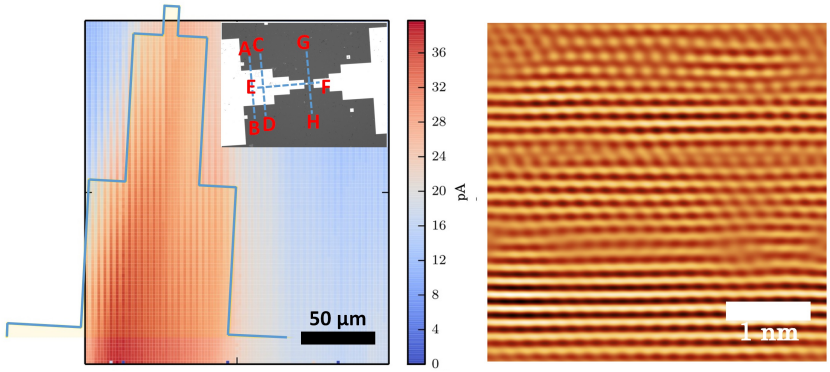


Figure 7.2: COMSOL Multi-physics output of an electric potential surface showing large gradients at edges marked by black arrows. The substrate (dark blue) is put at a potential of -1 V, while the sample (red) is put at 1 V. The color scale at the right encodes for the strength of the local electric potential.

the conductor (as shown in Figure 7.2). By combining these two ideas and by measuring the large electric field gradient one can image the boundaries of the gold leads that guide us to graphene by scanning at a distance of few microns above the surface. Figure 7.3(a) shows the capacitive image of the sample with the inset showing the corresponding optical image. The capacitive image shown here is a low-pixel image with only a small number of line scans, just to show the proof of concept that the implementation works. For landing on the graphene flake, we used a more direct method which we call the 'saddle point method' which will work for the symmetric leads geometry like ours. Here we first make two parallel line scans along the x-axis (AB, CD shown in the inset of Figure 7.3(a)). Then connecting the peak positions in AB and CD line scans, we define a new scan direction EF. The minimum in the capacitance measurement along this line gives the position of graphene. One can do a last check again along the line GH (parallel to AB or CD) if needed. Figure 7.3(b) shows an atomic resolution image we obtained after landing the STM tip into tunneling distance on graphene.

For the above test, we used a sample without HIM cuts. For our sample with HIM cuts, we decided to test it first in the ambient JPK STM. For this, as mentioned before, we used an optical microscope and mechanically etched tip to navigate to the micrometre size graphene sample. We also used a map of the surface topography and cuts made before by an ambient AFM measurement for navigation. Figure 7.4 (a) and (b) shows the HIM cuts in height and phase AFM image. This AFM map was essential as we want to keep the fast scan direction in STM mode perpendicular to the cut axis. This is to minimize the risk of tip crashes when the tip moves over



(a) (b)

Figure 7.3: (a) Image of the gold electrode using the capacitive scan (b) Atomic resolution using STM after approaching on the small patch of exfoliated graphene.

the cut as the BN substrate is an insulator. After this, we approached with the STM, but on scanning with STM, we found that there was a lot of contamination deposited close to the cuts. A line profile crossing all the cuts is shown in Figure 7.4 (c). The contamination could be due to bad vacuum in the HIM setup, which causes carbon deposit due to activation by the helium ions themselves. Unfortunately, we could not make another attempt with better vacuum due to technical problems in the HIM setup in TU Delft. However, it will be important in future to further explore cuts made on graphene using HIM and other FIB techniques.

With this experience we started to look for less intrusive techniques like SPM tip cutting techniques where the damage is very local and less sensitive to the cleanliness of the environment, so that there is minimal to no damage close to the place where the cut is made.

7.4.2 Scanning probe microscopy based cutting

The main benefit of cuts made by tips of atomic force microscope and scanning tunnelling microscopes is that there will be hardly any damage on the graphene lattice near the cut. We started by exploring the parameters for cuts made using atomic force microscope tips. This turned out to be a less promising approach because while attempting making smaller cuts we suspect we are creating local strains in the graphene rather than cutting through it. This is due to strong sp^2 bonds and high flexibility of the graphene lattice[46].

Scanning tunnelling microscope based cutting of graphene seems a better option to make smaller cuts. It needs to be made not by dragging the tip over the graphene surface as in AFM but rather by the localized breaking of bonds due to high field gradient between tip and sample. Although it shares some similarity with the electro-burning technique, there are also marked differences between the two. In electro-burning, a large cross-section (from 100 to 400 nm wide) of graphene is heated and partly burned, and the profile of the cut is not uniform or parallel. Here, in STM based cutting uniform parallel edges can be formed. Further, as the cuts are made

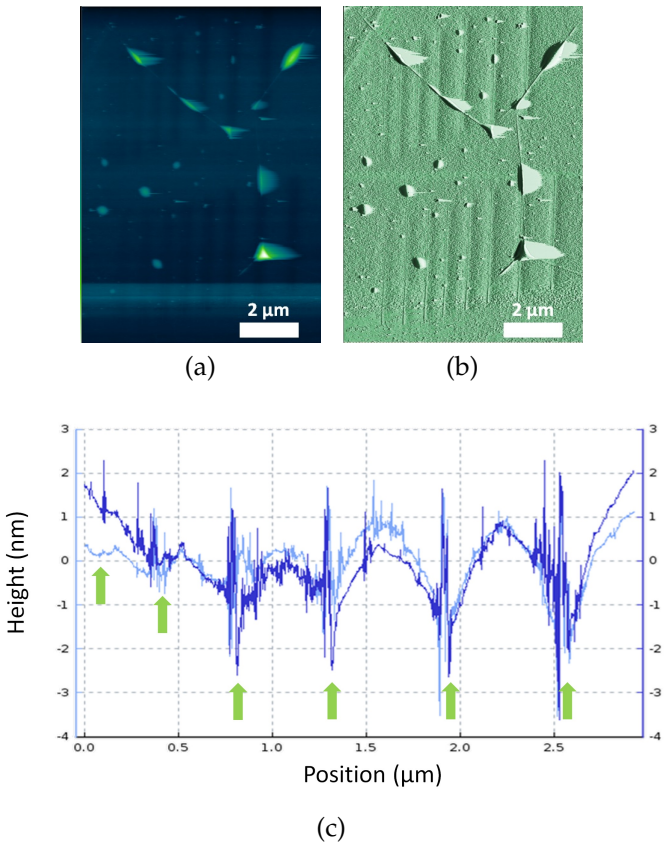


Figure 7.4: (a) AFM height image of a graphene sample on top of BN showing He ion beam induced cuts for doses ranging from 1×10^{16} to 8×10^{16} ions/cm^2. (b) Phase image using AFM of the same area. (c) Topography line profile crossing all the cuts using STM shows lot of contamination deposited close to the cut regions (marked by green arrows).

by moving the STM tip over the surface, any desired pattern can be cut into the graphene, which makes it very easy to shape multiple electrodes.

Such type of STM based cutting of graphene layers and graphite has been demonstrated earlier by many groups[47,48,55,56]. Albrecht et al.[55] in 1989 have shown a procedure for making cuts in graphite. They have tested it in air, vacuum, O_2, N_2, water, benzene and in water vapour environment. They report that the cut happens only in air and also in the presence of a mild partial pressure of water vapour (such as a vapour pressure of 25 mbar) but have not seen any cut formation in vacuum below 13 mbar and not in oxygen or nitrogen environment nor in pure water and benzene environment. They claim that the cutting cannot be a mechanical effect and further

[55] T. R. Albrecht et al. In: *Applied Physics Letters* 55 (1989), p. 1727.
[56] Hidefumi Hiura. In: *Applied Surface Science* 222 (2004), p. 374.

claim that water is important for cutting. A chemical reaction induced by the pulse may be responsible for cutting. Similar results with better control over the cleanliness of the cuts have been shown later by Kondo *et al*.[57], Hiura[56] and Tapaszto *et al*.[47] who have used it for making graphene nanoribbons. Magda *et al*.[48] have used this method to make nano-ribbons in graphene transferred onto a Au surface. In contrast to the work by Albrecht et al.[55], Kondo *et al*.[57] have shown that cuts in graphite can also be made in UHV which takes place via sublimation at higher bias.

Study of the mechanism behind STM cutting

Important to note is that the mechanism proposed for this cutting technique suggests that a water layer on top of the graphene is essential. This is interesting because the electroburning of graphene is also performed mostly in ambient conditions, but the oxidation of graphene there is supposed to be initiated by oxygen in the environment rather than water layer on the surface. The close proximity of the STM tip to the surface may limit the number of oxygen molecules striking the region below the tip, and the cutting by the STM tip does not result from burning due to poor heat transport to the bulk but is rather a chemical reaction in the presence of water. Using the STM based localized cutting technique for graphene placed on insulating substrates will be an interesting test of the mechanism. One can further test this STM based cutting over pre-patterned graphene nanoribbons, where heat transport to the banks is also reduced.

To show the potential of this technique, I present sub 5 nm clean, controlled cuts (Figure 7.5) made into the top graphene layer on graphite using an STM tip. The parameters used here were 2.8 V bias, 6 nA tunnel current, 5 nm/sec tip speed. Very few attempts have been made in the past in this direction due to the exponential dependence of the tunnelling current. On cutting the layer below the tip, the size of the vacuum gap changes which reduces the tunnelling current abruptly and the feedback control loop could start to rattle[45]. Further, this could also lead to a tip crash when there is only one layer of graphene and an insulator below it. So before we start with graphene on an insulating substrate, we need to get the process under control and the parameter space properly tested.

I will discuss now in detail, the effect of different parameters (tunnelling current, bias, and tip speed) and try to understand the cutting mechanism at the atomic scale[10]. We will also show a time evolution study of the cut. For this, we test bias values from 2.6 V to 2.9 V and tunnelling currents from 500 pA to 1.5 nA, by making a 10×10 grid as shown in Figure 7.6. Here, instead of making line cuts, we decided to test the parameters by making pits or holes into the top graphene layer. So, instead of the tip speed, we kept a fixed tip hold time[11] of 2 seconds while fixing the position of the STM tip. We see in Figure 7.6, that the cuts are less sensitive to the tunnelling current than to the bias voltage. As the reaction in the presence of water is endothermic, high tunnel currents could increase the reaction rate. However, the magnitude of tunnel current we are working with will generate a very small amount of heat and thus it

[10] This work is done together with Kim Akius, PhD student in our group.

[11] Hold time is a time-period in which the STM tip is kept at a particular (x,y) position above the graphene layer (at a tunnel gap) where the cut is supposed to be made.

[57] Seiichi Kondo et al. In: *Applied Surface Science* 75 (1994), p. 39.

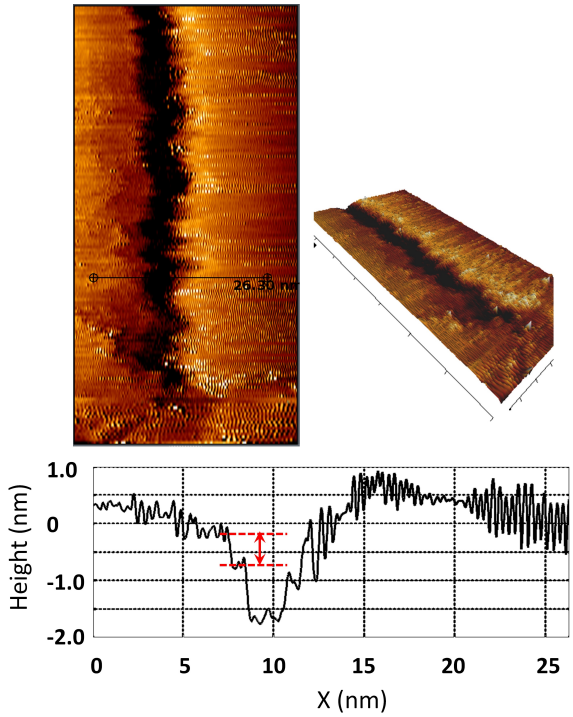


Figure 7.5: Sub 5 nm cut made using STM tip manipulation. A layer step height is marked with the red arrow.

may not increase the local temperature more than 5 deg[56], so the effect of the tunnel current is estimated to be minimal.

Next, we fixed the tunnel current value to 500 pA and bias to 2.85 V and we performed a scan over the hold time (from 10 ms to 1 sec). Figure 7.7 shows, how the cut topography changes for different hold times. The procedure starts at the bottom-left corner with 10 ms hold time and ends at the top-right corner with 1 sec hold time. The hold time is always increased (with equal steps) moving up in each column. This is in fact, a time evolution of the cut for a particular bias and tunnel current value. What we see in this time evolution is that at the earlier stages of the cut, the top layer graphene seems to be only deformed, while as the time evolves, at some point cuts start to appear.

To understand the process further, we need to examine the sequence of operations performed. The procedure used for cutting is– first change the tunnel current setpoint to 500 pA while keeping the bias at 100 mV, this moves the tip closer to the surface. Until this point, there will be no cut as the bias is very small. Next, we slow down the feedback, to avoid rattling of the STM tip. Then we set the bias to the desired value of 2.85 V with a ramp speed of 10 V/s. Due to slow feedback, the STM tip slowly moves away from the surface. Such a procedure lifts locally the top layer graphene with the tip due to electrostatic forces. This breathing mode of graphene has been reported

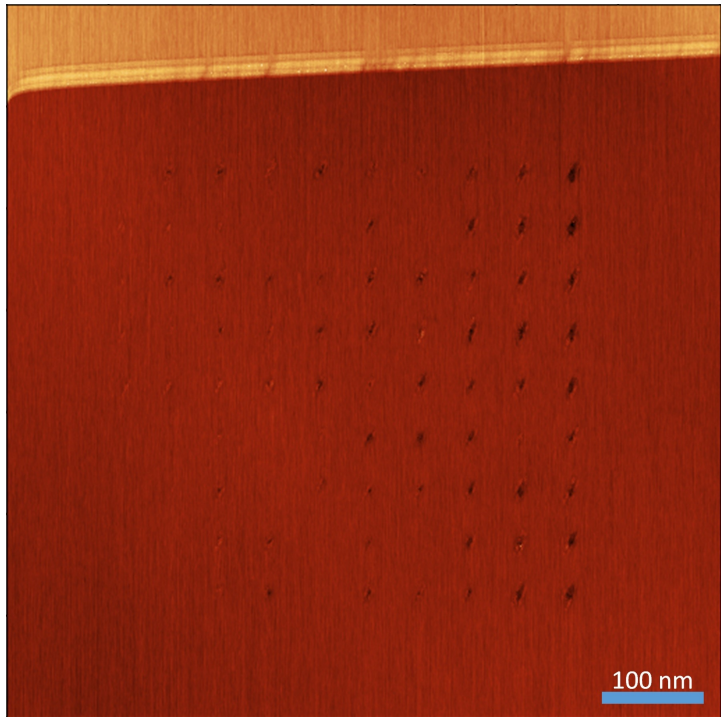


Figure 7.6: Parameter space study of STM current and voltage controlled cutting: In this 10×10 grid the tip-sample bias is increase from 2.6 V to 2.9 V with equal steps in the horizontal direction from left to right, so each column corresponds to one bias value. The tunneling current setpoints are increased from 0.5 nA to 1.5 nA in the vertical direction from bottom to top. Each point is spatially separated by a distance of 50 nm in the horizontal and vertical direction.

earlier[58,59]. As the tip is pulled up by the feedback, the bias is also increasing. The hold time is measured from the moment the bias is set by the software. Figure 7.8 shows an STM image of such a lift of the top layer graphene.

At the same time during this feedback-controlled lifting the bias continues to increase, which can create sufficiently large field gradients to initiate reactions with the layer of water on top of graphene. This reaction of carbon with water can remove carbon from the graphene by forming CO and H_2 gases[47,56,57] as products. Lifting of the top layer of graphene due to electrostatic forces can also break C-C bonds in graphene[60] by stretching. This was shown under ultra-high vacuum conditions where the presence of water on the surface can be neglected. This means that the cut in the top layer graphene that we see at the end can also be occurring due to the strain caused by the STM tip.

In either case, by controlled selection of parameters, we could attain cuts with

[58] Hong Seng Wong et al. In: *ACS Nano* 3 (2009), p. 3455.
[59] P. Xu et al. In: *Phys. Rev. B* 86 (2012), p. 085428.
[60] C. Rubio-Verdu et al. In: *Phys. Chem. Chem. Phys.* 19 (2017), p. 8061.

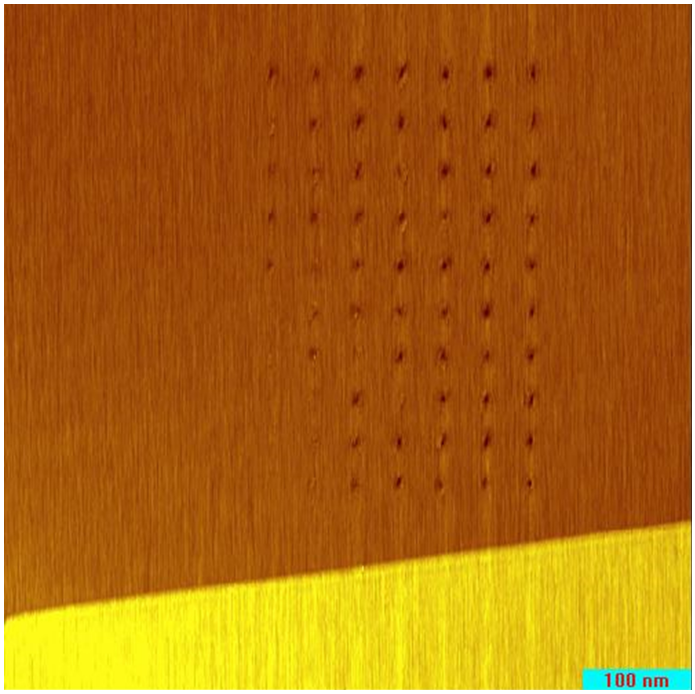
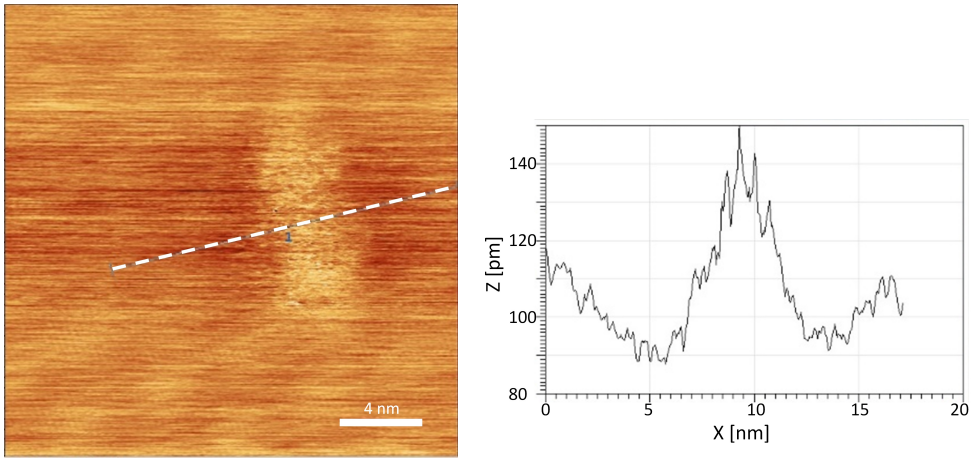


Figure 7.7: Time evolution study of the cut: In this 10×10 grid the tip-sample bias and tunneling current setpoint are fixed at 2.85 V and 500 pA. The hold time is increased with equal steps between 10 ms to 1 sec. Each point is spatially separated by a distance of 50 nm in the horizontal and vertical direction.

the full width half maximum (FWHM) of around 1.61 nm as shown in Figure 7.9. As the cuts happen while the top-layer graphene is isolated from the bulk graphite, we think this technique should be easily applicable to make controlled cuts on graphene over an insulator.

7.5 Conclusion

We have demonstrated the potential of STM based technique for making controlled nano-gaps into the top-layer of graphene over graphite. This technique holds strong similarities with the commonly used electro-burning technique with an added advantage that here the burning due to oxidation or sublimation (under UHV)[57] can be done locally and with better control. This STM based technique needs to be developed further and applied to graphene over an insulator. In order to decide whether the cutting of the top layer graphene shown here is because of strain induced by electrostatic forces or oxidation due to the presence of water or both, we need to repeat the experiments by changing the order of operations. In the experiments described above, we first define the setpoint tunnel current and tuned the feedback slow. Following this we ramped the bias to the desired value. This made the STM tip to first come close to the surface and then retract pulling with it the top graphene layer. Another procedure to do this is to start by first retracting the tip a couple



(a) (b)

Figure 7.8: (a) A hump formation due to pull out of a single layer graphene at early stages (49.6 ms hold time) of the cut with 500 pA tunnel current and 2.85 V bias. (b) Line profile made along the white line.

of nanometers above the scanning position and slowing down the feedback. Then change to the desired tunnel current setpoint and begin ramping the bias. This will make the STM tip to move only closer to the surface until the height corresponding to the set tunnel current and bias is achieved. This will avoid lifting of the top layer.

Alternatively, one could match the speed of tip retraction and the rate of bias change such that the field gradient is kept constant throughout. By doing this, the cut (if any) will only be formed because of tip-induced electrostatic pulling of the top graphene layer. However, the cuts where multiple graphene layers are cut using STM tip induced manipulation are more likely due to oxidation.

For cuts to be made in graphene over an insulator using STM tips, we need to implement a custom feedback loop. As we cut the part of graphene below the tip, the tunnel current will decrease, and the standard feedback will bring the tip closer looking for the desired setpoint. This is also what happens in graphite, but there the tip on coming closer by one atomic layer distance starts to tunnel into the layer below and ideally stops there until new water molecules arrive or the operation is aborted when the hold time is finished. In graphene on an insulator, as there is no conducting layer beneath, the STM tip will come to the surface until the setpoint tunnel current is achieved by tunneling from the side of the etched region. On arriving at this point, the cutting may continue through the sides as there is water all over the graphene. This may thus lead to crashing of the tip to the insulator. A custom-made feedback system with a predefined cut-off limiting the z displacement to less than one atomic layer height can be implemented.

A first application of this method would be the possibility of making more than two electrodes on a molecular junction using the STM cutting technique, in the form of a side-gate. Puczkarski et al.[22] have demonstrated the fabrication of a three-terminal single electron transistor (SET) using graphene electrodes with a side gate using the electroburning technique. They claim a three-fold increase in gate coupling

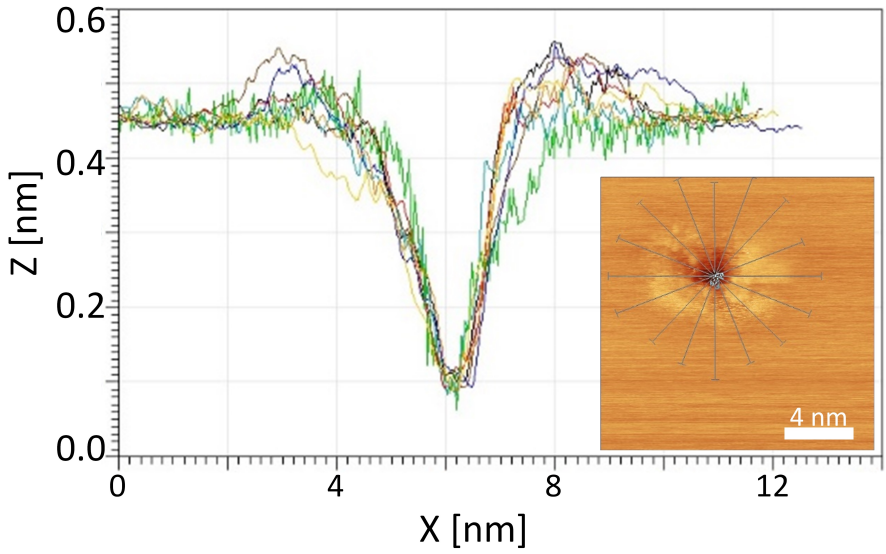


Figure 7.9: Line scans over a cut made with optimized parameters shows a full width half maximum (FWHM) of 1.61 nm with depth of one layer of graphene. Inset shows the corresponding STM image.

in comparison to the conventional back-gate technique and further claim a gap size of several nanometers as obtained from a Simmons fit.

Appendix

A. Atomic manipulation

A.1 Force derivation

Here the force on an atom resulting from the potential energy (E) of Equation 2.1 is derived.

$$E = -\zeta \sum_{i}^{N} \sqrt{\sum_{j \neq i}^{N} e^{-2q(r_{ij}/r_0 - 1)}} + A \sum_{i}^{N} \sum_{j \neq i}^{N} e^{-p(r_{ij}/r_0 - 1)} \tag{A.1}$$

Now calculating the gradient of this energy will provide the forces acting on atom a,

$$\vec{F}_a = -\vec{\nabla}_a E \tag{A.2}$$

We will have to find

$$\vec{F}_a = -\vec{\nabla}_a \left[-\zeta \sum_{i}^{N} \sqrt{\sum_{j \neq i}^{N} e^{-2q(r_{ij}/r_0 - 1)}} + A \sum_{i}^{N} \sum_{j \neq i}^{N} e^{-p(r_{ij}/r_0 - 1)} \right] \tag{A.3}$$

For the component k of the force ($k = x, y, z$), this becomes

$$
\begin{aligned}
F_{a,k} &= -\frac{\partial E}{\partial k_a} \\
&= -\frac{\partial}{\partial k_a}\left[-\zeta \sum_{i}^{N} \sqrt{\sum_{j\neq i}^{N} e^{-2q(r_{ij}/r_0-1)}}\right] - \frac{\partial}{\partial k_a}\left[A \sum_{i}^{N}\sum_{j\neq i}^{N} e^{-p(r_{ij}/r_0-1)}\right] \\
&= \zeta \frac{\partial}{\partial k_a}\left[\sum_{i\neq a}^{N} \sqrt{\sum_{j\neq i}^{N} e^{-2q(r_{ij}/r_0-1)}} + \sqrt{\sum_{j\neq a}^{N} e^{-2q(r_{aj}/r_0-1)}}\right] \\
&- A \frac{\partial}{\partial k_a}\left[\sum_{i\neq a}^{N}\sum_{j\neq i}^{N} e^{-p(r_{ij}/r_0-1)} + \sum_{j\neq a}^{N} e^{-p(r_{aj}/r_0-1)}\right] \\
&= \zeta \sum_{i\neq a}^{N} \frac{\partial}{\partial r_{ia}} \sqrt{\sum_{j\neq i}^{N} e^{-2q(r_{ij}/r_0-1)}} \frac{\partial r_{ia}}{\partial k_a} + \zeta \frac{\partial}{\partial k_a} \sqrt{\sum_{j\neq a}^{N} e^{-2q(r_{aj}/r_0-1)}} \\
&- A \sum_{i\neq a}^{N} \frac{\partial}{\partial r_{ia}} \sum_{j\neq i}^{N} e^{-p(r_{ij}/r_0-1)} \frac{\partial r_{ia}}{\partial k_a} - A \frac{\partial}{\partial k_a} \sum_{j\neq a}^{N} e^{-p(r_{aj}/r_0-1)} \\
&= \zeta \sum_{i\neq a}^{N} \left[\frac{1}{2\sqrt{\sum_{j\neq i}^{N} e^{-2q(r_{ij}/r_0-1)}}} \left(\frac{-2q}{r_0}\right) e^{-2q(r_{ia}/r_0-1)} \frac{\partial r_{ia}}{\partial k_a}\right] \\
&+ \frac{\zeta}{2\sqrt{\sum_{j\neq a}^{N} e^{-2q(r_{aj}/r_0-1)}}} \left(\frac{-2q}{r_0}\right) \sum_{j\neq a}^{N} \left[e^{-2q(r_{aj}/r_0-1)} \frac{\partial r_{aj}}{\partial k_a}\right] \\
&- A \sum_{i\neq a}^{N} \left[\left(-\frac{p}{r_0}\right) e^{-p(r_{ia}/r_0-1)} \frac{\partial r_{ia}}{\partial k_a}\right] - A \sum_{j\neq a}^{N} \left[\left(-\frac{p}{r_0}\right) e^{-p(r_{aj}/r_0-1)} \frac{\partial r_{aj}}{\partial k_a}\right] \qquad \text{(A.4)}
\end{aligned}
$$

where, when we take k to be x,

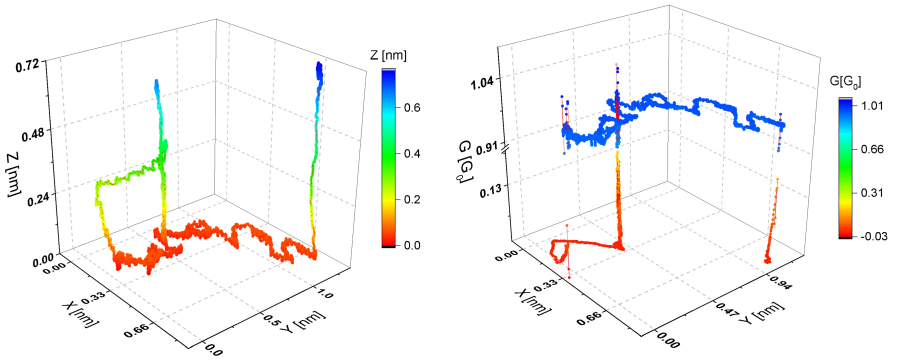
$$
\begin{aligned}
\frac{\partial r_{ij}}{\partial x_a} &= \frac{\partial}{\partial x_a} \sqrt{(x_i - x_j)^2 + (y_i - y_j)^2 + (z_i - z_j)^2} && \text{(A.5)} \\
&= \frac{2(x_a - x_j)}{2\sqrt{(x_a - x_j)^2 + (y_a - y_j)^2 + (z_a - z_j)^2}} \delta_{ia} \\
&- \frac{2(x_i - x_a)}{2\sqrt{(x_i - x_a)^2 + (y_i - y_a)^2 + (z_i - z_a)^2}} \delta_{aj} && \text{(A.6)} \\
&= \frac{x_a - x_j}{r_{aj}} \delta_{ia} - \frac{x_i - x_a}{r_{ia}} \delta_{aj} && \text{(A.7)}
\end{aligned}
$$

and similarly for y and z component, with δ_{ij} the Kronecker delta function. Substituting this in the force, we get

$$
\begin{aligned}
F_{a,k} = \zeta \sum_{i \neq a}^{N} & \left[\frac{1}{2\sqrt{\sum_{j \neq i}^{N} e^{-2q(r_{ij}/r_0 - 1)}}} \left(\frac{-2q}{r_0} \right) e^{-2q(r_{ia}/r_0 - 1)} \left(\frac{k_a - k_i}{r_{ia}} \right) \right] \\
& + \frac{\zeta}{2\sqrt{\sum_{j \neq a}^{N} e^{-2q(r_{aj}/r_0 - 1)}}} \left(\frac{-2q}{r_0} \right) \sum_{j \neq a}^{N} \left[e^{-2q(r_{aj}/r_0 - 1)} \left(\frac{k_a - k_j}{r_{aj}} \right) \right] \\
& - A \sum_{i \neq a}^{N} \left[\left(-\frac{p}{r_0} \right) e^{-p(r_{ia}/r_0 - 1)} \left(\frac{k_a - k_i}{r_{ia}} \right) \right] - A \sum_{j \neq a}^{N} \left[\left(-\frac{p}{r_0} \right) e^{-p(r_{aj}/r_0 - 1)} \left(\frac{k_a - k_j}{r_{aj}} \right) \right] \\
& = -\zeta \frac{q}{r_0} \sum_{i \neq a}^{N} \left[\frac{e^{-2q(r_{ia}/r_0 - 1)}}{\sqrt{\sum_{j \neq i}^{N} e^{-2q(r_{ij}/r_0 - 1)}}} \left(\frac{k_a - k_i}{r_{ia}} \right) \right] \\
& - \frac{\zeta (q/r_0)}{\sqrt{\sum_{j \neq a}^{N} e^{-2q(r_{aj}/r_0 - 1)}}} \sum_{j \neq a}^{N} \left[e^{-2q(r_{aj}/r_0 - 1)} \left(\frac{k_a - k_j}{r_{aj}} \right) \right] \\
& + 2A \frac{p}{r_0} \sum_{j \neq a}^{N} e^{-p(r_{aj}/r_0 - 1)} \left(\frac{k_a - k_j}{r_{aj}} \right)
\end{aligned}
\tag{A.8}
$$

A.2 Lifting of gold atomic chain

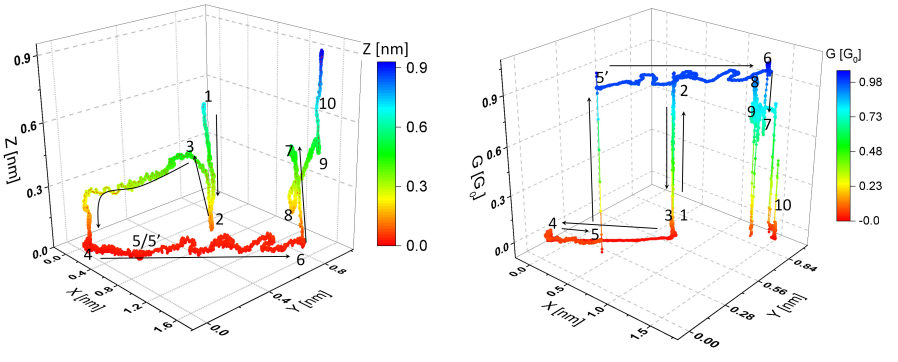
In chapter 2 a controlled formation of free standing atomic chain between STM tip and sample is demonstrated. The total operation is divided into two steps. In first step the ad-atom 'A' (marked in Figure 2.6) is pushed from position 'i' to 'ii' and then a STM image is taken (Figure 2.6(b)). The corresponding x,y,z and x,y,G curves for this operation are given here in Figure A.1. In the second step we start from position 'ii'



(a) (b)

Figure A.1: (a) Complete tip trajectory for the first step starting from position 'i' in the lattice and (b) variation in conductance over the time of operation.

and move the ad-atom 'A' to position 'iii' and then continue with the lifting operation followed by taking the STM image at the end (Figure 2.6(c)). Figure A.2(a) shows the tip trajectory for the second step and Figure A.2(b) shows the corresponding conductance variation over the time.



(a) (b)

Figure A.2: (a) Complete tip trajectory for the second step ending in a lift-off of a mono-atomic gold chain from the Au(111) surface and (b) variation in conductance during the lift-off of the atomic chain.

A.3 Point-contact push manipulation technique

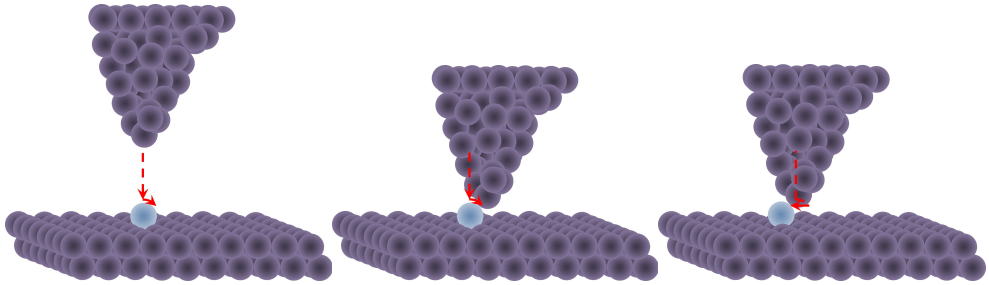


Figure A.3: Point contact push technique: (a) The tip is placed vertically over the ad-atom before a point contact is made by bringing the STM tip vertically downwards, (b) Once the a point contact is made the STM tip is moved in a circular trajectory while keeping into point contact to bring the tip behind the ad-atom, (c) Once the tip is placed behind the ad-atom it moves the later to the next hollow site.

Appendix

B. Molecular manipulation

B.1 GPU programming

What is a GPU (Graphics Processing Unit), how it is different from a CPU (Central Processing Unit) and what makes a GPU useful? Although both CPU and GPU have high computational abilities, the main difference between them is the type of computation they are designed for. CPUs are optimized for doing serial computation (or 'integer calculations' as they are called) for example: writing a text document, browsing the web etc. These are serial tasks because if you have to write a text: "*CPUs are very good in serial computation.*", you have to go one word after the other, you cannot type a text in parallel. GPUs, on the other hand, are good in performing parallel computations (or 'floating-point calculations') for example rendering 3D graphics, processing video compression etc. So, why is rendering 3D graphics a parallel process? In 3D graphics, everything is made of many small triangles (for example see Figure B.1) and rendering the image means moving (or transforming) of the three vertices of these triangles. These transformations (scaling, translation or rotation) are done by matrix multiplications which include a large number of mutually independent computations, that can be executed simultaneously as a parallel computation.

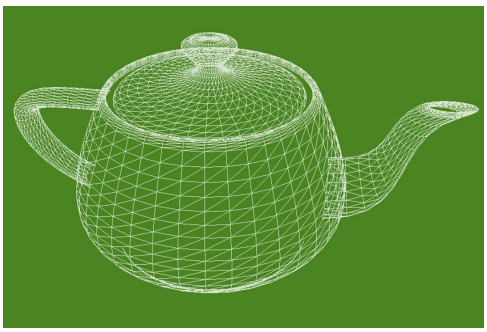


Figure B.1: Image of a kettle with triangular mesh used in 3D graphics.

B.1.1 Programming in the CUDA framework

The CUDA programming interface provides an abstraction to general purpose GPU (GPGPU) programming through the use of a number of models, most importantly the programming model and the memory model[1]. The programming model drives the programmer to follow a certain structure in writing his/her code, which is then mapped to the GPU architecture. This allows for optimizing the code at a low level while retaining the functionality and high flexibility of the C++ language. The memory model obeys this same principle, requiring to some extent manual memory management that is, manual memory allocation and de-allocation on the GPU, and explicit data copying without having to interfere with the details of transfers at the assembly level.

Hardware structure

nVidia GPUs[1] come with three sets of hierarchy: a hardware-based hierarchy, a programming model or task execution based hierarchy and last a memory model based hierarchy. To understand the complete hierarchy with concrete numbers, let us look at the specs of our nVidia GPU only and start with the hardware-based hierarchy. Table 3.1 shows the main device structure related configurations. The highest in the hierarchy sits the GPCs (Graphics Processing Clusters), our nVidia GPU has 2 GPCs. Each GPC further has 4 Streaming multiprocessors (SMM, The extra 'M' coming from 'Maxwell Architecture'). Now, each SMM has four processing blocks, which have their instruction buffer and *warp* scheduler. Inside each processing block, there are 4×8 i.e., 32 CUDA cores, which makes a total of 4×32, i.e., 128 CUDA cores per SMM and a total of 1028 CUDA cores in the GPU card. These CUDA cores are also called SPs (Streaming Processors). More abstract entities like threads, blocks etc. comes under the task execution stream.

Programming model or task execution model

The basic building block of any CUDA application is a *kernel*. This *kernel* is the operation or mutually independent computation that you want to be repeatedly computed many times. For example, if you have to add two matrices then 'adding a pair of elements with same indices in the two matrices' is a mutually independent computation and so is a *kernel*. Such a *kernel* can be called either from the CPU or the GPU. In a GPU many instances of the same instructions or computations defined in *kernels* are executed by what are called *threads*[2]. through a very hierarchical task execution model. In the CUDA programming guide by Cook[1] this hierarchy in which the tasks are performed is seen in analogy with a hierarchy in an army. This analogy helps in appreciating the task divisions, so we will explain it like that. A schematic is shown in Figure B.2. The lowest in the hierarchy are the *threads* or the 'soldiers'. These 'soldiers' are divided into different 'units' called *blocks*. A 'unit' is split into 'squads' of 32 'soldiers' called a *warp*. Different 'units' together constitutes an 'army' called a *grid* in GPU terminology. Though each 'soldier' or *thread* does its individual job, but a task coming from the 'Colonel' or the *kernel* is always allotted per 'squad' and not to an individual 'soldier'. So, a 'squad' or *warp* forms a basic unit

[1] http://docs.nvidia.com/cuda/cuda-c-programming-guide/index.html#axzz4r4uG4Vkc

[2] The *thread* is just an abstract entity that represents the execution of the *kernel*.

[1] Shane Cook. Newnes, 2012.

of execution on the GPU. The 32 number of *threads* in *warp* called *warpSize* is set by nVidia and it reserves the right to change this in the future. How the information flow happens between different parts of this task execution model will be discussed in the next section where we will discuss the memory model based hierarchy. Lets now look at some more quantitative numbers from the Table 3.1. The maximum block size is given as $1024 \times 1024 \times 64$, but this does not mean that we have a number of $1024 \times 1024 \times 64$ threads per block. The maximum number of threads per block is given as 1024 in Table 3.1, this means that the dimensions of the *thread block* i.e. $[\tau_x, \tau_y, \tau_z]$ should be chosen such that $\tau_x \times \tau_y \times \tau_z \leq 1024$. For example: one could have block dimensions $(32, 32, 1)$ or $(1, 1024, 1)$ or $(16, 1, 64)$ etc. *Thread blocks* can also have lower dimensions, though the execution of these *threads* happens in the same way irrespective of whether one uses multiple dimensions or not, doing so can ease the design of algorithms that have to handle multi-dimensional data, such as matrices. The size of each *grid* is normally dictated by the size of the data set to be processed by the *kernel*, while the *block* size is often algorithm-specific. Depending on the algorithm, it may occur that calling a *kernel* with a certain *block* size may result in better performance than other sizes, and the optimal *block* size may depend on many variables[2]; hence, this size is often chosen empirically.

Memory model

As we know, a CPU has different types of memory in it like drive memory, random access memory (RAM), register memory and others. Similar to this a GPU also has a memory architecture which could vary a little from one GPU to other. Data is transferred between CPU and GPU device memory via the PCI-e bus, in our case it is PCIe 3.0 (with x16 link) having a total bandwidth of 32 GB/s. GPU device memory in our case is the GDDR5 graphics RAM and can be divided broadly into global and local memory. Out of the two, the global memory (4096 MB) is what connects to the CPU and can also be accessed by all the threads, through an L2 cache. The memory declared[3] in the global memory stays untill the end of the lifetime of the application or can only be erased by a host command[4] and will then be available for other applications. A schematic view of the CUDA memory model is shown in Figure B.3.

Within each thread block, threads can write to a chunk of so-called shared memory, which may vary in size as defined by the user upon calling a kernel. This shared memory lies on-chip on the streaming multiprocessors (SMM) directly, and so has two orders of magnitude lower latency than global memory. A lot of performance optimisation involves maximising shared memory usage above global memory. One must keep in mind, though, that shared memory is limited (in our case we have around 96 KB of shared memory per SMM), and using too much of it per block will reduce the number of blocks that can run in parallel. By sharing the memory access among different threads, redundant computations can be avoided and thus can reduce the global memory bandwidth. In fact, shared memory is very similar to a memory cache of a CPU with a major advantage in GPU that here it can be

[3] You can declare a part in the global memory by calling *cudamalloc*

[4] *cudaFree* can be used to erase the global memory

[2] Henry Wong et al. In: *Performance Analysis of Systems & Software (ISPASS), 2010 IEEE International Symposium on*. IEEE. 2010, p. 235.

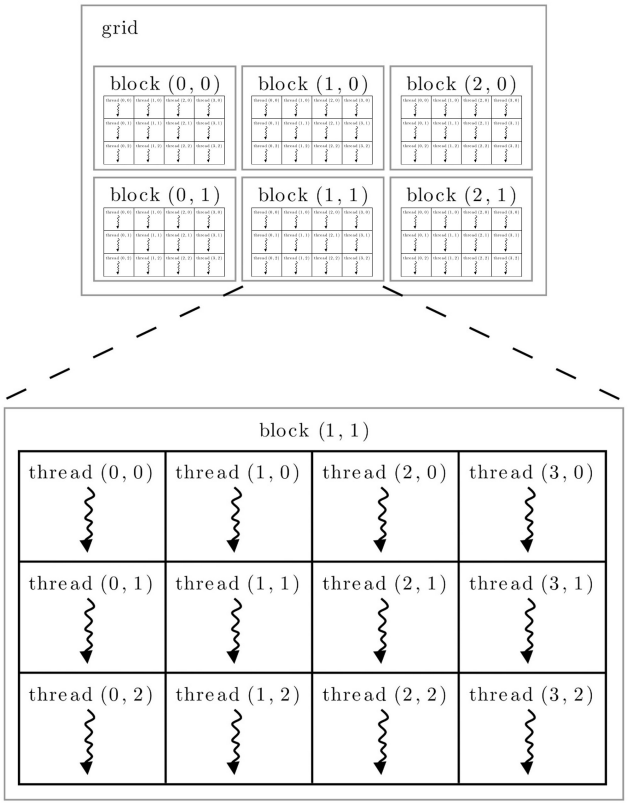


Figure B.2: A two-dimensional grid of blocks, where each *thread block* also has two dimensions. Typical *thread* blocks will in reality contain more than twelve *threads*, since *threads* are dispatched in groups of 32 on the GPU.

completely managed by the programmer. A part of the device memory where you can declare constants directly from the host code[5] is called constant memory. Being in the device memory this readout is slow but each SMM has around 8 to 10 KB of constant memory cache, which means every time you read from constant memory (which is total 64 KB in size) lying in the device memory the data will be cached in the constant memory cache. This helps in reducing the waiting time during one complete task execution.

Lastly, each thread can store its local variables in thread memory, which is implemented as a 32-bit register file. Registers are on-the-chip and thus also the fastest parts of GPU memory with least latency. This memory is private to the thread and so cannot be shared with other threads. In case of insufficient space in the registers, a thread can store its local variable in the local memory which sits off-chip in the device memory and thus is almost two orders of magnitude slower than registers. Both these private thread memories are managed by the compiler directly and cannot

[5] using *cudaMemcpyToSymbol()* command

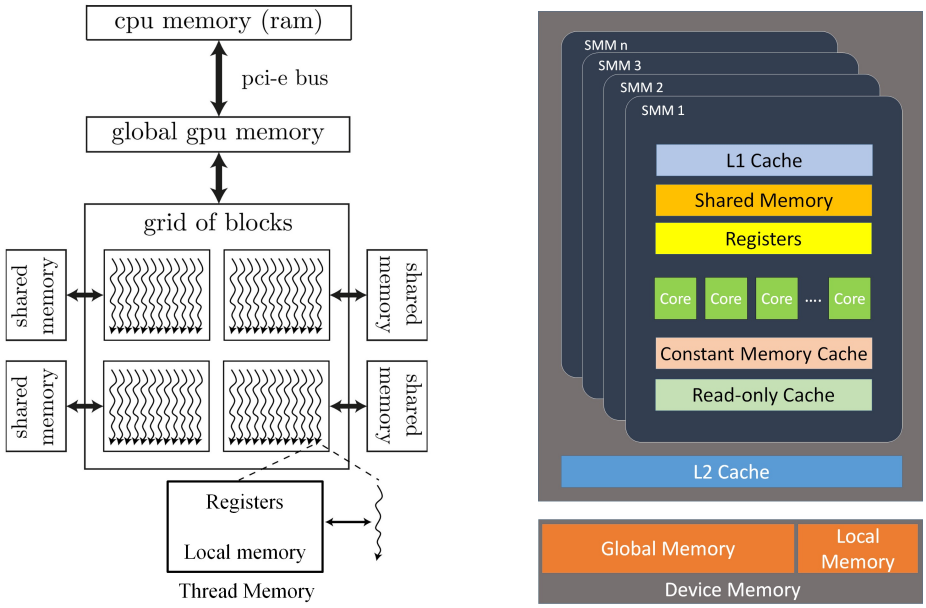


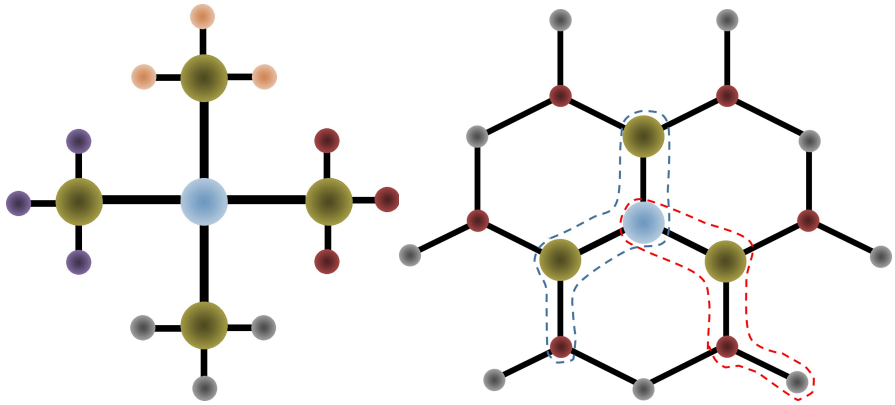
Figure B.3: The Cuda memory arrangement. Each grid of blocks (that is, all threads within a grid of thread blocks) is connected to the global memory, which is bridged to the cpu ram via a pci-e bus. Each thread block has a separate chunk of block memory, and each thread can also use its own thread memory.

be controlled by the programmer. The lifetime of these is equal to the lifetime of the thread itself. So, when a thread has finished executing all the tasks, these thread memories will be automatically erased.

B.2 Intramolecular forces

The intramolecular forces consist of bond forces, angular forces and torsional forces. For a molecule, with a maximum of n bonds per atom (single, double or triple covalent bonds are all counted as one bond), the maximum number of bond forces calculations n_b per atom is n.

Next, we estimate the maximum number of angular forces calculations n_a per atom and the maximum number of torsional forces calculations n_t per atom. For this, consider the illustration in Figure B.4 (a). It shows a simplified geometric construction of a molecule with four bonds per atom. In reality, a molecule with four bonds per atom is more likely to be non-planar, but for the sake of simplicity, we draw it planar here. In the picture, the centre atom (shown in blue colour) has four 1^{st} neighbour atoms (shown in green colour), and each of them has their respective four neighbour atoms including the central blue atom.



(a) (b)

Figure B.4: A geometric construction of a molecule with (a) $n = 4$ bonds per atom and (b) $n = 3$ bonds per atom .

To estimate the *maximum* number of angular forces calculations per atom we calculate them for the central blue atom. The number of ways in which the central blue atom makes an angular bond with only first neighbours (green atoms) is equal to the number of ways in which it can choose any two of the green atoms, which is ${}^4C_2$. In general case for n bonds per atom, it is ${}^nC_2$ which is $n(n-1)/2$. Next, the central blue atom can also make angular bonds with one green atom and one of its other neighbours (i. e. purple, grey, orange or red atoms). The number of ways in which this can be done is equal to the number of ways the central blue atom chooses one of the green atoms (i. e. n ways) times the number of ways the chosen green atom chooses one of its neighbours excluding the blue atom (i. e. $(n-1)$ ways). This makes the total equal to ${}^nC_2 + n(n-1)$. Thus the maximum number of angular forces calculations n_a per atom is $\mathbf{\frac{3}{2}n(n-1)}$.

The estimation of the maximum number of torsional forces calculations n_t per atom is done similarly as the previous calculation. However, the difference is that for torsional forces we have to make a group of four atoms connected in a chain fashion.

For this we look at Figure B.4(b). We need to calculate how many groups of four atoms the central blue atom can make. The central blue atom can make an outer group (shown with the red dashed loop) or an inner group (shown with the blue dashed loop) depending on its position in the group. The number of outer groups that the central atom makes is equal to the number of ways in which the central blue atom chooses one of its first green neighbours times the number of ways the chosen green atom further chooses one of its red neighbours times the number of ways the chosen red atom, finally chooses one of its grey neighbours. This combines into $= n \times (n-1) \times (n-1)$

The number of inner groups (shown with the blue dashed loop in Figure B.4) which the central blue atom makes is equal to the number of ways the central blue atom chooses any two of its first neighbour green atoms times the number of ways one of the two chosen green atoms is selected times the number of ways the selected green atom then chooses one of the red neighbour atoms. This combines into ${}^{n}C_2 \times 2 \times (n-1)$.

This gives the total torsional groups and thus the maximum number of torsional forces calculations n_t per atom is ${}^{n}C_2 2(n-1) + n(n-1)^2 = \mathbf{2n(n-1)^2}$.

B.3 Gold-molecule force calculations

Covalent bonds are usually modeled using harmonic potentials, where the restoring force increases linearly with the bond-length. This simple potential can describe the intermolecular bonds very well and is a good assumption in most situations where the bonds are not stretched enough to break them. However, for studying or simulating the bond formation between the metallic lead (Au) and the anchoring group (N or S) one has to look for more advance potentials like Morse and Lennard-Jones (LJ) potentials. As the Morse potential decays faster than the LJ potential, we use it to simulate the stronger Au-N bond, while LJ potentials are used to simulate Au-C and Au-H bonds.

B.3.1 Morse potential: Au-N bond

The Morse potential is given as:

$$E = \sum_{i}^{N} \sum_{j \neq i}^{N} D_{\mathrm{e}} \left(1 - e^{-\alpha(r_{ij} - r_{\mathrm{eq}})}\right)^2 \tag{B.1}$$

Here, $\alpha = \sqrt{\kappa_{\mathrm{e}}/2D_{\mathrm{e}}}$ and $\kappa_{\mathrm{e}} = \kappa_{\mathrm{Au-N}}$ is the force constant at the minimum of the potential where a harmonic approximation is valid. From here the k^{th} component of the force on an atom with index a can be written as

$$
\begin{aligned}
F_{ak} &= -\frac{\partial E}{\partial r_{ij}}\frac{\partial r_{ij}}{\partial k_a} \\
&= -\frac{\partial}{\partial r_{ij}}\sum_{i}^{N}\sum_{j\neq i}^{N} D_{\mathrm{e}}\left(1-e^{-\alpha(r_{ij}-r_{\mathrm{eq}})}\right)^2\frac{\partial r_{ij}}{\partial k_a} \\
&= -\sum_{i}^{N}\sum_{j\neq i}^{N} 2D_{\mathrm{e}}\left(1-e^{-\alpha(r_{ij}-r_{\mathrm{eq}})}\right)\alpha e^{-\alpha(r_{ij}-r_{\mathrm{eq}})}\left[\frac{x_a-x_j}{r_{aj}}\delta_{ia}-\frac{x_i-x_a}{r_{ia}}\delta_{aj}\right] \\
&= -2\alpha D_{\mathrm{e}}\left[\sum_{j\neq a}^{N} e^{-\alpha(r_{aj}-r_{\mathrm{eq}})}\left(1-e^{-\alpha(r_{aj}-r_{\mathrm{eq}})}\right)\frac{x_a-x_j}{r_{aj}}\right. \\
&\quad \left.-\sum_{i\neq a}^{N} e^{-\alpha(r_{ia}-r_{\mathrm{eq}})}\left(1-e^{-\alpha(r_{ia}-r_{\mathrm{eq}})}\right)\frac{x_i-x_a}{r_{ia}}\right] \\
&= -4\alpha D_{\mathrm{e}}\sum_{i\neq a}^{N} e^{-\alpha(r_{ia}-r_{\mathrm{eq}})}\left(1-e^{-\alpha(r_{ia}-r_{\mathrm{eq}})}\right)\frac{x_a-x_i}{r_{ia}}
\end{aligned}
\tag{B.2}
$$

B.3.2 Lennard-Jones (LJ) potential

The LJ potential has the folowing functional form

$$
E = 4\epsilon\sum_{i}^{N}\sum_{j\neq i}^{N}\left[\left(\frac{\sigma}{r_{ij}}\right)^{12}-\left(\frac{\sigma}{r_{ij}}\right)^{6}\right] \tag{B.3}
$$

Same as before the k^{th} component of the force on an atom with index a can be written as

$$
\begin{aligned}
F_{ak} &= -\frac{\partial E}{\partial r_{ij}}\frac{\partial r_{ij}}{\partial k_a} \\
&= -4\epsilon\frac{\partial}{\partial r_{ij}}\sum_{i}^{N}\sum_{j\neq i}^{N}\left[\left(\frac{\sigma}{r_{ij}}\right)^{12}-\left(\frac{\sigma}{r_{ij}}\right)^{6}\right]\frac{\partial r_{ij}}{\partial k_a} \\
&= -4\epsilon\sum_{i}^{N}\sum_{j\neq i}^{N}\left[-12\frac{\sigma^{12}}{{r_{ij}}^{13}}+6\frac{\sigma^{6}}{{r_{ij}}^{7}}\right]\left[\frac{x_a-x_j}{r_{aj}}\delta_{ia}-\frac{x_i-x_a}{r_{ia}}\delta_{aj}\right] \\
&= -48\epsilon\sum_{i\neq a}^{N}\left[-2\frac{\sigma^{12}}{{r_{ai}}^{14}}+\frac{\sigma^{6}}{{r_{ai}}^{8}}\right](x_a-x_i)
\end{aligned}
\tag{B.4}
$$

The position of the energy minimum and the width and depth of the potential well in both the Morse and the LJ potentials have to be determined using the experiments. For this the deformation in the molecular structure on absorption on a metallic surface, its absorption height and absorption energy can be used to fix the unknown parameters. For a proof of principle demonstration of the simulation, we have used the following parameters in our case:

Table B.1: Parameters used in the simulation

Parameters	Values	Units
κ_{Au-N}*	325	N/m
D_e¶	1	eV
r_{eq}	2.5	Å
σ	2.2	Å
ϵ	0.02	eV
κ_{Au-Au}*	8	N/m

* Value from Rascón-Ramos *et al.*[3].
¶Value similar to Fournier *et al.*[4].

[3] Habid Rascón-Ramos et al. In: *Nature Materials* 14 (2015), p. 517.
[4] N. Fournier et al. In: *Phys. Rev. B* 84 (2011), p. 035435.

Appendix

C. Shot noise

C.1 Excess Noise derivation

We start by writing the total noise power as the sum over noise coming from individual sources times the respective transfer function they see.

$$S_{\text{tot}}(\omega, V) = \sum S_n H_n = S_{\text{m}}/\left|\beta(\omega)\right|^2 \tag{C.1}$$

It is important to note that these transfer functions depend on the position of the source in the system and can be different for each noise source. Expanding this over the known sources we have,

$$S_{\text{m}}/\left|\beta(\omega)\right|^2 = S(V,\omega)\left|H_1\right|^2 + S_{\text{R1}}(V,\omega)\left|H_{\text{R1}}\right|^2 + S_{\text{amps}}(V,\omega)\left|H_{\text{amps}}\right|^2 + S_{\text{x-talk}}(\omega) \tag{C.2}$$

Here, all the transfer functions ($H_1, H_{R1}, H_{\text{amps}}$) depend on $R_s(V)$. Now we can lump all the noise sources together, except the one we are interested in (i.e. $S(V,\omega)$)

$$S_{\text{m}}/\left|\beta(\omega)\right|^2 = S(V,\omega)\left|H_1\right|^2 + \tilde{S}_{\text{x}}(V,\omega) \tag{C.3}$$

Here we define, $\sum S_X(V,\omega)\left|H_X\right|^2 = \tilde{S}_{\text{x}}(V,\omega)$. Next, we make the assumption that the extrinsic noise sources can be taken as voltage independent, and that they depend only on frequency and temperature i.e.,

$$S_{\text{m}}(V) = \left|\beta(\omega)\right|^2\left[S(V,\omega)\left|H_1\right|^2 + \tilde{S}_{\text{x}}(T,\omega)\right] \tag{C.4}$$

The validity of this assumption is supported by the test described in the paper, with a 10 k Ω resistor in the position of the sample. This demonstrates that the voltage dependent noise remains well below our claimed accuracy limit, even up to 1V bias. Note that the small spurious voltage dependent noise observed in this test includes Joule heating of the test resistor, so that the actual voltage dependence of instrumental noise sources is even smaller. The above equation C.1 is the same as the equation for the measured noise power given in Chapter 4 equation 4.4.

Next, we explain how the expression for the shot noise we are interested in can be extracted. We now introduce the notion of excess noise ($S_{\text{e}} = S(V) - S(0)$).

Introducing the quantity of excess noise is used extensively in shot noise theory and experiments alike. Now, using the assumption that $\tilde{S}_x$ is not voltage dependent, we write

$$S_m(0) = \left|\beta(\omega)\right|^2 \left[S(0)\left|H_1\right|^2 + \tilde{S}_x(T,\omega)\right] \tag{C.5}$$

so that,

$$S_m(V) - S_m(0) = \left|\beta(\omega)\right|^2 (S(V) - S(0))\left|H_1\right|^2 = \left|\beta(\omega)\right|^2 S_e \left|H_1\right|^2, \tag{C.6}$$

which gives us the equation 4.5 in Chapter 4.

C.2 Two channel fit

We will include here a second constant transmission channel to our model described in chapter 5 to explain the nonlinear shot noise data shown in Figure 5.3. The transmission value for this second channel is extracted from the experimental dataset. For this we need to solve a set of equations for the low bias noise and differential conductance:

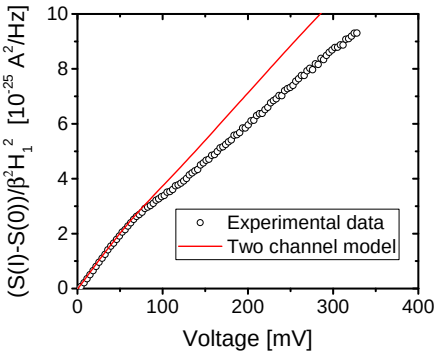
$$S_I = 4\frac{e^3}{h} V \left[T_1(1-T_1) + T_2(1-T_2)\right] \tag{C.7}$$

Next, one can input T_2 in terms of T_1 using Landauer's conductance formula i. e. $T_2 = G_0 - T_1$, here $G_0 = G(0V)$. This gives:

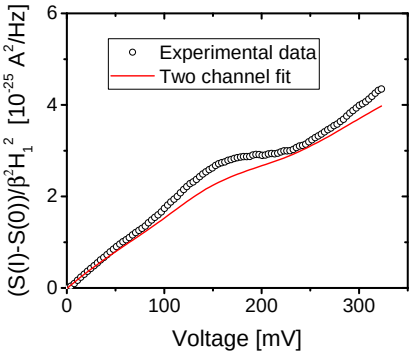
$$\frac{S_I}{V} = 4\frac{e^3}{h} \left[T_1(1-T_1) + (G_0 - T_1)(1 - G_0 + T_1)\right] \tag{C.8}$$

In the above equation left hand side is the slope of measured experimental noise close to zero bias. This can be obtained from experiment. Thus we are left with a quadratic equation in T_1. On solving this we can get the zero bias transmission for the two channels involved in transport i. e. T_1 and T_2.

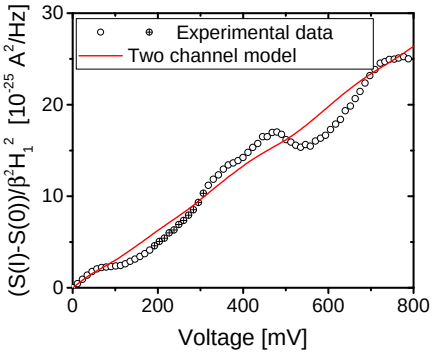
However, we don't know how the transmission of two channels will evolve at higher bias. So, we make an assumption that the second channel transmission remains constant at all bias and the first channel transmission mimics the measured differential conductance shifted down by a value equal to the transmission of second channel. This constant transmission assumption though adds to the noise calculated by the model, but it smooths out the non-linearity as shown in Figure C.1.



(a)



(b)



(c)

Figure C.1: Two channel fit after assuming a constant transmission contribution from the second channel for (a) Ex1, (b) Ex2 and(c) Ex3. The points for which the noise spectra show non-white character are shown with filled circles.

Appendix

D. Robust procedure for creating and characterizing the atomic structure of scanning tunneling microscope tips

The work is done in collaboration with - Koen M. Bastiaans, Milan P. Allan and Jan M. van Ruitenbeek and is published in *Beilstein Journal of Nanotechnology, 8, 2389-2395 (2017)*

Scanning tunneling microscopes (STM) are used extensively for studying and manipulating matter at the atomic scale. In spite of the critical role of the STM tip, procedures for controlling the atomic-scale shape of STM tips have not been rigorously justified. Here, we present a method for preparing tips *in-situ* and for ensuring the crystalline structure and reproducibly preparing tip structure up to the second atomic layer. We demonstrate a controlled evolution of such tips starting from undefined tip shapes.

Many techniques are available for preparing atomically clean sample surfaces, including repeated cycles of sputtering and annealing in case of metals, by fresh cleavage in case of suitable materials, and by high-temperature annealing, as for many semiconductors. However, a well defined tip structure at the atomic scale is still hard to achieve. Mechanical grinding[1], electro-polishing[2] or electrochemical etching[3,4] are standard *ex-situ* methods for preparing microscopically sharp tips. The tip apex can be cleaned *in-situ* using e.g. Ar ion sputtering or electron bombardment[5], but this may disrupt crystalline structure, which cannot be repaired by annealing since this renders a blunt tip. For all these methods, at the atomic scale the tip structure is poorly controlled and could even have multiple local apexes. For many purposes this does not hamper STM operation, since the tunnel current decays exponentially with tunnel gap so that the atom closest to the surface will dominate the imaging signal. However, the reproducible shape of current-voltage spectra depends strongly on the

[1] Gerd Binnig et al. In: *Phys. Rev. Lett.* 49 (1982), p. 57.
[2] Kojima Isao and Kurahashi Masayasu. In: *Hyomen Kagaku* 9 (1988), p. 621.
[3] Michael J. Heben et al. In: *Journal of Microscopy* 152 (1988), p. 651.
[4] Victor A. Valencia et al. In: *Journal of Vacuum Science & Technology A: Vacuum, Surfaces, and Films* 33 (2015), p. 023001.
[5] S. Ernst et al. In: *Science and Technology of Advanced Materials* 8 (2007), p. 347.

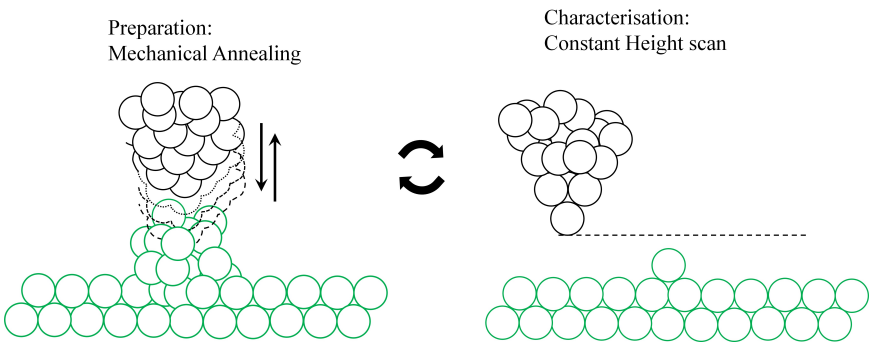


Figure D.1: Schematic representation of the tip preparation process, where mechanical annealing cycles were followed by constant height scans made over a single ad-atom deposited on the surface.

tip shape[6]. Controlled manipulation by STM of ad-atoms and molecules over metal surfaces depends also on the precise knowledge and reproducibility of the atomic tip structure. In the field of molecular electronics, where researchers are now trying to connect single molecules between an STM tip and a flat metal surface[7], knowledge of tip shape is crucial.

We will now present a procedure, illustrated in Fig. D.1, based upon mechanical annealing procedure[8,9] that permits arriving at reproducible crystalline tip shapes starting from any random initial tip shape, and we show how we can verify the evolution of the tip shape. For this the STM tip is indented into the flat metal surface up to a pre-set conductance value and then retracted and this cycle is repeated many times. We then exploit the capabilities of the low-temperature STM setup for imaging the evolution of the tip structure by scanning over an isolated ad-atom on the surface. The obtained STM images are convolutions of the topography and electronic states of sample and tip. Lang[10] has shown theoretically using two planar metal electrodes with a single ad-atom on each of them, that upon scanning one with the other symmetric convolutions of the topography and electronic states are expected, giving circularly symmetric images. Any asymmetry in the STM images of an isolated ad-atom will reflect the asymmetry of the atomic structure behind the front atom.

We start the experiments by depositing a single ad-atom from the Au covered PtIr tip in the center of the FCC sector of the Au(111) herringbone reconstruction, following the procedure summarized by Hla[11]. The result is imaged in the usual topographic mode of STM shown as an inset in Fig. D.2 (a), which demonstrates that the ad-atom does not have circular symmetry. In order to verify that this asymmetry is associated with the tip, we deposit a second ad-atom. The image of the second

[6] B. Ludoph and J M van Ruitenbeek. In: *Physical Review B* 61 (2000), p. 2273.
[7] Christian Wagner and Ruslan Temirov. In: *Progress in Surface Science* 90 (2015), p. 194.
[8] I. Guillamon et al. In: *Physica C: Superconductivity and its Applications* 468 (2008), p. 537.
[9] C. Sabater et al. In: *Phys. Rev. Lett.* 108 (2012), p. 205502.
[10] N. D. Lang. In: *Phys. Rev. Lett.* 56 (1986), p. 1164.
[11] Saw Wai Hla. In: *Reports on Progress in Physics* 77 (2014), p. 056502.

atom is a replica of the first, in shape and orientation, confirming that the asymmetry is associated with the tip shape.

In the next steps we use an individual ad-atom for imaging the structure of the tip apex, employing constant-height mode scans with a box size of 2 nm centered on the ad-atom. The goal is to pick up tunneling current signal from the second row of atoms above the apex atom. For FCC packing the distance to the second row is 2.5 Å larger than that to the apex atom, from which we estimate the current level to the second-row atoms at 100 pA for a current of 30 nA at the apex atom. As the tunnel current varies exponentially with distance, even small deviations from surface-parallel FCC packing of the second-layer tip atoms will give a detectable contribution. In order to scan at such high tunnel current we first switch off the current feedback and bring the tip closer to the flat part of the surface to a fixed tunnel current value. This value is chosen to ensure that the current is as high as 30 nA, when the tip is over the ad-atom during scan. Then we take the constant-height scan at a tip speed of 2 nm/s. Figure D.2(a) shows an example of the resulting image at the initial stage, before starting the tip preparation procedure.

After imaging the tip apex we move the tip to an edge of the scan range, about 700 nm away from the ad-atom, and perform a series of 20 mechanical annealing cycles. For this we use the same MATLAB controlled procedure as described above, except that we indent the tip farther until it reaches a preset conductance of 4 G_0. After 20 of these mechanical annealing cycles, we return to the original ad-atom and image it again using the same procedure as above. We repeat these steps of mechanical annealing and imaging until we obtain a symmetric tip image, as illustrated in Figs. D.2(a-f).

For analyzing the results of this procedure more quantitatively we would like to define a parameter which could capture the convergence of the tip structure to this symmetric state. For comparing the constant height images we select a contour at a fixed tunnel current level (which for our case is 13.3 nA) and fit an ellipse to this contour. From the fit we extract the ratio of major to minor axis of the ellipse, a/b, as a measure of the deviation from circular symmetry. Figure D.3 shows a plot of the evolution of the a/b ratio with the number of annealing cycles. The blue and the green data points show two independent runs, for different tips and different samples. The red dots show the start and end points for a third set of data applying 1000 mechanical annealing cycles. Surprisingly, the evolution of the tip is very regular and reproducible. Starting from uncontrolled and asymmetric tip apex configurations, we find that the a/b ratio decays following a common pattern, and arrives at similar minimum values. The deviation of about 4 % from 1 for the a/b ratio is probably limited by thermal drift and electrical noise of our system. The curve shows that the data are closely described by an exponential dependence.

To conclude, we have demonstrated a method for shaping a metallic tip apex in STM. By placing an ad-atom over a smooth Au surface the structure of the tip apex can be imaged, and we find that the shape of the STM tip evolves surprisingly smoothly and reproducibly towards an atomically sharp and symmetric structure of the second layer from the tip apex atom, starting from any random and poorly defined tip shapes.

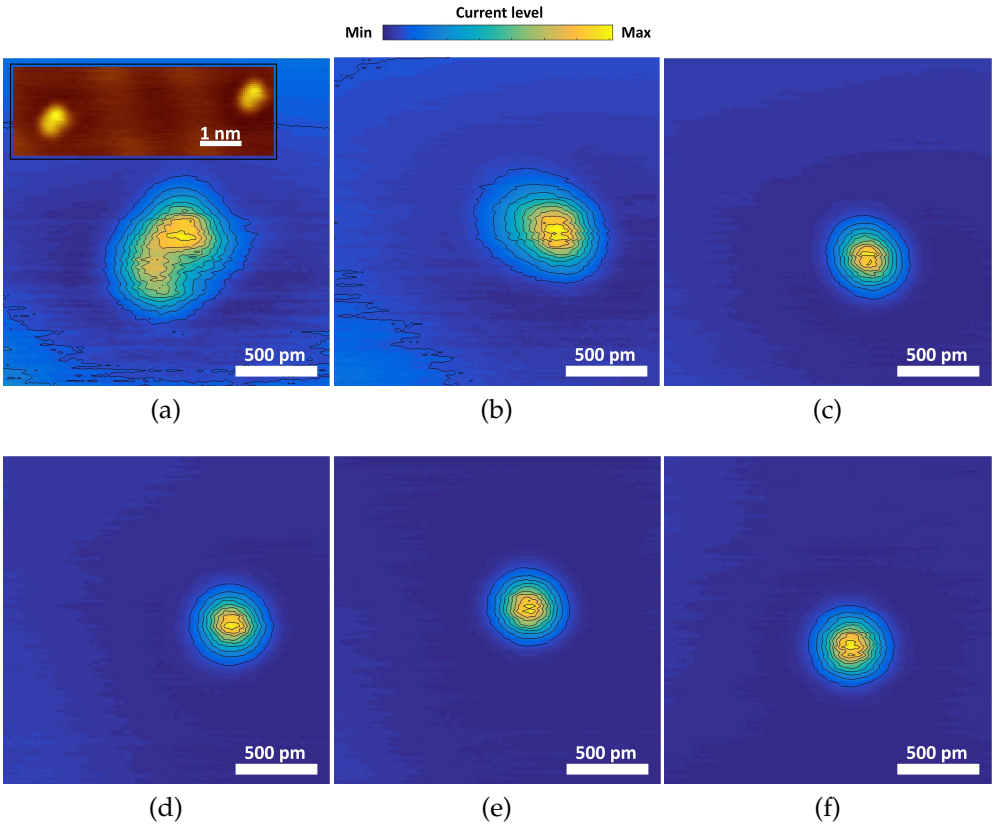


Figure D.2: The six panels show constant-height images of a single ad-atom. Here (a) shows a non-circular image of an ad-atom due to the random tip structure at the start. The inset of (a) shows constant-current image of two separate ad-atoms prepared on the surface to confirm that the asymmetric structure is due to the tip. The evolution of tip apex is shown in the next panels, leading towards a symmetric and reproducible structure (b-f). Between each of the images we apply 20 mechanical annealing cycles. The contours shown are linearly spaced in current. For ease of comparison the current levels in the images have been normalized to the maximum current level, which for the panels (a)-(f) are 66 nA, 31 nA, 26 nA, 26 nA , 25 nA and 22 nA, respectively.

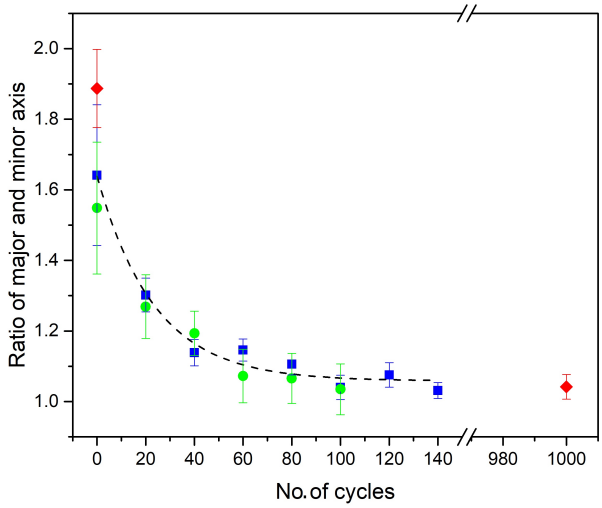


Figure D.3: Ratio of the major to minor axis of the ellipses fit showing convergence of the tip apex structure to a circularly symmetric shape. Three independent runs are shown by blue, green and red symbols. The two points shown as red diamonds represent initial and final images of an ad-atom for 1000 mechanical annealing cycles. The black dashed curve is a guide to the eye showing exponentially smooth transition to a circularly symmetric state.

Appendix

E. Inhomogeneous broadening of the conductance histograms for molecular junctions

The work is done in collaboration with - Julian M. Bopp, Carlos Sabater and Jan M. van Ruitenbeek and is published in *Low Temperature Physics, 43, 8, 905-909, (2017)*

Scanning tunnelling microscopy based break junction[1] and lithographic mechanically controlled break junction systems (MCBJ)[2] are commonly used tools for studying single-molecule electronic transport. We demonstrate here using notched-wire MCBJ technique an electronic transport study on an oligo phenylene-ethynylene (OPE-3) molecule (shown in Fig. E.1). OPE3 is a conjugated rod-like molecule with a conductance of $1 - 2 \cdot 10^{-4}\, G_0$,[3–5] where $G_0 = 2e^2/h$ is the conductance quantum. For the deprotection of the anchor groups we follow the procedure by Frisenda *et al.*[4].
Pure OPE3 is a powder, that we dissolve in dichloromethane at a concentration of 1 mmol/l. For splitting off the protecting acetyl groups we use a hydrate of tetrabutylammonium hydroxide (TBAH) solution of 10 mmol/l . The solutions were prepared by sonication for one hour to fully dissolve the compounds. Immediately following sonication of the solutions, the deprotection was done by adding 42 μL of the TBAH solution to 2 mL of the OPE3 solution. The color of the OPE3 solution changes from a pale yellow to a slightly brighter yellow.

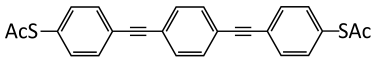


Figure E.1: Chemical structure of the OPE3 molecules used in this study.

The procedure for deposition of molecules on the junction proceeds according to the

[1] Bingqian Xu and Nongjian J. Tao. In: *Science* 301 (2003), p. 1221.
[2] J. Reichert et al. In: *Phys. Rev. Lett.* 88 (2002), p. 176804.
[3] R. Frisenda and H. S. J. van der Zant. In: *Phys. Rev. Lett.* 117 (2016), p. 126804.
[4] R. Frisenda et al. In: *physica status solidi (b)* 250 (2013), p. 2431.
[5] Veerabhadrarao Kaliginedi et al. In: *Journal of the American Chemical Society* 134 (2012), p. 5262.

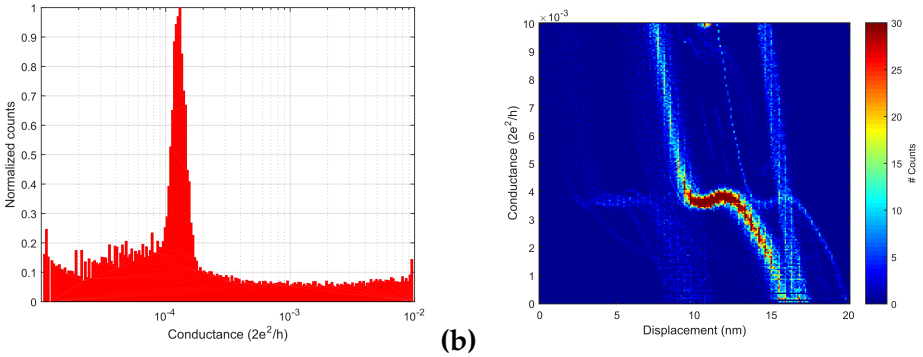


Figure E.2: Conductance histograms for OPE3 molecular junctions at 4.2 K. (a) Logarithmic one-dimensional conductance histogram showing the counts of conductance data collected for the first 900 breaking cycles of the NW-MCBJ junction. (b) The same data represented as a two-dimensional color coded histogram, with the electrode displacement plotted along the horizontal axis.

following steps. Under continuous flow of dry nitrogen the gold junction is broken by manual control and reformed to verify that the mechanism is working properly. A drop of the solution is then deposited, immediately after deprotection. The contact is then broken again to allow the OPE3 to completely cover the electrodes. The vacuum can is then closed, evacuated and the system is cooled down by immersion of the dip-stick sample holder into liquid helium.
After deposition of OPE3, already at room temperature, a broad asymmetric peak becomes visible at about $2 \cdot 10^{-4}\ G_0$ (not shown here), in agreement with the typical conductance values for OPE3 reported in the literature.[3,4,6,7] Approximately 10 % of the recorded traces contained signatures of OPE3 here. While this already demonstrates that the NW-MCBJ technique can be employed for the investigation of thiol-coupled molecules, the most remarkable observation was made when cooling down to liquid helium temperatures. After reaching helium temperatures it required several attempts at deep indentation of the wire ends for signatures of OPE3 molecules to manifest themselves in the conductance traces. But as soon as they appeared they persisted in a large number of subsequent traces. Fig. E.2a shows a logarithmic histogram for 900 breaking traces. The histogram has a sharp peak at $1.3 \cdot 10^{-4}\ G_0$, and has an unprecedently narrow width of only 40 % at FWHM. The typical width of the conductance histogram for such molecular junctions is one decade.
We gain more insight into the nature of the sharp conductance peak by making a rupture trace density plot. The same data as for the histogram we re-analyzed by aligning the points of metal-metal contact breaking in the horizontal axis for all curves. In practice we identify this point as the point with the steepest slope, and it occurs when the conductance suddenly drops below the gold atomic contact value of 1 G_0. Fig. E.2b shows a color coded plot of the density of points obtained in the plane spanned by displacement (x-axis) and conductance (y-axis). The conclusion

[6] Songmei Wu et al. In: *Nature nanotechnology* 3 (2008), p. 569.
[7] Roman Huber et al. In: *Journal of the American Chemical Society* 130 (2008), p. 1080.

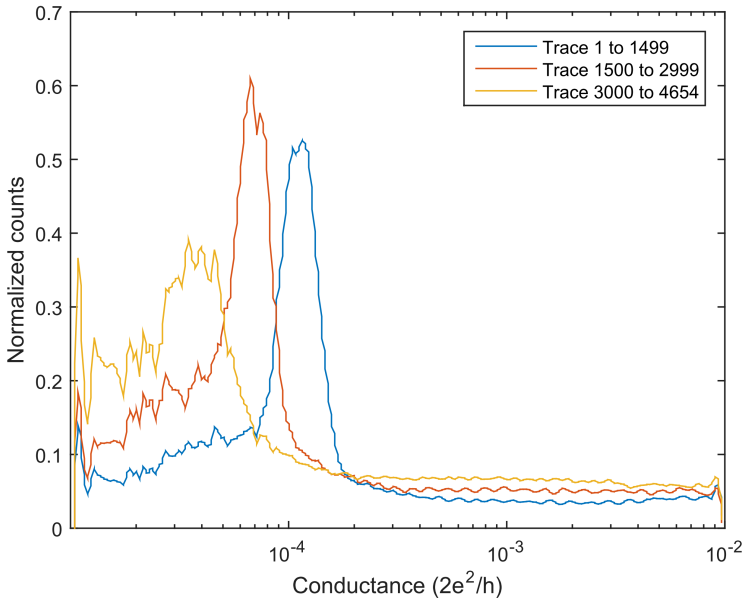


Figure E.3: Logarithmic conductance histogram of OPE3 at 4.2 K built from 4654 rupture traces, including the first 900 of Fig. E.2. The histogram shows a broad peak which can be decomposed into several distinct peaks indicating different configurations of OPE3 anchoring to the gold electrodes.

we draw from this graph is that the far majority of breaking traces follows the same pattern. The finite width of the peak in the conductance histogram is not the result of statistical variation in the molecular junction properties, but is an intrinsic property of the dependence of the molecular junction on the state of stretching of the junction. The reproducibility of the conductance traces exists despite the fact that the range of displacement is about 8 nm, much larger than the size of the molecule of less than 2 nm. During the breaking cycles the indentation of the metal-metal contacts is at least 3 nm, equivalent to a conductance of several times the conductance quantum. It seems plausible that a single OPE3 molecule is being repeatedly caught in the same junction configuration.

The data shown in Fig. E.2 represent the first 900 breaking cycles. Continuing the measurements beyond this point and taking into account the full set of rupture traces yields a much broader peak in the conductance histogram, as shown in Fig. E.3. This peak has an appearance and a width that is much better comparable with typical results presented in the literature.[3,4,6] However, in our case the wide peak appears as if being a superposition of several sharper peaks with slightly shifted conductances. This is confirmed by splitting the data set into three subsets of consecutively recorded traces, as depicted in Fig. E.3. This observation suggests that at least three different contact configurations have been probed. Each of the three is highly reproducible, but spontaneous switches from one configuration to the next occur that make the previous configuration inaccessible.

To conclude, as a first remarkable observation we find exceptionally sharp conductance histogram peaks for about 1000 conductance breaking cycles. We attribute the sharp peaks to precisely recurring molecular configurations. At the same time we find that the regularly found broad histogram peaks reported in the literature can be attributed to inhomogeneous broadening resulting from the contribution of many different molecular configurations. The reproducibility of molecular configurations is possibly related to a similar phenomenon observed for atomic contacts.[8] After training metallic contacts, i.e. applying many cycles of contact making and breaking, the conductance is found to repeatedly retrace the same evolution during breaking. This has been attributed to the effect of mechanical annealing, which removes defects from the junction area and induces ordered stacking of the atoms near the contact. We speculate that for such annealed contacts a molecule present in the junction may also retrace the same conductance many times. The fact that this has not been reported before may be associated with the fact that L-MCBJ are usually operated by mechanical motor control, which is much less precisely repeatable than the piezo control, allowed for NW-MCBJ.[9]
The observations indicate that only a single molecule takes part in the process. Although the method of deposition leads to a high degree of coverage of molecules over the metal surface, we suspect that hard closing of the junction during cool down expels a large part of the molecules. This explains why several deep-indentation attempts are required for molecular signatures to re-appear at low temperatures.

[8] C. Sabater et al. In: *Phys. Rev. Lett.* 108 (2012), p. 205502.
[9] Christian A Martin et al. In: *New Journal of Physics* 10 (2008), p. 065008.

Summary

It is fascinating that it is now routinely possible to wire nanoscale entities as small as a single molecule between two metallic leads and measure its charge transport characteristics. It has been three decades ago that the first single-molecule measurement was performed by Reed et al. Since then, many different measurements and analysis techniques have been developed to probe single-molecules. This includes the mechanically controlled break junction (notched-wire and lithographically fabricated) setups, electromigration made junctions and scanning tunnelling microscope based break junctions. In parallel, many theoretical tools have been also developed and refined for describing such transport properties and for obtaining numerical predictions. However, such theoretical tools require a large number of inputs e. g. the shape and atomic structure of the electrodes, binding configurations of the molecule, nature of the chemical bond, orientation and conformation of the molecule, the presence of defects in the leads, the presence of unwanted adsorbates, counter ions and protection groups near the molecule. However, most of the experimental techniques are statistical and do not provide these essential inputs. These inputs together can form a multi-dimensional parameter space which in experiments results in a broad peak in conductance histograms, whose width points towards spontaneous changes of these parameters from one measurement to another. Usually, only the peak value is taken as an estimate of the characteristic conductance of the molecule and compared to the theoretical models which make use of educated guessing for the input parameters. We have worked on three fronts to remove these obstacles, described in the three parts of this thesis.

Benchmark testing system for single molecules

We prepared a benchmark system for measuring the electronic transport of single-molecules, which could provide many of the above mentioned input parameters. To this effect, we modified an ultrahigh vacuum low-temperature scanning tunnelling microscope (STM) by connecting to it a real-time molecular dynamic simulator along with a home-built 3D motion control sensor. To controllably lift off a molecule de-

posited on an atomically flat metallic surface, a certain STM tip trajectory is required. This tip trajectory is not known *a priori* and will depend on the dynamics of different atoms in the molecule and the sequence in which the bonds break. As the tip trajectory is not known, it will not be possible to pre-program a trajectory for the STM tip. For this, we use a 3D motion control system which allows the operator to make an adaptable trajectory as desired. Then to know what tip trajectory has to be taken, we developed a real-time molecular dynamic simulator, which provides a visual feedback showing different dynamics involved during manipulation. This not only helps in deciding the trajectory but also provides information about the molecular conformation and binding as we lift the molecule. To demonstrate the capability of this system we have shown a successful lifting of a chain of gold atoms above the surface, and subsequently placing it back and lifting it again. This controlled manipulation of the chain is confirmed by measuring the conductance parity oscillations. These parity oscillations occur due to a different interference of electron waves when the length of the chain switches between an even and an odd number of atoms in the chain. With our controlled lifting experiment, we could also determine with certainty, the phase of these oscillations, showing that the even number of atoms in the chain leads to higher conductance.

High-bias shot-noise measurement on atomic point contacts and molecules

Earlier, low-bias shot-noise measurements have been widely used for obtaining information about the number of channels involved in electronic transport through single molecules. It has been shown recently, that shot noise can also be used for studying inelastic interactions. These measurements were performed on gold atomic contacts by recording noise up to 100 kHz, which corresponds to a bias range of around 20mV before the $1/f$ noise will start to interfere. For studying the inelastic interactions in molecules where vibration energies can be much higher than for gold, we present here an extension of this system to MHz frequency regime. This is done by introducing cryogenic amplifiers close to the atomic junction, which reduced the input capacitance by nearly two orders of magnitude. Working at higher frequencies has an additional advantage that data acquisition and averaging of the spectra can be much faster. In order to profit from this advantage, the Fourier transform and other spectral manipulations are programmed on an FPGA module, such that the speed of measurement is only limited by data acquisition. The acquisition time scales with the inverse of the lowest frequency in the spectral window. By shifting the spectral window for the Fourier transform from 250 Hz–100 kHz to a window of 122 kHz–100 MHz the measurement time is reduced by a factor 500. With the present speed-up of the system, we can perform Fourier transforms and average 10000 spectra in about 85 ms.

Using this system, a shot-noise measurement on single atom point contacts in non-linear regimes was performed, even up to 800 mV bias. These shot-noise data show highly non-linear behaviour with applied bias, which has no specific trend and is different for each contact. We recorded noise spectra showing a flat dependence on bias or even sometimes a decrease in shot noise. Our work confirmed the white character of the noise by checking its frequency spectra at each bias. Based on this the possibility of other noise sources influencing our measurements can be neglected.

Non equilibrium phonon population and heating can cause V^n (with $n = 2, 3, 4$) character in noise, as predicted by many theoretical works. The non-linearities that we measure do not show such power law characteristics. In fact, many of the non-linear deviations that we record happen at energies much higher than the Debye energy of gold. We have shown that these non-linearities can be explained in the framework of the Landauer formalism as arising due to quantum interference of electronic waves. These interferences occur because of the multiple paths that an electron can take due to elastic scattering on the defects present in the leads close to the point contact. Such quantum interference due to defect scattering gives rise to energy and voltage dependent transmission, which manifests itself as oscillations in differential conductance and non-linear shot noise. This shows that the usual interpretation of linearly increasing shot noise with applied bias or current ($S_I = 2eIF$) is valid only when there are no defects in the leads within the electron phase-coherence length, which could be up to a micron in gold. The results presented here suggest that if the position of defects in the vicinity of the point contact can be controlled, then by exploiting the quantum interference of electronic waves, one could design the transmission as desired and achieve favourable properties in conductance and noise. In a metallic point contact it is not easy to control the position of defects, but in a pre-designed molecular system, a graphene based system or a mesoscopic systems like 2DEG, it might be possible.

Furthermore, we used this state of the art high-bias shot-noise measurement setup to probe a single D_2 molecule between Pt electrodes. We show that at the energies where a vibrational mode or vibron of the molecule exists, a two-level fluctuation (TLF) is excited. Although, the contact shows the usual differential conductance spectra, the TLF is visible in the measured noise. Further, we have demonstrated that an enhanced noise spectroscopy can be done using this TLF, by studying the third derivative of the noise signal (d^3S_I/dV^3). We call this inelastic electron noise spectroscopy-3 (IENS-3). We have shown using several examples how the IENS-3 spectrum can detect inelastic scattering processes more precisely than the usual IETS spectrum. In addition to this, we also report the detection of a step-up or increase in differential conductance in the few of our Pt-D_2-Pt junctions. This increase is in contrast to the conventional picture where for a junction with conduction close to 1 G_0 shows a step-down or decrease in conductance due to back-scattering of electrons. This increase is attributed by Kristensen *et al*. to the coupling of the d-orbital of the Pt junction to its usual s-orbital, under a transverse rotational mode of vibration.

Graphene electrodes

By imaging the complete electrode-molecule junction, a better understanding of the transport measurements through single molecules can be obtained. However, it is rather impossible to image it for three dimensional metallic electrodes. Two-dimensional electrodes like graphene provide an interesting possibility to image the complete electrode-molecule junction. Other than imaging, it also provides access to modify its atomic structure and create electron scattering defects on demand. Moreover, graphene based electrodes have a stable atomic lattice at room temperature which could help in making stable room temperature devices. The electroburning technique is used widely to make graphene nanogaps. However, it does not provide

the control needed for proper characterization of the gap and it also does not allow to scale to multiple electrode circuits. Therefore, more direct cutting methods for making graphene nanogaps, specially the STM tip based cutting are explored here. Cutting using a STM tip can be seen as a controlled localized electro-burning technique. It is understood as an oxidation reaction between the C atoms in the graphene lattice and a layer of water adsorbed under ambient conditions. We have explored the parameter space, which includes tip-sample bias, current set-point and cutting duration or tip speed. Our results show that the cutting technique is more sensitive to the applied bias than to the set-point current. Furthermore, by doing a time domain analysis we found that the top layer graphene on graphite first gets lifted out of the surface and then burns. We have shown that by correctly tuning the parameters one can achieve gap size of around 1.6 nm full width half maximum.

Samenvatting

Het is fascinerend dat het nu routinematig mogelijk is om nanoschaal componenten zo klein als een enkel molecuul tussen twee metalen draden te verbinden en de elektronische transportkarakteristieken ervan te meten. Het is drie decennia geleden dat de eerste meting met een enkel molecuul werd uitgevoerd door Reed et al. Sindsdien zijn veel verschillende metingen en analysetechnieken ontwikkeld om afzonderlijke moleculen te onderzoeken. Hieronder vallen de mechanisch bestuurde breakjunctionopstellingen (zowel de ingekeepte als de lithografisch gefabriceerde constricties), de techniek om nanoschaal verbindingspunten te maken door middel van elektromigratie en puntcontacten gebaseerd op een scanning-tunnelingmicroscopie. Tegelijkertijd zijn er ook veel theoretische hulpmiddelen ontwikkeld en verfijnd voor het beschrijven van dergelijke transporteigenschappen en het doen van numerieke voorspellingen. Dergelijke theoretische gereedschappen vereisen echter een groot aantal invoer-gegevens (inputs) waaronder informatie over de vorm en atomaire structuur van de elektroden, bindingsconfiguraties van het molecuul, aard van de chemische binding, oriëntatie en conformatie van het molecuul, de aanwezigheid van defecten in de verbindingsdraden, de aanwezigheid van ongewenste adsorbaten en informatie over tegenionen en beschermende groepen nabij het molecuul. Echter, de meeste experimentele technieken zijn gebaseerd op statistische gegevens en kunnen daarom deze essentiële inputs niet leveren. Samen kunnen deze inputs een multidimensionaal domein van parameters vormen dat bij experimenten resulteert in een brede piek in een geleidingshistogram, waarvan de breedte de spontane veranderingen van deze parameters van de ene naar de andere meting aangeeft. Gebruikelijk is het om alleen de piekwaarde te nemen als een schatting van de karakteristieke geleiding van het molecuul en deze te vergelijken met het theoretische model dat deze inputs als vrije parameters neemt. We hebben op drie fronten gewerkt aan het verwijderen van deze beperkingen, zoals beschreven in de drie delen van dit proefschrift.

Benchmark-testsysteem voor afzonderlijke moleculen

We hebben een benchmarksysteem ontwikkeld voor het meten van het elektronische transport van afzonderlijke moleculen, dat veel van de bovengenoemde invoerparameters kan leveren. Hiertoe hebben we een ultrahoge vacuüm lage-temperatuur scanning tunneling microscoop (STM) aangepast door er een real-time moleculaire dynamica simulator aan te koppelen samen met een zelfgebouwde sensor waarmee 3D bewegingen gestuurd kunnen worden. Om een molecuul dat is gedeponeerd op een atomair plat metallisch oppervlak controleerbaar op te tillen, is een bepaald traject van de STM punt (de tip) vereist. Het traject van de tip is niet a priori bekend en zal afhangen van de dynamica van verschillende atomen in het molecuul en de volgorde waarin de bindingen breken. Omdat de baan van de tip niet bekend is, is het niet mogelijk om vooraf een traject voor de STM-tip te programmeren. Hiervoor gebruiken we een 3D-bewegingscontrolesysteem waarmee de operator een aanpasbaar traject kan maken naar wens. Om vervolgens te weten welk tiptraject moet worden genomen, hebben we een realtime moleculaire dynamica simulator ontwikkeld, die visuele feedback kan leveren over de verschillende dynamische processen tijdens de manipulatie. Dit helpt niet alleen bij het bepalen van het traject, maar biedt ook de gewenste informatie over de moleculaire conformatie en binding terwijl we het molecuul optillen. Om de prestaties van dit systeem te demonstreren, hebben we getoond dat een ketting van goudatomen succesvol van het oppervlak kan worden opgetild, en vervolgens kan worden teruggeplaatst en opnieuw kan worden opgetild. Deze gecontroleerde manipulatie van de ketting wordt bevestigd door tijdens de experimenten de pariteitsoscillaties in de geleiding te meten. Deze pariteitsoscillaties treden op door interferentie van de elektronengolven wanneer de lengte van de ketting schakelt tussen even en een oneven aantal atomen in de keten. Met ons gecontroleerd hefexperiment konden we ook met zekerheid de fase van deze oscillaties bepalen, wat aantoont dat een even aantal atomen in de keten tot een hogere geleiding leidt.

Hagelruismeting bij hoge spanning op atomaire puntcontacten en moleculen

Eerder werden metingen van zogeheten Hagelruis, met een lage bias (potentiaal verschil) gebruikt voor het verkrijgen van informatie over het aantal kanalen dat betrokken is bij elektronisch transport door enkele moleculen. Onlangs is aangetoond dat hagelruis ook kan worden gebruikt voor het bestuderen van inelastische interacties. Deze metingen werden uitgevoerd op atomiare contacten van goud door het registeren van ruis tot 100 kHz, wat overeenkomt met een biasbereik tot ongeveer 20mV voordat de $1/f$ -ruis begint te interfereren. Voor het bestuderen van de niet-elastische interacties in moleculen waar de trillingsenergie veel hoger kan zijn dan voor goud, presenteren we hier een uitbreiding van dit systeem naar een MHz frequentiebereik. Dit wordt gedaan door cryogene versterkers in de buurt van het atomaire circuit te introduceren, waardoor de ingangscapaciteit met bijna twee ordes van grootte is verminderd. Werken op hogere frequenties heeft het bijkomend voordeel dat data-acquisitie en middeling van de spectra veel sneller kunnen zijn. Om van dit voordeel te profiteren, zijn de Fourier-transformatie en andere spectrale manipulaties geprogrammeerd op een FPGA-module, zodanig dat de snelheid van

de meting alleen wordt beperkt door data-acquisitie. De acquisitietijd schaalt met de inverse van de laagste frequentie in het spectrale venster. Door het spectrale venster te verschuiven van 250 Hz - 100 kHz naar een venster van 122 kHz - 100 MHz, is de meettijd verminderd met een factor 500. Met de huidige versnelling van het systeem, kunnen we Fourier-transformaties en middeling van 10000 spectra uitvoeren in ongeveer 85 ms.

Door middel van dit systeem is het mogelijk om een hagelruismeting uit te voeren met contacten van één atoompunt in niet-lineair regime, zelfs tot 800mV bias. Deze gegevens voor hagelruis tonen zeer niet-lineair gedrag bij de toegepaste bias, die geen specifieke trend heeft en voor elk contact anders kan zijn. We hebben ruisspectra waargenomen die met bias een afvlakking, of soms zelfs een afname laten zien van de hagelruis. Ons onderzoek bevestigt het witte karakter van de ruis door bij elke bias spanning de frequentiespectra te controleren. Op basis hiervan kan de kans dat andere ruisbronnen onze metingen beïnvloeden worden verwaarloosd. Een niet-evenwichtsverdeling van roostertrillingen en opwarming kunnen V^n (met $n = 2, 3, 4$) karakter veroorzaken in de ruis, zoals voorspeld door diverse theoretische werken. De niet-lineariteiten die wij meten, laten dergelijke machtswetten niet zien. Sterker nog, veel van de niet-lineaire afwijkingen die we waarnemen, vinden plaats bij energie-niveaus die veel hoger liggen dan de Debye-energie van goud.

We hebben aangetoond dat deze niet-lineariteiten in het kader van het Landauer-formalisme kunnen worden verklaard als het gevolg van kwantuminterferentie van elektronische golven. Deze interferenties treden op als gevolg van de verschillende paden die een elektron kan nemen vanwege elastische verstrooiing van de defecten die aanwezig zijn in de draden dichtbij het puntcontact. Een dergelijke kwantuminterferentie als gevolg van defectverstrooiing leidt tot energie- en spanningsafhankelijke transmissie, die zich manifesteert als oscillaties in differentiële geleiding en niet-lineaire hagelruis. Dit toont aan dat de gebruikelijke interpretatie van lineair toenemende hagelruis met toegevoerde bias of stroom ($S_I = 2eIF$) alleen geldig is als er in de draden geen defecten zijn binnen de elektronenfase-coherentie lengte, die in goud tot een micron lang zou kunnen zijn. Het hier gepresenteerde resultaat suggereert dat als de positie van defecten in de buurt van het puntcontact kan worden gecontroleerd, door de kwantuminterferentie van elektronische golven te benutten, de transmissie naar wens kan worden ontworpen en gewenste eigenschappen in geleiding en ruis worden bereikt. In een contact met een metalen punt is het niet eenvoudig om de positie van defecten te controleren, maar in een vooraf ontworpen moleculair systeem, een systeem gebaseerd op grafeen of mesoscopische systemen zoals een twee-dimensionaal elektrongas, is dit mogelijk.

Daarnaast hebben we gebruik gemaakt van deze state-of-the-art high bias hagelruis meetopstelling om een enkel D_2 molecuul tussen Pt-elektroden te onderzoeken. We laten zien dat op de energie-niveaus waar een vibrationele toestand of vibron van het molecuul bestaat, een twee-niveaufluctuatie (TLF) wordt opgewekt. Hoewel het contact de gebruikelijke differentiële geleidingsspectra weergeeft, is de TLF zichtbaar in de gemeten ruis. Verder hebben we aangetoond dat een verbeterde ruis spectroscopie kan worden bereikt met behulp van deze TLF, door het bestuderen van de derde afgeleide van het ruissignaal (d^3S_I/dV^3). We noemen dit inelastische elektronenruis-spectroscopie-3 (IENS-3). We hebben met behulp van verschillende voorbeelden aangetoond hoe het IENS-3-spectrum inelastische verstrooiingsprocessen nauwkeuriger kan detecteren dan het gebruikelijke IETS-spectrum.

Daarnaast rapporteren we ook een detectie van een toename (step-up) van de differentiële geleiding in enkele van onze Pt-D_2 -Pt-verbindingscircuits. Deze verhoging is in tegenstelling met het conventionele beeld, waarbij voor een verbindingspunt met een geleiding dicht bij 1 G_0, een afname (step-down) van de geleiding te zien is als gevolg van terugverstrooiing van elektronen. Deze toename wordt toegeschreven door Kristensen *et al*. aan de koppeling van het d-orbitaal van een Pt junctie aan zijn gebruikelijke s-orbitaal, onder invloed van een transversale rotatie modus van vibratie.

Grafeenelektroden

Door de volledige elektrode-molecuulverbinding zichtbaar te maken, is het mogelijk om de transportkarakteristieken van metingen door afzonderlijke moleculen beter te begrijpen. Het is echter onmogelijk om driedimensionale metalen elektrodes in beeld te brengen. Tweedimensionale elektroden zoals grafeen bieden een interessante mogelijkheid om de volledige elektrodemolecuulverbinding in beeld te brengen. Naast de mogelijkheid tot visuele analyse, is het ook mogelijk om de atoomstructuur ervan aan te passen en desgewenst elektronenverstrooiingsdefecten te creëren. Bovendien hebben op grafeen gebaseerde elektroden een stabiel atomair rooster bij kamertemperatuur dat zou kunnen helpen bij het ontwikkelen van atomaire circuits die stabiel zijn op kamertemperatuur. De elektroburning (branden van electrodes) techniek wordt op grote schaal toegepast om grafeen-nanogaps te maken. Deze techniek biedt echter niet de mate van controle die nodig is voor een goede karakterisering van de nanogap en kan niet geschaald worden voor een circuit met meerdere elektroden. Daarom zijn meer directe snijmethoden voor het maken van grafeen nanogaps verkend, waarbij een specifieke focus is gelegd op bewerkingstechnieken met behulp van de STM-tip. Snijden met een STM-tip kan worden gezien als een gecontroleerde gelokaliseerde elektro-verbrandingstechniek. Er wordt voorgesteld dat dit optreedt vanwege een oxidatiereactie tussen de C-atomen in het grafeenrooster en een geadsorbeerde laag water in de toegepaste omgevingsomstandigheden. We hebben de verschillende parameters voor de wijze van snijden onderzocht, waaronder de bias van het tip-sample, het stroom set-point tijdens het bewerken, en de snijduur of de tipsnelheid. Onze resultaten laten zien dat de snijtechniek gevoeliger is voor de toegepaste potentiaal dan voor de ingestelde stroomsterkte. Bovendien, door een tijdsdomeinanalyse uit te voeren, ontdekten we dat de toplaag van grafeen die op het grafiet ligt, eerst van het oppervlak wordt getild en vervolgens wordt verbrand. We hebben aangetoond dat door het correct afstemmen van de parameters een kloofgrootte bereikt kan worden van ongeveer 1,6 nm halfwaardebreedte.

Acknowledgement

Knowledge is in the end based on acknowledgement. - Ludwig Wittgenstein

With gratitude, I would like to acknowledge the roles of various individuals whose suggestions and contributions helped me in acquiring the knowledge and shaping the work that I did during my PhD. At the onset, I would like to thank Jan, my PhD supervisor for providing consistent positive inputs and an environment with openness to new ideas and directions. I gained a lot from his vast experience and clarity on different topics. I also want to acknowledge the Nanofront funding provided by the Netherlands Organisation for Scientific Research (NWO/OCW) which made my work possible.

I would like to thank Christian Wagner, with whom I got an opportunity to work during the first year of my PhD. I learned a lot from him and it provided me a good kick start on the project on atom manipulation. Thanks Federica for being there in the lab all throughout like a ghost - monitoring, talking, assisting, supporting and of course making lame Italian jokes. Helpful discussions and brainstorming with you helped me stay focused and keep moving on track. A warm and big thanks to Carlos whose ever charming take on problems and never give up attitude provided a jolly environment during work. His late working hours fitted my schedule as well, making us also good chat buddies. He encouraged me also to continue his work on shot noise and spent hours explaining and sharing his complicated LabVIEW program which he built to control the system.

I worked with a lot of bachelors and masters students, a total of eight, during my PhD period. This includes in chronological order Jacob, Ujjwal, Kim, Ahmad, Dyon, Julian, Akira and Tobias. I would like to give my sincere thanks to all of you and acknowledge your contributions which make parts of my PhD thesis. I was lucky to get so many bright young minds to work with. I would not be able to put you in any particular order, but after working with different students in different research projects, I realized that a student or a good researcher has (or requires) the following attributes in increasing order - knowledge, intelligence and perseverance (or KIP).

I would like to give a special thanks to Kim who did his masters project and

then also joined for a PhD in our group. Without his significant contributions in the graphene electrodes project, we would not have made much progress there. I still enjoy immensely the helpful and intriguing discussions throughout with him. And many times his habit of repeating next day the same discussion as we never had one on the topic earlier was really fun.

It would not be complete if I would not thank Kaveh, Sander, Jaap, Aniket, Sasha, Hasan, Johannes, Daniel, Nikita, Koen, Gesa, Vitaly, Irene, Martin, Prateek, Amrita, Alexander, Daan, Stefano and Huseyin for providing an interesting and charming environment. I would like to thank also the fine mechanical department and the electronics department, especially Chris, Bert, Peter, Emiel, Fred, Ruud, Raymond and Arno for their prompt and immediate help. Chris and Bert, thanks for your constant help in repairing the STM, making the gas injection lines, protecting my cryogenic amplifiers and lending various tools and measurement instruments for an indefinite time. I don't think without your support I could have gone very far. Helium was at the heart of all my experiments and even after the large appetite of 'the Beast', Hans you never let it go empty, thanks for that. Thanks also to Wilfred, René and Ruud, who kept the supply of Helium running when Hans retired. Thanks to Eric and Ruud in the ICT department who helped me in solving the problems with my laptop. A sincere thanks goes to Charlotte and Ellie who made all the administrative tasks extremely streamlined and easy. I would also like to thank Marcel Hesselberth, although he was not directly linked to my projects, occasional discussions with him helped in casting my ideas. Thanks, Prof. Peter Gast and Christian Glass with helping me in the MRI experimental course which I taught in the first three years of my PhD. Thanks, Milan and Koen for the wonderful few-weeks-project we did together. I would like to thank Dr. Manohar Kumar for leaving behind such a beautifully written PhD thesis. Your thesis was almost like a full-time post-doc who I could ask in case of any doubt.

I enjoyed the Casimir courses and summer schools and I made many friends from Leiden and also other colleges. Among those, I would like to thank Gaurav from TU Delft together with whom I began the graphene project. I have profited from the exchange of ideas with him and he also provided the graphene samples with cuts made with the helium ion milling process. Thanks also for giving me the opportunity to become a *paranymph* in your PhD defence ceremony in TU Delft. I want to thank also Biswajit whom I met in one of the summer schools and enjoyed since then having many informal discussions on various topics ranging from the current political situation in India and the growing trend in artificial intelligence. Thanks for also introducing me to the Sublime editor and I have to say it was way better than TeXworks that I was using earlier to write my thesis.

I would like to thank all my close friends from India who kept a consistent and sometimes overwhelming supply of messages in WhatsApp, keeping the Indian humour alive in the Netherlands. I would like to thank Samyak, my high-school friend who moved to the Netherlands 1.5 years back. Catching-up with you was always a quick revival of my childhood days and my hometown in India. I want to thank my amma, babba, dadi, Mudit, Akansha and Willine for the wonderful support as a family. I can't thank you enough Eva for the love and support you provided all these years and before. The time that I spent during my PhD in Leiden was beautiful and I will never forget it.

Curriculum vitae

I was born in India in the beautiful city of Nainital in 1985. Being intrigued by the mechanics of the things around me, I did my graduation and postgraduation in mechanical engineering. At the end of my post-graduation from the Indian Institute of Science Bangalore in India, I got interested to study and understand the mechanics at the scale of fundamental particles. So, following my interest, I decided to quit my job in the automobile industry to study physics. I then completed my second postgraduation in physics with honours from the University of Paris Diderot in France. Subsequently, I joined for my PhD at Leiden University in the field of molecular electronics in September 2013. I would like to continue doing further research and link fundamental studies with applications.

Publications

1. S. Tewari, C. Sabater, M. Kumar, S. Stahl, B. Crama and J. M. van Ruitenbeek "Fast and accurate shot noise measurements on atomic-size junctions in the MHz regime". In: Review of Scientific Instruments **88**, p. 093903 (2017).

2. S. Tewari, K. M. Bastiaans, M. P. Allan and J. M. van Ruitenbeek "Robust procedure for creating and characterizing the atomic structure of scanning tunneling microscope tips". In: Beilstein Journal of Nanotechnology **8**, p. 2389 (2017).

3. J. M. Bopp, S. Tewari, C. Sabater and J. M. van Ruitenbeek "Inhomogeneous broadening of the conductance histograms for molecular junctions". In: Low Temperature Physics **43**, p. 905 (2017).

4. S. Tewari, J. Bakermans, C. Wagner, F. Galli and J. M. van Ruitenbeek "Human-machine augmented system to control single atoms and molecules" to be submitted.

5. S. Tewari, J. M. van Ruitenbeek, R. Korytár and F. Evers "Review: Advances and challenges in single-molecule electronics" to be submitted.

6. S. Tewari and J. M. van Ruitenbeek "Anomalous non-linear shot noise at high voltage bias" to be submitted.

7. D. van Vreumingen, S. Tewari, F. Verbeek and J. M. van Ruitenbeek ""Real-time" molecular dynamics simulation using GPU implementation to control single molecules over metallic surfaces using STM" to be submitted

8. S. Tewari, J. Bakermans, C. Wagner, F. Galli and J. M. van Ruitenbeek "Testing monoatomic gold chains using a 3D motion controlled scanning tunneling

microscope" Nederlandse Vacuümvereniging (NEVAC) blad, 12 (2015).

9. S. Tewari, P. Roulleau, C. Grenier, F. Portier, A. Cavanna, U. Gennser, D. Mailly and P. Roche "Robust quantum coherence above the Fermi sea". In: Physical Review B **93**, p. 035420 (2016).

10. S. Tewari, T.N.C. Anand, M.P. Nishikant and R.V. Ravikrishna "Study of liquid fuel transport in a small carburetted engine in the context of cold-start HC emission control". In: Sadhana **39**, p. 549 (2014).

Index

1,4-bis(4-pyridyl)benzene, 68
1/f-noise, 92

Alkane dithiols, 15
Atomic chains, 44
  Lifting, 48, 52, 187
Atomic manipulation
  3D, 37
  Lateral, 36, 46
  Vertical, 36

Benzenedithiol, 13

Capacitive scanning technique, 168
Conductance histogram, 5, 11, 211
Conductance quantization, 4
Cryogenic amplifiers, 95, 100

Deuterium molecule, 146
  Step-down conductance, 147
  Step-up conductance, 143, 151
Dickie's Relation, 106
Differential shot-noise, 127
Dipstick design, 96

Excess noise, 103
  Derivation, 200

Field Programmable Gate Array (FPGA), 95
  Fast Fourier transform, 101

GPU implementation, 70, 190
  CUDA, 70, 191
  Frameworks, 70
  Hardware structure, 191
  Memory model, 192
  Programming model, 191
Graphene
  Dash-line lithography, 165
  Direct cutting methods, 163, 166
    AFM based cutting, 170
    Helium-ion milling, 167
    STM based cutting, 172
  Electroburning, 163
  Estimation of nanogap size, 166
Graphene vs metallic electrodes, 162

Herringbone reconstruction, 37, 45

Inelastic electron noise spectroscopy (IENS), 149
Inelastic electron noise spectroscopy-3 (IENS-3), 149
Inelastic electron tunneling spectroscopy, 142, 149, 150
Inhomogeneous conductance broadening, 210
Injection capillary, 95, 96
Intrinsic energy dependence, 130

Joule heating, 106
Jump to contact, 47

Landauer conductance formula, 3, 120
Linear regime, 120, 129
  Noise spectroscopy, 20, 121
  Shot-noise, 120

Molecular electronics, 5, 161
  Data analysis, 11
  Electromigration BJ, 8
  MCBJ, 6, 94
  SPM, 10

Negative differential conductance (NDC), 131
Negative differential shot-noise (NDSN), 131
Non-linear regime, 122

Differential conductance, 126
Differential shot-noise, 127
T(E,V), 125

Oligo phenylene-ethynylene (OPE-3), 210

Parity oscillations, 45, 50
1D model, 51
Phase, 51
Point contact pushing, 46, 188

Quantum interference, 45, 51, 120, 124

Real-time molecular dynamic simulation
All metallic, 38
Boundary Au atoms, 40
Distance cutoff, 43
Energy, 39
Flowchart, 40, 41
Force, 40, 184
Force cut-off, 42
Normal Au atoms, 40
Setup Builder, 44
Thermostat, 42
With molecules, 69
Anchoring bonds, 68
Forces on molecule atoms, 74
Gold-gold forces, 71
Gold-molecule force, 196
Gold-molecule forces, 75
GPU implementation, 70
Intramolecular force, 195
Intramolecular forces, 76
Lennard-Jones potential, 197
Morse potential, 196
Performance, 77
Quasi-static regime, 69
Time-step, 69, 75

Scanning tunnelling microscope (STM), 2
Sharvin conductance, 3
Shot noise, 20, 91
Bandwidth, 93
Excess noise, 103
Fano factor, 92, 104, 107
Lesovik-Levitov expression, 92, 120
Negative differential shot-noise (NDSN), 131
Power spectral density, 21, 102
Single-shot measurements, 66
Smoluchowski effect, 47
STM surface
Crystallographic directions, 45
lattice, 46
Preparation, 45
STM Tip
Lateral spring stiffness, 53
Preparation, 44, 204
Super-Landauer single channel (SLSC), 131

T(E,V) surface, 129
Transmission channels, 4
Two-level fluctuations, 21, 93, 109, 144, 146, 149, 150

Vibrationally induced two-level system (VITLS), 144, 149